

UC San Diego

UC San Diego Electronic Theses and Dissertations

Title

Investigations of fluid-strain interaction using Plate Boundary Observatory borehole data /

Permalink

<https://escholarship.org/uc/item/33q4s4wn>

Author

Barbour, Andrew Jacob

Publication Date

2014

Peer reviewed|Thesis/dissertation

UNIVERSITY OF CALIFORNIA, SAN DIEGO

**Investigations of fluid-strain interaction using Plate Boundary
Observatory borehole data**

A dissertation submitted in partial satisfaction of the
requirements for the degree
Doctor of Philosophy

in

Earth Sciences

by

Andrew Jacob Barbour

Committee in charge:

Duncan C. Agnew, Chair
Prabhakar R. Bandaru
Kevin M. Brown
Yuri A. Fialko
David T. Sandwell
Frank K. Wyatt

2014

Copyright
Andrew Jacob Barbour, 2014
All rights reserved.

The dissertation of Andrew Jacob Barbour is approved,
and it is acceptable in quality and form for publication
on microfilm and electronically:

Chair

University of California, San Diego

2014

DEDICATION

To my Mother and Father, for their unwavering support.

EPIGRAPH

Remember, George: no man is a failure who has friends.

—Clarence the Angel (1946), IT'S A WONDERFUL LIFE

TABLE OF CONTENTS

Signature Page	iii
Dedication	iv
Epigraph	v
Table of Contents	vi
List of Figures	x
List of Tables	xii
Acknowledgements	xiii
Vita, Publications, and Software	xiv
Abstract of the Dissertation	xv
Chapter 1 Introduction to Plate Boundary Observatory Borehole Instrumentation	1
1.1 Instruments in PBO Boreholes	2
1.2 Borehole Strainmeters	2
1.2.1 Principles of Operation	4
1.2.2 Calibration of Instrument Strain to Earth Strain	6
1.3 Pore Pressure	8
1.3.1 Principles of Operation	9
1.3.2 Relating Pore Pressure to Volume Strain	9
1.4 Installation Effects	11
1.5 Data Resources	12
Chapter 2 Noise Levels on Plate Boundary Observatory Borehole Strainmeters in Southern California	14
2.1 Introduction	15
2.2 Data and Methods	16
2.2.1 PBO Borehole Instruments in the Anza Region	16
2.2.2 Noise-Level Estimation	19
2.3 Instrumental Noise	22
2.4 Observed Strain Noise Levels	27
2.5 Comparison with Other Estimates	30
2.6 Conclusions	35
2.7 Data and Resources	36
2.8 Appendix: Nonlinearity of the GTSM sensor	36

	2.9 Acknowledgments	41
Chapter 3	Detection of Seismic Signals Using Seismometers and Strain-	
	meters	42
	3.1 Introduction	42
	3.2 Relative Detection Threshold for Strainmeters and Seis-	
	meters	45
	3.3 Noise Estimates	48
	3.4 Results	49
	3.5 Conclusions	52
	3.6 Data and Resources	54
	3.7 Appendix: Effects of Wavefront Curvature and Attenuation	55
	3.8 Acknowledgments	56
Chapter 4	Coseismic Strains on Plate Boundary Observatory Borehole	
	Strainmeters in Southern California	58
	4.1 Introduction	59
	4.2 Coseismic Strain Estimation	60
	4.2.1 Probabilistic Offset Detection	61
	4.2.2 Application to Strain Records: Processing and	
	Calibration	62
	4.2.3 Classification of Detections	63
	4.3 Coseismic Strain Prediction	65
	4.3.1 Earthquake Catalog	67
	4.4 Results	72
	4.5 Discussion	78
	4.5.1 Comparison with Longbase Laser Strain	81
	4.5.2 Consideration of Simplifying Assumptions	82
	4.5.3 Alternative Explanations	84
	4.6 Conclusion	85
	4.7 Appendix A: Sensitivity to Strike: the Collins Valley	
	Earthquake	86
	4.8 Acknowledgements	86
Chapter 5	Modeling Strains Associated with Fluid Extraction: the Pathfinder	
	Ranch Experiment	87
	5.1 Introduction	88
	5.2 Observations at the Pathfinder Ranch	90
	5.2.1 Records of Fluid Extraction	92
	5.2.2 Validity of Calibrations	95
	5.3 Poroelasticity: Coupled Deformation and Fluid Diffusion	97
	5.3.1 General Poroelastic Boundary Value Problem	99
	5.3.2 Parameter Constraints	100

	5.3.3	Numerical Solutions	101
	5.3.4	Model Misfit: Isolated Events at PR-M	103
	5.4	Modeling Results	104
	5.5	Discussion	106
	5.5.1	Weak Diffusivity Contrast	106
	5.5.2	Low Shear Modulus	111
	5.5.3	Effects of Basin Geometry?	113
	5.5.4	Hydraulic Properties from GV3	116
	5.6	Conclusion	117
	5.7	Appendix A: Nomenclature	118
	5.8	Appendix B: Analytical Solutions to Fluid Extraction/Injection Problems	120
	5.9	Acknowledgements	120
Chapter 6		Strain Sensitivities of Well-Aquifer Systems in Southern California: Effects of the San Jacinto Fault	121
	6.1	Introduction	122
	6.2	Permeability and Fluid Flow in the Crust	123
	6.3	Methods	124
	6.3.1	Instruments	125
	6.3.2	Surface Wave Catalog and Data Processing	127
	6.3.3	Regression Analysis	134
	6.3.4	Spectral Analysis: Empirical Transfer Functions	136
	6.4	Results	137
	6.4.1	Regression Analyses	137
	6.4.2	Spectral Analyses	138
	6.5	Discussion	139
	6.5.1	Tidal Response	142
	6.5.2	Hydraulic Properties from Radial-flow Models	145
	6.5.3	Fault-normal Variation in Response	146
	6.6	Conclusions	155
	6.7	Appendix A: Time Varying Tidal Responses	155
	6.8	Appendix B: Radial Flow Models of Harmonic Well Response	161
	6.8.1	Water Heights from Pressure Head	161
	6.8.2	Pore Pressure from Strain	162
	6.9	Appendix C: Fault-normal Variation in BSM Calibrations	165
	6.10	Acknowledgements	165
Appendix A	psd:	Adaptive Sine Multitaper Power Spectral Density Estimation for \mathbf{R}	167
	A.1	Introduction	168
	A.2	Power Spectral Density Estimation	169

A.3	Further Properties of Sine Multitapers	173
A.4	Algorithm Summary	177
A.5	Application to Borehole Strainmeter Noise	179
A.6	Conclusion	184
A.7	Data and Resources	184
A.8	Appendix A: Example Usage	185
A.9	Appendix B: Comparisons with Other Methods in R . . .	187
A.10	Acknowledgments	189
Appendix B	Figures from Published Electronic Supplements	190
B.1	Laser and Wire Strainmeter Noise Variation	190
B.2	Seismic Noise, and Seismometer and LSM Detection Curves	190
B.2.1	Seismometer Noise Levels and Variation	190
B.2.2	Detection Curves for Seismometer Pairs	197
B.3	Acknowledgements	200
Bibliography	220

LIST OF FIGURES

Figure 1.1:	Schematic of a typical Plate Boundary Observatory borehole . . .	3
Figure 1.2:	Diagram of GTSM gauge configurations	5
Figure 2.1:	Map of Anza region showing PBO boreholes	17
Figure 2.2:	Processing steps to produce summary spectra	23
Figure 2.3:	Temporal changes in power levels associated with battery voltage	24
Figure 2.4:	Comparison of nominal and simulated strain data filters	28
Figure 2.5:	Median noise levels in Anza strainmeter data	29
Figure 2.6:	Variation in strainmeter noise levels	31
Figure 2.7:	Comparison of high-frequency strainmeter spectra	33
Figure 2.8:	Diagrams of GTSM installation and circuitry	37
Figure 2.9:	Non-linear gain as a function of bridge ratio	40
Figure 3.1:	Strain and seismic noise levels used in this study	50
Figure 3.2:	Relative detection curves for strain-seismometer pairs	51
Figure 3.3:	Relative SNR for strain-seismometer pairs	53
Figure 4.1:	Validation of the SN method for offset detection	64
Figure 4.2:	Example of the SN method applied to strain data	66
Figure 4.3:	Earthquakes tested for coseismic strains	73
Figure 4.4:	Coseismic strain estimates	74
Figure 4.5:	Strain offsets regressed against peak vertical velocity	79
Figure 4.6:	Strain offsets regressed against peak dynamic strain	80
Figure 4.7:	Calibration effects in offset estimation	83
Figure 5.1:	PBO borehole strainmeters in the Anza region	91
Figure 5.2:	Map of the Pathfinder Ranch	94
Figure 5.3:	Strains, pore pressures, and pumping at the Pathfinder Ranch .	96
Figure 5.4:	Shear strain variances in Pathfinder Ranch strainmeter data . .	98
Figure 5.5:	Poroelastic parameter enhancement	102
Figure 5.6:	Misfit space for poroelastic models	105
Figure 5.7:	Best-fitting model of areal strains	107
Figure 5.8:	Best-fitting model of differential extension	108
Figure 5.9:	Best-fitting model of shear strains	109
Figure 5.10:	Best-fitting model of pore pressures	110
Figure 5.11:	Hydraulic diffusivities for common geologic materials	112
Figure 5.12:	Shear modulus of crustal rock in California	114
Figure 5.13:	Generalized lithologic units at Pathfinder Ranch	115
Figure 6.1:	Pore pressure measurements in Anza	130
Figure 6.2:	Catalog magnitudes versus distance	131
Figure 6.3:	Pore pressure and strain for the Tohoku-Oki earthquake	133

Figure 6.4:	Seismic responses of pore pressure measurements	135
Figure 6.5:	Pore-pressure regressions by station	138
Figure 6.6:	Cross-spectral density analysis for the Tohoku-Oki earthquake .	140
Figure 6.7:	Pore pressure tidal response in Anza	143
Figure 6.8:	Rock porosities and densities in Anza	144
Figure 6.9:	Fracture orientations at Anza	147
Figure 6.10:	Fault-normal variation in seismic response	148
Figure 6.11:	San Jacinto fault shear strain rates	149
Figure 6.12:	Pore pressure response compared to crustal shear-strain slowness	150
Figure 6.13:	Comparison of pore pressure tidal response at B084	156
Figure 6.14:	Comparison of pore pressure tidal response at B088	157
Figure 6.15:	Comparison of pore pressure tidal response at B081	158
Figure 6.16:	Comparison of pore pressure tidal response at B086	159
Figure 6.17:	Comparison of pore pressure tidal response at B082	160
Figure 6.18:	Response functions of water wells	164
Figure 6.19:	Fault-normal variation in calibration coefficients	165
Figure A.1:	Spectral kernels	174
Figure A.2:	Spectral weighting factors	175
Figure A.3:	Effective multitaper spectral kernels	176
Figure A.4:	Adaptive PSD estimation history	180
Figure A.5:	Strainmeter data at B084 for 2011 M9 Tohoku	181
Figure A.6:	Strain spectra at B084 for 2011 M9 Tohoku	183
Figure B.1:	Noise levels and variation for the LSM	191
Figure B.2:	Noise levels and variation for wire strainmeters at the BFO . .	192
Figure B.3:	Median noise levels for borehole seismometers	193
Figure B.4:	Variation in noise levels for borehole seismometers	194
Figure B.5:	Median noise levels for surficial broadband seismometers	195
Figure B.6:	Noise variation for surficial broadband seismometers	196
Figure B.7:	Relative SNR for seismometer pairs	197
Figure B.8:	Relative detection curves for LSM-seismometer pairs	198
Figure B.9:	Relative SNR for LSM-seismometer pairs	199

LIST OF TABLES

Table 1.1: Plate Boundary Observatory data repositories	13
Table 2.1: Locations and other parameters for stations in Anza	18
Table 2.2: Spectrum estimation and fitting parameters	20
Table 2.3: Dominant periods of instrumental noise peaks	25
Table 2.4: Borehole strainmeter noise levels	32
Table 3.1: Plate Boundary Observatory instruments in Anza	44
Table 4.1: Classifications of strain offset estimates	65
Table 4.2: Locations and other parameters for stations in Anza	68
Table 4.3: Coseismic earthquake catalog	69
Table 4.4: Coseismic strains for the El Mayor Cucapah earthquake	76
Table 4.5: Comparison of statistical models of strain offsets ranked by correlation	77
Table 5.1: Representative poroelastic models	104
Table 5.2: Best-fitting poroelastic parameters	106
Table 5.3: Poroelasticity nomenclature used	119
Table 5.4: Analytical solutions to fluid extraction (or injection) problems .	120
Table 6.1: PBO stations with pore pressure sensors	126
Table 6.2: Earthquakes used in this study	127
Table 6.3: Elastic moduli based on pore pressure seismic response	141
Table 6.4: Interseismic slowness parameters	153
Table A.1: Power spectral density estimators in R	188

ACKNOWLEDGEMENTS

I am fortunate to have Prab Bandaru on my committee, as it was he who introduced me, as an undergraduate, to the fundamental aspects of academic research. Frank Wyatt inspires me through his enthusiasm and genuine nature as much now as he did before I entered graduate school. Duncan Agnew carries an incredible wealth of knowledge, which has helped me immensely. Duncan has been especially patient with me despite my poor spelling, silly mistakes, and perhaps even sillier questions. He is also one of the best listeners I know – a trait which I deeply appreciate.

I owe immense gratitude to the friends made before, and during, this process who have managed to keep me grounded in humor. In no particular order: The Matuzaks, K-Boss Ross, Lu-Bags, Crowell-Brajts, Adolph, Surly Chris, Sambo, Viggs, Latin Eric, Brentus-the-beer-snob, M’Erica, Frenchie, Danny Boy, Banger, Dylly Bob Thorton, and others I’ve assuredly missed.

I’ve known only love from my family members, and it has made all the difference in the world. Mom and Dad: as the dedication suggests, your loving support has been a major reason for my success. Grammie and Poppa Ray: I can only hope to be as vibrant, fun, and wise when I’m your age. You are shining examples of living life to its fullest. Matt and Pat: I still take all the nice stuff. Carey: the patience and love you’ve shown me over the years has been especially important to me, and I love you all the more for it.

Published Material

Chapter 2 is a reprint of *Barbour and Agnew* (2011), Chapter 3 is a reprint of *Barbour and Agnew* (2012), and Appendix A is a reprint of *Barbour and Parker* (2014). The dissertation author was the primary investigator and author of these papers, which were adapted for the dissertation.

VITA

- 2006 B. S. in Mechanical Engineering, Jacobs School of Engineering, University of California, San Diego
- 2006-2007 Staff Research Associate, University of California, San Diego (SIO/JSOE)
- 2007-2014 Graduate Student Researcher, University of California, San Diego
- 2014 Ph. D. in Earth Sciences, University of California, San Diego

PUBLICATIONS

Barbour, A. J., and D. C. Agnew, “Noise Levels on Plate Boundary Observatory Borehole Strainmeters in Southern California”, *Bulletin of the Seismological Society of America*, 101(5), 2453 – 2466, 2011, doi: 10.1785/0120110062.

Barbour, A. J., and D. C. Agnew, “Detection of Seismic Signals Using Seismometers and Strainmeters”, *Bulletin of the Seismological Society of America*, 102(6), 2484 – 2490, 2012, doi: 10.1785/0120110298.

Barbour, A. J., and R. L. Parker, “psd: Adaptive, sine multitaper power spectral density estimation for R”, *Computers & Geosciences*, 63, 1 – 8, 2014, doi: 10.1016/j.cageo.2013.09.015.

SOFTWARE

kelvin: Solutions to the Kelvin differential equation using Bessel functions. *Licensed under GNU General Public License, available at*
<http://cran.r-project.org/package=kelvin>

kitagawa: Spectral response of water wells to harmonic strain and pressure. *Licensed under GNU General Public License, available at*
<http://cran.r-project.org/package=kitagawa>

psd (with R. L. Parker): Adaptive sine-multitaper power spectral density estimation. *Licensed under GNU General Public License, available at*
<http://cran.r-project.org/package=psd>

ABSTRACT OF THE DISSERTATION

**Investigations of fluid-strain interaction using Plate Boundary
Observatory borehole data**

by

Andrew Jacob Barbour

Doctor of Philosophy in Earth Sciences

University of California, San Diego, 2014

Professor Duncan Carr Agnew, Chair

The aim of this thesis is to explore poroelastic properties near the surface of crust, on and off fault zones, using pore-pressure and strain data from the borehole strainmeter (BSM) network operated by the Plate Boundary Observatory (PBO) component of Earthscope. In particular, fluid diffusivities provide critical insight into the relationship between fluid-pressures and strain, and we use pore-pressure and borehole strain (BSM) data from the PBO to better understand this relationship. In this thesis we focus on PBO stations in the Anza region of the active San Jacinto fault, which has a seismic slip gap (and observed seismicity gap), and accommodates significant plate boundary strain. Anza is also well-instrumented: it ranks second in density of broadband seismometers, next to Parkfield in central

California.

Chapter 1 outlines the PBO borehole instrumentation, and offers some requisite background information. The remaining chapters of this thesis can be grouped into two basic categories: (I) characterization of the instruments (Chapters 2, 3, and 4), and (II) focused studies of fluid-strain interaction (Chapters 5 and 6). *Note: With the exception of the Introduction (Chapter 1), each chapter has been either reproduced from a previous publication, or written with the intent to submit for publication; hence, the attentive reader will notice redundant information (e.g., station metadata).*

Chapter 2 establishes the statistics of noise in the seismic band for data from PBO borehole strainmeters BSMs and seismometers, including cyclic (daily, weekly, or annual) variations, since a full statistical description is important in finding anomalous behaviors, and in characterizing physical sources themselves. This statistical description has been reported in *Barbour and Agnew (2011)*; a related paper (*Barbour and Parker, 2014*) documents the primary spectral-analysis tool used for this characterization (reprinted in Appendix A).

Chapter 3 builds upon Chapter 2: we used data from the same instruments to compare the seismic-wave detection capabilities of the different sensors. To make this comparison, we use the instruments' noise spectra to determine the relative signal-to-noise ratio on different sensors, as a function of the phase velocity and frequency of a signal. The BSM is less sensitive to seismic waves than surficial broadband instruments are, but more sensitive than colocated short-period geophones in the surface-wave frequency band. We reported these results in *Barbour and Agnew (2012)*.

Chapter 4 is a systematic study of the nature of apparent coseismic strains observed by the BSM using a probabilistic detection method. Rarely do the observed strains agree with predictions based on elastic dislocation modeling, and independent observations from longbase strainmeters. Surprisingly, we find no statistical evidence suggesting the effect is controlled by seismic energy density, or poroelastic effects, which suggests a localized effect or an instrumental hysteresis.

Chapter 5 presents the results from a semi-controlled experiment in fluid-

extraction. We collected multiple years of water-well pump activity near a pair of PBO strainmeters, and find remarkable agreement with the calculated extraction volumes, and the strain and pore-pressure observations. We are able to fit the borehole observations by simulating withdrawal from a poroelastic halfspace with relatively high values of hydraulic diffusivity, and low values of elastic shear modulus.

Chapter 6 is a systematic study of the pore-pressure response to seismic waves. We find strong correlations between strain and pressure at each station, and in southern California we observe a clear reduction in effect-size (scaling) at stations near the San Jacinto fault (compared to much further away). We show that this reduction is directly linked to crustal shear strain rates.

Chapter 1

Introduction to Plate Boundary

Observatory Borehole

Instrumentation

The Plate Boundary Observatory (PBO)¹ is the geodetic component of the EarthScope Facility², which has the goal of recording the spatial and temporal spectra of crustal deformation associated with the Pacific/North American tectonic plate boundary. Towards this goal the PBO maintains a large network of geodetic instrumentation: currently 1132 continuous Global Positioning Stations (GPS), 78 borehole strainmeters (BSM), 26 tiltmeters, and 6 longbase laser strainmeters (LSM), all located along the western United States. Nearly all of the boreholes with BSMs are also equipped with three-component, short period geophones (seismometers); 22 are also equipped with pore-fluid pressure (PP) and temperature (PT) sensors, and seven (all in southern California) are also equipped with strong-motion accelerometers.

Each subsequent chapter of this thesis will use data coming from many of these instruments, but primarily the BSM and PP instruments. The focus of this chapter is to outline principles of operation of these instruments, as well as discuss pertinent issues for data quality and processing. Some of the topics discussed in

¹ <http://pbo.unavco.org/>

² <http://www.earthscope.org>

this chapter will be seen in later chapters, in greater detail.

1.1 Instruments in PBO Boreholes

PBO stations located in the Anza region of southern California have the most diverse set of geophysical instrumentation. Most of these nine stations are instrumented with all of the following: BSM, PP/PT, seismometer, and accelerometer. Depths to the instruments vary among stations, but in all cases the BSM is deepest, ranging from 150 m to 300 m. The relative positions of the instruments in the borehole are consistent:

[PP containment →] PP/PT transducers → PP screen → seismometer
→ accelerometer → BSM

“PP containment” is in reference to the pressure containment device, which not all PP systems have: an inflated packer installed at locations where the screened section (“PP screen”) taps into an artesian (naturally flowing) aquifer. Figure 1.1 is an example of a schematic diagram of the orientation of the instruments in the borehole (not to scale), drawn by PBO using information obtained during installation.

Signals from these instruments are transmitted to the surface, digitized, downsampled, and logged. The logged data are then telemetered to a few centralized repositories for further distribution (Table 1.1).

The PBO borehole stations also have a number of ancillary instruments at the surface to monitor environmental conditions (barometric pressure, rain, etc.) and instrumental states (housing/electronics temperature, etc.).

1.2 Borehole Strainmeters

As was intended from the early planning stages (*Silver et al.*, 1998), nearly every PBO borehole has a BSM, installed in the top few hundred meters of the surface of the earth. Even though this style of BSM – a Gladwin-style tensor

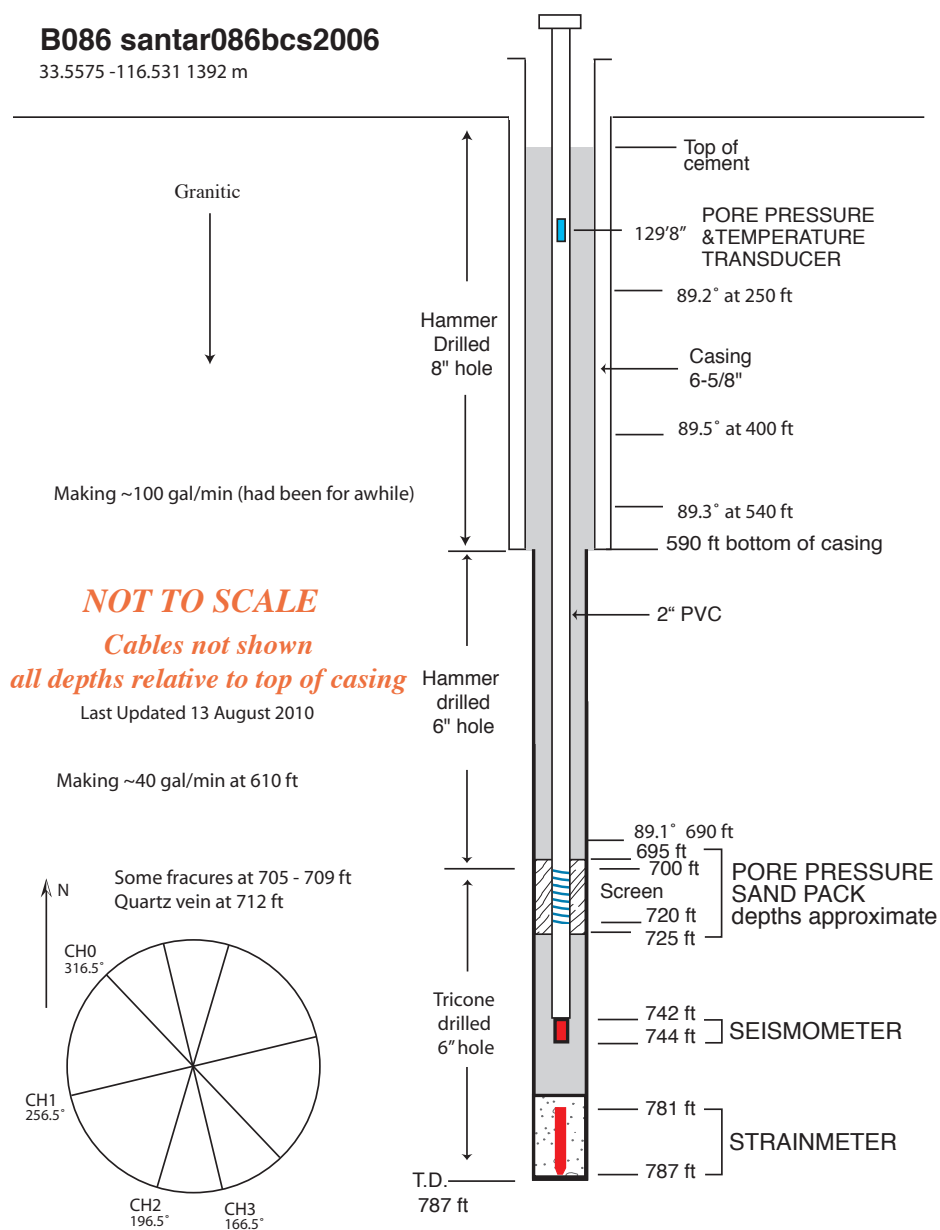


Figure 1.1: Schematic of the depths of the various instruments in the PBO borehole, taken from the geophysical logging data repository (Table 1.1) for station B086 in southern California.

strainmeter (GTSM: *Gladwin*, 1984) – has a comparatively short horizontal baseline (the outer diameter, 87 mm), the thermal stability at the depths of the BSM ensures that tectonic signals occurring over seconds-to-weeks are resolved with a large signal-to-noise ratio. In fact, a number of BSMs record episodic strain transients associated with slow slip on the Cascadia subduction zone (e.g., *Wang et al.*, 2008).

In contrast to seismic data, which are usually supported by specialized analysts and quality assurance mechanisms, BSM data are fraught with many complications which must be considered by most end-users; this has proven to be a substantial barrier to adoption over a wider user-base. The following section outlines the principles behind the operation and calibration of the BSM, and discusses signals that are commonly found in their data.

1.2.1 Principles of Operation

The GTSM is a set of four cylindrical horizontal-extensometers, mechanically fixed to each other. The four ‘gauges’, as we refer to them here, are oriented at precise angles relative to each other (-30° , 30° , and 60° from a reference gauge). The orientation of three of the gauges effectively form a ‘Delta’ strain rosette, used in analyses of engineering materials to measure the full horizontal strain tensor (see *Hetényi*, 1950, Ch. 9); the fourth gauge is included for redundancy in case of malfunction or failure, and can be used to validate calibration coefficients under normal operation. Figure 1.2 shows a simplified representation of the orientation of these gauges in map view, and how they are oriented relative to each other in the borehole.

The individual gauges measure differential changes in their diameter through a Stacey-type differential capacitance bridge (*Stacey et al.*, 1969). This mechanism relies on a pair of capacitors: one of which changes its capacitance in response to changes in instrument diameter (the plate-normal direction is in the radial direction), and another where the plate separation (and thus its capacitance) is fixed precisely³. The bridge ratio created by the capacitors – a differential capacitance

³There are two plate-separation distances used in the PBO BSM network: 100 and 200 μm

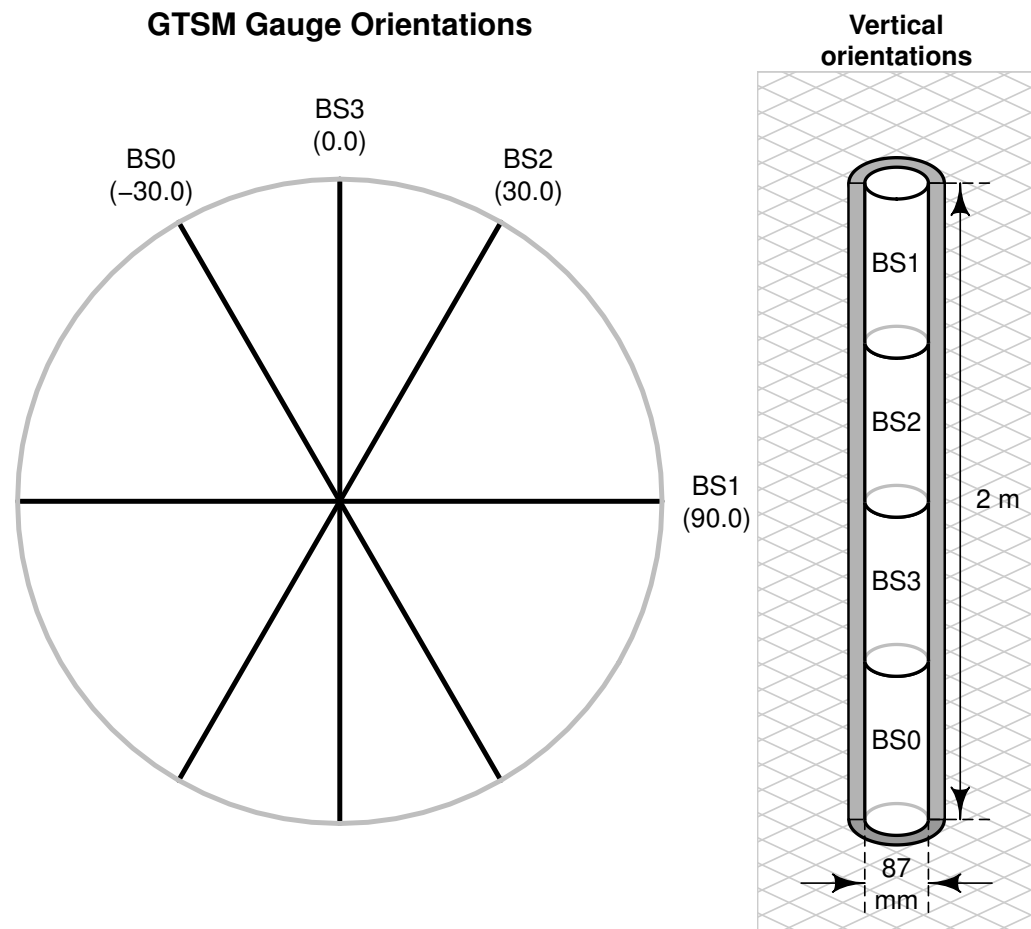


Figure 1.2: Schematic diagrams of the GTSM gauges. *Left:* The angular configuration of the individual GTSM gauges in an arbitrary horizontal coordinate system. *Right:* The configuration of the gauges as they would be installed in the borehole, surrounded by grout.

– can be directly related to the amount of uniaxial strain inside the instrument (see Section 2.8, and *Agnew, 1986*) which can be related to the horizontal strain tensor in the surrounding rock, as we shall see.

1.2.2 Calibration of Instrument Strain to Earth Strain

Even though what the BSM gauges actually measure is internal deformation, their signals can be related to strain in the rock through the theory of linear elasticity. Noting that displacement gradients $\nabla \mathbf{u}$ are assumed to be infinitesimally small, the most-general relationship between strain in the rock, $\mathbf{E}^\infty \equiv (\nabla \mathbf{u} + \mathbf{u} \nabla)/2$, and strain in the instrument, \mathbf{E}^I , includes a coupling tensor \mathbf{C} in the linear system

$$\mathbf{E}^I = \mathbf{C} \mathbf{E}^\infty \quad (1.1)$$

where \mathbf{C} is a fourth-order tensor with 36 unique components.

Before proceeding, it is important to note the state of stress in the rock, \mathbf{T}^∞ , is assumed to be *plane stress*. In this stress state, the free surface (with unit normal direction $\hat{\mathbf{z}}$) must be traction free and have zero vertical loading ($\hat{\mathbf{z}} \cdot \mathbf{T}^\infty = 0$ and thus $\hat{\mathbf{z}} \cdot \mathbf{E}^\infty = 0$). We can justify this assumption for some signals by noting that the wavelengths of strains encountered (tens of km for tectonic strains, and thousands of km for tidal strains) are much greater than the depth of burial of the strainmeter (again, in the range 150 m to 300 m). In other words the strainmeter is installed at depths which are effectively equivalent to it being at the surface, except in the case of high-frequency seismic waves in shallow material: these can have wavelengths of hundreds of meters or less.

In general the plane stress assumption is valid, but can be violated in practice by surface loading – atmospheric pressure fluctuations, for instance. In such a case the vertical strain will depend on the distribution of material parameters with depth (see *Rojstaczer and Agnew, 1989, Appendix A*). When the plane stress assumption does hold, though, there are only three independent strains in the rock: E_{11} , E_{22} , and E_{12} . Vertical strain only depends on the areal strain ($E_{11} + E_{22}$) and

the Poisson's ratio ν , and can be expressed as

$$E_{33} = -\frac{\nu}{1-\nu}(E_{11} + E_{22}) \quad (1.2)$$

Volumetric strain – the trace of \mathbf{E} – can thus be expressed as

$$\text{Tr}(\mathbf{E}) = \frac{1-2\nu}{1-\nu}(E_{11} + E_{22}) \quad (1.3)$$

The number of independent components in the coupling tensor, Equation (1.1), reduces to nine in this case:

$$\begin{bmatrix} E_{11} \\ E_{22} \\ E_{12} \end{bmatrix}^{\text{I}} = \begin{bmatrix} c_{11} & c_{12} & c_{13} \\ c_{21} & c_{22} & c_{23} \\ c_{31} & c_{32} & c_{33} \end{bmatrix} \begin{bmatrix} E_{11} \\ E_{22} \\ E_{12} \end{bmatrix}^{\infty} \quad (1.4)$$

Assuming that the material is isotropic, with axial symmetry about the vertical axis \hat{z} , this reduces further to

$$\begin{bmatrix} E_{11} \\ E_{22} \\ E_{12} \end{bmatrix}^{\text{I}} = \begin{bmatrix} c_1 + c_2 & c_1 & 0 \\ c_1 & c_1 + c_2 & 0 \\ 0 & 0 & c_2 \end{bmatrix} \begin{bmatrix} E_{11} \\ E_{22} \\ E_{12} \end{bmatrix}^{\infty} \quad (1.5)$$

Section 1.4 discusses how the isotropic assumption is often violated in practice.

Uniaxial strain in the direction $\hat{\mathbf{n}}$, θ degrees counterclockwise from an arbitrary coordinate system, can be found by the tensor transformation:

$$e_{nn}(\theta) = \hat{\mathbf{n}} \cdot \mathbf{E}^{\infty} \cdot \hat{\mathbf{n}} \quad (1.6)$$

where $E_{11} \equiv e_{11}$ when $\theta = 0^\circ$, and $E_{22} \equiv e_{22}$ when $\theta = 90^\circ$. The change in angle between $\hat{\mathbf{n}}$ and an orthogonal direction $\hat{\mathbf{m}}$ (the deformation, or *pure shear*) is

$$\hat{\mathbf{n}} \cdot 2\mathbf{E}^{\infty} \cdot \hat{\mathbf{m}} \quad (1.7)$$

It is common to parameterize the tensor strains in terms of the *areal strain* Δ ($\equiv E_{11} + E_{22}$) and the two components of shear strain: *differential extension* γ_1 ($\equiv E_{11} - E_{22}$) and *engineering shear* γ_2 ($\equiv 2E_{12}$). Differential extension is a form of shear strain, given by Equation (1.7). Engineering shear is the tensor shear

strain in a coordinate system oriented 45° to the original system. Expressing (1.5) in terms of these strains gives a diagonal calibration tensor:

$$\begin{bmatrix} \Delta \\ \gamma_1 \\ \gamma_2 \end{bmatrix}^I = \begin{bmatrix} d_1 & 0 & 0 \\ 0 & d_2 & 0 \\ 0 & 0 & d_2 \end{bmatrix} \begin{bmatrix} \Delta \\ \gamma_1 \\ \gamma_2 \end{bmatrix}^\infty \quad (1.8)$$

Equation (1.6) can be used to relate the coefficients d_1, d_2 to the individual gauge measurements (where θ is generally known very well).

Strainmeters recording earth strain are calibrated using the diurnal and semi-diurnal earth tides, because the complex tidal potential at any point on earth, and at any point in time, can be predicted with great accuracy (*Agnew, 2007b*). Although the potential tide can be predicted very well for a homogeneous earth model, distortions to the strain field at a given location arise from topographic variation, contrasts in material properties, and ocean loading (*Beaumont and Berger, 1975; Berger and Beaumont, 1976; Agnew, 1997*); improper accounting of these effects can lead to systematic errors in calibration coefficients (*Langbein, 2010b*). For these reasons, and because vertical strain coupling has been shown to have an adverse effect on calibration efforts (e.g., *Roeloffs, 2010*), the formulation given in Equation (1.8) has been found to be inappropriate in a number of studies: *Hart et al. (1996); Grant (2010); Roeloffs (2010); Hodgkinson et al. (2013)*. The “fully unconstrained” model – Equation (1.4) – yields generally suitable calibration coefficients (*Hodgkinson et al., 2013*). A calibration method using seismic waves has been developed (*Langston and Liang, 2008*) and tested (*Grant, 2010*), but it is not yet clear how the method compares to tide-based methods, and how it may be applied to stations not located amid a dense broadband seismic network.

1.3 Pore Pressure

For many years prior to conception of the PBO, water wells at numerous locations on earth had been observed to respond to seismic waves (*Cooper et al., 1965*) and tidal strains (*Bredehoeft, 1967*) much like a volume strainmeter (dilatometer) would. In later years it would become clear that water levels can

also reflect various earthquake-related processes including, for example, fault creep (*Roeloffs et al.*, 1989) and transient changes in permeability (*Rojstaczer and Wolf*, 1992; *Elkhoury et al.*, 2006). Acknowledging the potential scientific impact that colocated strain and pressure measurements might offer, the PBO also installed specialized pore fluid pressure (PP) sensors in the boreholes, sampling at depths near the BSM. In later chapters we will see how PP measurements are complementary to the BSM measurements, rather than proxies for volume strain.

1.3.1 Principles of Operation

The PP sensing system is rather simple: an open section of the borehole – typically very close to the strainmeter – is packed with high-permeability sand (rather than relatively impermeable grout), exposing a screened portion of a rigid, two inch diameter tube (extending to the surface) to the surrounding fluid-saturated rock. Absolute pressure of the fluid inside the tube is measured near the surface, with a Paroscientific⁴ pressure transducer affixed rigidly at some depth below the top of the borehole casing. The sensor depth is sufficiently below the phreatic level to allow for seasonal variation in pressure head associated with recharge and discharge of the aquifer. The dimensions of the tube are designed so that the pressure measurements are minimally affected by wellbore storage and inertial effects common in water-height measurements (e.g., *Cooper et al.*, 1965). As we mentioned previously, artesian (naturally flowing) stations have a pressure containment system inside the tube.

1.3.2 Relating Pore Pressure to Volume Strain

Unlike the borehole strainmeters, the PP sensors do not need specialty calibration methods: they can be easily calibrated in a laboratory, either by the manufacturer, or PBO engineers. But, the relationship between pore pressure and strain in fluid-saturate rock is considerably more complicated because deformation and fluid flow are coupled quantities that depend on the mechanical and hydraulic

⁴Model 8WD060: <http://www.paroscientific.com/>

properties of the rock.

The theory of *linear poroelasticity* (Biot, 1941; Rice and Cleary, 1976; Wang, 2000) can be used to relate changes in *effective stress* (which includes the effect of pore pressure) to strain in the rock. The elastic stress-strain relationship is expressed as

$$\mathbf{E} = \frac{1}{2\kappa} \left[\frac{1+\nu}{1-2\nu} \mathbf{T} - \frac{\nu}{1-2\nu} \text{Tr}(\mathbf{T}) \mathbf{I} \right] \quad (1.9)$$

where $\text{Tr}(\cdot)$ is the trace of the tensor inside the parentheses, \mathbf{T} is the stress tensor, and \mathbf{I} is the identity tensor. An increment of excess pore pressure P contributes a strain of $\alpha P \mathbf{I}$, where $\alpha \equiv 1 - \kappa/\kappa_u$, κ is the bulk modulus of the fluid-filled matrix, and κ_u is the undrained bulk modulus of the solid matrix (the ‘undrained’ state is discussed later). With this additional strain, Equation (1.9) becomes

$$\mathbf{E} = \frac{1}{2\kappa} \left[\frac{1+\nu}{1-2\nu} \mathbf{T} - \frac{\nu}{1-2\nu} \text{Tr}(\mathbf{T}) \mathbf{I} + \alpha P \mathbf{I} \right] \quad (1.10)$$

and the effective stress is $\mathbf{T} + \alpha P \mathbf{I}$ (Rice and Cleary, 1976). These equations can be used to examine how pore pressure is related to the volume strain in the rock, $\text{Tr}(\mathbf{E})$.

A common assumption made is that fluids diffuse through interconnected pore space following *Darcy’s law*, where the fluid flux q and pressure gradient ∇P are proportional to each other by the permeability of the material, k , and the kinematic viscosity of the fluid, μ :

$$q = -k \nabla P / \mu \quad (1.11)$$

(The fluid velocity would thus be the flux q divided by the effective porosity.)

The general theory of linear poroelasticity predicts two end-member states: (1) *drained*, where pore-fluid pressure is constant during changes in applied stress (pore-fluid may flow into or out of a control volume); and (2) *undrained*, where pore-fluid pressure is variable, and scales linearly with the change in applied stress (zero flow) (Wang, 2000). Using the Darcy flow-model (Equation (1.11)), a simple relationship between strain and excess pore-fluid pressure can be derived for rock in an undrained state:

$$P = -B\kappa \cdot \text{Tr}(\mathbf{E}) \quad (1.12)$$

where B is *Skempton's coefficient*.

There are many ways to express B : in words, it represents the amount of pressure inside a control volume relative to the confining pressure. *Rojstaczer and Agnew* (1989) express it as a combination of fluid and solid compressibilities (β , the inverse of bulk modulus) and the porosity ϕ :



$$B = \frac{\beta - \beta_u}{(\beta - \beta_u) + \phi(\beta_f - \beta_u)} \quad (1.13)$$

where β_f is the compressibility of the fluid. Skempton's coefficient is bound within $[0, 1]$: a value of zero corresponds to $\beta_u = \beta_f$ (entirely fluid) and a value of one corresponds to a solid matrix devoid of fluid.

Two types of coupling between stress and pore-fluid diffusion may occur under this theory: (1) “solid-to-fluid”, or when changes in effective stress are due to deformation of the solid matrix, and (2) “fluid-to-solid”, or when changes in effective stress are due to removal (or addition) of pore fluids. Coupling of type (1) is commonly associated with solid earth tides, seismic waves (long-period P and SH body waves, or Rayleigh waves (*Roeloffs*, 1996)), and elastostatic deformation; whereas, type (2) coupling is associated with fluid injection (or extraction). Of course, these generalizations represent gross simplifications of processes in heterogeneous crustal rock, but they are useful for understanding the types of signals measurement systems, such as the BSM record *in situ* (*Segall et al.*, 2003).

1.4 Installation Effects

The borehole is drilled using standard geophysical methods, and the casing of the borehole extends as far deep as needed in order to prevent borehole collapse (i.e., until competent bedrock is reached). Once the borehole is drilled, geophysical logging data are collected and used to select appropriate depths for installation, and then the instruments are cemented in the borehole with specialty grout that expands during the curing process, rather than contracting. Using this type of grout is an attempt to emplace the BSM into a compressive environment, where it's designed to operate optimally. As the grout cures (and expands) localized strain adds a long term “relaxation” trend into the data; unfortunately, this trend

precludes the BSM from accurately recording secular strain accumulation, unless it can be corrected for. A convenient mathematical model of the trends is a sum of decaying exponential responses , but this yields little information about local material properties, and the stress field perturbation associated with drilling. That the strength and duration of these relaxation trends might reflect the prior stress state of the rock and the poro-mechanical response of the local rock to drilling has been investigated very little, but at a number of installations the trend can be characterized by a poroelastic relaxation mechanism (*Day-Lewis, 2007*). Pore-fluid pressures are expected to be perturbed by circulating fluids during the drilling process, but this perturbation appears to be transient, decaying as excess pore fluids diffuse away from the borehole and the material relaxes .

1.5 Data Resources

Raw data from the PBO borehole instruments is logged on site, at the surface, and telemetered to a centralized repository. Once there the data is disseminated to various repositories so that it may be accessed by the broader scientific community. The main repositories are known as the Data Management Centers (DMC), at the Incorporated Research Institutions for Seismology (IRIS) and Northern California Earthquake Data Center (NCEDC). Other repositories include databases self-maintained by PBO. A list of these repositories by instrument type can be found in Table 1.1.

Table 1.1: Some repositories for Plate Boundary Observatory borehole data

Type	Source	Samp [†]
Acceleration	IRIS-DMC	250 Hz
Velocity	IRIS-DMC	100 Hz
Strain \star	http://bsm.unavco.org/bsm	20 Hz
Pore-fluid pressure \star	http://pore.unavco.org/pore	1 Hz
Pore-fluid temperature \star	http://pore.unavco.org/pore	1 Hz
Tilt \star	http://tilt.unavco.org/tilt	1 Hz
Geophysical Logging	http://borehole.unavco.org/borehole	

\star Listing excludes <http://www.iris.edu> (IRIS) and <http://www.ncedc.org> (NCEDC) Data Management Centers (DMC)

\dagger Maximum sampling rate (lower rates may be available)

Chapter 2

Noise Levels on Plate Boundary Observatory Borehole Strainmeters in Southern California

To establish noise levels for the borehole strainmeters of the Plate Boundary Observatory, we have analyzed data recorded by eight of these instruments, all in the Anza region of southern California. We determine time-varying power spectra for frequencies from 10^{-3} Hz to 10 Hz, using a new method that combines multitaper spectrum estimation, smoothing by local regression, and computation of cumulative distribution functions. From about 2 Hz to the Nyquist frequency of 10 Hz, the noise floor is set by instrument resolution; for frequencies between 0.1 Hz and 1 Hz it is set by microseisms. The lowest noise level is between 0.01 and 0.1 Hz, with a rapid increase at lower frequencies. However, in most instruments this low-noise range also contains narrow-band noise that appears to be caused by power-supply fluctuations. We compare these results with noise spectra from other types of strainmeters, which suggest two things: (1) they are in agreement with results for surficial, long-baseline instruments; and (2) other subsurface strainmeters have lower noise in the seismic band than the PBO instruments do.

2.1 Introduction

The noise level of any measurement determines its limit for signal detection. The most elementary characterization of this noise is to assume it to be independent from one measurement to the next, in which case it is often called the “error” or “resolution”. For many geophysical measurements the noise level requires a more complicated description, most usually by its power spectral density. Of course, the distinction between signal and noise in a record depends on the aim of the measurement. In seismology, the usual signals are transients from particular sources, so that “noise” comes not just from instrumental sources, but also from the motion constantly present in the Earth: such noise levels often depend on both time and location.

Brune and Oliver (1959) provided one of the first descriptions of the spectrum of seismic noise; routine use of the power spectrum largely awaited the coming of digital data. *Peterson* (1993), used a collection of such data to set lower and upper levels for seismic noise on a global scale. Regional and global noise models, the variation of noise with time, and causes of noise have since been studied by extensively (e.g. *Rodgers et al.*, 1987; *Given*, 1990; *Wilson et al.*, 2002; *Berger et al.*, 2004; *McNamara and Buland*, 2004; *Sheen et al.*, 2009; *Stutzmann et al.*, 2009), as well as the seismic noise wavefield (e.g. *Webb*, 2002; *Bonnefoy-Claudet et al.*, 2006).

Recognizing the temporal variability of noise even at a single location, an increasing number of studies have presented the noise spectrum not as just a single function of frequency, but as a set of probability distributions for different frequencies. This mode of description is explicit in methods developed by *McNamara and Buland* (2004) and *McNamara and Boaz* (2005), which are now frequently used to determine seismic system performance.

All these studies are of noise levels on inertial seismometers, which respond to acceleration at a point. Much less data is available for the spatial derivatives of ground displacement (strain and rotation), and consequently there are many fewer estimates of ground noise for these observables. *Fix and Sherwin* (1972) gave results from a solid-bar strainmeter at a very quiet site, *Berger and Levine* (1974)

summarized spectral estimates from three long-baseline strainmeters in three different locations, and *Borcherdt et al.* (1989) provided a spectrum from data from a Sacks-Evertson borehole dilatometer.

One goal of the Plate Boundary Observatory (PBO) was to increase the amount of strainmeter data available by installing 105 borehole strainmeters along the Pacific / North-American plate boundary; in fact, 74 were installed from 2005 through 2008, 39 along the subduction boundary in the Pacific Northwest, with 26 in five clusters further south, and 9 in two clusters in volcanic regions. The strainmeters installed were the four-component Gladwin Tensor Strainmeter (GTSM) described in *Gladwin* (1984) and *Gladwin and Hart* (1985). Many installations also have barometers and a three-component short-period seismometer, and some include pore-pressure transducers, accelerometers, and tiltmeters.

In this paper we estimate noise levels in the seismic band (0.001 Hz to 10 Hz) on borehole strainmeters installed by the PBO in southern California. After outlining our methods, we discuss a few instrumental noise sources, describe the noise variation at several stations, and conclude with a summary model for borehole strainmeter noise. We discuss the nonlinear response of the instrument in Appendix 2.8.

2.2 Data and Methods

2.2.1 PBO Borehole Instruments in the Anza Region

We analyzed data for 2009 from the PBO borehole strainmeters in the Anza, California region. These eight strainmeters are at seven locations around the Anza segment of the San Jacinto fault zone in southern California (Figure 2.1); one location includes two strainmeters (B082 and B089) spaced 190 m apart. This region is centered on a segment of the fault that has long been identified as a slip gap on the San Jacinto fault (*Thatcher et al.*, 1975), although there is a high level of microseismicity and three earthquakes at or above magnitude 5.0 have been observed since 2001. This area is especially suitable for borehole strainmeters because the near-surface rocks are mostly batholithic granites and granodiorites,

with relatively low fracture densities (*Fletcher et al.*, 1990). Table 2.1 summarizes the geology and installation details of each site. At two stations (B081 and B089) the system batteries are recharged by solar cells; the rest are connected to local power. All stations transmit their data over digital telemetry.

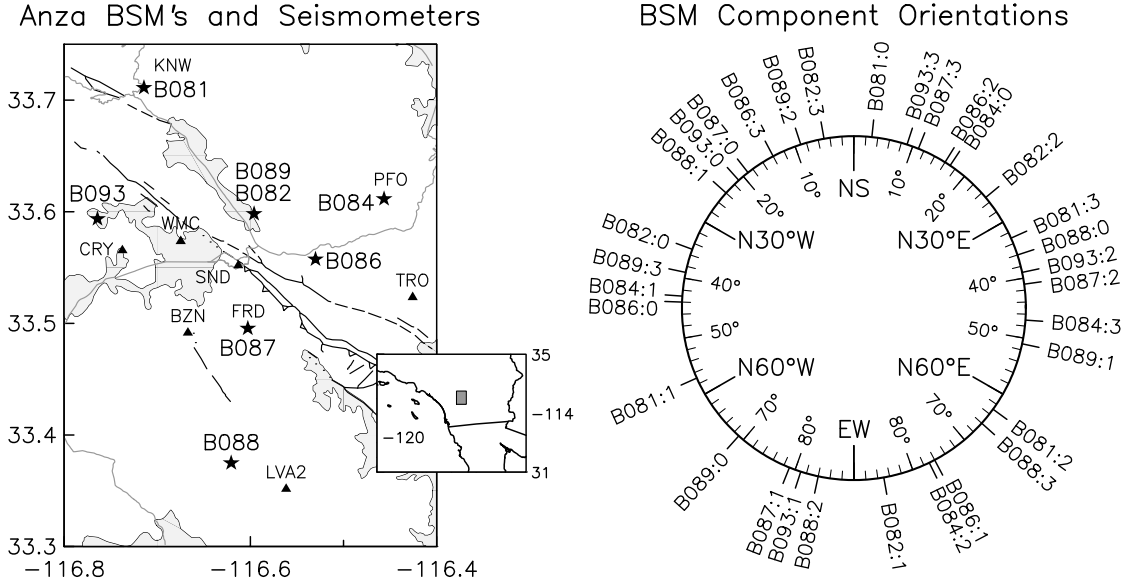


Figure 2.1: Left: map of the Anza region, showing the locations of the borehole strainmeters (e.g., B081) and broadband seismic stations (e.g., KNW). Shaded areas are recent alluvium, and major roads are shown. Right: the orientation of all channels analyzed, identified by installation and channel number (0 through 3). Orientations are the azimuths clockwise from north, plotted at twice the value of the azimuth to cover the complete circle. For instance, the bottom of the circle is thus where azimuths of either -90° or 90° are plotted: both measure east-west oriented uniaxial strain in the instrument.

For noise studies the Anza region has the advantage of being far enough from the coast that ocean loading is not a significant noise source, and a locally unpopulated area; Table 2.1 gives the population density within 10 and 20 km. Using the strainmeters here also allows us to make comparisons with the co-located surface broadband stations of the Anza seismic network, and in one location (Piñon Flat Observatory, the site of B084) with both a co-located very broadband station of the IDA-IRIS network and three co-located long-baseline laser strainmeters.

Table 2.1: Locations and other parameters for the borehole strainmeters in the Anza cluster.

Code	Latitude (N, deg)	Longitude (E, deg)	Elev. (m)	Date installed	Depths ^a (m)		Azim. ^b (deg)	Gap ^c (mm)	Dist. ^d (km)	Pop. ^e (10 ³)			
					PP	SEIS				BSM	LOG	10 km	20 km
B081	33.7112	-116.7142	1467	2006:167	212	229	243	244	3	0.2	84	3.1	28.9
B082	33.5982	-116.5960	1375	2006:161	192	220	242	244	-35	0.2	86	1.9	5.7
B084	33.6116	-116.4564	1271	2006:258	135	147	158	213	17	0.1	98	1.9	92.5
B086	33.5575	-116.5310	1392	2006:168	216	226	240	244	-44	0.2	88	1.1	5.4
B087	33.4955	-116.6027	1139	2006:168	94	147	161	219	-19	0.2	79	1.2	4.6
B088	33.3749	-116.6205	1404	2007:028	137	147	160	202	36	0.1	72	0.5	3.9
B089	33.5999	-116.5961	1362	2006:240	—	—	133	151	-69	0.1	86	1.9	6.6
B093	33.5937	-116.7638	1244	2007:263	—	124	145	153	-21	0.1	74	1.9	9.0

^a If present, depths are from the top of the borehole casing to PP: to the center of the pore-pressure inlet screen; SEIS: to the center of the downhole seismometer package; BSM: to the bottom of the borehole strainmeter package; and LOG: to the end of borehole logging data, typically a few meters from the maximum drilling depth.

^b Orientation of channel 0, given in degrees clockwise from north, in the range $[-90^\circ, 90^\circ]$ because, for example, a uniaxial strain oriented to the north is indistinguishable from an equivalent one to the south.

^c Fixed-plate capacitor separation.

^d Distance to the Pacific coast.

^e Population densities from gridded population data (see Data and Resources section).

2.2.2 Noise-Level Estimation

We download raw data in the “bottle” format used by the BSM dataloggers from the Northern California Earthquake Data Center (see Data and Resources section). To be interpreted as strain, these data need to be corrected for the slightly nonlinear response of the GTSM differential capacitance bridge (*Stacey et al.*, 1969; *Agnew*, 1986), which measures diameter changes in the borehole strain-meter casing; Appendix 2.8 describes this correction, which adjusts power levels by approximately -3 dB from 10^{-3} to 10 Hz.

Earth noise varies in a variety of ways with time: in statistical terms it is not stationary. However, over sufficiently short time intervals, and excluding obvious transients such as earthquakes, the noise is approximately stationary. We thus do not need the kind of methods that are used with very nonstationary data, such as the evolutionary spectrum (e.g. *Priestley*, 1981), or wavelet analysis.

Insofar as they can be measured, we seek to establish actual ground noise levels, and so try to remove obvious instrumental problems such as times of missing data. We remove instrumental artifacts, including hourly calibration pulses, and gaps and outliers in the strain data. We also automatically remove outliers that are more than 3 standard deviations away from a trimmed running mean; the standard deviation is scaled by the variance so that as noise levels change the level of detection will not. We fit sinusoids with periods of 12 and 24 hours, a mean, and a trend to each day of data to remove most of the long-term change and the tides.

We compute a number of spectral estimates using series of different lengths and sample intervals, as described in Table 2.2. In order to get the highest time resolution, we use the shortest series compatible with getting reliable spectral estimates. For the highest frequencies the sections analyzed are only 3 minutes long; for the lowest frequencies we use sections of 6 hours.

We estimate the power spectral density using sine multitapers (*Riedel and Sidorenko*, 1995, 1996), which provide good spectral resolution. We use an autoregressive filter to prewhiten the data so that what is analyzed has a small spectral range; this eliminates the need for the extreme bias rejection of the prolate tapers

Table 2.2: Spectrum estimation and fitting parameters

Section ^a		Spectrum Fitting ^b					Time-
Length	samples/ (s)	f_l	f_h	pts/ decade	Δf_l	Δf_u	bandwidth ^c
	day	(Hz)			(mHz)		
20 Hz data ^d							
180	480	1.0000	9.5000	25	96.5	835.9	17–150
300	288	0.2500	1.0000	25	24.1	88.0	7–26
1 Hz data ^e							
900	96	0.0600	0.2500	25	5.79	22.00	5–20
1800	48	0.0300	0.0600	25	2.89	5.28	5–10
3600	24	0.0150	0.0300	25	1.45	2.64	5–10
5400	16	0.0090	0.0150	25	0.87	1.32	5–7
7200	12	0.0060	0.0090	25	0.58	0.79	4–6
10800	8	0.0036	0.0060	20	0.44	0.65	5–7
14400	6	0.0020	0.0036	15	0.33	0.51	5–7
21600	4	0.0010	0.0020	10	0.26	0.41	6–9

^a Lengths of a section of data from which the PSD is estimated, and the resulting number of PSD samples per day.

^b Lower and upper frequencies, as well as decadal resolution and frequency spacing (for the loess fit).

^c The product of frequency spacing and section length: an approximate time-bandwidth measure.

^d Using original 20 Hz data.

^e Using 1 Hz data, which we create by lowpassing and decimating the 20 Hz data.

(*Thomson, 1982*) usually used for multitaper analysis. Use of the sine multitapers allows efficient computation of an adaptive estimate of the spectrum; this finds a quadratic fit to the local spectrum, and varies the number of tapers depending on the estimated second derivative of the spectrum. If the spectrum varies smoothly with frequency, many tapers are applied, giving a lower-variance estimate.

We should note that that for our time-bandwidth settings (detailed in Table 2.2), and at periods longer than 10 seconds, data outliers can significantly bias the spectrum estimate because of spectral leakage; prolate spheroidal tapers then become more useful.

The spectra of seismic noise can be summarized adequately with functions that are piecewise linear in logarithmic power and logarithmic frequency, a description that shrinks the data volume by several orders of magnitude. We use a preliminary analysis to determine the density with which we sample the spectrum over different frequency ranges; within each range, we find a weighted linear fit to the spectrum (in log-log frequency-power space) over non-overlapping sets of frequencies, with the weights coming from the multitaper analysis; this is essentially the local regression (loess) method of *Cleveland and Devlin (1988)*, though applied at a variable spacing. Our final result is thus spectral estimates at selected frequencies, which can easily be corrected for instrument response.

To describe the range of spectral behavior we form empirical cumulative probability functions at each frequency. We take the “typical” level to be the median, which is exceeded half the time. To show the variability, we plot other levels of cumulative probability relative to the median, to avoid the known visual problems with evaluating the distances between sloping lines (*Cleveland, 1993*).

We have taken the calibration of the borehole strainmeters to be the nominal value determined by the manufacturer, and assumed that this represents horizontal uniaxial strain. This assumption ignores the effects (*Gladwin and Hart, 1985; Hart et al., 1996*) of the inhomogeneity introduced by the instrument and borehole, which requires a tensor-product correction based on tidal calibrations. We have avoided this correction for several reasons: (1) as *Roeloffs (2010)* demonstrates, *in-situ* calibrations show that strain measurements from GTSM instruments can

be a complicated combination of horizontal and vertical strain, for reasons that are not fully understood; (2) as *Langbein* (2010b) shows, in the absence of a direct strain comparison (e.g. a long-baseline laser strainmeter), these *in-situ* calibrations are sensitive to errors in theoretical tidal models; and (3) we have found the noise levels on different components of the same instrument to be significantly different. Because of all this, it would be confusing rather than helpful to work with combinations of sensors (e.g. areal strain).

We produce estimates of spectral variability similar to those found by the method developed by *McNamara and Boaz* (2005). Known as PQLX, this method has become a standard for evaluating seismic station quality. The PQLX method estimates the power spectrum using the Fourier transform of the time series windowed by a 10% cosine taper, a method that has much poorer consistency and bias rejection than multitaper estimation does. The spectrum is then averaged over 1-octave intervals at a frequency spacing of 1/8 octaves, and binned at 1-dB power intervals to produce a probability density function. These steps provide a less flexible description of the power spectrum than our method of local fitting does, although there may be advantages in allowing completely automatic operation. Figure 2.2 summarizes our procedure, which is designed to be both more flexible and more accurate than that of PQLX.

2.3 Instrumental Noise

We first discuss noise that appears to come from sources within the instruments: primarily from the strainmeter power supplies, but also from the limited resolution of the systems, compared with the very low levels of strain present at the high-frequency end of the seismic band.

All spectra of strainmeter data from the Anza area show at least one large, narrow peak; the frequency of this differs from one sensor to another, but usually has a period between 10 and 60 seconds (detailed in Table 2.3). Often, the exact frequency of the peak varies with time, in ways that are correlated with the battery voltage (recorded as one of many diagnostic signals); but, the variation can have

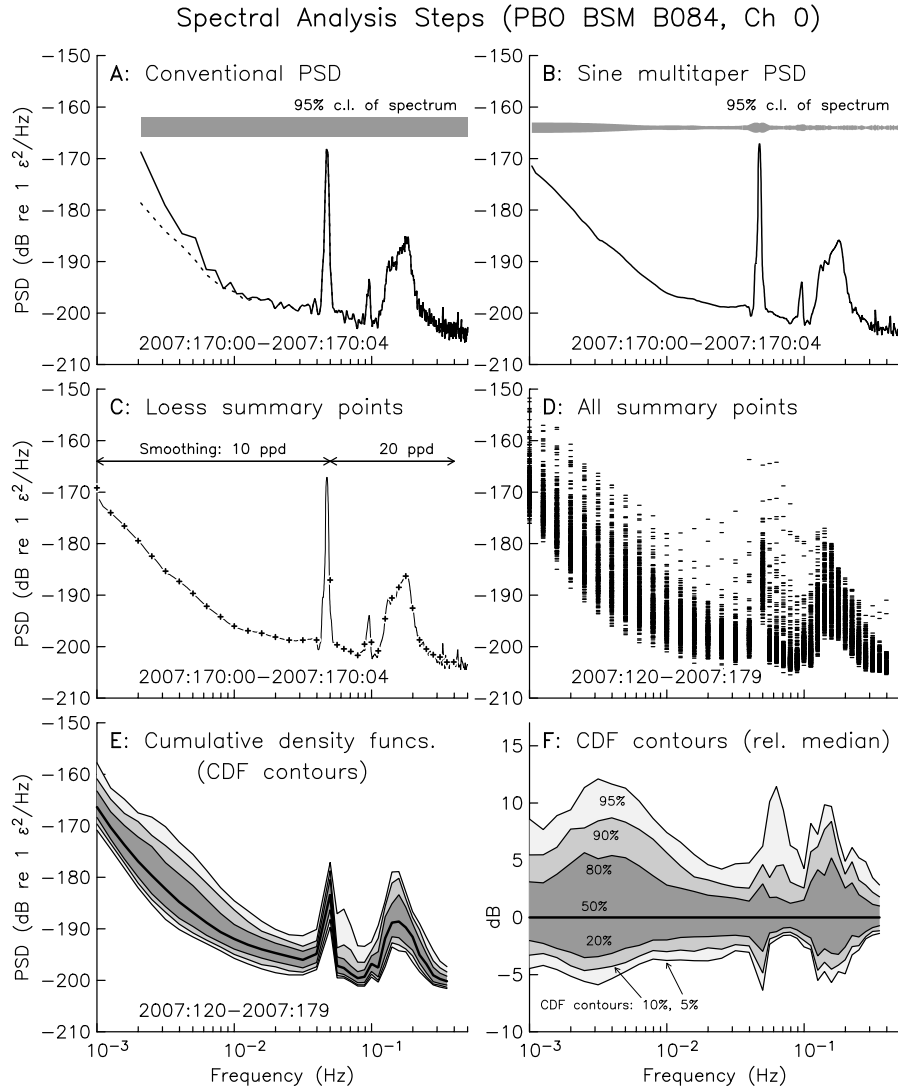


Figure 2.2: Data processing steps. A: a spectrum of four hours of 1 Hz BSM data at B084 for channel 0, found using Welch’s method (960-term sections, Hann taper, 50% overlap); the dashed line shows the effect of detrending each section. The gray band is the 95% confidence limits on the estimated spectrum. B: the sine multitaper version of the same data. Note the improved low frequency resolution and decreased error. C: the sine multitaper spectrum, with summary points fit to it by loess; the smoothness settings are shown in points-per-decade (ppd). D: all summary points for spectra computed over 60 days. E: empirical cumulative density functions of summary points in D at each frequency, connected to make continuous functions (CDF contours). F: CDF contours, relative to the median contour.

characteristics that differ among the four channels at a given station. Figure 2.3 shows a channel where the correlation is obvious, by plotting the time-varying spectra of data at B087 (channel 0) using darker colors for higher power, and in each case overplotting the battery voltage, for which the y-axis is on an arbitrary scale. The frequency of the narrow peak in the spectrum varies between day and night very much as the battery voltage does. This suggests that the peaks in the spectrum are caused by crosstalk from the power supply, perhaps because the rate of voltage adjustments in the power supply depends on the battery voltage.

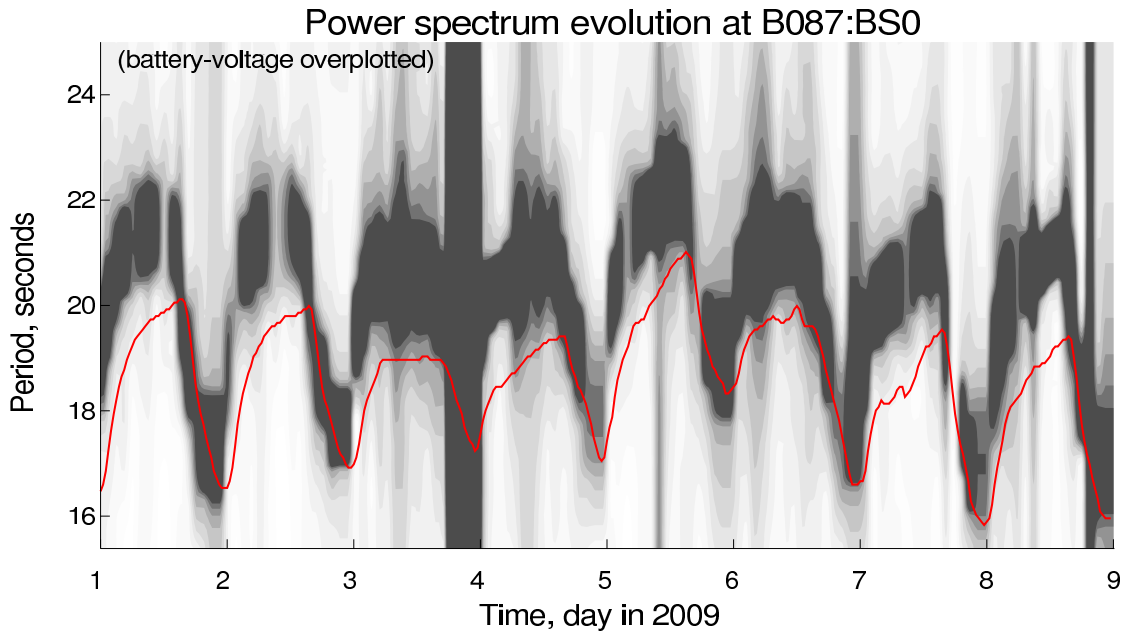


Figure 2.3: Time-frequency plot showing changes in the power spectrum at B087 over eight days in early 2009: darker shades of grey are higher power. The solid line, with arbitrary vertical scale, is the level of the battery voltage. This signal varies diurnally, as does the period of the narrowband noise.

Even though there is strong evidence for a power-supply noise source, we cannot exclude the possibility of an effect from diurnal temperature variation. At sites using solar power, the battery voltage varies with respect to the box-temperature (recorded near the data logging equipment) in an anti-correlated manner. Since this anti-correlation is not observed at all stations, the daily variation in ambient temperature is likely not a direct source of noise, but may be indirectly influencing the data.

Table 2.3: Characteristic periods of the instrumental noise peaks in the Anza cluster.

Code	Period [†] (s)			
	Channel 0	Channel 1	Channel 2	Channel 3
Solar				
B081	2, 3, 6	2, 3, 6	2, 3, 6	2, 3, 6, 30–33
B089	5–11	33–67	22–40	10–12
Local				
B082	×	×	×	10
B084	21	21	22	20, 23–33
B086	12–14	10–13, 14–20	10–13	10–13
B087	16–23	12–21	17–22	16–19
B088	22–35	25–35	25–35	20–35
B093	15	11, 15	11, 15, 21	11, 21

* See Instrumental Noise section for discussion.

[†] If the value is a single number, the frequency of the noise peak doesn't vary much; otherwise, a range indicates that the peak varies diurnally (through that range of periods). The symbol × indicates the noise peak is often obscured by troubled data, and cannot be precisely determined. The stations are segregated by the primary power source: Solar panels, or local.

Whatever the source, this noise means that the BSM data must be treated with care before it is used to study seismic surface waves, which have similar frequencies.

Two other sources of instrumental noise appear to come from the way in which the data are produced, and perhaps from the least-count noise of the system. The analog output from the capacitance bridge is filtered using a 6-pole filter with a corner at 32 Hz (M. Gladwin, pers. commun. to K. Hodgkinson, May 2006); this is converted to a digital signal by an analog-to-digital converter with a sample rate of 100 Hz. The 20 Hz record is the mean of the five values of the 100 Hz signal, taken around the 20 Hz sample time. The 1 Hz record is in turn constructed using a nonoverlapping 20-point mean of all values within 0.5 s of the time of the 1 Hz sample. While this simple filter introduces minimal aliasing at the lowest frequencies (and none at zero frequency), it allows significant aliasing at frequencies above 0.1 times the Nyquist frequency.

The noise level resulting from the finite precision of the strain data (pure least-count noise) is the same for all three sample rates, and would set a lower-bound noise level of -228 dB (relative to $1 \epsilon^2 \text{ Hz}^{-1}$) for the 100 Hz data, -221 dB for the 20 Hz data, and -208 dB for the 1 Hz data. The spectra for frequencies greater than about 1 Hz have a higher level than this (-200 to -203 dB), but the lack of spectral character, small amount of temporal variation, and similarity between sites all suggest that this level is caused by instrument noise rather than actual variations in the Earth. For the 20 Hz data this level corresponds to a white noise with a variance of about 10 counts.

It is difficult to confirm the nominal data filtering algorithm. We have compared the actual 1 Hz data with a version produced by applying a running mean to the 20 Hz data as recorded; these in fact differ, though only by a few counts – one count is nearly 0.1 nanostrain for a transducer plate-separation of 200 microns (see Appendix 2.8). Figure 2.4 shows a section of such a comparison, along with the spectrum of the difference series, and the coherence between them, from a longer sample of data. As the figure shows, there is a significant difference between the two 1 Hz timeseries (actual and simulated); the nature of this difference seems

to depend on the signal present, since it changes at the times of significant seismic energy. The coherence shows relatively large values for frequencies at which the signal is relatively large; the spectrum of the difference series is, however, relatively smooth. As with the coherence estimates, the spectra of the different series show, again, good agreement in regions of high signal; outside these regions the spectrum of the actual 1 Hz data is lower than either the simulated series or the 20 Hz series from which it is derived. This suggests that the filtering applied to the raw 20 Hz data smooths preferentially at frequencies with lower power levels. In addition, the difference between actual and modeled 1 Hz data has varied with time, notably when the internal software (firmware) changes. Lacking access to this firmware, we have chosen to not use the 1 Hz records. Instead, we use only the 20 Hz record for our analysis, lowpassing and decimating it (with better filters) to 1 Hz before estimating the spectrum at the lower frequencies; we use the filtering methods of *Kaiser and Reed (1977)*.

2.4 Observed Strain Noise Levels

Figure 2.5 shows the noise levels for all four channels of all eight borehole strainmeters in the Anza area. On each plot the thick black line is the median level and the gray region is enclosed by the maximum and minimum of most of the medians. In finding this region we have left out stations at which the spectral levels are consistently high or much more variable, since these probably represent some instrumental problem. The maximum of the medians shows the long-period noise peaks discussed in Section 2.3, but the minimum of the reliable medians largely eliminates these.

Figure 2.6 shows the variability of the spectra relative to the median; the contours are of the pdf of the noise level. At frequencies greater than 1 Hz the variation is small, but through the microseism band it increases, showing the familiar variability of this noise source. At slightly lower frequencies the variations can be even larger, because of the frequency shifts in the periodic signals described in Section 2.3. At longer periods, at least at those stations with acceptable medians,

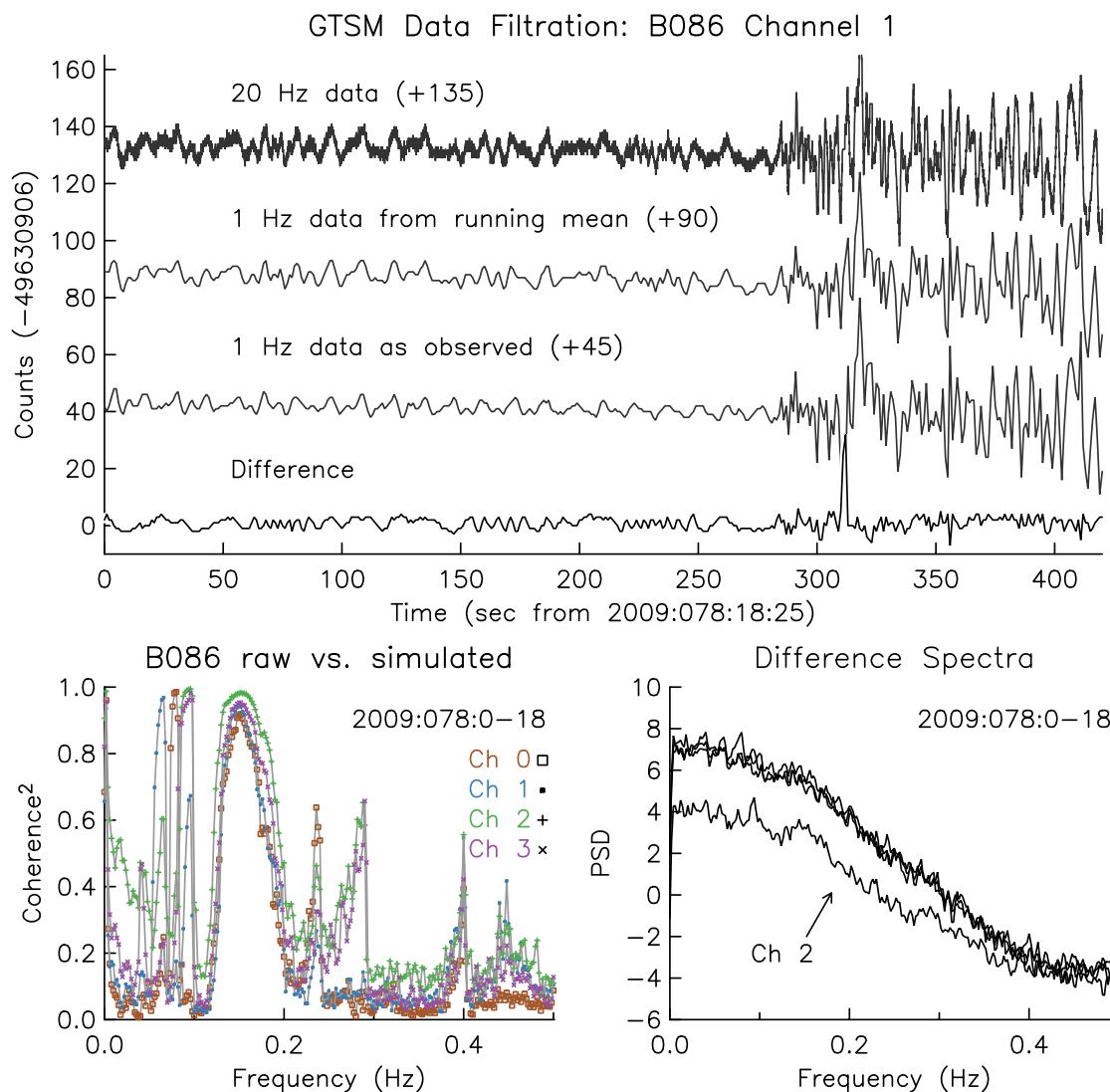


Figure 2.4: Top: An example comparison of 1 Hz data as recorded, and as simulated using 20-point means of the corresponding 20 Hz data, for B086 on 2009:078 channel 1: the difference of the two is not zero, and the timeseries appears to show frequency-dependent behavior. Bottom left: Coherence estimates between the recorded and simulated 1 Hz data for all channels, except only for the first 18 hours of 2009:078 in order to omit the signal from a large teleseism. The coherence is high in the microseism band, and at the frequencies of the narrowband noise source discussed in the Instrumental Noise section. Bottom right: Power spectral density estimates for the difference between the simulated and actual 1 Hz data. Noting the significant spectral character, the recorded 1 Hz data appears to have been smoothed using a filter whose response varies with frequency.

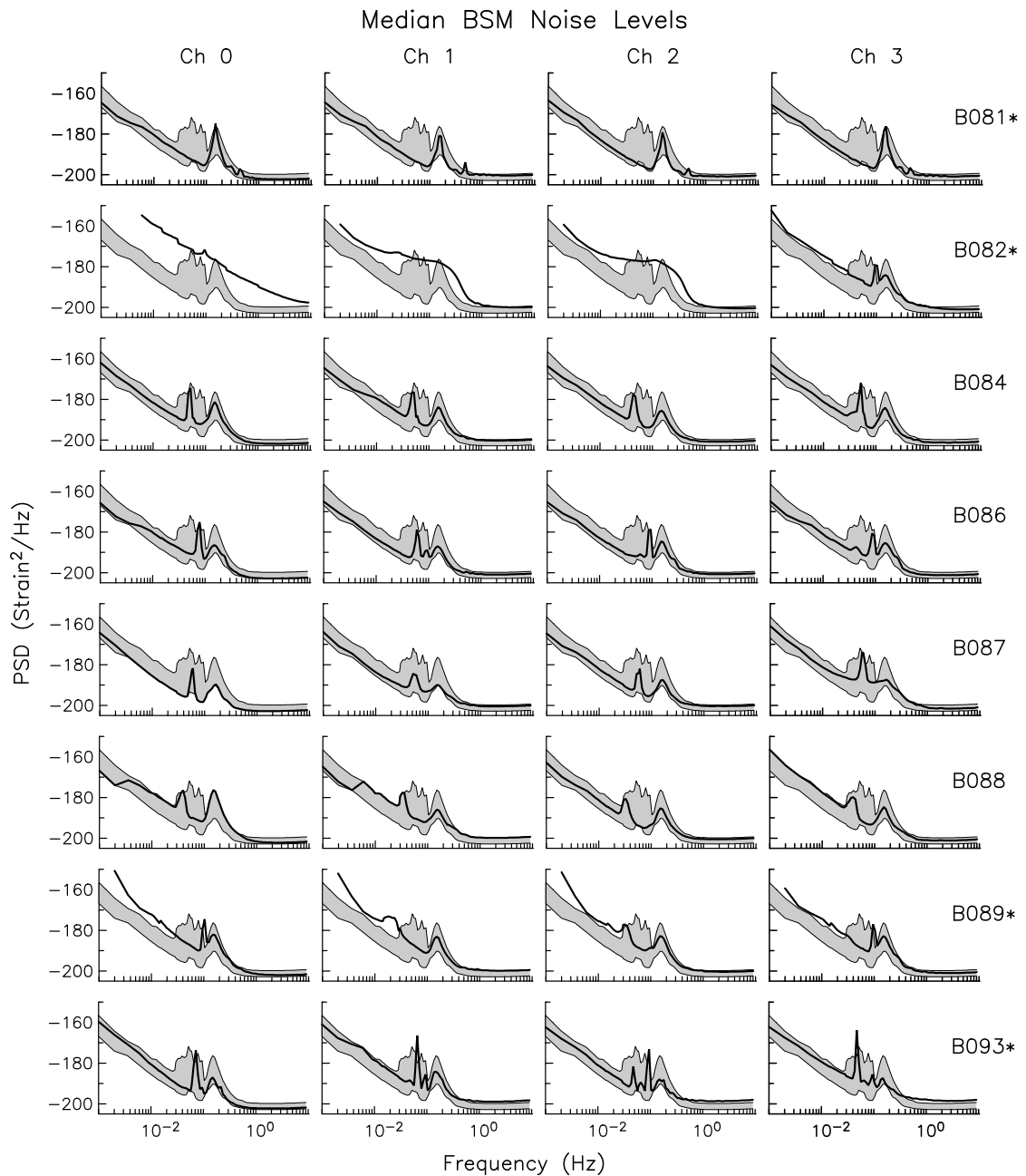


Figure 2.5: Median levels of the power spectral density for all channels and sites of the PBO borehole strainmeter cluster in Anza. For each plot, the thick black line is the median; the gray region shows the range covered by the medians. The range excludes stations B081, B082, B089, and B093; because their spectral levels are consistently high or much more variable.

the variations are again smaller. At many frequencies the density function for the distribution of power is skewed, with its long tail on the higher side: This reflects occasional larger signals, such as microseism storms and earthquakes.

To summarize our results, we again ignore those sites at which the median appears to be anomalous, and take the minimum over all channels of the median and of the 10th percentiles of the noise distribution. We believe that the median level represents a reasonable estimate of typical noise levels, and the 10% level similarly shows what levels have to be reached for an instrument either to see ground noise or to have less noise than the borehole strainmeters examined here. Table 2.4 gives our estimates that summarize the noise level. For this table we omit the frequencies affected by the peaks described in Section 2.3 because these differ from one system to another – and if we are correct that these arise from noise from an instrumental source (e.g., the power supply), they are only incidental to the borehole strainmeter measurement.

2.5 Comparison with Other Estimates

It remains to compare these results with previous estimates of strainmeter noise at seismic frequencies, which we do in Figure 2.7. The most direct comparison would be with data collected at the same time, and in the same region, by other types of strainmeters. The left panel of Figure 2.7 shows such a comparison for site B084, with the other estimates coming from the long-baseline laser strainmeters at Piñon Flat Observatory (PFO), the location of B084. We have performed the same analysis as described in Section 2.2 for data from the three laser strainmeters at this site, using data from 2009 for days without known instrumental problems (94% of the total). The results, in a form similar to Figures 2.5 and 2.6, are shown in Figure B.1 in Appendix B. Figure B.1 also includes the results for two other laser strainmeters located in a rural area near Cholame, California. Figure 2.7 shows the 10% and median levels found in Table 2.4 for the borehole strainmeters, and the same levels for the laser strainmeters. The levels shown, for the laser strainmeters, are found by choosing, at each frequency, the lowest spectral level

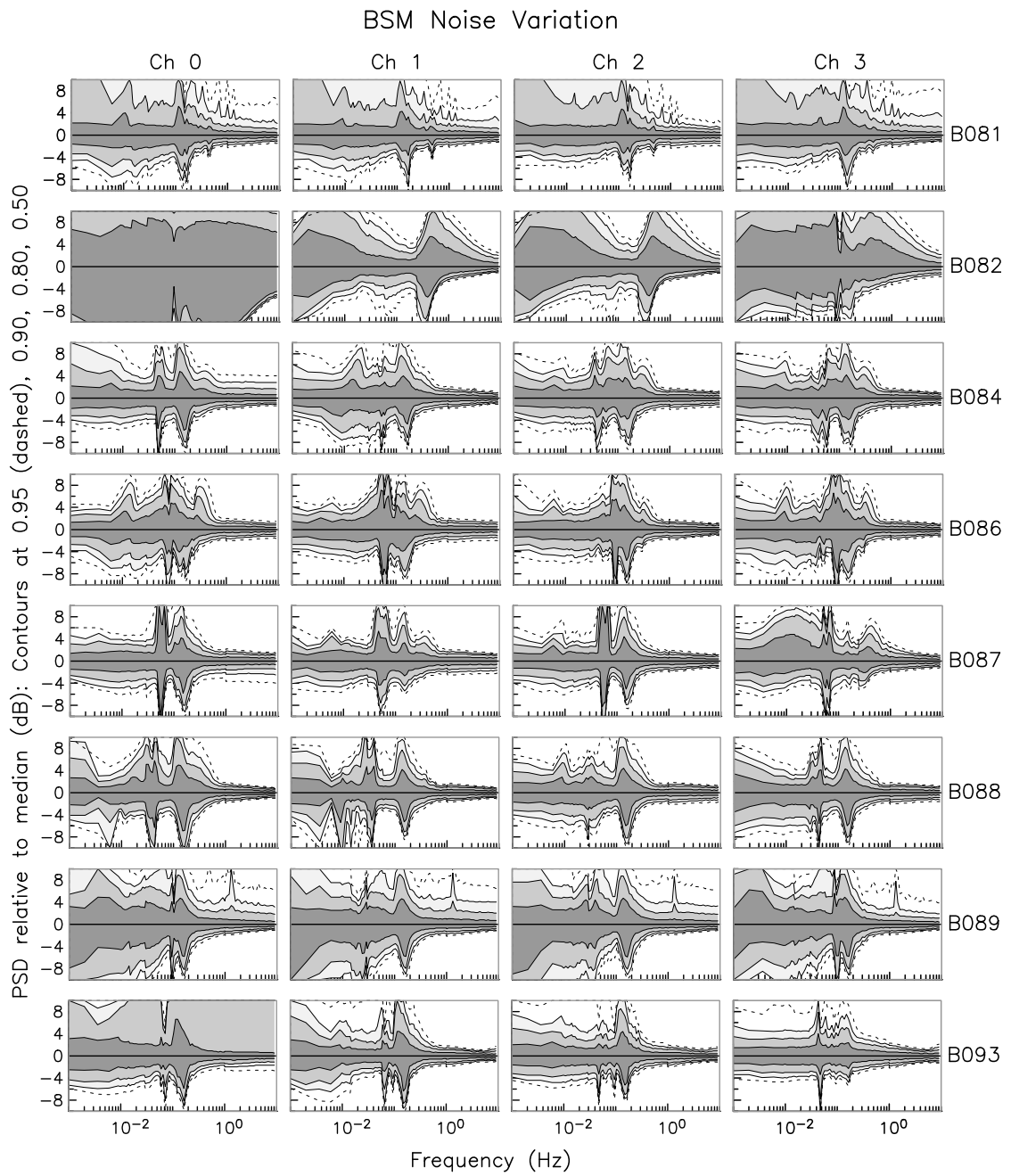


Figure 2.6: The variation in spectral levels relative to the median levels shown in Figure 2.5. The top and bottom dashed lines are the 2.5% and 97.5% levels of the cumulative density function: that is, at each frequency the power spectrum will be between these lines 95% of the time. The other levels shown are the 5% and 95% values, the 10% and 90% values, and the 25% and 75% values.

Table 2.4: A summary of borehole strainmeter noise levels as a function of frequency.

f (Hz)	P_{50} (dB rel. ϵ^2/Hz) ^{†,§}	P_{10}	f	P_{50}	P_{10}	f	P_{50}	P_{10}
0.001000	-166.8	-171.7	0.072136	-197.2	-201.1	0.907700	-202.7	-204.8
0.002000	-174.0	-179.5	0.079095	-198.1	-201.4	0.995270	-202.7	-204.8
0.003600	-176.4	-185.2	0.086726	-198.4	-201.6	1.000000	-202.7	-205.1
0.006000	-181.0	-186.0	0.095094	-198.3	-201.8	1.096500	-202.8	-205.2
0.009000	-184.6	-192.5	0.104270	-196.5	-201.4	1.202300	-202.8	-205.2
0.009868	-185.4	-192.1	0.114330	-193.8	-200.2	1.318300	-202.8	-205.2
0.010820	-186.1	-191.0	0.125360	-192.9	-199.1	1.445400	-202.8	-205.2
0.011864	-186.9	-191.6	0.137450	-191.8	-199.0	1.584900	-202.8	-205.2
0.013009	-187.7	-192.3	0.150710	-190.3	-199.1	1.737800	-202.8	-205.1
0.014264	-188.4	-193.0	0.165250	-190.3	-198.8	1.905500	-202.8	-205.1
0.015000	-188.6	-193.6	0.181200	-191.6	-198.6	2.089300	-202.8	-205.1
0.016447	-189.3	-194.2	0.198680	-193.4	-199.8	2.290900	-202.8	-205.1
0.018034	-190.0	-194.9	0.217850	-195.6	-200.1	2.511900	-202.8	-205.1
0.019774	-190.7	-195.5	0.238860	-196.9	-200.5	2.754200	-202.8	-205.0
0.021682	-191.4	-195.9	0.250000	-197.1	-200.9	3.019900	-202.7	-205.0
0.023773	-192.0	-196.4	0.274120	-197.9	-201.3	3.311300	-202.8	-205.0
0.026067	-192.6	-196.8	0.300570	-198.9	-201.9	3.630800	-202.8	-205.0
0.028582	-193.1	-197.2	0.329560	-200.1	-202.9	3.981100	-202.7	-205.0
0.030000	-193.9	-199.0	0.361360	-200.9	-203.5	4.365200	-202.7	-204.9
0.032894	-194.5	-199.1	0.396220	-201.3	-203.8	4.786300	-202.7	-204.9
0.036068	-195.1	-199.4	0.434450	-201.5	-204.0	5.248100	-202.7	-204.9
0.039548	-195.5	-199.6	0.476370	-201.8	-204.1	5.754400	-202.6	-204.9
0.043363	-195.8	-199.8	0.522320	-202.0	-204.3	6.309600	-202.6	-204.9
0.047547	-195.4	-199.8	0.572720	-202.2	-204.5	6.918300	-202.5	-204.8
0.052134	—	—	0.627970	-202.4	-204.6	7.585800	-202.5	-204.8
0.057164	—	—	0.688560	-202.5	-204.7	8.317600	-202.5	-204.8
0.060000	—	—	0.754990	-202.5	-204.7	9.120100	-202.4	-204.8
0.065789	—	—	0.827830	-202.6	-204.8			

* We show two noise levels: P_{50} , the 50% (median) variation level; and P_{10} , the lowest 10% power-variation level. We believe these represent quiet, and typical noise behavior, respectively.

† Units of decibels relative to nominal strain.

§ Values at frequencies with the marker “—” are highly influenced by the instrumental noise source (see Instrumental Noise section) and have been excluded from the table.

from the three strainmeters at PFO.

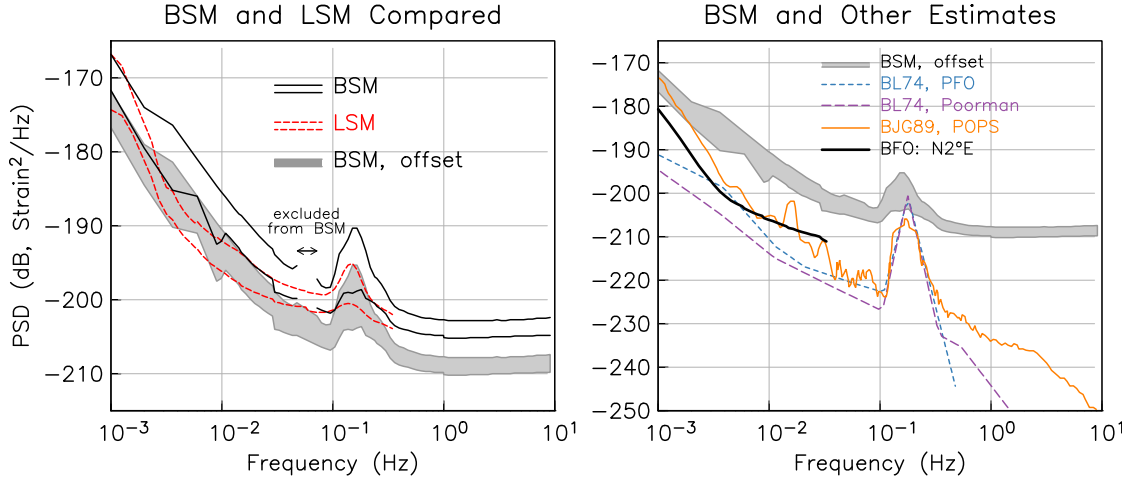


Figure 2.7: Comparison of the spectra from the borehole strainmeters and from other strain measurements. The set of solid lines in the left panel show the median and 10% levels for the borehole strainmeters (BSM): both are the lowest level measured over all channels and sites. It also shows (set of dashed lines) the same levels for the long-baseline laser strainmeters (LSM) at PFO, again taking the lowest value over the three systems there. The filled grey band is the borehole strainmeter levels shifted by -5 dB to make the microseism levels match. The right panel shows this shifted estimate for the borehole strainmeters, along with spectral levels estimated by *Berger and Levine* (1974) (BL74), and *Borcherdt et al.* (1989) (BJG89), and with the 5% spectral level from a Black Forest Observatory (BFO) strainmeter. Plots for each system at PFO and BFO, and noise levels for the laser strainmeters can be found in Appendix B.

As noted in Section 2.2, we have assumed that the data from individual components of the borehole strainmeters is horizontal uniaxial strain, and that the relevant calibration is that given by the manufacturer. As an approximate correction for any systematic errors introduced by this, the left panel of Figure 2.7 also shows the 10% and median levels of the borehole strainmeter noise, reduced by 5 dB (a factor of 1.8) to make the spectra match the laser strainmeter spectra at the one frequency range where we can be sure that both systems measure Earth noise: the microseism band. After making this adjustment, which is consistent with the amplification factor described by *Gladwin and Hart* (1985), we see that the borehole strainmeter noise level falls slightly below that of the laser strainmeter at frequencies slightly above and below that of the microseism peak, with the two

systems being comparable for frequencies from 3×10^{-2} Hz to 3×10^{-3} Hz. It should be noted that we do not expect the LSM spectra at these frequencies to be especially quiet because of surface noise (e.g. wind and other variations) that cannot be completely shielded against.

The right panel of Figure 2.7 compares this adjusted noise estimate for the borehole strainmeters with noise spectra determined by some of the earlier workers listed in Section 2.1; we note that for these earlier results, it is generally not clear if the spectra shown are typical results (as our median level attempts to represent) or exceptionally quiet ones. The spectrum in *Fix and Sherwin* (1972) is well below any of the others; but this is stated to be for data at a very quiet time, at a site with seismic noise levels that are among the quietest ever given, so we do not include it as a comparison. We also note that the low noise levels given by *Berger and Levine* (1974) for the PFO laser strainmeters are significantly below those we have observed more recently with the same instruments.

As an additional check, we computed time-varying spectra for data (kindly provided by R. Widmer-Schmidrig – see Data and Resources section) from three strainmeters at the Black Forest Observatory (BFO), in southern Germany (48.3301° N, 8.3231° E). These instruments are 10 meters long, with wire length standards, having been modified from the design of *King and Bilham* (1976); they are located in purpose-built tunnels, with 170 m overburden, and sealed by airlocks (*Richter et al.*, 1995). *Widmer et al.* (1992) have shown normal-mode results from these strainmeters. We analyzed data from 2004:336 through 2005:343, sampled at 0.2 Hz, after removing (and interpolating across) small gaps and calibration steps. Figure B.1 shows the spectra and their variations; in Figure 2.7 we plot the 5% level for the quietest of these systems.

Assuming the reliability of the other spectral estimates shown, 2.7 certainly suggests that for seismic frequencies outside the microseism band, the PBO borehole strainmeters are not measuring actual strain in the Earth. The lowest possible noise level for the borehole strainmeter is set by least-count noise, which with the 5 dB adjustment used in this plot would fall at -216 dB, well above the noise levels claimed for other systems. It is worth noting that these other systems have in-

trinsically much finer resolution: the Poorman long-baseline strainmeter because it used a Fabry-Perot interferometer, and the dilatometer analyzed by *Borcherdt et al.* (1989) because its hydraulic amplification system makes the displacements to be measured about 3000 times larger than they would be on the PBO borehole strainmeters, for the same strain.

2.6 Conclusions

We have computed power spectra for a year of data from the PBO borehole strainmeters in southern California in order to quantify typical background noise for frequencies from 10^{-3} Hz to 10 Hz. We have developed software for this purpose that provides a compact, reliable, and flexible estimate of spectral levels, which we apply over intervals that depend on frequency, and from which we can estimate the probability density function at each frequency.

The median spectral level is fairly consistent across installations and across sensors in each installation, with two exceptions. The first exception is two stations (B082 and B089) show much higher noise levels; at these two stations, and possibly also at B081, the power spectral density is much more variable than at the other locations. The second exception is that all systems have increased noise over a narrow band with characteristic frequencies that differ from one installation to another. This increased noise is usually non-stationary, usually varying over a day in a way similar to voltage changes in the batteries used to power the system.

All well-functioning systems record ground noise in the microseism band. At frequencies below this band the median spectral level on PBO borehole strainmeters is consistent with data from nearby long-baseline laser strainmeters, analyzed using the same procedures. At frequencies higher than the microseism band, the spectral level is consistent with a few counts of white noise being present; it also appears that the relationship between the 20 Hz data and the 1 Hz data derived from it is not entirely straightforward. Previously published data from other types of strainmeter installations, although sparse, suggest that the level of strain ground noise at frequencies above 0.5 Hz, and from 0.001 Hz to 0.1 Hz, is most

likely below the resolution of the PBO borehole strainmeters.

2.7 Data and Resources

Raw PBO borehole strainmeter data used in this study were downloaded from the Northern California Earthquake Data Center (NCEDC) at <http://www.ncedc.org/pbo/strain/raw/bsm>. Laser strainmeter data used in this study are from the Piñon Flat Observatory archive, but the equivalent raw data may also be downloaded from NCEDC at <http://www.ncedc.org/pbo/strain/raw/lsm>. Information about laser strainmeter operation and data processing techniques may be found at <http://escholarship.org/uc/item/21z72167>. Data for the Black Forest Observatory strainmeters was provided by Ruedi Widmer-Schmidrig and Walter Zürn. More information regarding the observatory may be found at <http://www.gpi.kit.edu>. Gridded population data was downloaded from National Climatic Data Center at <http://www.ncdc.noaa.gov/oa/climate/research/population>. Other data used for comparison came from published sources listed in the references. The adaptive sine-multitaper spectral estimation is modified from the software *psd*, developed and maintained by Robert L. Parker, which may be found at <http://igppweb.ucsd.edu/~parker>.

2.8 Appendix: Nonlinearity of the GTSM sensor

The GTSM uses a differential capacitance bridge to measure displacements across the instrument, equivalent to uniaxial strain inside it. A cartoon cross-section of the GTSM, as grouted into rock, is shown in Figure 2.8 (left). As this diagram shows, the bridge consists of two capacitors: One capacitor is formed by a pair of fixed plates, and the other is formed by one of the fixed plates and another plate which is allowed to translate during instrument straining. These are fed AC current from a ratio transformer (a very precise adjustable voltage divider), as shown in Figure 2.8 (right). This is the bridge described by *Stacey et al.* (1969) and the capacitor system described by *Gladwin* (1984).

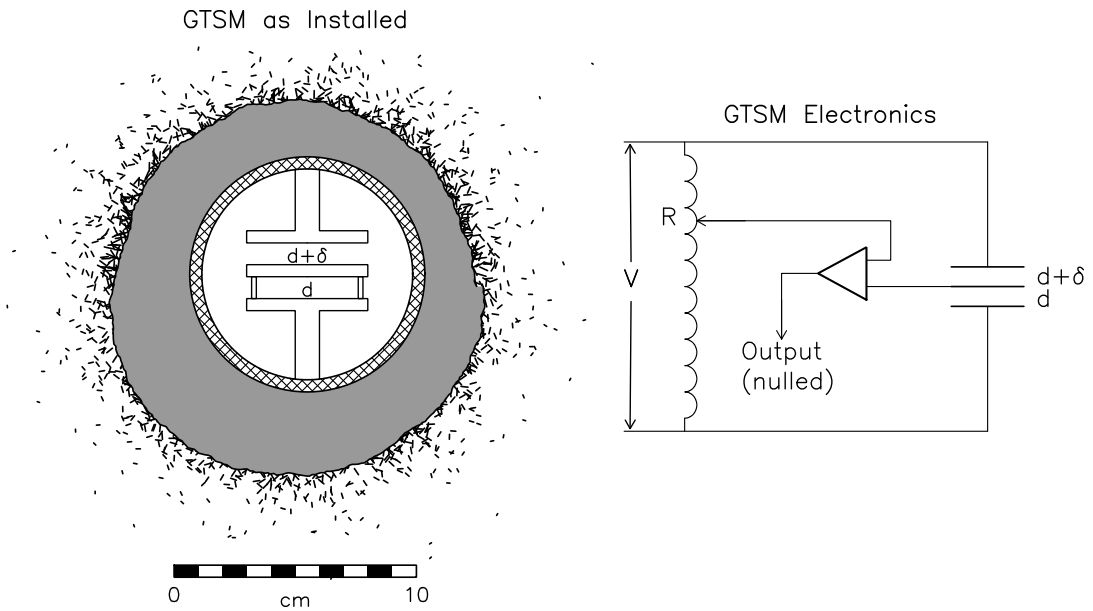


Figure 2.8: Left panel: cross-section of GTSM as installed, with hole and outside of instrument to scale; inside is a cartoon of the capacitor-plate sensor. Right panel: simplified circuit diagram for GTSM transducer and bridge. The transducer is a differential capacitance, one fixed with plate separation d , the other variable with plate separation $d + \delta$. A ratio transformer divides the voltage sent to each plate pair, and the output is measured with a low impedance detector. The ratio transformer setting, R , is varied to make the output close to zero; the output is a combination of R and this output.

To highlight the inherent non-linearity in the instrument, we first take the voltage at the detector for a differential capacitance system, given by

$$V_d = \frac{\sum_n V_n Y_n}{\sum_n Y_n} \quad (2.1)$$

where Y_n are the admittances (defined as the inverse of impedance, Z) of the bridge system. The ratio bridge is balanced when

$$\sum_n V_n Y_n = 0$$

For a balanced GTSM bridge, Equation (2.1) becomes

$$V_1 Y_1 + V_2 Y_2 = 0$$

or, in terms of the bridge ratio R , this can be expressed as

$$\frac{Y_1}{Y_2} = -\frac{V_2}{V_1} = \frac{1-R}{R} \quad (2.2)$$

since V_1 and V_2 correspond to the voltage across the fixed-distance, and variable-distance capacitor, respectively.

We take $Y_n \propto 1/Z_n$ and $Z_n \propto d_n$, where d is the plate separation, and define the fixed- and variable-capacitor separation as

$$\begin{aligned} d_1 &= d \\ d_2 &= d + \delta \\ &= d(1 + \epsilon) \end{aligned}$$

where $\epsilon \equiv \delta/d$ is relative instrumental strain. Using this relationship the bridge-balance expression (Equation (2.2)) becomes

$$\frac{d(1 + \epsilon)}{d} = \frac{R}{1 - R}$$

Uniaxial strain across the instrument is $e = \epsilon d/D$, where D is the instrument diameter, so we have

$$e = \frac{d}{D} \left(\frac{2R - 1}{1 - R} \right) \quad (2.3)$$

which is nonlinear.

The gain (change in strain for a change in R) can be found by differentiating e with respect to R :

$$\frac{de}{dR} = \frac{d}{D}(1 - R)^{-2}$$

which, if $\delta \ll d$ so that $R \approx 0.5$ (infinitesimal strain), the gain will be approximately $4d/3D$. The instrument dimensions are $D = 87$ mm and, depending on the site, d is either 100 or 200 microns; hence, the theoretical gain of the system is 0.0015 or 0.0030 respectively. A change in R of 10^{-8} (one step of the ratio transformer) means the effective resolution of the system is 0.0046 or 0.0092, again with respect to gap distance; so, one least count is very nearly a strain of 10^{-10} at 200 microns (extension is positive). Furthermore, the amount of strain necessary to induce a $\pm 10\%$ variation in gain would be $\{-2.6, 2.3\} \times 10^{-6}$. Figure 2.9 demonstrates the gain-change effect, and highlights the 10% variation level.

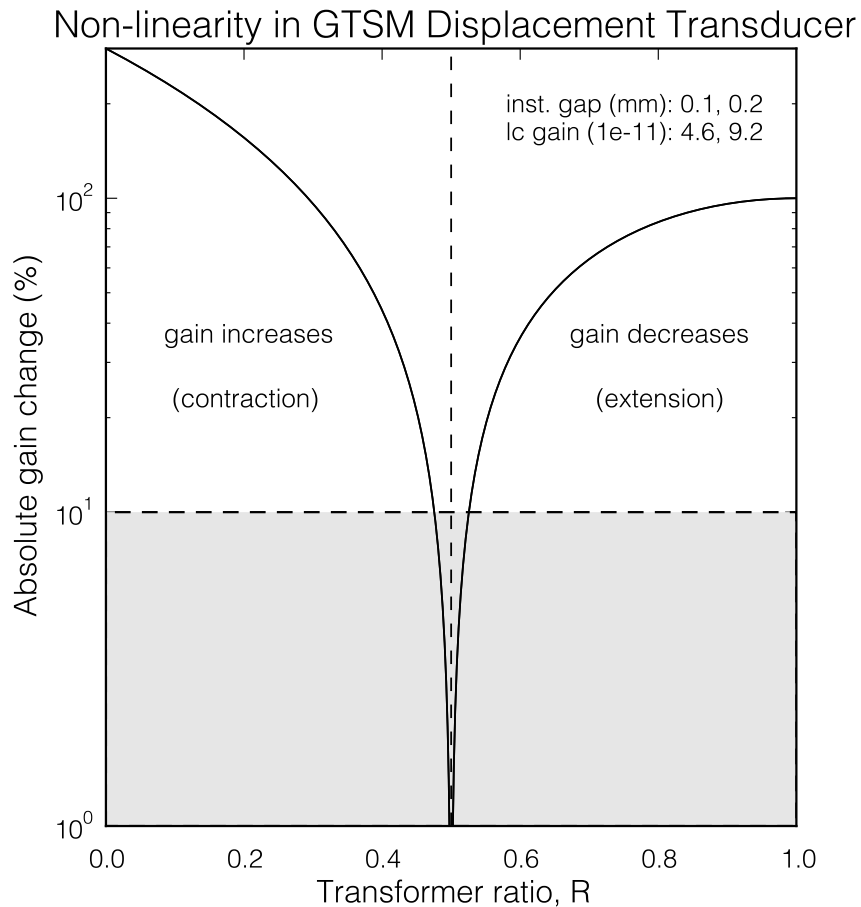


Figure 2.9: Response of the GTSM as a function of the bridge transformer ratio (R). The vertical scale shows absolute gain deviation in percent of the instrument's null-strain state, $\delta \approx 0$ or $R \approx 0.5$. Any contractional strain ($\delta < 0$) on the instrument will result in a gain increase, placing it to the left of the vertical dashed line; whereas, any extensional strain ($\delta > 0$) will result in a decrease in gain, placing it to the right of the line. The filled region indicates the 10% gain variation level, or when $R \approx \{0.475, 0.525\}$. Also shown are least-count resolutions for the two possible plate-separation gaps, based on the 160 dB analog-to-digital conversion of the transformer ratio signal, R .

2.9 Acknowledgments

We thank Frank Wyatt for useful discussions, Kathleen Hodgkinson for invaluable insight over the course of this work, and a helpful review; and Bob Parker for developing and maintaining the program *plotxy*, and especially the multitaper spectrum estimation program *psd*, both of which we have used extensively. We especially thank Ruedi Widmer-Schmidrig and Walter Zürn for very generously providing us with the BFO strainmeter data at very short notice. This work has been supported by the National Science Foundation Earthscope program under grant NSF EAR-0843878.

Chapter 2 is a reprint of Barbour and Agnew (2011), adapted for the dissertation. The dissertation author was the primary investigator and author of this paper.

Chapter 3

Detection of Seismic Signals Using Seismometers and Strainmeters

Using data from borehole and longbase strainmeters and from borehole and surface seismometers, we compare the seismic-wave detection capability of strainmeters and seismometers. We use noise spectra to determine the relative signal-to-noise ratio (SNR) on different sensors, as a function of the phase velocity and frequency of a signal. For the instruments we analyze, signals with frequencies from 10^{-3} Hz to 10 Hz and phase velocities typical of (or higher than) surface and body waves will have a lower SNR on the strainmeters than on broadband seismometers. At frequencies from 0.1 Hz to 10 Hz the borehole (short-period) seismometers have a better SNR than strainmeters for typical phase velocities; at lower frequencies the strainmeter data signal would have a higher SNR.

3.1 Introduction

The different response of strain and inertial seismometers to seismic waves has been studied at least since *Benioff and Gutenberg* (1952). *Romney* (1964) proposed that these different responses could be used to discriminate between different types of seismic waves, although further investigations by *Fix and Sherwin* (1970) and *Fix* (1973) did not result in generally useful methods. *Mikumo and Aki* (1964) and *Sacks et al.* (1976) suggested that strain and velocity records could be

combined to determine surface-wave phase velocity at a single site. Because of the difficulty of calibrating strainmeters this has not usually been practicable, though *Blum et al.* (2010) estimated Rayleigh-wave velocities by combining data from a vertical strainmeter in the borehole of the San Andreas Fault Observatory at Depth (SAFOD) and a broadband seismometer a few kilometers away. *Gomberg and Agnew* (1996) used strainmeter data to investigate how well data from seismometers, alone, could be used to estimate strains from seismic waves.

Of these investigators, only *Fix* (1973) compared noise levels and detection capabilities of strain and inertial seismometers. Noise levels on instruments determine what signals they can and cannot detect, and relative noise levels determine their relative performance in detecting and measuring similar signals. Combining data from strain and inertial instruments will be most effective if signals have similar signal-to-noise ratios (SNR's) on both sensors; if the SNR's are different for some class of signals then the instrument with the higher one would usually be preferred.

Barbour and Agnew (2011) determined noise levels at seismic frequencies for two types of strainmeters. We use these estimates, and similar ones for several types of inertial seismometers, to find the relative performance of these sensor types for typical seismic signals. We use data from the Anza region in Southern California because of the many seismic and strain instruments there, some of which are co-located. The Anza digital seismic network (*Vernon*, 1989) has operated since 1984, and since 1993 has used broadband instruments (Streckeisen STS-2) in surface vaults. A very-broad-band seismometer (Streckeisen STS-1) has operated at Piñon Flat Observatory (PFO) as part of the IDA-IRIS seismic network since 1989; since mid-2006 it has been located on a pier in a purpose-built vault at 5 m depth. PFO is also the location of three surface longbase laser strainmeters (LSM's) that have operated since 1973. Since mid-2006 the Plate Boundary Observatory (PBO) component of EarthScope has operated nine borehole strainmeters (BSM's) in this region, in several cases within 1 km or less of an existing surface seismometer. Each PBO borehole contains a four-component Gladwin Tensor Strainmeter (GTSM: *Gladwin* (1984)) at depths between 132 and 242 meters. All boreholes but one

also contain a three-component short-period seismometer (2 Hz Geospace HS-1) 10 m to 20 m above the strainmeters. Table 3.1 gives summary information about the sites we use.

Table 3.1: Some characteristics of Plate Boundary Observatory borehole strainmeters (BSM) and seismometers (Seis) in the Anza area used in this study, and distances to the two nearest surface seismometers.

site	Instrument depth [*]		V_R^\dagger (km/s)	Interval [‡] (m)	Nearest seismometers			
	BSM	Seis			dist	name	dist	name
	(m)	(m)			(km)		(km)	
B093	145	124			3.99	CRY	8.57	WMC
B088	147	137	1.92	100-200	13.40	FRD	13.64	BZN
B082	220	189	2.49	169-242	5.37	SND	7.80	WMC
B087	147	94	2.67	116-216	0.10	FRD	5.99	BZN
B086	226	216	2.93	143-242	7.63	SND	8.96	PFO
B081	229	211	2.97	142-242	0.39	KNW	15.32	RDM
B084	147	135	3.08	111-211	0.13	PFO*	0.28	PFO

^{*} Depths are relative to the top of the borehole casing.

[†] Halfspace Rayleigh-wave velocity, found from the median P-wave velocity, as measured by a sonic logging tool over the depth interval given ([‡]), and the relationships in *Brocher* (2005).

[‡] Depth interval used for calculation of V_R .

* A station in the IDA-IRIS seismic network; otherwise, a station in the Anza network.

All the strainmeters we study have a flat response from zero frequency to the cutoff imposed by the recording system. Because the response of inertial seismometers to velocity or displacement falls off with decreasing frequency, only a few instruments (such as the STS-1) have noise levels comparable to Earth noise at very low frequencies (*Agnew and Berger, 1978; Berger et al., 2004*). The flat response of strainmeters thus suggests that they might be valuable for measuring such low-frequency phenomena as the Earth’s normal modes (*Widmer et al., 1992; Park et al., 2008*).

In principle the finite length of strainmeters affects their response to seismic

waves. Many strainmeters measure differential displacement between two points separated by a distance L : 0.087 m for the GTSM's and 720 m for the LSM's. Other borehole strainmeter designs (*Sacks et al.*, 1971; *Sakata et al.*, 1982; *Linde and Sacks*, 2008) measure changes in a volume V with lengths of a few meters. So all strainmeters in fact measure average strain over a distance L , and their response to seismic waves with wavelength $\lambda = c/f$ is therefore proportional to

$$\frac{\sin(\pi L/\lambda)}{\pi L/\lambda} = \frac{\sin(\pi Lf/c)}{\pi Lf/c} \quad (3.1)$$

where c is the apparent velocity and f the frequency; this expression will be close to one if $Lf/c \ll 1$. For example, if $c = 1$ km/s and $L = 0.1$ m, this would require f to be much less than 10 kHz; for $L = 600$ m, f must be much less than 1.5 Hz. Spatial filtering is thus significant only for short-period signals recorded on the LSM's; partly for this reason, data from these instruments is recorded (after analog lowpass filtering) only for frequencies below 0.5 Hz. For the BSM's the effect is negligible at the usual seismic frequencies.

3.2 Relative Detection Threshold for Strainmeters and Seismometers

The relative performance of strainmeters and seismometers will depend on two things: for large signals their accuracy (dynamic range), and for small signals their noise levels (detection threshold).

The dynamic range of seismometers is well-studied. *Agnew and Wyatt* (2003) discussed the dynamic range of the LSM's: these instruments can record strains up to about 10^{-6} , but for larger strains the deformation of the instrument is so large that the light beam does not return from the remote end, and there is no interference signal to measure. This occurred, for example, on the laser strainmeters within 150 km of the April 4th, 2010 $M_w 7.2$ Sierra El-Mayor/Cucapah earthquake, though not on more distant ones. In keeping with the dynamic range suggested by *Gladwin* (1984), the Anza-area BSM's recorded these same signals with no problem, though there is some evidence that their response to large signals

includes spurious coseismic offsets.

For signals not too large to exceed the dynamic range, the relative performance of strainmeters and seismometers depends on their relative SNR for a particular signal. The noise on both seismometers and strainmeters varies with frequency and must be described by its power spectral density (PSD). We therefore perform our analysis entirely in the frequency domain.

Suppose we have a transient signal $u(t)$, with Fourier amplitude spectrum $U(f)$, recorded along with a stationary stochastic process (the “noise”), with PSD $N(f)$. A standard result from signal-detection theory (*Helstrom*, 1968, Section 4.3) is that the detectability of the signal depends on the signal-to-noise ratio (SNR), the square of which is R^2 , given by

$$R^2 = \int_0^\infty R^2(f) df = \int_0^\infty |U(f)|^2 N^{-1}(f) df \quad (3.2)$$

where the frequency range is $[0, \infty)$ because $N(f)$ is a single-sided power spectral density. Note that the integrand is everywhere positive, but will be close to zero if $|U(f)|^2$ is small relative to $N(f)$; we will thus get a nearly equivalent R^2 if we integrate only over frequencies where $|U(f)|^2$ is large relative to $N(f)$.

Now suppose that we have two instruments that record the same signal but have different noise spectra, say $N_A(f)$ and $N_B(f)$. These differences might arise from different levels of ground noise or from different instrument behavior. Suppose the energy of the signal is concentrated in a narrow frequency band of width $2\Delta f$; then the relative SNR is

$$\frac{R_A^2}{R_B^2} = \frac{\int |U(f)|^2 N_A^{-1}(f) df}{\int |U(f)|^2 N_B^{-1}(f) df} \quad (3.3)$$

where the limits of integration are $[f - \Delta f, f + \Delta f]$.

As the bandwidth $2\Delta f$ becomes small, we can assume $U(f)$ and the $N(f)$'s are approximately constant over the range of integration, in which case this expression becomes

$$\frac{R_A^2(f)}{R_B^2(f)} = \frac{2\Delta f |U(f)|^2 N_A^{-1}(f)}{2\Delta f |U(f)|^2 N_B^{-1}(f)} = \frac{N_B(f)}{N_A(f)} = D(f) \quad (3.4)$$

which gives the relative SNR levels of the two sensors. as a function of frequency. We can think of this ratio as the relative detectability as a function of signal

frequency. For signal frequencies with $D(f) = 1$, the sensors have equivalent performance; for signal frequencies with $D(f) < 1$, sensor B will have a better SNR and can detect smaller signals; and if $D(f) > 1$, sensor A can detect smaller signals.

This derivation assumes that the two sensors measure the same quantity, as would be the case for a pair of inertial seismometers, since these respond to acceleration. But to compare strainmeters and seismometers we have to allow for one being a measurement of acceleration (or an integral of it), and the other of strain. Suppose the displacement u is (in the one-dimensional case) from a plane wave traveling with phase velocity c , so that $u(t, x) = u(t - x/c)$. The strain is $\epsilon(x, t) = \partial_x u(t, x) = -c^{-1}u'$, and the particle velocity is $v(x, t) = \partial_t u(t, x) = u'$, so the amplitude spectra of the signal in strain and velocity will be $U_\epsilon(f) = -2\pi i f c^{-1}U(f)$ and $U_v(f) = 2\pi i f U(f)$ respectively. The ratio of amplitude spectra is then

$$\frac{U_v(f)}{U_\epsilon(f)} = c = p^{-1} \quad (3.5)$$

where p is the slowness. The corrections to Equation (3.5) in the case of a wave undergoing attenuation and geometrical spreading are usually small (see Appendix 3.7).

If the signal is measured by a strainmeter with noise spectrum $N_\epsilon(f)$, and a seismometer with noise spectrum $N_v(f)$, then the relative performance at any frequency is again the ratio of their squared SNR's:

$$D(f, c) = \frac{|U_\epsilon(f)|^2 N_v(f)}{N_\epsilon(f) |U_v(f)|^2} = \frac{N_v(f)}{c^2(f) N_\epsilon(f)} \quad (3.6)$$

where the relative detectability now becomes a function of the ratio of noise levels, which depends on f , and the phase velocity c . For any particular wave-type and Earth-structure, c will also be a function of f , but for now we leave it a general parameter.

We could imagine making a contour plot of $D(f, c)$, but the most useful way to show relative performance is to take a single contour for which $D(f, c) = 1$, along which the two types of instruments have the same SNR. In practice we can

express this contour as a value of c for each f :

$$c_d(f) = \sqrt{\frac{N_v(f)}{N_\epsilon(f)}} \quad (3.7)$$

Equation (3.7) gives, from observed noise levels, a phase velocity $c_d(f)$. If the noise on both instruments is actual ground motion, c_d will equal the actual phase velocities of the waves that the noise consists of; if the noise on one instrument (or both) is above the level of ground noise, c_d will have a different value. To see if a signal will be better recorded on one instrument type or the other, we need to compare its phase velocity, which we denote by $c(f)$, with $c_d(f)$. If at some frequency $c(f) = c_d(f)$, the signal will be recorded with the same SNR on the strainmeter and the seismometer. If $c(f) < c_d(f)$, the SNR will be larger on the strainmeter; and, if $c(f) > c_d(f)$, the SNR will be larger on the seismometer. Equation (3.7) can thus be thought of as dividing $c - f$ space into two regions. The relative SNR for a seismic signal will depend on which region its dispersion curve falls into, whether at a higher or lower phase velocity than $c_d(f)$.

3.3 Noise Estimates

Barbour and Agnew (2011), estimated noise spectra for the BSM's and LSM's in the Anza area using a sine-multitaper method applied to time windows ranging from 3 minutes to 6 hours. The spectral estimates for each window were summarized using piecewise linear functions in log frequency and PSD. We used the noise estimates at each frequency to find an empirical probability distribution function (pdf); our summary value for a particular sensor was the median.

For seismometer noise spectra we follow the same procedures to form empirical pdf's of seismic noise, again for data during 2009. Figure 3.1 shows the summary spectra for all sensors examined. When multiple comparisons are available (true for all but the PFO STS-1) we show the range of medians and the average between the maximum and minimum; this average is the spectral level we use in finding the relative detection threshold. The seismic spectra have three features, all well-known. At the highest frequencies, the PBO borehole instruments

are the quietest, but because of their poor low-frequency response, their apparent noise level rises steeply for frequencies below the microseism peak around 0.15 Hz. For surface instruments at low frequencies, vertical seismometers are quieter than horizontals. The STS-1 instrument that is installed in a vault has the lowest noise at periods longer than 15 s, though still above the New Low Noise Model (NLNM) values of *Peterson* (1993).

Figure 3.1 also shows the spectra for the BSM's. To compute $c_d(f)$ we have adjusted the levels to remove the increased noise observed on the BSM's at periods of 10 to 20 seconds, since we believe this is caused by voltages induced by the battery-charging circuits [see Instrumental Noise in *Barbour and Agnew* (2011)], an effect which does not appear on all GTSM's in the PBO network.

In Appendix B we show the medians and pdf's of the acceleration PSD's of seismic noise above 10 mHz for individual borehole seismometers (Figures B.3 and B.4). Figures B.5 and B.6 show the same quantities for the surface seismometers for frequencies above 1 mHz. In Figure B.7 we show the relative SNR, $D(f)$, for comparisons between the median noise-level of surface broadband instruments in the Anza network, and the median noise-levels of the other seismometer types we analyze.

3.4 Results

Figure 3.2 shows the results of applying the noise spectra in Figure 3.1 to Equation (3.7), with separate plots for comparing strainmeters with horizontal and vertical broadband seismometers. As would be expected from the relative values of the noise spectra, the PBO borehole seismometers give the lowest value of $c_d(f)$ for frequencies above the frequencies of microseisms, and the highest values at frequencies below them. Figure B.8 shows the same comparison for the LSM noise levels: the $c_d(f)$ curves are also very similar since over the seismic band these levels are not much different from those for the BSM's.

All seismometer/strainmeter noise ratios give about the same value of c_d in the microseism band: roughly 3 km s^{-1} , which is the phase velocity of surface

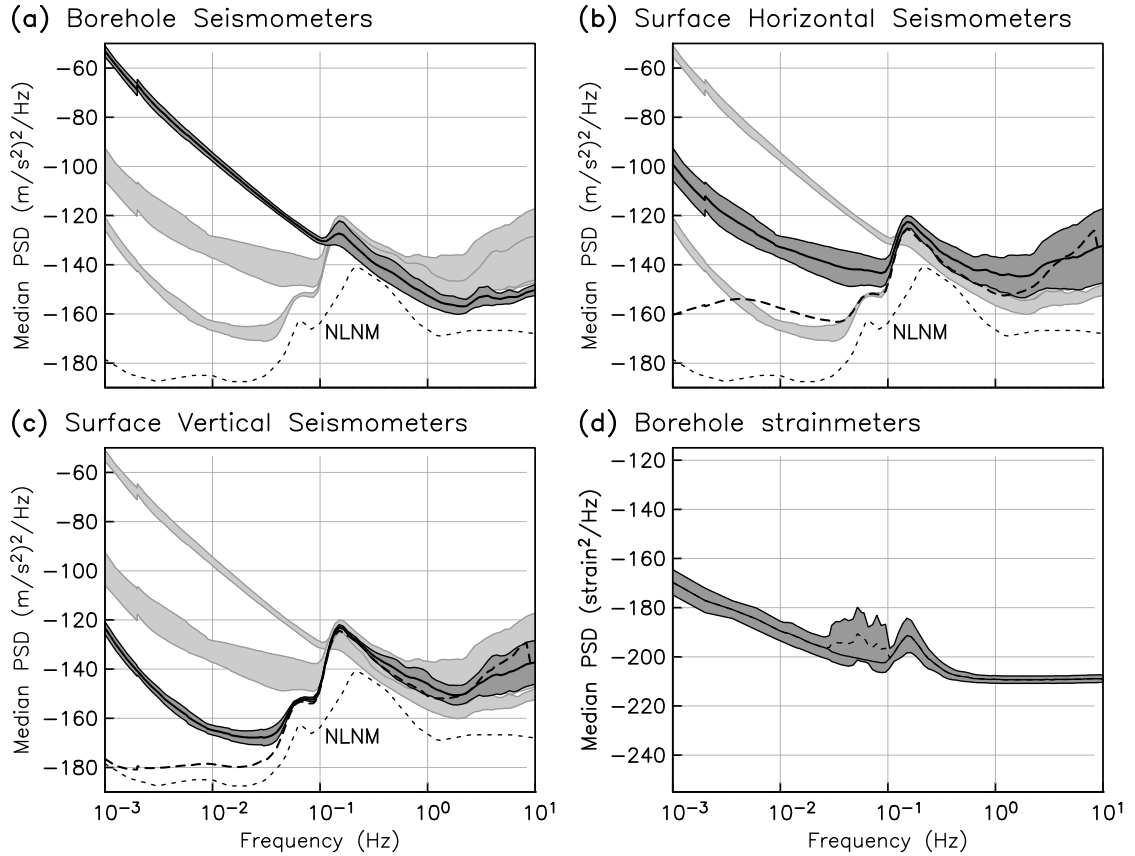


Figure 3.1: Median noise levels (power spectral density) of the seismometers and strainmeters used in this study, for acceleration and strain. In each frame the dark gray regions show the range of medians for the instrument type given, with the black line being the value halfway between these limits. The light gray regions in each plot are shown as comparisons between instrument type and component. (a) shows spectral levels for the vertical components of the Plate Boundary Observatory borehole seismometers. (b) and (c) show levels for the horizontal and vertical components of broadband instruments at the surface; in these the the heavy dashed line shows the median noise level for the single STS-1 sensor in a shallow vault at PFO. (a), (b), and (c) also show the NLNM from *Peterson (1993)* as a dotted line. (d) shows strainmeter noise levels, the dashed line being the true middle level, which we have adjusted to the level of the solid line to avoid the effects of spurious noise at these frequencies.

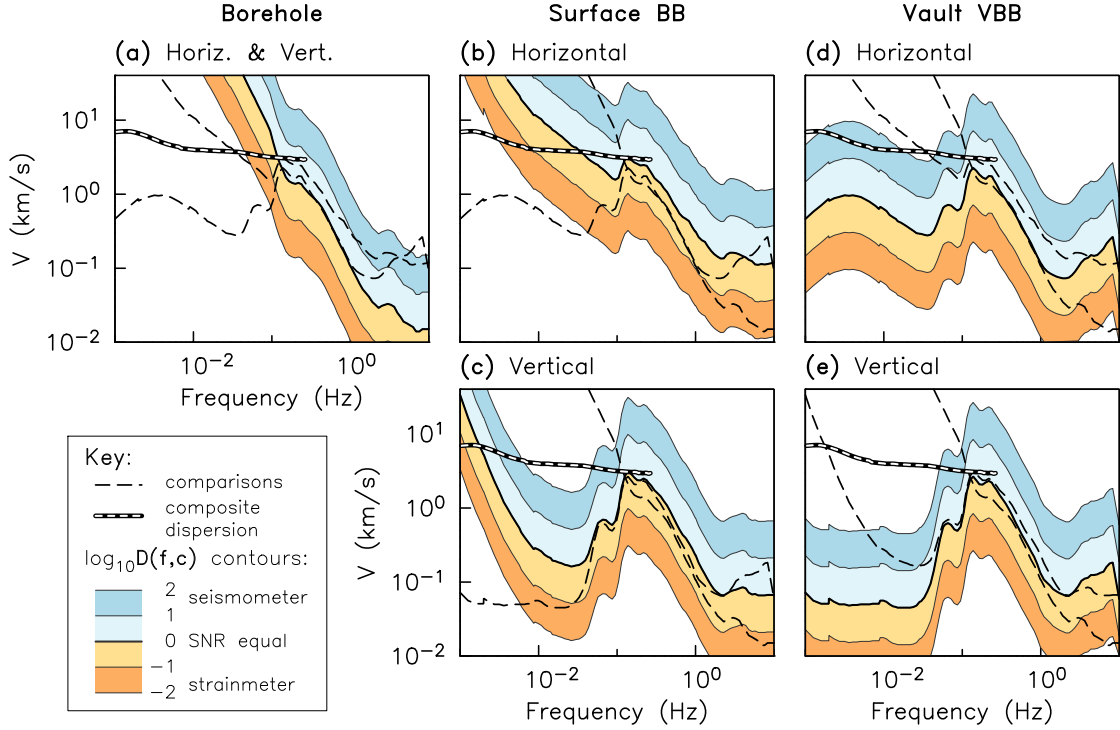


Figure 3.2: Selected contours of relative detectability, $D(f, c(f))$, for Plate Boundary Observatory borehole strainmeters (GTSM) compared to nearby short-period and broadband seismometers. The heavy line shows the $c_d(f)$ contour, the curve in $c-f$ space for which the signal-to-noise ratio (SNR) would be the same for strainmeters and seismometers [Equation (3.7)]. Other contour levels shown are $\log_{10} D \in N$ for $N = \pm\{1, 2\}$: the lower the level the more favorable the SNR is for the strainmeters. (a) compares the GTSM with the PBO borehole seismometers, for which the noise level is very similar on vertical and horizontal channels. (b) and (c) compare the GTSM and horizontal and vertical broadband (BB) seismometers at the surface; (d) and (e) compare the GTSM and horizontal and vertical very-broad-band (VBB) seismometers in a shallow vault. Thin dashed lines are c_d contours from the other frames, included for easy intercomparison. The thick, dotted black line shows a composite Rayleigh-wave dispersion curve (see text); this is the lower bound for seismic-wave phase velocities as a function of frequency.

waves at these frequencies. As noted above, this occurs because the microseism energy is large enough to be the noise source on both the seismometers and the strainmeters.

Which side of the $c_d(f)$ curve will other seismic signals fall on? For a given Earth structure the lowest values of c will be associated with fundamental-mode surface waves; the apparent velocities of body waves must be larger than this, and will be infinite for vertical incidence. Figure 3.2 includes a composite Rayleigh-wave dispersion curve which, for frequencies above 0.01 Hz, is an average for Southern California (*Yang and Forsyth, 2006; Prieto et al., 2009a*) and at longer periods is for a spherically-averaged Earth (see Data and Resources). At frequencies above 0.25 Hz the phase velocity of a signal will depend on local structure, but it will almost always be greater than the Rayleigh-wave phase velocity for a halfspace. Sonic logging of the boreholes at the BSM sites gives a halfspace velocity of 2 km s^{-1} to 3 km s^{-1} (Table 3.1), though *Fletcher et al. (1990)* and *Radzevicius and Pavlis (1999)* show values as low as 0.5 km s^{-1} very close to the surface. On land, lower values than 0.5 km s^{-1} are observed only in very soft materials such as mud and sand (*Brocher, 2005*); even in seafloor sediments, values below 0.1 km s^{-1} are confined only to the uppermost 100 m (*Kugler et al., 2007*).

In Figure 3.3 we take a slice through the $D^{-1}(f, c)$ surfaces shown in Figure 3.2. This slice is taken in $c - f$ space along the composite curve of phase velocity for surface waves. The different curves in Figure 3.3 thus show, for surface waves and for each type of seismometer, the relative SNR between that seismometer and the GTSM. Because $D^{-1}(f, c) \propto c(f)^2$, this relative SNR would be higher for other types of seismic waves with larger phase velocities, showing a better relative performance by the seismometer.

3.5 Conclusions

We have shown that for recording seismic waves, the BSM system used in the PBO network (the GTSM) will have a lower SNR than current broadband seismometers, except perhaps when compared to horizontal-component measure-

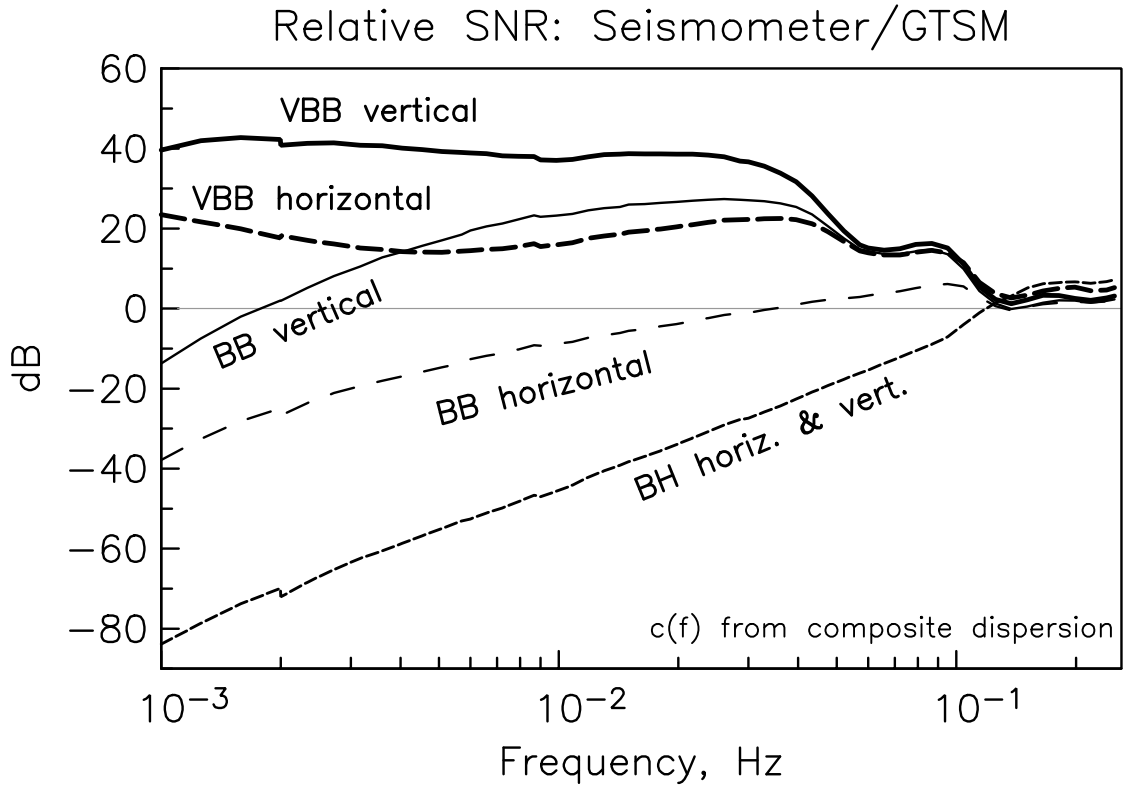


Figure 3.3: Relative signal-to-noise ratio (SNR) for seismometers relative to borehole strainmeters, for the lowest expected phase velocity for seismic signals. These curves are found from $D(f, c(f))$, where $c(f)$ is given by the composite dispersion curve in Figure 3.2. Units are decibels (dB) relative to the ratio between seismometer and strainmeter SNR's; hence, positive values indicate a greater SNR on the seismometer than the strainmeter, and negative ones the opposite. The slightly positive SNR in the double-frequency microseism band suggests that these curves may be biased by differences in the data that the median was computed from, or reflect calibration issues with the borehole strainmeters.

ments near the surface (Figures 3.2 and 3.3). Because of the high level of ground motion in the dual-frequency microseism band, the SNR for other signals will be equivalent on the BSM and seismometers. At periods longer than 6 s to 10 s the BSM will have a better SNR than a short-period sensor with a velocity transducer (Figure 3.3). These conclusions also apply to the LSM's, which additionally have unsuitable dimensions for recording short-period seismic waves.

Our conclusions about the relative merits of strainmeters and seismometers are driven by the relatively high noise of the former. It is worth noting that these BSM's and LSM's were installed primarily to measure crustal deformation over much longer periods, from hours to (possibly) years: neither strainmeter design was optimized for recording seismic waves. The short baselength of the GTSM (87 mm) means that the very small strains from small seismic waves put severe demands on its displacement transducer. For example, given the level of broadband seismometer noise at periods of 15 s to 100 s, the $c_d(f)$ curve could be as low as 4 km s^{-1} only if the strain noise was between -225 and -240 dB (on the scale used in Figure 3.1). Such low noise levels would require the displacement transducer to have an rms displacement noise of 10^{-14} m, about the size of a large atomic nucleus. BSM designs which use hydraulic amplification can have effective baselengths (in terms of transducer displacement for a given strain) up to a thousand times larger than the GTSM baselength, and this may make them more suitable for recording seismic waves. Even relatively simple strainmeters can do well if installed in the right setting, for example the 10-m wire strainmeters operated in a mine (the Black Forest Observatory) at 165 m depth (*Widmer et al.*, 1992). But only with noise spectra for other candidate sensors will a full evaluation of them be possible.

3.6 Data and Resources

Borehole strainmeter data are from the PBO data at the Northern California Earthquake Data Center (NCEDC). Laser strainmeter data are from files held by the authors, and are also available at the NCEDC. Continuous seismic data are from the IRIS-DMC using SOD (*Owens et al.*, 2004). The longest-period

dispersion curve is from the Reference Earth Model website (<http://igppweb.ucsd.edu/~gabi/rem.html>) last accessed in July 2012. All other data are from published sources.

3.7 Appendix: Effects of Wavefront Curvature and Attenuation

In the main text we show that for a one-dimensional wave propagating at speed c , the ratio of particle velocity to strain is just that wave velocity. Here we generalize this to include two-dimensional motions, wavefront curvature, and attenuation for an axisymmetric propagating wave. In cylindrical coordinates the horizontal displacement of such a wave is

$$\mathbf{u}(r, t) = \frac{e^{-r/D}}{r^2} \left[\hat{r}u_1(t - r/c) + \hat{\theta}u_2(t - r/c) \right] \quad (3.8)$$

where \hat{r} and $\hat{\theta}$ are the radial and azimuthal directions. In Equation (3.8) the leading term expresses amplitude changes from geometrical spreading and from attenuation, where D is the attenuation distance; see also *Gomberg and Agnew (1996)*. Because the waveform is axisymmetric, the tensor components of strain in a cylindrical reference frame become

$$e_{rr} = \frac{\partial u_r}{\partial r} \quad (3.9)$$

$$e_{\theta\theta} = \frac{u_r}{r} \quad (3.10)$$

$$\gamma_{r\theta} = 2e_{r\theta} = \frac{\partial u_\theta}{\partial r} - \frac{u_\theta}{r} \quad (3.11)$$

Substituting the expression (3.8) into the definition of e_{rr} in (3.9), we find that

$$e_{rr}(r, t) = -\frac{e^{-r/D}}{r^2} \left[\left(\frac{1}{D} + \frac{2}{r} \right) u_1 + \frac{1}{c} u_1' \right] \quad (3.12)$$

while the radial velocity is

$$v_1(r, t) = \frac{e^{-r/D}}{r^2} u_1' \quad (3.13)$$

Taking Fourier transforms of e_{rr} and v_1 gives the functions $E_{rr}(r, f)$ and $V_1(r, f)$; the ratio of the second to the first is

$$\frac{V_1}{E_{rr}} = -2\pi i f \left[\frac{1}{D} + \frac{2}{r} + \frac{2\pi i f}{c} \right]^{-1} = -c \left[1 - i \frac{\lambda}{2\pi} \left(\frac{1}{D} + \frac{2}{R} \right) \right]^{-1} \quad (3.14)$$

and if we take absolute values in order to get relative magnitudes this becomes

$$\frac{|V_1|}{|E_{rr}|} = c \left[1 + \frac{\lambda^2}{4\pi^2} \left(\frac{1}{D} + \frac{2}{R} \right)^2 \right]^{-\frac{1}{2}} \quad (3.15)$$

where in the final expression we have replaced r with R to indicate that this is the radius of curvature of the wavefront (unrelated to the signal-to-noise ratio defined in the main text). In Equation (3.8), this value is equivalent to the distance from the source, but could be altered due to focusing or defocusing by local heterogeneities. Simply for the wave to be observed the attenuation must be small enough that $\lambda/2\pi D \ll 1$. Except in the near field, or with significant focusing, we would also expect $\lambda/2\pi R \ll 1$, so that the ratio in Equation (3.15) will be c , as in the plane-wave case. But if R is small enough for the λ/R term to matter, the ratio will be smaller than it would be in the plane-wave case. Thus for strongly-curved wavefronts, the strainmeter has a higher SNR, relative to the seismometer, than it would in the absence of curvature.

Similar derivations follow for the other strain components, giving the ratios:

$$\frac{|V_1|}{|E_{\theta\theta}|} = \frac{2\pi\lambda}{R} c \quad (3.16)$$

$$\frac{|V_2|}{|\Gamma_{r\theta}|} = \frac{|V_2|}{|2E_{r\theta}|} = c \left[1 + \frac{\lambda^2}{4\pi^2} \left(\frac{1}{D} + \frac{3}{R} \right)^2 \right]^{-\frac{1}{2}} \quad (3.17)$$

where $\Gamma_{r\theta}$ is the Fourier transform of $\gamma_{r\theta}$. Again, so long as the wavelength is much shorter than the radius of curvature of the wavefront ($R \gg \lambda$), the one-dimensional model is an adequate approximation.

3.8 Acknowledgments

We thank Germán Prieto for making his surface-wave results available, and Gabi Laske for assistance with the global velocity model. We thank both anonymous reviewers for comments which led to significant improvements in clarity, and

one for suggesting that we consider the corrections for a curved wavefront. This research was supported by NSF grants EAR08-43878 and EAR10-53208. This is Contribution 1530 from the Southern California Earthquake Center.

Chapter 3 is a reprint of Barbour and Agnew (2012), adapted for the dissertation. The dissertation author was the primary investigator and author of this paper.

Chapter 4

Coseismic Strains on Plate Boundary Observatory Borehole Strainmeters in Southern California

Plate Boundary Observatory (PBO) borehole strainmeters (BSMs) can show strain offsets coincident with seismic waves. We use a probabilistic detection method to compile a catalog of such offsets on PBO BSMs in southern California for 34 medium to large earthquakes since 2006. The “near-field” term in the elastodynamic equations produces a static strain offset at the same time as the S wave arrival. However, most of the offsets we detect (1) differ substantially from the static strain predicted by elastic dislocation theory, (2) correlate with the level of seismic energy density of the waves and (3) do not agree with colocated longbase laser strainmeter data, when this is available. We conclude that waves causing high levels of dynamic strain induce apparent strain offsets, presumably because of hysteresis effects, either in the rock close to the BSM’s, or in the instruments themselves. Offsets seen in these BSM data should therefore be viewed with caution before being applied to measure coseismic deformation induced by faulting.

4.1 Introduction

Fault slip in the Earth produces, along with radiated energy, static deformations that reflect the decrease in elastic energy associated with elastic rebound. These deformations appear in the elastodynamic equations (*Aki and Richards, 2002*) as a “near-field” term, with strains and tilts decaying away from the source region as the inverse cube of the distance. Because the relationship between the slip and deformation is relatively simple and relatively insensitive to Earth structure (*Okada, 1985; Segall, 2010*), measurements of the static deformation can provide detailed information about the geometry and distribution of fault slip. This has become more and more common with the increasing amount of precise geodetic data, whether GPS, InSAR, or LIDAR.

Prior to the advent of these newer methods, one of the main sources of information on static deformations was measurements made using continuously-recording strainmeters and tiltmeters. At the periods relevant to measuring static offsets (seconds to minutes) such instruments have much lower noise levels than geodetic methods that measure displacement (*Agnew, 1986; Reuveni et al., 2012*) and so remain potentially useful in measuring small signals.

However, measurements of this type have also been dogged by evidence that they often do not reflect the true tectonic strain. Because the static offset is concurrent with the much larger dynamic strains from the radiated seismic waves, there is the potential for the static offset to be more or less affected by instrumental hysteresis or triggered local effects. A study (*Press, 1965*) of strain offsets at teleseismic distances fostered considerable interest in such offsets, summarized at the time by *Wideman and Major (1967)* (see *Agnew (2007a)* for a general discussion). However, evidence accumulated that these steps could be caused by local effects (*Stacey and Rynn, 1970*), something that *Sacks et al. (1971)* attempted to eliminate by developing a strainmeter cemented into a borehole. While this instrument was shown to be unaffected by large dynamic strains induced by nearby explosions, subsequent data from other installations (e.g., *Linde and Johnston (1989)*) have sometimes shown static offsets inconsistent with other data. *Johnston et al. (1987)* note other cases of observed coseismic strain offsets that disagree with dis-

location models. A comparison (*Wyatt, 1988*) of coseismic strain offsets measured by longbase laser strainmeters (LSM) (*Agnew and Wyatt, 2003*) with dislocation models showed generally good agreement unless the shaking at the LSM location was large.

In this study we examine the static strain offsets observed at borehole strainmeters (BSM's) that are a subset of those installed by the Plate Boundary Observatory (PBO), namely the Gladwin Tensor Strainmeters (*Gladwin, 1984*) installed in the Anza region of southern California. We use a probabilistic detection method to estimate the strain offsets for 34 earthquakes recorded on these instruments; these earthquakes are spread among local, regional, and teleseismic distances, and over a wide range of magnitudes. We compare our estimates with strains predicted from dislocation models to determine under what circumstances these observed offsets can (or cannot) be relied on, and find a number of cases of disagreement, usually when the energy density of the associated seismic waves is large. This suggests that coseismic strain offsets from these sensors should be critically scrutinized before being used to infer source parameters.

4.2 Coseismic Strain Estimation

We first need to obtain a reliable estimates of static strain in an otherwise noisy record. Offset estimation is common in geophysical data processing, especially in processing of continuous GPS data; these data are often contaminated with signals from non-physical sources (e.g., antenna swaps), and the associated steps must be removed before estimating interseismic station velocity and other parameters. There are a number of automated methods for finding and estimating offsets, though a recent test (*Gazeaux et al., 2013*) suggests that none of them have a clear advantage over manual inspection and estimation. *Langbein (2010a)* developed a statistical method for removing steps in BSM data, for the purposes of routine processing long-period data, but this requires an assumption of the times of offsets. Because the noise in BSM data generally increases with decreasing frequency (*Barbour and Agnew, 2011*) finding steps requires examining only the data

nearby (*Williams*, 2003); but, estimating coseismic steps remains a challenging problem because these occur at the same time as much larger dynamic strains.

We have applied the probabilistic approach of *Auger and Lawrence* (1989), which makes no *a priori* assumptions of the existence or location of an offset – the algorithm estimates them automatically, and consistently.

4.2.1 Probabilistic Offset Detection

The fundamental assumption made in our estimation method is that a record is possibly “segmented”, meaning that individual sections of a strain record may have varying statistical properties (mean and variance) but all data are normally distributed. More formally, if a record X has N segments (and thus $N - 1$ parameter changes), then for each segment $X_n \sim \mathcal{N}(\mu_n, \sigma_n)$, $n = 1, 2, \dots, N$; where $\mathcal{N}(\cdot)$ denotes the normal probability distribution function (pdf) with mean μ and standard deviation σ .

In order to estimate the mean values in each segment, μ_n , we define a test statistic, Λ , which we base on a likelihood ratio between the following hypotheses:

- H_0 : (the null hypothesis) no static changes are present in the record
- H_a : (the alternate hypothesis) the record of length M is segmented into N components

and the following criteria for rejecting H_0 , based on a threshold λ :

- $\Lambda > \lambda$: do not reject H_0 (there are no static changes)
- $\Lambda \leq \lambda$: reject H_0 in favor of H_a (there are static changes)

For clarity we illustrate this for $N = 2$, a single-change alternate hypothesis. In this case we express the log-likelihood \mathcal{L} as the sum of probability density functions f for each segment, conditional upon the parameter estimates of each segment, θ :

$$\mathcal{L}(i) = \log f(X_{1:i}|\theta_1) + \log f(X_{i+1:M}|\theta_2) \quad (4.1)$$

The maximum log-likelihood is simply $\mathcal{L}(m)$, where m is the position in the record where the segmentation maximizes \mathcal{L} ; the test statistic is thus

$$2[\mathcal{L}(m) - \log f(X|\theta)] \quad (4.2)$$

However, in practice we wish to estimate parameters for multiple segments ($N > 2$), and this is where we apply the ‘Segment Neighborhood’ (SN) method (*Auger and Lawrence, 1989*). Briefly, the SN method is a minimization of the L_1 -norm of the penalized likelihood that N offsets exist at positions τ in the record:

$$\min_{\tau} \| -\mathcal{L}(\tau) \|_1 + \beta \mathcal{F}(N) \quad (4.3)$$

iterating over $N = 2, \dots, N_{\max}$. The optimal solution is found most efficiently by dynamic programming (*Bellman and Dreyfus, 1966*), and we have found that a penalization function based on the Schwartz Information Criterion (*Schwarz, 1978*), with $\beta = \log M$ and $\mathcal{F}(N) = N$, provides favorable results.

The computational cost of the SN method can be burdensome [$\mathcal{O}(N_{\max} M^2)$]; but this expense can be mitigated by choosing a suitable downsampling filter (e.g., *Agnew and Hodgkinson, 2007*), or by using a less expensive (but possibly less accurate) method (e.g., PELT, *Killick et al., 2012*). In practice we use relatively short records in order to reduce computational expense. For a more detailed description of the SN algorithm, with computational considerations, we refer the reader to the original paper by *Auger and Lawrence (1989)*, and a review by *Eckley et al. (2011)*.

4.2.2 Application to Strain Records: Processing and Calibration

We process the strainmeter records as follows. For each earthquake we obtain raw 20 Hz data (see Data and Resources section) and window them around the predicted P-wave arrival time (i.e., *Kennett and Engdahl, 1991*), with a length proportional to the relative S-wave arrival time. After removing the mean value from the pre-seismic portion, the windowed records are transformed into linearized gauge strain (see *Barbour and Agnew, 2011, Appendix*); the linear strains are transformed further by taking the logarithm of the absolute values. This series of transformations makes the strain records approximately normally distributed – an assumption implicit in the SN algorithm. The log-strain records are passed to the SN algorithm, where we control N_{\max} , the maximum number of segments that may be identified; the number is increased from three, when necessary, to account for

any seismic wave duration effects that might bias the estimation. The mean value of the last identified segment is compared to the SN-determined value in order to determine the sign of the offset.

The SN results are subsequently classified based on the effective signal-to-noise ratio, \bar{R} , which we define as the cumulative offset (relative to the initial mean value) divided by the sum of variances in the initial and final sections:

$$\bar{R} = (\sigma_1 + \sigma_N)^{-1} \sum_{n=2}^N \{\mu_n - \mu_{n-1}\} \quad (4.4)$$

Calibration of the PBO BSM is an important matter to consider, especially when comparing predictions of strain magnitudes. Many researchers have addressed the issue (*Hart et al.*, 1996; *Grant*, 2010; *Langbein*, 2010b; *Roeloffs*, 2010; *Hodgkinson et al.*, 2013), and we make use of this suite of calibrations to form estimates of the tensor strain components.

4.2.3 Classification of Detections

We validated the SN detection method by testing it on a series X_{sim} comprised of a Heaviside step function at a known location, αS , and normally distributed noise: $X_{\text{sim}} \sim \mathcal{N}(\alpha S, \sigma)$. In the validation we vary the signal-to-noise ratio R_{sim} ($\approx |\alpha|/\sigma$) by fixing the standard deviation of the noise, σ , and changing the size of the step, α . We then evaluate the accuracy of the estimates of the size and location of the best-fitting step. The residuals of the simulated series and the predicted step function are bootstrap-resampled 1000 times to calculate confidence intervals of the Mean Squared Error (MSE), which is defined as the sum of the variance and the squared bias of the series ($\sigma^2 + \beta^2$). Based on this testing, we find that small offsets ($R_{\text{sim}} \lesssim 0.2$) cannot be accurately identified; whereas, larger signals can be identified accurately, and consistently. The relative MSE as a function of R_{sim} shows small variation about the expected value, and has a typical range of ≈ 0.2 . See Figure 4.1.

We define several categories of “offset quality” so that we can objectively assess the quality of our estimates. See Table 4.1.

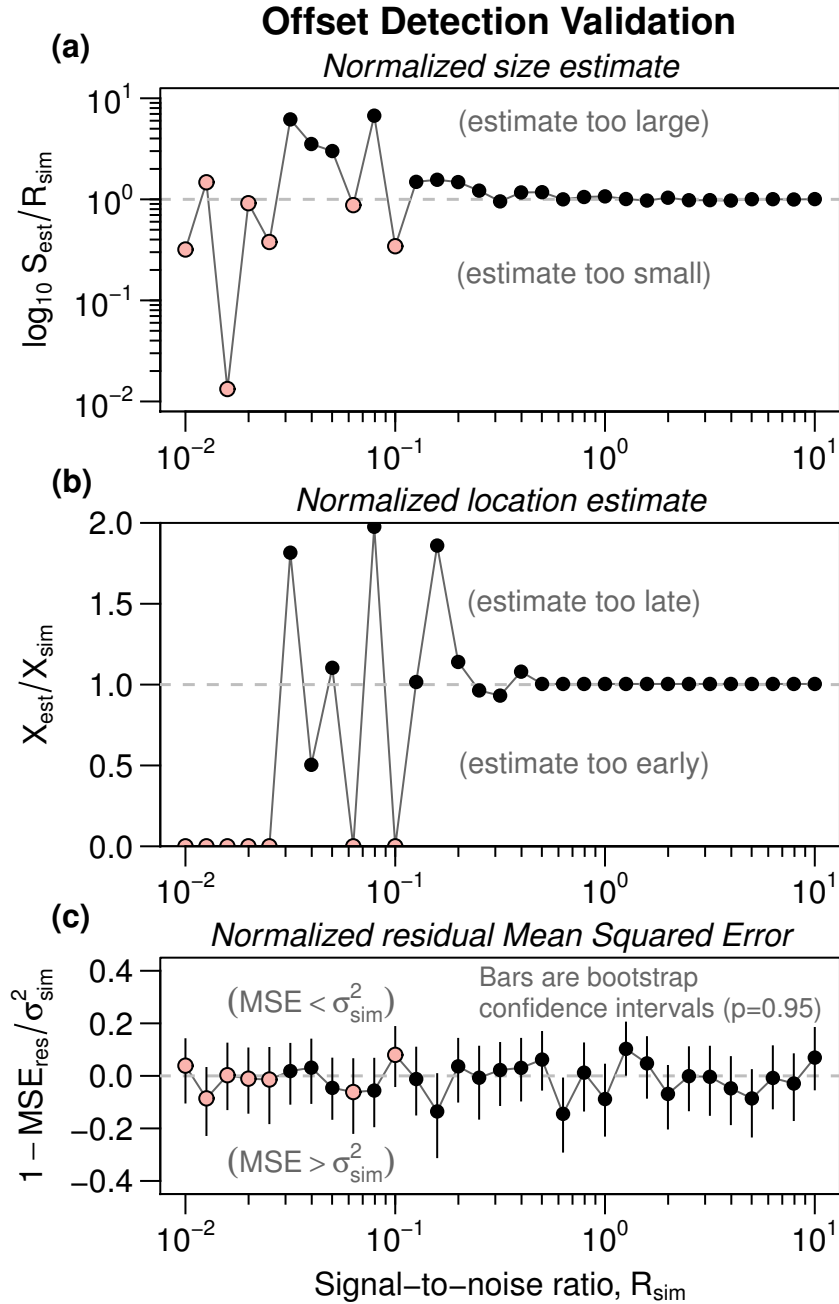


Figure 4.1: Validation of the SN method for offset detection: the method is applied to a series of the form $\alpha S + \mathcal{N}(0, \sigma)$, where S is a Heaviside step function, over a range of signal-to-noise ratios $R_{\text{sim}} (\approx |\alpha|/\sigma)$. Shown in (a) is $S_{\text{est}}/R_{\text{sim}}$, the estimated size of S relative to known R ; in (b) is $X_{\text{est}}/X_{\text{sim}}$, the estimated location of S relative to the known location; in (c) is $1 - (\sigma_{\text{res}}^2 + \beta_{\text{res}}^2)/\sigma_{\text{sim}}^2$, the Mean Squared Error of the residuals (sum of variance and bias) relative to the known variance. Open circles show failed estimates (no offset detected). Dashed lines represent ‘correct’ values.

Table 4.1: Classifications of strain offset by the effective signal-to-noise ratio \bar{R}

Range of \bar{R}	Quality	Weight*
$\bar{R} \geq 1.0$	A	1
$1.0 > \bar{R} \geq 0.7$	B	1/4
$0.7 > \bar{R} \geq 0.2$	C	1/9
$\bar{R} < 0.2$	–	

* Relative weight in linear regressions

In Figure 4.2 we show an example of the method applied to two classes of offsets observed: type ‘A’, at B084, during the 2010:094 M_W 7.2 El Mayor Cucapah earthquake (see *Hauksson et al.*, 2011); and type ‘C’, at B093, during the 2009:138 Inglewood earthquake.

4.3 Coseismic Strain Prediction

In this study we use two models of expected coseismic strain due to an earthquake: Model 1 gives the root-mean-squared (RMS) strain ϵ expected for a strike-slip earthquake in a homogeneous material. The model is derived from the Volterra strain-energy relation (c.f., *Savage*, 1969) and is given in *Wyatt* (1988) as a function of moment-magnitude M_W (for earthquakes in California) and epicentral distance r (in meters):

$$\log \epsilon = 1.5M_W - 3 \log r - 2.3 \quad (4.5)$$

This expression agrees well with observations from a set of long-baseline laser strainmeters operating in Anza, at the Piñon Flat Observatory (PFO). *McGarr et al.* (1982) shows that a similar relationship agrees well with observations from Sacks-Evertson dilatometers installed in a deep mine; hence, it is reasonable to expect similar agreement with observations from BSMs. This model tends to break down with very large strains ($> 10^{-6}$) in the near field.

Model 2 is an exact solution for a general dislocation in an elastic halfspace

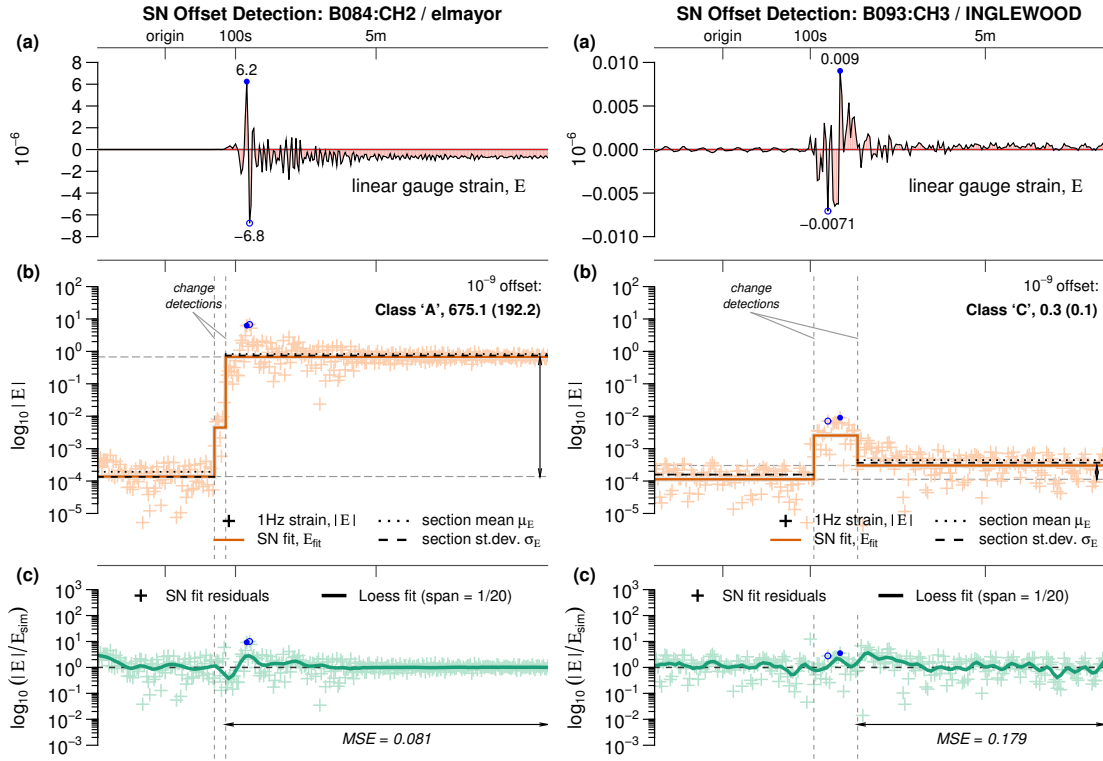


Figure 4.2: A demonstration of the SN method, applied to strain data. Left: an offset at B084:CH2 from the 2010:094 El Mayor Cucapah earthquake, categorized as class ‘A’ (see Table 4.1). Right: an offset at B093:CH3 from the 2009:138 Inglewood earthquake, with class ‘C’. In both figures we show (a) linearized gauge-strain with the deviation from zero filled in red and the range of dynamic strains labeled in blue ; (b) the logarithm of absolute strain (+ symbols) overlain by the SN fit (thick line) ; and (c) SN fit residual values (+ symbols) overlain by local polynomial regression curves (‘Loess’, thick line) (*Cleveland and Devlin, 1988*).

(with a free surface boundary condition), given by *Okada* (1985). The earthquake is treated as a single source on a planar fault, with a slip vector specified by published moment tensor (MT) solutions from any of the following sources: the Harvard Centroid-Moment-Tensor project, the Northern California Earthquake Data Center (NCEDC), the National Earthquake Information Center (NEIC), or the Southern California Seismic Network via the Southern California Earthquake Center. These sources are, collectively, the most thorough database of significant ($M_W \geq 4$) global earthquakes since the inception of the PBO BSM network (in mid-2006). By default we use the NEIC solution, if only because the (independent) solutions agree very well. This type of model is, to first-order, an accurate predictor of elastic deformation in the crust, and is used extensively in the literature. In Appendix 4.7 we discuss the sensitivity of strain predictions to uncertainty in the strike of the MT solution.

4.3.1 Earthquake Catalog

We analyze data from the nine BSMs in southern California (Table 4.2), for 34 earthquakes since 2006 having published MT solutions. These events are spread among local, regional, and teleseismic distances, and over a wide range of magnitudes (Table 4.3); in Figure 4.3 we plot the expected strains from Model 1, and the expected seismic energy densities (in J m^{-3}), from *Wang* (2007), based on their moment magnitudes and epicentral distances to the center of the BSM cluster.

Table 4.2: Some characteristics of Plate Boundary Observatory boreholes used in this study.

Station	Year:Day installed	Longitude (°East)	Latitude (°North)	Elevation (m)	Depths*			
					PP (m)	SEIS (m)	ACCEL (m)	BSM (m)
B081	2006:166	-116.7142	33.7112	1467	212	229	230	243
B084	2006:169	-116.4564	33.6116	1271	135	147	148	158
B089	2006:240	-116.5961	33.5999	1362				133
B082	2006:161	-116.5960	33.5982	1375	192	220	221	242
B093	2007:263	-116.7638	33.5937	1244		124	125	145
B086	2006:168	-116.5310	33.5575	1392	216	226	227	244
B946	2010:204	-116.5925	33.5373	1429	134	143		147
B087	2006:168	-116.6027	33.4955	1139	94	147	148	161
B088	2007:027	-116.6205	33.3749	1404	137	147	148	160

* Depths, relative to the top of the borehole casing, of the pore pressure screen (PP), seismometer (SEIS), accelerometer (ACCEL), and strainmeter (BSM).

Table 4.3: Earthquakes used in this study, ranked by epicentral distance

ID \star	Year:Day (UTC)	H:M:S (UTC)	Longitude (East)	Latitude (North)	Depth (km)	Mw	Dist. Δ ($^\circ$)	Back Az. θ ($^\circ$)	
*	ci15296281	2013:070	16:56:6.0	-116.4582	33.5045	13.1	4.7	0.15	129.0
*	ci10736069	2010:188	23:53:33.0	-116.4827	33.4175	14.0	5.5	0.20	152.3
*	ci10701405 \ddagger	2010:164	03:08:57.0	-116.4193	33.3772	5.8	4.4	0.27	146.1
	ci14433456	2009:083	11:55:43.7	-115.7280	33.3180	5.8	4.8	0.78	110.8
*	ci10370141	2009:009	03:49:46.0	-117.3040	34.1070	14.1	4.5	0.78	310.9
*	ci14383980	2008:211	18:42:15.7	-117.7610	33.9530	14.7	5.5	1.03	290.4
*	ci14745580	2010:166	04:26:58.0	-115.9210	32.7000	5.4	5.7	1.06	147.5
	ci14601172	2010:075	11:04:0.0	-118.0820	33.9920	18.9	4.4	1.30	288.0
*	ci10410337	2009:138	03:39:36.3	-118.3360	33.9380	15.1	4.7	1.49	283.6
*	ci14565620 \ddagger	2009:364	18:48:57.7	-115.1650	32.4370	6.0	5.9	1.67	133.5
*	ci14607652	2010:094	22:41:40.0	-115.2870	32.2590	10.0	7.2	1.73	140.1

* Induced *at least* a single offset on any Anza station.

\star USGS NEIC identifier, unless noted otherwise by \dagger for NCEDC, or \ddagger for SCSN/SCEC.

Δ Geodesic distance from the earthquake epicenter to the medoid of the Anza stations (N33.6, W116.6).

θ Azimuthal direction (clockwise from North) between the Anza medoid and the epicenter.

Table 4.3 – *continued*

ID *	Year:Day (UTC)	H:M:S (UTC)	Longitude (East)	Latitude (North)	Depth (km)	Mw	Dist. ^Δ (°)	Back Az. ^θ (°)
ci10403777 [‡]	2009:122	01:11:13.7	-118.8820	34.0692	13.9	4.4	1.96	284.5
nc71863625	2012:294	06:55:9.0	-120.8560	36.3100	9.2	5.3	4.42	308.9
us2009jwbr	2009:215	18:40:50.1	-113.7030	29.3710	10.0	6.2	4.88	148.8
nc71508850 [†]	2011:012	08:51:3.0	-121.4987	36.7705	8.4	4.5	5.11	309.6
nc40234037	2009:089	17:40:29.0	-121.6197	37.2845	6.2	4.3	5.51	313.3
nc71506865 [†]	2011:008	00:10:16.0	-121.6580	37.2870	7.1	4.1	5.53	313.1
* us2009jwbh	2009:215	17:59:56.1	-112.9030	29.0390	10.0	6.9	5.53	144.2
usc000919m	2012:103	07:06:1.0	-113.0715	28.8409	10.1	6.2	5.62	146.6
usc00091a1	2012:103	07:15:48.0	-113.1418	28.7899	10.3	6.9	5.63	147.4
nc40204628	2007:304	03:04:54.0	-121.7760	37.4320	9.2	5.6	5.70	313.6
mn00242554	2008:117	06:40:10.6	-119.9300	39.5200	1.4	5.0	6.49	336.5
ushmal	2006:004	08:32:32.4	-112.1170	28.1640	14.0	6.6	6.64	143.4
us2008nsa9	2008:054	14:16:2.7	-114.8670	41.1530	6.7	6.0	7.67	9.8

* Induced *at least* a single offset on any Anza station.

* USGS NEIC identifier, unless noted otherwise by † for NCEDC, or ‡ for SCSN/SCEC.

Δ Geodesic distance from the earthquake epicenter to the medoid of the Anza stations (N33.6,W116.6).

θ Azimuthal direction (clockwise from North) between the Anza medoid and the epicenter.

Table 4.3 – *continued*

ID \star	Year:Day (UTC)	H:M:S (UTC)	Longitude (East)	Latitude (North)	Depth (km)	Mw	Dist. Δ ($^\circ$)	Back Az. θ ($^\circ$)
nc40216664	2008:121	03:03:6.9	-123.4990	40.8370	28.5	5.4	9.08	324.7
uu00002715	2010:105	23:59:39.0	-111.0940	41.6030	7.9	4.9	9.10	27.0
nc51210149	2008:300	09:27:21.0	-124.6370	40.3220	18.5	4.9	9.29	318.5
nc71734741	2012:044	21:07:2.0	-123.7900	41.1430	28.2	5.6	9.46	324.9
nc71348851	2010:035	20:20:21.0	-124.9610	40.4120	23.6	5.9	9.54	317.9
nc71338066	2010:010	00:27:39.3	-124.6920	40.6520	29.3	6.5	9.55	319.8
us2010crbl	2010:294	17:53:14.0	-109.1710	24.8430	10.0	6.7	10.87	141.5
* us2010rja6	2010:012	21:53:10.0	-72.5710	18.4430	13.0	7.0	42.02	99.8
* usc0001xgp	2011:070	05:46:24.0	142.3720	38.2970	30.0	9.0	77.63	307.8
us2010tfan	2010:058	06:34:14.0	-72.7330	-35.9090	35.0	8.8	80.39	145.2

* Induced *at least* a single offset on any Anza station.

\star USGS NEIC identifier, unless noted otherwise by \dagger for NCEDC, or \ddagger for SCSN/SCEC.

Δ Geodesic distance from the earthquake epicenter to the medoid of the Anza stations (N33.6, W116.6).

θ Azimuthal direction (clockwise from North) between the Anza medoid and the epicenter.

We also tested for effects associated with a complex slip distribution using two published distributed-slip models of the 2010:094 M_W 7.2 El Mayor Cucapah (EMC) earthquake, namely from *Fialko et al.* (2010) and *Wei et al.* (2011). The slip-model predictions are compared to the MT-based predictions, and to observations at the BSMs.

4.4 Results

We applied the SN detection algorithm to all available strainmeter data from the nine BSMs for the 34 earthquakes. After culling spurious detections, we find that 12 of these events induced static offsets which can be classified as class ‘C’ or better on *at least* one gauge among the stations (see Table 4.3); but, offsets are typically induced on all (functioning) gauges, and at multiple stations. We are unable to obtain reliable estimates for two of the stations (B089, and B946) because of data-availability and quality issues; otherwise, all stations show offsets. The total number of offsets observed is 220. These offsets are distributed in an approximately uniform manner among the stations, and between gauges: we do not observe significant bias in either the amplitude or frequency of offsets by both station and gauge number.

In Figure 4.4 we plot the RMS coseismic offset estimated with the SN method as a function of the predicted strain using the moment tensor solution. We find substantial disagreement with this model of strain, often with ratios of ten or greater. The figure also shows instances of ‘null-detections’, where we do not estimate a statistically significant offset. It appears that in many cases the BSM does *not* record a coseismic strain, even though it likely should.

We tested the quality of the moment-tensor prediction for the EMC earthquake against predictions from two distributed slip models, namely from *Fialko et al.* (2010) and *Wei et al.* (2011). These results, tabulated in Table 4.4, indicate that at the distances of the Anza BSMs, the strain field from the MT solution is roughly consistent with the theoretical strain field produced by complex slip models. The table also shows the considerable observational disagreement with

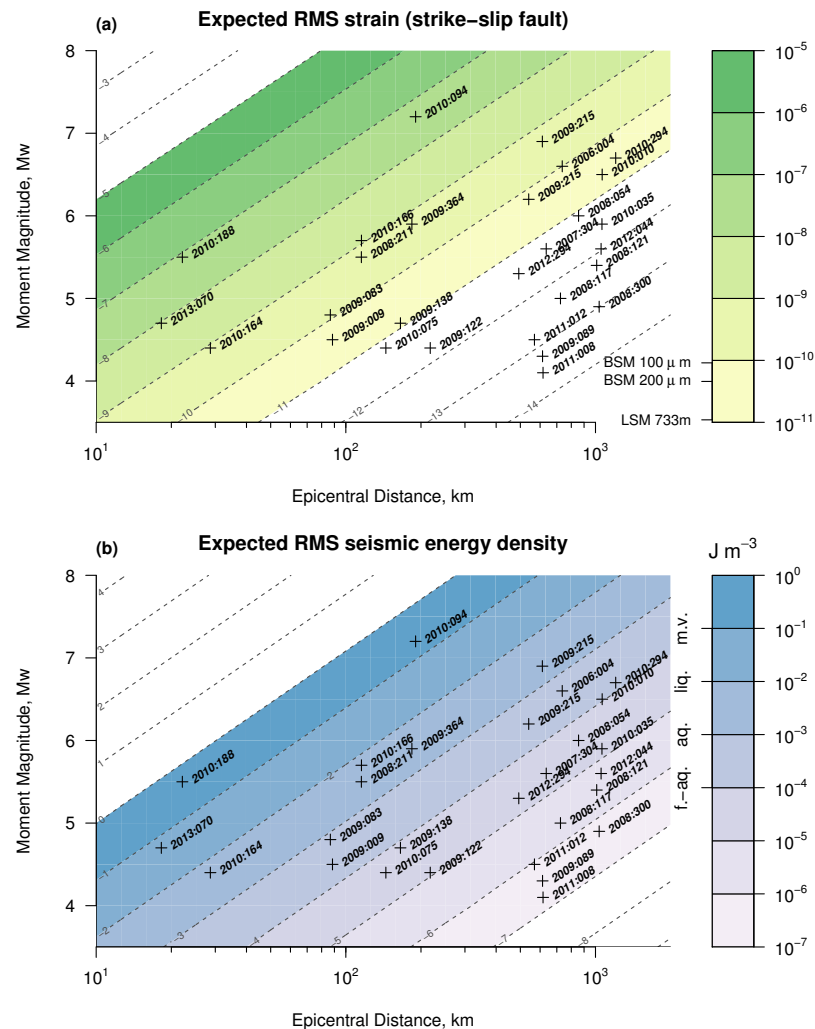


Figure 4.3: Earthquakes tested for coseismic strains, plotted by magnitude and epicentral distance over contours of (a) the expected RMS strain for a strike-slip fault, from *Wyatt* (1988); and, (b) the expected seismic energy density ($J m^{-3}$), from *Wang* (2007). Labeled in the color-scales are, in (a), theoretical resolutions of the BSM and LSM; and, in (b), general levels of energy density which tend to induce mud-volcano activity ('m.v.'), liquefaction ('liq.'). and static water-level changes in permeable aquifers ('f.-aq.') and fractured-rock aquifers ('f.-aq.').

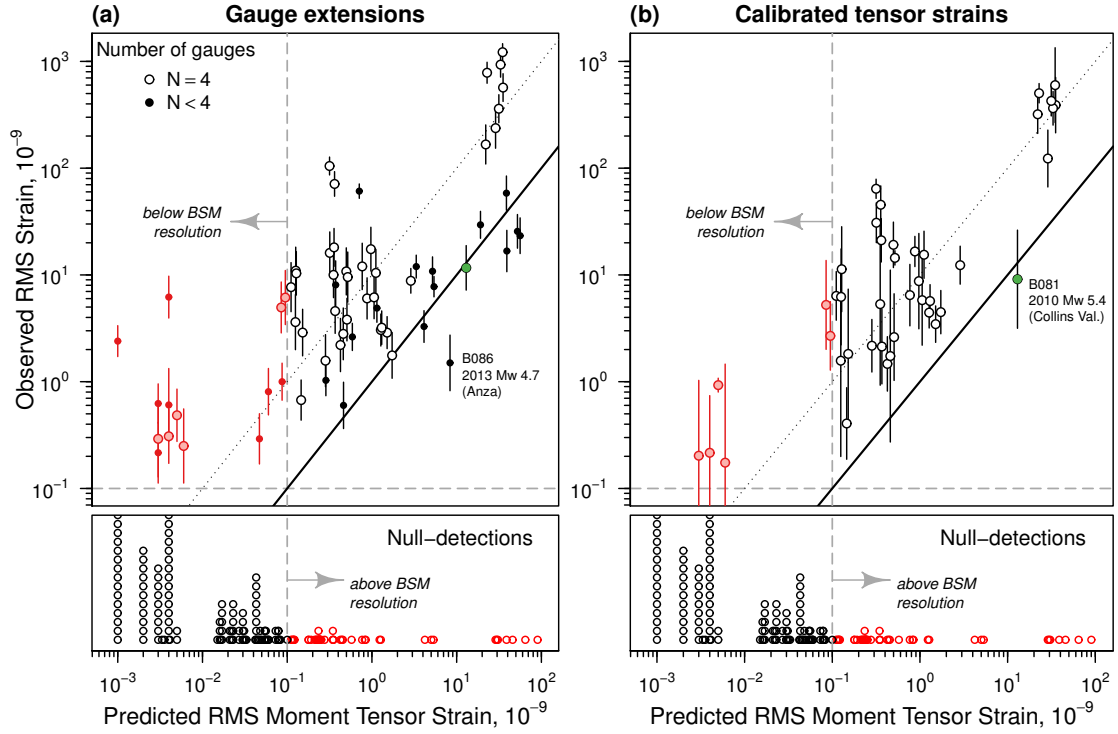


Figure 4.4: Estimates of RMS offset size as a function of moment-tensor derived strain prediction: (a) based on gauge extensions, and (b) based on calibrated tensor components. The lower frames show stacked ‘null-detections’, or where no offset is found using the SN method. Diagonal lines show equal agreement (solid), and a factor of ten disagreement (dotted). Vertical and horizontal dashed lines show the instrumental resolution of the BSM. Findings in red indicate, in the upper panels, observed offsets where nothing above the BSM resolution was expected; and, for the lower panels, the absence of observed changes where offsets were expected. We highlight the single instance where the observed offsets are consistent with predicted strains: at B081, for the 2010 M_W 5.4 Collins Valley earthquake.

observations at the Anza BSMs.

In order to explore the source of these apparent strains, we obtained concurrent timeseries of any of the following colocated instruments: velocity, acceleration, and pore pressure. We calculated peak values in the ‘seismic’ portion of the response-corrected records (culled for spurious signals) and regressed them against the observed strain offsets, with weightings as shown in Table 4.1, and also against the ratio of observed-to-predicted strain. In Table 4.5 we tabulate regression coefficients for the magnitude of the offsets (termed ‘absolute’), and the ratio of offset to prediction (termed ‘relative’).

Table 4.4: Modeled and observed coseismic strain (10^{-9} , extension positive) for the 2010:094 El Mayor Cucapah earthquake

BSM	E_{NN}			E_{EE}			E_{NE}			E_{RMS}			
	MT^*	W^\dagger	F^\ddagger	MT	W	F	MT	W	F	MT	W	F	Observed ^Δ
B084	4.7	20.6	17.1	44.4	57.6	47.0	41.7	49.9	41.4	35.3	45.6	37.5	243–511
B088	-34.0	-36.8	-30.5	48.8	65.8	53.5	10.3	6.2	4.4	34.8	43.7	35.6	633–974
B086	-7.8	2.3	1.8	46.1	61.2	50.0	32.8	39.1	32.2	33.0	42.0	34.3	221–522
B087	-19.3	-15.3	-12.7	45.9	61.7	50.2	22.1	24.6	20.0	31.5	39.3	32.0	118–248
B946	-14.3	-8.2	-6.9	44.4	59.2	48.1	25.4	29.2	23.8	30.6	38.4	31.2	–
B082	-8.8	-1.1	-0.9	40.8	53.8	43.6	27.2	31.8	25.9	28.8	36.1	29.3	105–273
B089	-8.6	-0.9	-0.8	40.7	53.7	43.4	27.2	31.8	25.9	28.7	36.0	29.2	–
B093	-16.9	-14.8	-12.0	33.3	43.8	35.0	13.1	13.6	10.6	22.9	27.8	22.2	333–638
B081	-7.0	-1.2	-1.0	31.4	40.7	32.5	20.5	23.5	18.8	22.0	27.2	21.7	78–212
(mean)	-12.4	-3.5	-2.9	41.8	55.5	45.0	24.5	30.0	24.5	29.7	38.2	31.1	247–483

Δ 95% confidence interval for observed BSM recordings

★ Moment tensor solution

Distributed slip models:

† *Wei et al.* (2011) ($M_W \approx 7.36$), and ‡ *Fialko et al.* (2010) ($M_W \approx 7.25$)

Table 4.5: Comparison of statistical models of strain offsets ranked by correlation

Predictor [†]	Regressor [‡]	Coefficients [*] : $\log f(x) \sim b + a \log x$			R ²	R ² ([*])	N _{obs}	
		Estimate	95% Conf.	Estimate				95% Conf.
		<i>b</i> (intercept)		<i>a</i> (slope)				
		Estimate	95% Conf.	Estimate	95% Conf.			
Pore pressure [kPa]	Absolute	-2.13	[-2.44, -1.82]	0.11	[-0.03, 0.26]	0.07	0.04	31
	Relative	0.33	[0.01, 0.66]	-0.05	[-0.20, 0.11]	0.01	-0.02	31
\langle Acceleration \rangle [%g]	Absolute	-1.45	[-1.76, -1.13]	1.20	[0.72, 1.68]	0.45	0.43	32
	Relative	-0.01	[-0.38, 0.37]	-0.48	[-1.06, 0.09]	0.08	0.05	32
\langle Velocity \rangle^2 [cm ² s ⁻²]	Absolute	-1.32	[-1.58, -1.06]	0.38	[0.30, 0.46]	0.58	0.57	66
	Relative	0.24	[-0.07, 0.55]	-0.15	[-0.25, -0.06]	0.13	0.12	66
Peak dyn. strain [10 ⁻⁶]	Absolute	-1.77	[-1.88, -1.65]	1.04	[0.92, 1.16]	0.82	0.81	66
	Relative	0.50	[0.29, 0.72]	-0.27	[-0.49, -0.04]	0.08	0.06	66

Estimates in **bold** have a *t*-statistic probability (two-sided *p*-value) of less than 0.001

[†] For the different entities: predictor values are peak values, and $\langle \cdot \rangle$ indicates they are an average of horizontal components

[‡] Strains in units of 10⁻⁶. ‘Absolute’ is RMS estimate, ‘Relative’ is ratio of ‘Absolute’ to predicted strain

^{*} Estimated by weighted least squares, following the classifications in Table 4.1

^{*} Adjusted $R^2 \equiv 1 - (1 - R^2) \cdot (N_{\text{obs}} - 1) \cdot (N_{\text{obs}} - 3)^{-1}$

4.5 Discussion

Our findings indicate the estimates of coseismic strain at PBO BSMs in southern California can be classified as follows:

- (I) No offset expected and none seen
- (II) No offset expected, but one seen
- (III) Offset expected and seen, but wrong based on dislocation model
- (IV) Offset expected and seen, and agrees with dislocation model

The largest proportion of our offset estimates fall into the third category (III): estimates are often much larger than predicted strains which are expected. We find a number of cases where we expect a small offset, and do not detect one above noise levels (I); but, we also find a number of cases where an offset is detected when it is not expected (II). In only one case the observed strain matches the predicted strain reasonably well (IV): at station B081 for the 2010 $M_W 5.4$ Collins Valley earthquake on the Coyote Creek strand of the San Jacinto Fault system. The results of *Hodgkinson et al.* (2012) suggest that this is one case where the strain offsets might represent true tectonic deformation.

There are two striking features in the regressions shown in Table 4.5. Firstly, we find strong correlations between the absolute size of the offset and the squared peak ground velocity (PGV^2 , Figure 4.5), and the peak dynamic strain (PDS, Figure 4.6); correlations with acceleration and dynamic pore pressure are nearly insignificant. The PGV^2 is generally considered to be proportional to the kinetic energy density of the radiated seismic energy, e , and can be related (*Wang, 2007*) to the magnitude and distance:

$$\log e = 1.45M_W - 3 \log r - 4.24 \quad (4.6)$$

We regress this expression against both PGV^2 and PDS, and find that PDS agrees most-strongly (although PGV^2 is also strong) with lowest residual variance:

$$\log PDS = 0.60(0.13) + 0.54(0.05) \log e \quad (4.7)$$

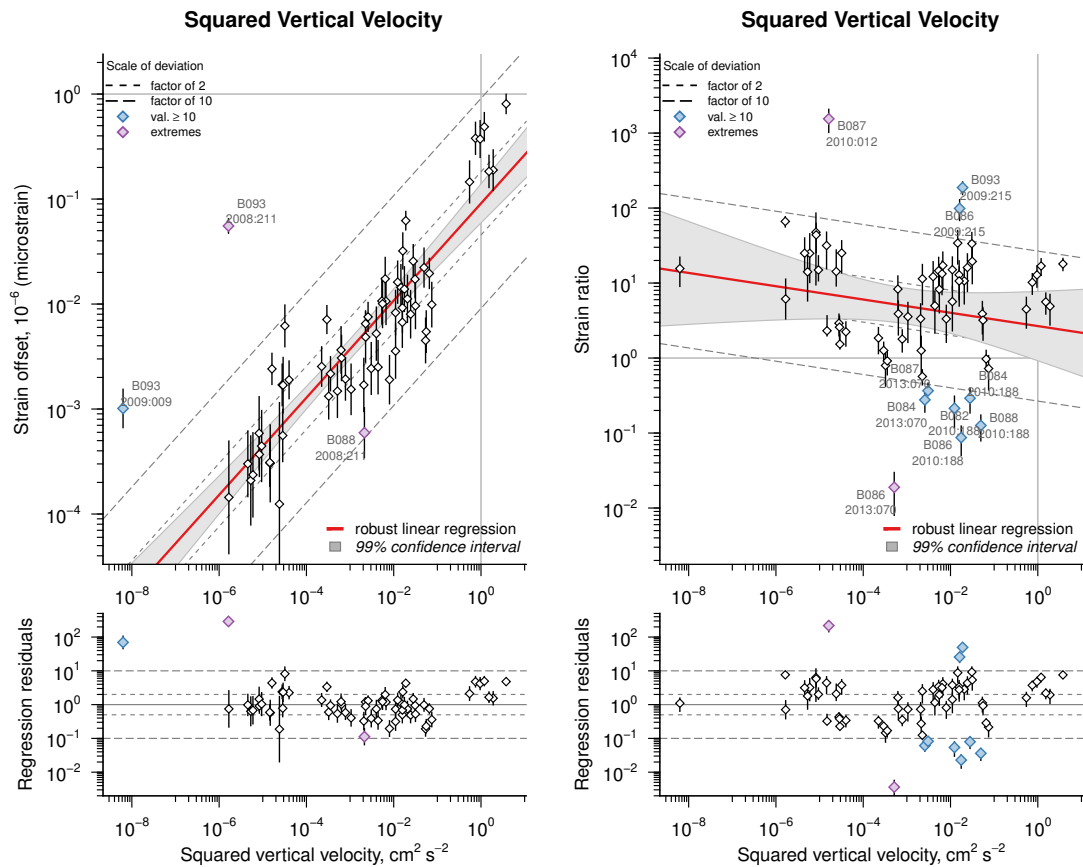


Figure 4.5: Regressions and misfit for absolute (left) and relative (right) RMS strain offsets against squared peak vertical velocity (PGV^2), where relative values are the RMS of the absolute values divided by the predicted values.

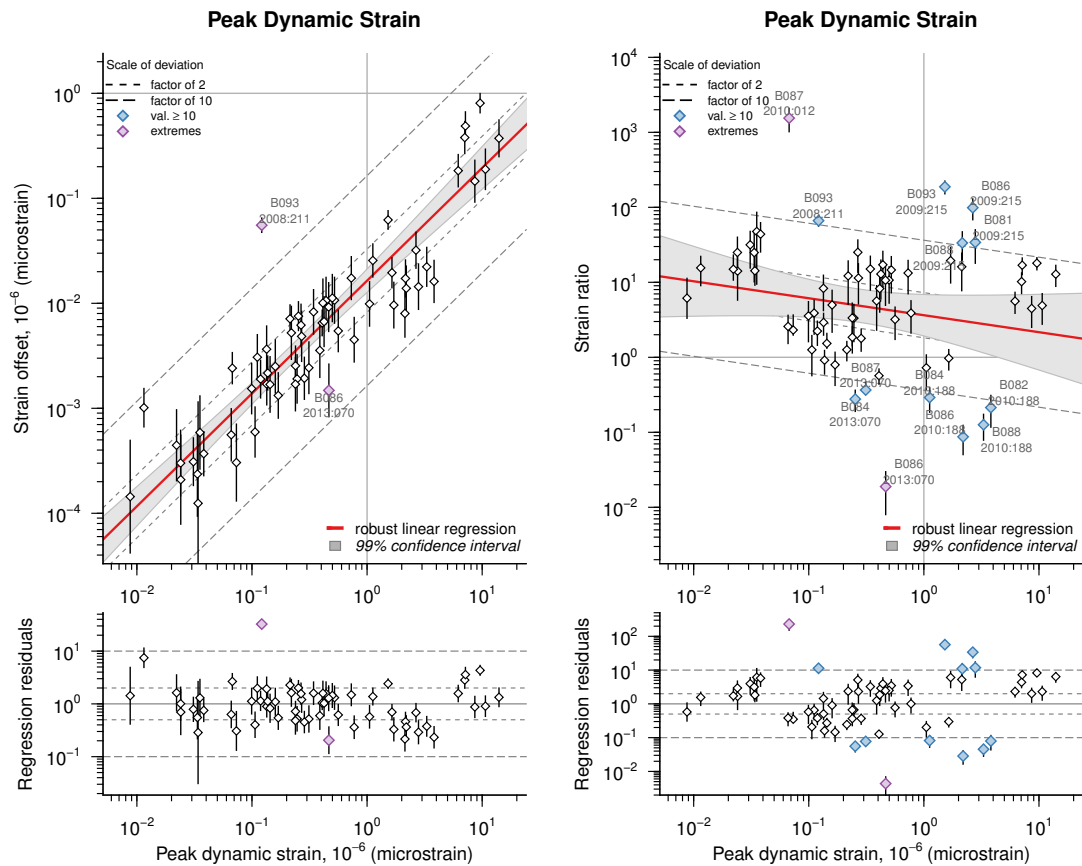


Figure 4.6: Regressions and misfit for absolute (left) and relative (right) RMS strain offsets against peak dynamic strain (PDS).

with $R^2 = 0.685$; standard errors from bootstrap resampling (500 times) are shown in parentheses.

The second striking feature is that correlations reduce to essentially zero for the ratio-based regressions. The level of seismic energy density is, apparently, an accurate predictor of offset size (although this is to be somewhat expected) but is not an accurate predictor of the discrepancy between observation and model: non-zero coefficients have relatively large confidence intervals and high p -values, indicating weak statistical significance, if there is any.

To further test the *lack* of an energy-density effect, we focus on cases where an offset is detected even though one is not expected (type II). We isolated these observations and performed a two-sided t -test of the PDS values, testing the alternative hypothesis that there is a difference in population mean greater than zero. In other words, we test whether a difference in PDS explains the positive and null detections. We also ran the test using the PDS normalized by the magnitude-distance model of *Agnew and Wyatt* (2014). There is no statistical evidence to support this alternative hypothesis, in either case: seismic energy density does not explain spurious observations of type II.

4.5.1 Comparison with Longbase Laser Strain

The longbase laser strainmeter (LSM) is, simplistically, a Michelson-type interferometer extended over hundreds of meters. In practice the instruments count optical interference fringes – a direct proxy of strain assuming stability of the lasing frequency, and the index of refraction of the light path. This style of strain sensing is relative because fringe counting, which depends on the stability of optical equipment, can be disrupted by strong shaking. If the integrity of fringe counting is maintained, however, the instrument generally has very high sensitivity and low noise: sensitivity is as good as 1.4×10^{-10} strain-per-count, for the longest strainmeter, and median noise levels at 0.5 Hz are near -200 dB (*Barbour and Agnew*, 2011).

The Canal de Ballenas transform system (south of the Lower Delfin Basin, in the Gulf of California, Mexico) produced similar sized earthquakes in 2009

(M_W 6.9, see *Castro et al.*, 2011), and 2012 (M_W 7.0); at similar epicentral distances to PFO: ≈ 609 km. At these distances the level of coseismic strain is expected to be less than $\approx 5 \times 10^{-10}$ – a level very nearly at the theoretical sensitivity limit of the BSM. As we expect, the three independent LSMs at PFO show no measurable offset in their records; whereas, station B084 – the PBO BSM located within tens of meters of the LSMs – shows an RMS offset of 8.1×10^{-9} with an uncertainty of 4.2×10^{-9} . This is a location where tidal strains are known very well (theoretically, and observationally), and calibration of the BSM using the tides has been successful (e.g., *Hodgkinson et al.*, 2013); thus, anomalous strains in BSM data absent in nearby LSM data cannot be explained by calibration errors. We note also the abnormally high seismic energies felt by the LSMs for these events (*Agnew and Wyatt*, 2014), and that other BSMs show offsets larger than 10^{-7} .

4.5.2 Consideration of Simplifying Assumptions

Inaccurate Strain Calibration

Calibration methods for the BSM have been demonstrably complicated (*Hart et al.*, 1996; *Roeloffs*, 2010; *Langbein*, 2010b), but defensible (*Hodgkinson et al.*, 2013). We admit that inaccuracies in the coefficients relating gauge-strain to ‘formation’ strain account for some proportion of the discrepancy between the modeled strain and the observed strain; however, the size of the discrepancy is generally *at least* one order of magnitude (Figure 4.4). Figure 4.7a demonstrates the effect of including calibration information in the determination of offset size. The discrepancy between RMS strains derived from gauge extensions, and from the calibrated tensor strains is small – not generally larger than a factor of 2 to 3.

Coseismic Strain Models

Equation 4.5 is inappropriate for modeling near field strains, but can be used to test for an ‘expected’ offset. For the comparisons here we have used elastic dislocation models based on published moment tensor solutions; these are considered first-order accurate. Neither topography or curvature are likely to contribute

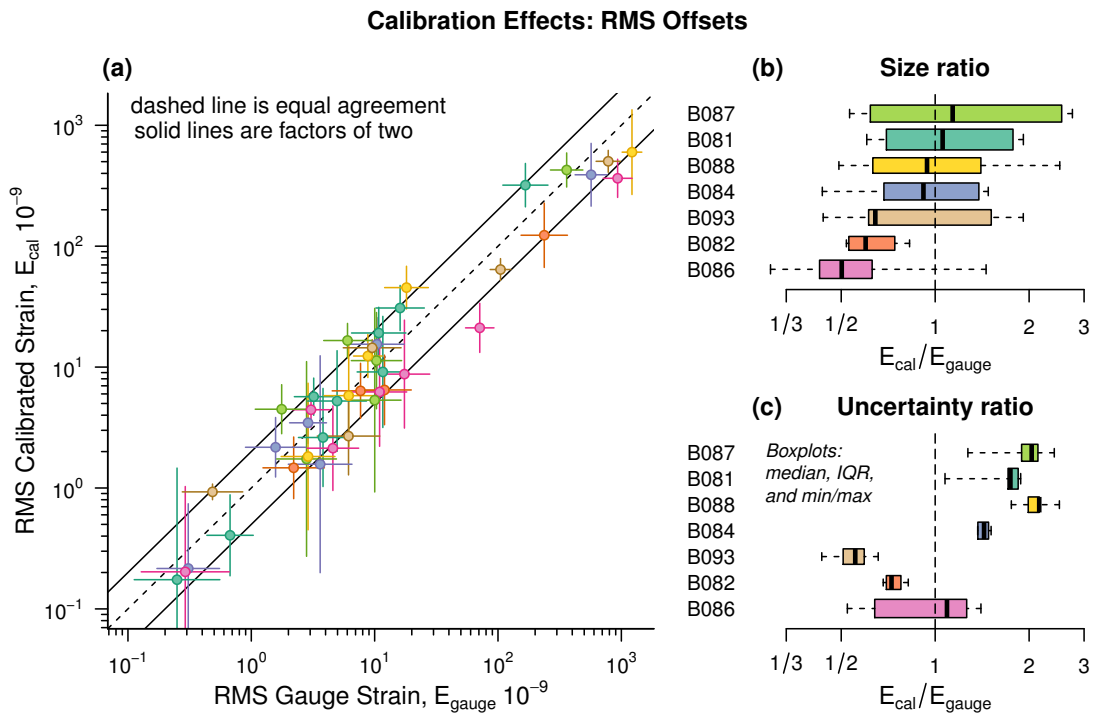


Figure 4.7: Relative scaling discrepancy of not including calibration coefficients when determining RMS offset size: (a) tensor-strain estimates against gauge-extension estimates, (b) full-range boxplots of the ratio of calibrated strains to gauge strains, and (c) full-range boxplots of the ratio of errors in the calibrated strains to errors in the gauge strains.

a significant biasing effect to our observations. In the near field of an earthquake the strain field will be complex; but, at distances greater than the fault length the strain field will resemble a point source. Our results for EMC support this principle: we find good agreement between the distributed slip models and the MT-based solution for stations in Anza. It is clear that including effects of distributed slip and complex geometry does not mitigate the level of disagreement between observed and modeled strains (e.g., Table 4.4)s.

4.5.3 Alternative Explanations

Poroelastic Effects

Coupled deformation and fluid flow could occur near the instrument if the earthquake induces a large volumetric strain, or a hydraulic gradient, and the rock is highly drained (*Segall et al.*, 2003). Under these conditions a transient poroelastic response would couple with the instrument, but we do not find instances of persistent changes in pore-fluid pressure (typical perturbation timescales are on the order of hours or less). and there is only a weak dependence on dynamic pore pressure (Table 4.5). The findings of *Barbour* (2012) imply that if this effect is important, the size of the effect should vary by station (because of their varying distances to the San Jacinto fault); and, yet, that does not appear to be a feature found in our offset catalog.

Microcrack Propagation

Plastic yielding of small-scale cracks (microcracks) in the host rock and/or the instrument grout is the most-likely of the alternative explanations. Drilling of a borehole in crystalline rock (e.g., the Peninsular Ranges batholith) will create tensile-fractures in the borehole wall, and these could be sensitive to seismic waves, yielding further at points of stress concentration (i.e., crack tips). Such an effect is commonly observed in concrete structures as a result of cyclic loading, and contributes to a gradual softening of the material (*Reinhardt*, 1984; *Lee and Fenves*, 1998). The lack of a seismic energy effect argues against this explanation,

though, and a comparison of energy scaling relationships (*Molnar et al.*, 2007) and sensitivity limitations of the BSM (*Barbour and Agnew*, 2012) indicates that such an effect would be difficult to investigate without high-sensitivity instrumentation in very close proximity to the instrument. The effect would likely have some appreciable time-dependent behavior, and a much larger dataset, spanning many more events over time, would be needed.

4.6 Conclusion

We have shown that the PBO BSMs in southern California are affected by seismic waves in a manner which often distorts the amplitude of static strains associated with earthquake ruptures by factors greater than three; the precise mechanism behind this effect is unclear, but apparently unrelated to the energy density in the seismic waves. Observed strains are inconsistent with elastic dislocation models by factors greater than three, in general; and disagree with independent observations from laser strainmeters (when available). The effect is similar among the stations we analyzed; hence, it must be a physical effect isolated to distances much smaller than the epicentral distance – likely on the order of the dimensions of the BSM (meters or less).

It is our contention that most likely explanation for the observed coseismic strains is a highly non-linear effect from accumulative disruptions in (1) the intra-gauge mechanical connections, and (2) the adhesive connection between either the instrument package and the grout, or the grout and the host-rock. Such a conclusion does not necessarily preclude the BSM from analyses of earthquake rupture, but it does warn strongly against cursory interpretations of their coseismic signals.

4.7 Appendix A: Sensitivity to Strike: the Collins Valley Earthquake

Uncertainties in moment tensor solutions can affect near-field predictions of deformation using an elastic dislocation model (see *Woessner et al.*, 2012, for examples). Here we analyze the sensitivity of our models to variations in fault-strike for the the 2010/07/07 M_W 5.4 Collins Valley (CV) earthquake, a local earthquake with epicentral distances to Anza BSMs from 14 km to 39 km. Specifically, we vary the MT-derived strike angle within a $\pm 3^\circ$ range, and then predict strains at every station. The derivatives of the predictions with respect to the strike angle ($\partial\epsilon/\partial\phi$) are used to quantify the relative sensitivity. We estimate that the maximum absolute sensitivity for RMS strain is $\approx 10^{-9} \text{ }^\circ^{-1}$ (at B087). Allowing for a modest uncertainty in the value of strike in the MT, the upper limit of uncertainty in the strain predictions for the CV earthquake is less than ten nanostrain.

4.8 Acknowledgements

Strain data are from the Northern California Earthquake Data Center (NCEDC), and seismic data are from Incorporated Research Institutions in Seismology, accessed through their Web-Services (IRIS-WS). Laser strainmeter data are from a local archive, but can also be obtained through either NCEDC or IRIS-WS.

We used the `changepoint` software package (*Killick and Eckley*, 2014, version 1.1) to apply the SN detection method to strain data, and the `dislopack` software package for the elastic dislocation modeling. These packages can be found at the following respective locations:

<http://cran.r-project.org/web/packages/changepoint/index.html>
<http://igppweb.ucsd.edu/~agnew/Miscsoft/miscsoft.html>

We thank Billy Hatfield for comments.

This work was supported by NSF grants EAR08-43878 and EAR10-53208.

Chapter 5

Modeling Strains Associated with Fluid Extraction: the Pathfinder Ranch Experiment

Strainmeters can be subject to hydrologic effects from pumping of nearby water wells depending on the state of the local rock. These effects are generally not used and regarded as troublesome because they are much larger than most tectonic signals (e.g., tides, and slow slip episodes in Cascadia); but, here we show that pumping-induced strain and pore-pressure signals can be used to constrain valuable material properties, namely the hydraulic diffusivity and shear modulus of the rock. We collected multi-year records of the pump activity at two actively-pumped water wells near a pair of Plate Boundary Observatory borehole strainmeters in southern California. These data demonstrate clearly the connection between fluid extraction and deformation: they indicate a strong correlation between the times of fluid extraction and the onset of significant strain and pore-fluid pressure changes; and, between cumulative extraction volumes and the sizes of the transient pressure and strain signals. Poroelastic modeling indicates the local rock is drained, has a relatively high diffusivity, and has a relatively low shear modulus. That a strong contrast in diffusivity between the major lithologic units (bedrock overlain by sediment) is *not* necessary suggests that hydraulically conductive fractures pervade the shallow crustal rock; borehole logging data and drillers' logs corroborate this.

Diffusivity estimates are consistent with the range expected for fractured igneous rock, and the exceptionally low shear modulus is consistent with observations for shallow granodiorite – expected to be weak from weathering, and other sources of damage. These findings suggest that as a result of changes in applied stress, shallow crustal rock near the San Jacinto fault favors vigorous fluid flow over elevated pore pressures.

5.1 Introduction

The causes of coupled deformation and diffusive pore fluid flow in the near-surface crust can be separated into two general categories: from naturally occurring processes, and from anthropogenic activities. Poroelastic post-seismic rebound – a naturally occurring process generally at depth and associated with fault rupture – may contribute a large proportion of the time-dependent signal seen in near-field observations (*Peltzer et al.*, 1998; *Jónsson et al.*, 2003). Altering the presence of groundwater by pumping or injection – an anthropogenic activity – also induces coupled deformation; the associated geodetic effects have been studied since the seminal work of *Biot* (1941), who formed a general theory describing compaction of fluid-saturated soils in response to changes in loading. If the reduction in applied normal stress generated by fluid extraction (or injection) is great enough, then critically stressed rock can reach its failure state (*Segall*, 1989), which causes earthquakes. Increases in background seismicity rates have been linked to, for example, sustained hydrocarbon and geothermal energy production (*Segall*, 1989; *Brodsky and Lajoie*, 2013), carbon dioxide sequestration (*Zoback and Gorelick*, 2012), and wastewater disposal from injection (*Healy et al.*, 1968; *van der Elst et al.*, 2013; *Keranen et al.*, 2013).

In rural areas it is common for land owners to pump well water for consumption, irrigation, or various other uses. The volume of water removed from aquifers from this activity is generally small relative to wastewater injection, for example, and the activity has negligible hazard in regards to alteration of tectonic stresses. But, a measurement of strain or tilt made nearby will likely record the

associated deformation with a high signal-to-noise ratio, and the deformation will carry information about the mechanical and hydraulic properties of the rock. For instance, tiltmeters at the surface, or in boreholes, have been commonly used to study fine scale deformation associated with fluid removal (*Fabian and Kämpel, 2003*), to model aquifer fluid dynamics (*Vasco et al., 2000*) and the distorting effects fracture networks might have on those dynamics (*Longuevergne et al., 2009*).

Far fewer studies of extraction involving strainmeter data have been published, though. *Evans and Wyatt (1984)* investigate the signature of controlled fluid extraction at a longbase laser strainmeter (LSM) anchored into granite, and determine that flow within a single hydraulically-conductive fracture can produce appreciable strains at the surface (compared to typical earth tide amplitudes). It should not be surprising that studies investigating hydrologic effects in strain data are uncommon: the intended purpose of a strainmeter is to study crustal strain, rather than hydrology. In the case of borehole observations, hydrologic effects are very difficult to predict, and can only be observed once the installation is completed and data is flowing. Out of the 78 strainmeters in the current Plate Boundary Observatory (PBO) network, seven are either known, or presumed, to be affected by nearby pumping; three others are affected by naturally occurring hydrologic processes (e.g., aquifer recharge).

In this paper we compare strain and pore-pressure records from a closely-spaced pair of PBO borehole strainmeters (BSM) in southern California with multi-year records of pump activity collected at two active water wells nearby. These records demonstrate clearly the connection between pumping, deformation (strain), and pore-fluid pressure changes. We find remarkably high correlations between (1) the onset of long-lasting pumping episodes and the onset of large, transient strain signals; and (2) cumulative pumping records and changes in strain-rate. We model fluid extraction in a layered poroelastic halfspace, and find strong observational agreement with horizontal tensor strains, and pore fluid pressure, based on justifiable model parameters.

5.2 Observations at the Pathfinder Ranch

In the Anza region of southern California, the PBO maintains nine borehole stations. All stations are instrumented with a Gladwin-style BSM (*Gladwin*, 1984), and seven are equipped with an absolute pore-fluid pressure (PP) transducers sampling at depths near the strainmeter. Two of these stations are located on the grounds of the Pathfinder Ranch (PR), which is used for an annual youth educational and recreational camp. The parcel of land owned by PR is located at the southeast end of the Garner Valley, roughly 5 km Northeast of the main trace of San Jacinto Fault system (Figure 5.1). Pumping of groundwater is common at PR, and data from the two strainmeters there – B082 and B089 – have long been considered to be contaminated by pumping signals.

Our interpretation of drillers' logs around the Garner Valley and logging data taken during the installation of B082 indicates the shallow lithologic unit of the region is primarily alluvial fan and flood deposits. Deeper units include weathered rock, and the fractured metamorphosed granodiorite in which the strainmeters are cemented. According to the United States Department of Agriculture¹ the surficial soils in this area are classified as follows. To the northeast of the boreholes, the material is primarily Wapi-Pacífico rock outcrop (weathered granodiorite), which is known to be highly drained, exhibit moderate runoff characteristics with moderately high permeability; further northeast the material becomes primarily intact granodiorite rock outcrop. Within the extents of the PR parcel, the material is mostly Cagey alluvium (flood deposits), which is moderately well-drained, and exhibits slow runoff characteristics with high permeability; the seasonal high water table may be seen at the surface from approximately November to April. Material to the southwest, extending to the base of Thomas Mountain, is Oak Glen-Ruch alluvium (fan deposits), which is well drained, and exhibits moderate runoff characteristics with high permeability. The borehole strainmeters are installed below the contact between the Cagey alluvium and the Wapi-Pacífico rock, at the mountain toeslope.

The intermontane basin of the Garner Valley is an alluvial aquifer recharged

¹ <http://www.nrcs.usda.gov>

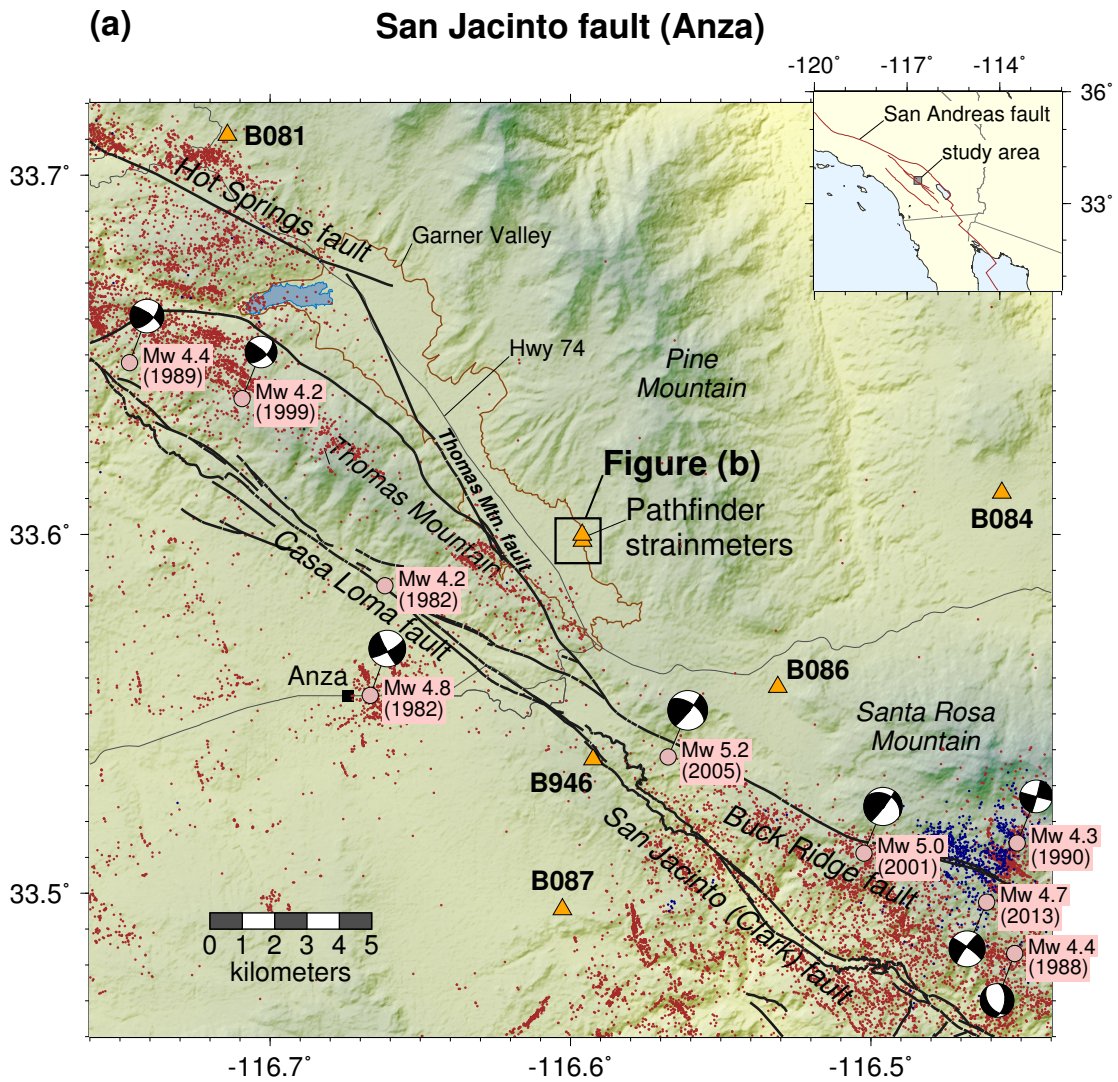


Figure 5.1: Map of the San Jacinto fault zone near Anza with PBO borehole strainmeters in the region (triangles), seismicity since 1981 (*Hauksson et al.*, 2012), and focal mechanisms for the largest earthquakes since 1981. The square region marks the study region, and the extents of Figure 5.2.

primarily by precipitation; groundwater flows slowly ($\approx 30 \text{ m yr}^{-1}$) from the South to the North, where it drains into the San Jacinto river, and hydraulic conductivities have been estimated to range from $1.4 \times 10^{-5} \text{ m s}^{-1}$ to $4.3 \times 10^{-5} \text{ m s}^{-1}$ (*Durbin, 1975*). Groundwater levels are reduced primarily by transpiration from valley flora having root systems extending to the water table (phreatophytes). To a lesser extent, domestic and agricultural pumping, seepage into Lake Hemet, and natural evaporation also reduce levels. Pronounced lows in the Bouguer gravity anomaly field are observed along the western margin of the valley; inverse modeling of the lows indicates they are likely associated with the deepest point of the low-density alluvium basin fill, which contacts consolidated rock and the surface expression of the Thomas Mountain fault (*Durbin, 1975*).

5.2.1 Records of Fluid Extraction

There are four water pumps at PR: three to aerate and maintain the fill level of their artificial lake, and one to maintain the fill level of their large volume storage tank. The most actively used pump is the tank-fill pump, which we refer to as ‘PR-M’; this pump is capable of fluid extraction at 40 gallons per minute (gpm), or $\approx 2.52 \times 10^{-3} \text{ m}^3 \text{ s}^{-1}$, making it the most powerful pump too. The second most active pump is the primary lake-aeration pump, which we refer to as ‘PR-L’, which is capable of producing at $\approx 0.13 \times 10^{-3} \text{ m}^3 \text{ s}^{-1}$ (2 gpm); the remaining pumps have flow rates on the order of PR-L, but are rarely used.

We collected two years of information regarding the usage of PR-M and PR-L by installing Onset HOBOTM dataloggers to record times when the well-pumps are switched ‘on’, or ‘off’, at a temporal precision as good as one second. This type of datalogger has the benefits of being compact, inexpensive, power efficient, and does not require frequent maintenance. In practice we have found they are limited primarily by their storage capacity; loggers at more active well-pumps need to be serviced more frequently (to recover the data stored in ROM). The data provide high precision registration of the beginning and end of pumping, which can be converted to duration times. Pumping durations can then be converted to average extraction rates (or volumes) over a specified period of time with measured flow

rates.

There are other nearby pumps which may contribute to the observed strain signals. Two wells are located immediately to the south of the Ranch, owned and maintained by the Lake Hemet Municipal Water District (LHMWD); they are equipped with high-power pumps with extraction rates on the order of twice PR-M. One of these was installed since late 2010, and the other, namely ‘GV-3’, has existed since the mid-1980s but is rarely used because of the poor quality of potable water it produces (*GSi/water*, 2004, and M. Gow (LHMWD), pers. commun., 2010). Locations of the known pumps in the are shown in Figure 5.2, along with locations of the BSMs, and other features.

(b) Pathfinder Ranch

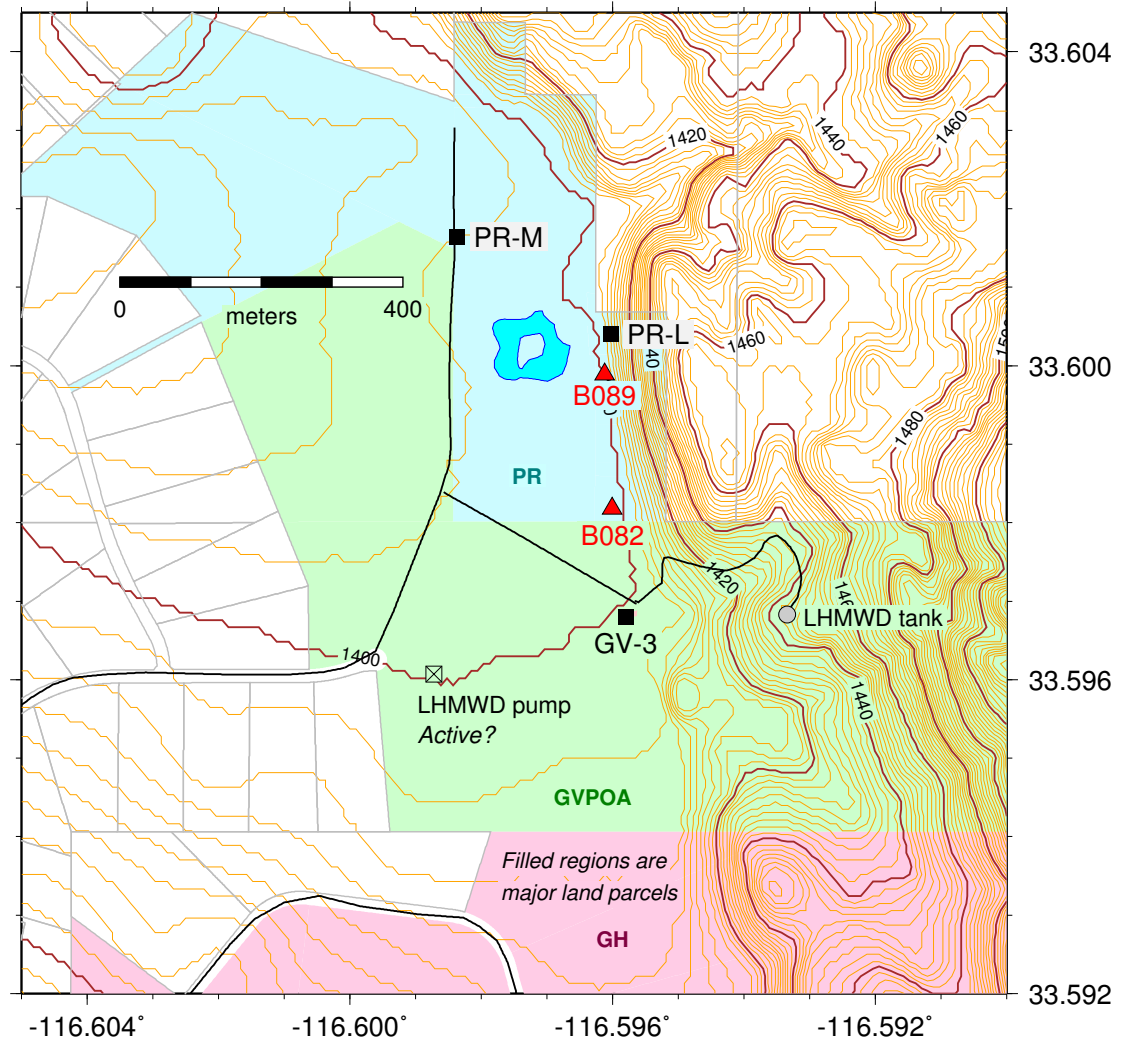


Figure 5.2: Map of the area around the Pathfinder Ranch, showing topography, parcel boundaries, and roads. Water pumps used in this study are marked with filled squares, and strainmeters are marked with triangles. The colored regions are large parcels which are mostly open space. The extents of this map are shown in the square region of Figure 5.1.

In Figure 5.3 we show a subset of the data collected at PR-M (volumes extracted from PR-L are very small and thus not shown) along with concurrent strain and pore pressure time series. We should note that the calibrated tensor strains in the figure have been corrected for grout-relaxation trends, and barometric effects; for visual emphasis, they have been rotated into the direction which generally maximizes the extensional strains in the direction of the pump. Tides have been removed, but their signals would be nearly imperceptible (on the order of the line thickness) on the scale required to show the pumping signals. The rainfall measured at B082 is shown, but adds no discernible effect on the scale of the pumping signals. We also note that the pore pressure record does not show sub-hydrostatic levels because the pressure-containment system failed sometime in mid-2010 (D. Mencin, pers. commun., Nov. 2011), resulting in the sensor not being immersed at times.

Even though the records for PR-M and PR-L explain nearly all anomalous strain and pore pressure signals observed at B082 and B089, they do not account for all of the anomalies in the strain and pressure records. (See, for example, the events in March 2012 in Figure 5.3.) The unexplained events have similar characteristics to those which are explainable; we speculate they are due to an incomplete record of the pump activity in the general vicinity of PR.

5.2.2 Validity of Calibrations

If the physics of the problem can be treated as approximately axisymmetric about the location of the dominant extraction well, as we should reasonably expect, then rotating the “calibrated” strain tensor into the direction of the well should reveal predominately uniaxial radial extension E_{rr} , with small levels of tangential extension $E_{\theta\theta}$. Shear strains are expected, but they should be very small (*Segall*, 1992). Thus we expect a large areal strain ($E_{rr} + E_{\theta\theta}$), and a similarly large differential extension ($E_{rr} - E_{\theta\theta}$), though reduced by $2E_{\theta\theta}$.

During the installation of the BSMs, the compass orientation of a reference gauge was estimated as accurately as possible, for the purposes of calibration. *Roeloffs* (2010) and *Hodgkinson et al.* (2013) have shown through tidal calibrations

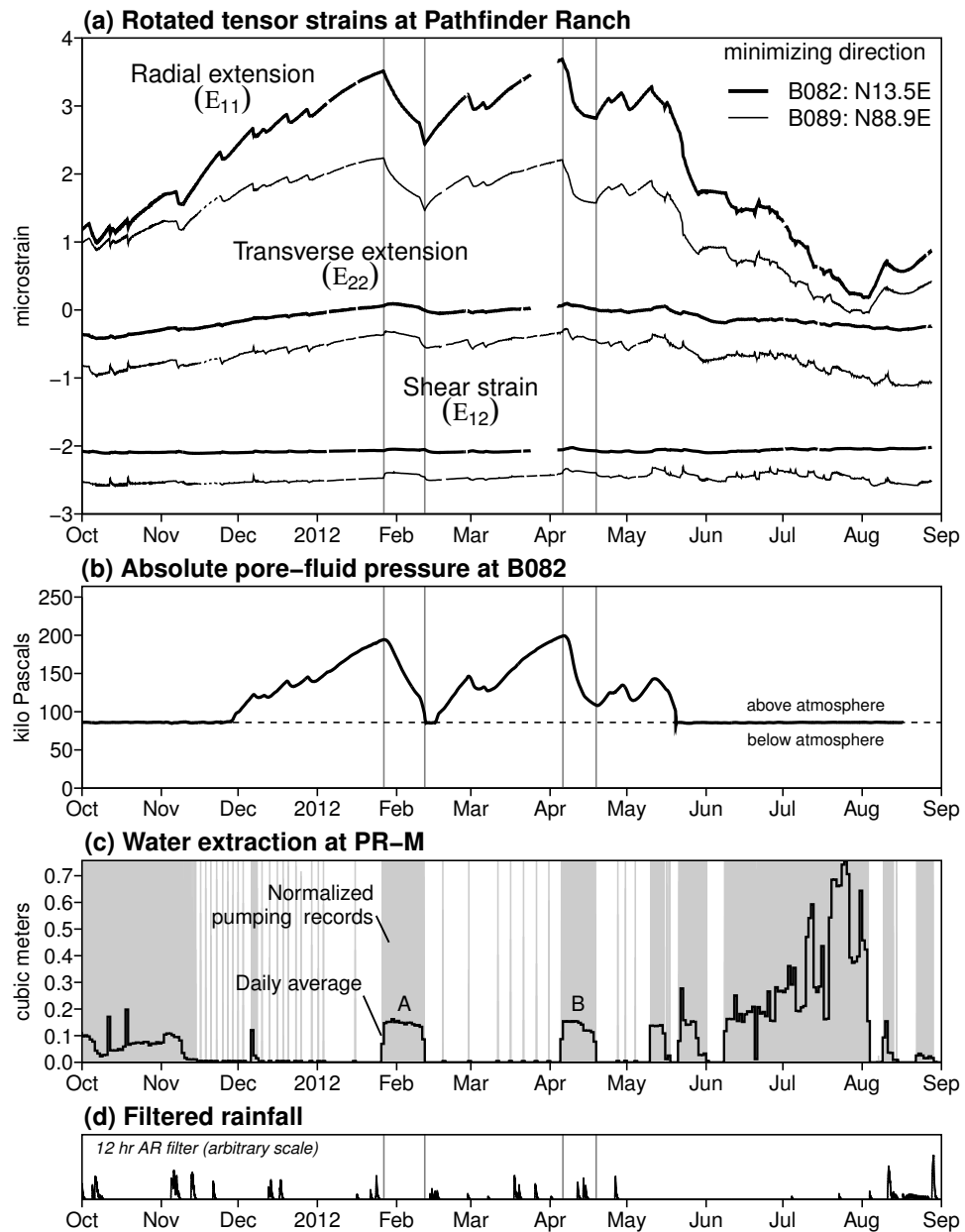


Figure 5.3: Some observations at the Pathfinder Ranch: (a) rotated tensor strains, corrected for earth tides, relaxation trend, and barometric pressure effects; (c) pore pressures, (d) normalized pumping record at PR-M (vertical grey lines) with average daily extraction volumes (thick black lines), (d) rainfall filtered with an $AR(1)$ recursive filter. The isolated pumping-episodes used for poroelastic modeling are labeled ‘A’ and ‘B’ in (c), and their start and end times are shown as vertical lines in the other frames.

that the nominal reference azimuth is erroneous by more than a few degrees for a number of stations in the network, although they did not analyze the Pathfinder strainmeters. We have found that a simple coordinate transformation (rotation) of the tensor strains into the direction of pump PR-M is approximately the direction which minimizes variance in the differential extension (γ_1) series, and maximizes variance in the engineering shear strain (γ_2) series. Figure 5.4 shows how the variances of corrected shear strains from 2011-01-01 to 2013-10-01 depend on the tensor transformation angle. The directions of optimal variance are -31.5° (East of North) for B082, and -46.1° for B089. Note the azimuths from B082 and B089 to PR-M are -29.6° and -47.0° , respectively. As is also apparent in Figure 5.3, the strains in this coordinate system are dominated by uniaxial extension in the radial direction (from the pump to the BSM), indicating that the calibrations are valid, and accurate.

5.3 Poroelasticity: Coupled Deformation and Fluid Diffusion

Our physical model of the relationship between fluid extraction and the observed strain and pore pressure signals is based on the general theory of linear poroelasticity (*Biot*, 1941; *Rice and Cleary*, 1976; *Wang*, 2000), which predicts two end-member states for a fluid-filled porous medium: (1) “drained”, where pore-fluid pressure is constant during changes in applied stress; and (2) “undrained”, where pore-fluid pressure is variable, and scales linearly with the change in applied stress. Put another way: in state (1) pore-fluid is allowed to flow into or out of a control volume; whereas, in state (2) zero pore-fluid flow occurs. Of course, these states represent gross simplification of the generally heterogeneous nature of crustal rock, but they are useful for understanding the types of signals strain measurement systems such as borehole strainmeters (BSMs) and dilatometers record *in situ* (*Segall et al.*, 2003).

Wang (2000) describes the two types of coupling that may occur between the fluid and solid: (1) “solid to fluid”, or when changes in effective stress are due

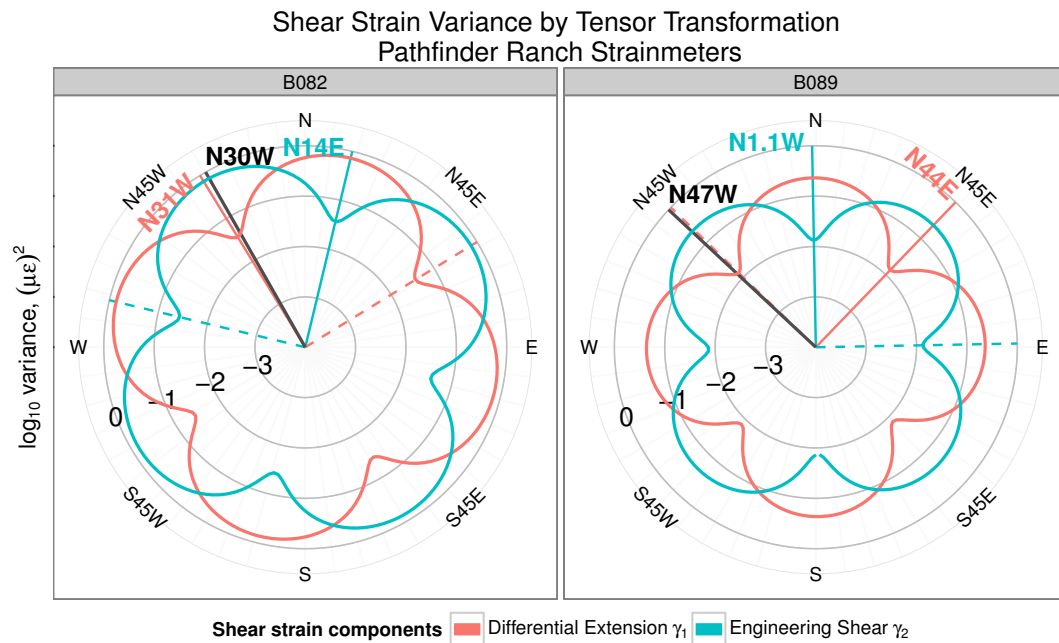


Figure 5.4: Observed variances in Pathfinder Ranch strainmeter data from 2011-01-01 through 2013-10-01, shown in logarithmic space as a function of coordinate transformation (tensor rotation). The orientations giving the minimum differential extension (γ_1) and engineering shear strain (γ_2) are shown in relation to the azimuth from the station to the well pump PR-M (black line). Areal strain is invariant, and thus not shown.

to deformation of the solid matrix, and (2) “fluid to solid”, or when changes in effective stress are due to removal or addition of pore fluids. Coupling of type (1) is commonly associated with solid earth tides, seismic waves, and elastostatic deformation (e.g., fault rupture); whereas, type (2) coupling is associated with fluid extraction or injection.

As (*Segall et al.*, 2003) points out, even a borehole strainmeter installed in permeable, fluid-saturated rock in a drained state will still be sensitive to deformation generated by relatively long-period signals, including natural or seasonal recharge (e.g., precipitation), and anthropogenic extraction (e.g., pumping).

5.3.1 General Poroelastic Boundary Value Problem

The stress equilibrium equations in linear poroelasticity are

$$\nabla \cdot \mathbf{T} = 0 \quad (5.1)$$

$$\mathbf{T} = \mu \mathbf{E} + (\lambda \nabla \cdot \mathbf{u} - \alpha p) \mathbf{I} \quad (5.2)$$

where \mathbf{T} , \mathbf{E} , \mathbf{I} are the stress, strain, and identity tensors; \mathbf{u} is the displacement, p is the pore pressure, and α is the effective stress coefficient. The strain tensor is given by

$$\mathbf{E} = \nabla \mathbf{u} + \mathbf{u} \nabla \quad (5.3)$$

(*Rice and Cleary*, 1976); λ and μ are the Lamé constants, with μ the shear modulus. See Appendix 5.7 for a list of symbols.

With Equations (5.1) – (5.3) we can derive the governing equations for the conservation of mass, assuming a homogeneous solution to the Navier-Stokes differential equations for incompressible flow. This solution is commonly referred to as Darcy’s law (*Wang*, 2000). Following *Wang and Kümpel* (2003) these equations are

$$(\lambda + 2\mu) \nabla(\nabla \cdot \mathbf{u}) - \mu \nabla \times (\nabla \times \mathbf{u}) - \alpha \nabla p = 0 \quad (5.4)$$

$$\beta^{-1} \frac{\partial p}{\partial t} + \alpha \frac{\partial}{\partial t} \nabla \cdot \mathbf{u} - \chi \nabla^2 p = q(\mathbf{x}, t) \quad (5.5)$$

Assuming fluid flow is laminar (Reynolds number $\simeq 1$), Equations (5.4) and (5.5) are valid, and changes in volumetric fluid content within the fluid saturated porous

medium are caused by the rates of change of both the pore-fluid pressure and the dilatation of the solid matrix; their relative contributions are determined by the bulk compressibility β and the effective stress coefficient, respectively. The gradient of pore-fluid pressure diffusion is determined by the Darcy conductivity χ .

For a layered half-space, the continuity conditions at each layer interface are (*Wang and Kümpel, 2003*):

$$\mathbf{u} = \mathbf{0} \quad (5.6)$$

$$\hat{\mathbf{n}} \cdot \mathbf{T} = \mathbf{0} \quad (5.7)$$

$$p = 0 \quad (5.8)$$

$$\hat{\mathbf{n}} \cdot \mathbf{v} = 0 \quad (5.9)$$

where in each case $\hat{\mathbf{n}}$ is a vector normal to the interface. The Darcy flux, \mathbf{v} , represents the volume of fluid flowing per unit area and time resultant from the gradient in pore pressure:

$$\mathbf{v} = -\chi \nabla p \quad (5.10)$$

The stress condition at the surface follows from the continuity equation, (5.7), where the pore pressure at the surface is either

$$\frac{\partial p}{\partial t} = 0 \quad (5.11)$$

$$p = 0 \quad (5.12)$$

for a confined or unconfined surface boundary condition, respectively.

5.3.2 Parameter Constraints

Kümpel (1991) demonstrates how the constants in Equations (5.4) and (5.5) can be unified with Skempton's coefficient B , the hydraulic diffusivity D , and the poroelastic equivalents of Poisson's ratio (ν and ν_u). The unified representations are

$$\lambda = \frac{2\nu\mu}{1-2\nu} \quad (5.13)$$

$$\alpha = \frac{3(\nu_u - \nu)}{B(1-2\nu)(1+\nu_u)} \quad (5.14)$$

$$\beta^{-1} = \frac{9(1 - 2\nu_u)(\nu_u - \nu)}{2\mu B^2(1 - 2\nu)(1 + \nu_u)^2} \quad (5.15)$$

$$\chi = \frac{9D(1 - \nu_u)(\nu_u - \nu)}{2\mu B^2(1 - \nu)(1 + \nu_u)^2} \quad (5.16)$$

Inspection of Equations (5.13) – (5.16) reveal a few restrictions on the range of parameters. The Poisson’s ratios are restricted to be $0 < \nu < \nu_u \leq 1/2$. Skempton’s coefficient B is restricted to $(0, 1]$, and can be thought of as the ratio of pressure inside the porous medium relative to the confining pressure. Figure 5.5 shows how Equations (5.14) – (5.16) are modified by changes in the Poisson’s ratios.

5.3.3 Numerical Solutions

A limited set of analytical solutions exists for problems involving fluid extraction from a poroelastic medium (see Appendix 5.8). Generally, these only consider situations where fluids are produced from a confined reservoir at great depths – a problem of interest to the petroleum industry, for example. To solve for coupled fluid flow and deformation (strain) due to extraction from a layered aquifer extending to the surface, we use numerical analysis.

We seek a solution that gives a good approximation to the general problem outlined in Section 5.3.1; but, we lack the sufficient instrument coverage to exploit full 4D finite element method solutions. The complexity of the problem can be reduced by assuming axial-symmetry about the extraction (or injection) well, and homogeneous layering of the subsurface. For this we use the software package `poe106`, which is based on the method of *Wang and Kümpel* (2003). Specifically, `poe106` is a spectral element toolkit which uses a stabilized Haskell propagator algorithm (*Wang*, 1999) to simulate fluid extraction from a layered poroelastic halfspace. Internally, response functions are inverted to solve for time-dependent pore pressure and solid- and fluid-displacement; deformation (strains and tilts). Darcian fluid velocities are also derived from displacements. We do not have observations of fluid velocity or tilt, so we do not include those solutions in our interpretations.

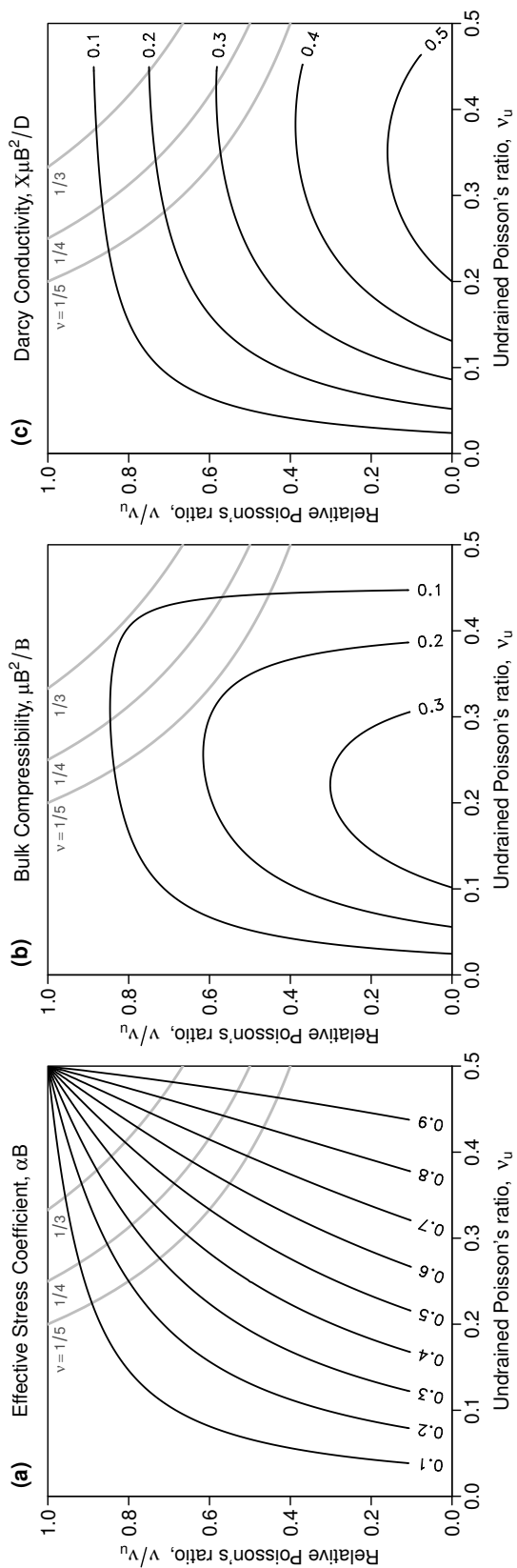


Figure 5.5: Contours of normalized poroelastic parameter size as a function of the undrained Poisson's ratio ν_u (horizontal axes) and the ratio of the drained Poisson's ratio ν to ν_u (vertical axes): (a) effective stress, αB ; (b) compressibility, $\mu B^2 \beta^{-1}$; and (c) Darcy conductivity, $\chi \mu B^2 D^{-1}$. Changes in the parameters' size are generally non-linear, but the effective stress coefficient is most sensitive to small changes in Poisson's ratio. Grey lines show contours of common values of constant ν .

5.3.4 Model Misfit: Isolated Events at PR-M

We have identified two “isolated” events in the pumping record for PR-M that show nearly constant pumping surrounded by periods of insignificant pumping: ‘A’, from 2012-01-26 to 02-11, and ‘B’, from 2012-04-05 to 04-18. We use these events (shown in figure 5.3) to test poroelastic simulations against because they provide a relative clear view of the effects of singular, sustained pumping episodes.

We require that the temporal characteristics (i.e., decay times) of the observations \mathbf{o} and poroelastic models \mathbf{p} be comparable, and that the magnitude of the tensor strains and pore pressure signals agree to within a factor of two or better. Our general findings are that the hydraulic diffusivity D strongly affects the time-constants of the model, and the shear modulus μ strongly affects the amplitudes of the transient signals; the remaining three parameters (B, ν, ν_u) affect the relative size of the strain and pressure signals.

The number of poroelastic model parameters (five) is greater than the number of observation points (three), meaning the problem is under-constrained, even for a halfspace computation. Because we are unable to perform a formal inversion for the “best” lithologic model, we test our modeling over a logarithmically spaced grid of D and μ , and compare contours of misfit. Following the recommendations of *Fox* (1981) and *Willmott* (1982), we calculate four measures of misfit which are based on the difference $\mathbf{d} = \mathbf{p} - \mathbf{o}$: the mean absolute error (MAE), the root mean square error (RMSE), and the (dimensionless) indices of agreement A_1, A_2 .

The MAE and RMSE statistics are difference measures of the “error” E between the prediction and the observation; they are related (assuming equal weight coefficients) as follows:

$$E^{1/\gamma} = \left[N^{-1} \sum_{j=1}^N |\mathbf{d}_j|^\gamma \right]^{1/\gamma}, \gamma > 0 \quad (5.17)$$

where $\gamma = 1$ for MAE and $\gamma = 2$ for RMSE (*Willmott et al.*, 1985). The indices A_1, A_2 are normalized descriptive statistics are related as follows:

$$A_\gamma = 1 - \left[\sum_{j=1}^N |\mathbf{d}_j|^\gamma \right] \cdot \left[\sum_{j=1}^N (|\mathbf{p}_j - \hat{\mathbf{o}}| + |\mathbf{o}_j - \hat{\mathbf{o}}|)^\gamma \right]^{-1}, \gamma > 0 \quad (5.18)$$

where $\hat{\mathbf{o}}$ is the mean value of \mathbf{o} , and $\gamma = 1$ for A_1 and $\gamma = 2$ for A_2 . These are bound from 0 to 1 where 0 indicates complete disagreement, and 1 indicates complete agreement.

Although these are relatively simple statistics to compute, they provide more informative and appropriate insight otherwise lost by using measures of determination (e.g., ‘ R -squared’), or correlation (e.g., Pearson’s product-moment coefficient) (Willmott *et al.*, 1985). Of these misfit measures, we find A_1 and MAE to be more robust than their $\gamma = 2$ counterparts: effects due to large errors in the observations, from unexplained pumping events, tend to be inflated.

5.4 Modeling Results

We simulated fluid extraction from two representative halfspace models, ‘bedrock’, and ‘sediment’; which have fixed values of Skempton’s coefficient and the Poisson’s ratios (Table 5.1). There is considerable uncertainty as to appropriate values of Skempton’s coefficient; however, the values chosen here reflect the approximate ratio of the hydrostatic gradient to the lithostatic gradient, where the bedrock is expected to have a higher density and thus a greater overburden stress. The Poisson’s ratios were chosen using data from Brocher (2005) (see also Figure 5.12).

Table 5.1: Representative poroelastic models

Model	B	ν	ν_u
bedrock	0.35	0.25	0.35
sediment	0.50	0.08	0.44

In logarithmic space we varied the shear modulus from $10^{7.5}$ to 10^{10} Pa (32 MPa to 10 GPa), and the hydraulic diffusivity from 10^{-2} to $10^1 \text{ m}^2 \text{ s}^{-1}$. The source-time function chosen for the extraction simulation is a boxcar function with the amplitude scaled by the average extraction rate at PR-M. Although there are typically subtle differences between the strain and pressure signals produced by

the two models, the sediment model is more inclined to generate signals with time-constants which are too short.

We interpolated misfits for each model (Figure 5.6 shows the case for bedrock), and both the sediment and bedrock models show similar features in the misfit contours. The quality of the fit to the tensor strain components is strongly

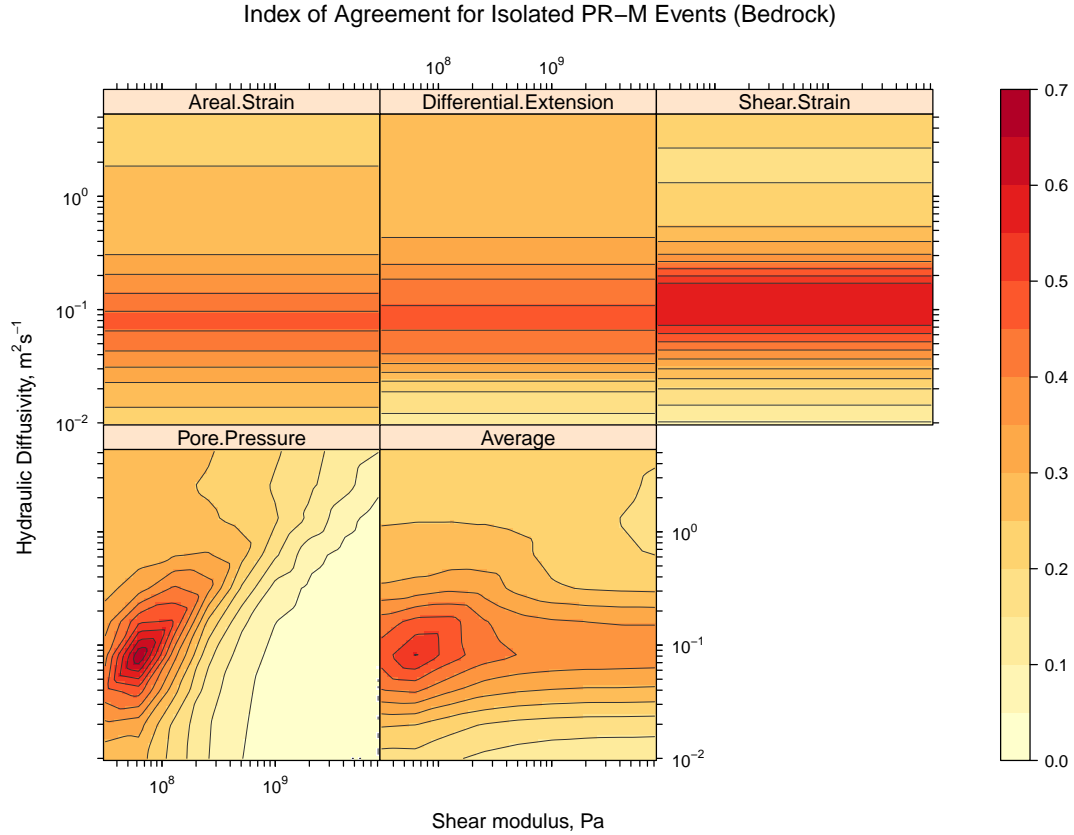


Figure 5.6: Contours of A_1 (Equation 5.18 with $\gamma = 1$) as a function of hydraulic diffusivity and shear modulus for the ‘bedrock’ halfspace model. Top row shows the strain misfits, and the bottom row shows the pore pressure misfit, and the average of the strains’ and pressure’s misfit.

sensitive to the hydraulic diffusivity, but only weakly sensitivity to shear modulus – a somewhat surprising result. In contrast, the quality of the pore pressure fit is sensitive to both quantities: misfit contours consistently show, in $\log \mu$ - D space, a single global maximum in A_1 and a single global minimum in MAE. Averaging the A_1 misfit contours for the strains and pressure gives the region of best agreement

for both quantities; these regions are summarized by the two highest contour levels in Table 5.2, and the fits based on these parameters are shown for the bedrock model in Figures 5.7 – 5.10.

Table 5.2: Ranges of poroelastic parameters for contours of A_1

Model	A_1	D $\text{m}^2 \text{s}^{-1}$	μ MPa
Bedrock	0.50 – 0.55	0.061 – 0.126	39.7 – 101
	> 0.55	0.081 – 0.083	61.6 – 66.1
Sediment	0.45 – 0.50	0.093 – 0.313	34.1 – 318
	> 0.50	0.122 – 0.223	84.6 – 193

The levels show are from two highest contour levels of the ‘average’ values (e.g., Figure 5.6)

5.5 Discussion

5.5.1 Weak Diffusivity Contrast

The first major result of our numerical analyses appears to be the requirements of a weak contrast in hydraulic diffusivity between the bedrock and sedimentary layers, and an extremely low shear modulus of rock at shallow depths (< 500 m). It is worth emphasizing here that the BSM and PP sample strain and pore-pressure from bedrock, not the upper sedimentary material. For the bedrock model, the range of values which produced the strongest agreement is 0.061 to $0.126 \text{ m}^2 \text{ s}^{-1}$, with the best agreement at $0.082 \text{ m}^2 \text{ s}^{-1}$. Figure 5.11 shows ranges of diffusivity expected for common geologic materials, compiled from *Brace* (1980); *Roeloffs* (1996); *Wang* (2000); *Wibberley* (2002); and *Doan et al.* (2006). The values we estimate are comparable to lower-end values expected for unconsolidated deposits, sandstone, and upper-end values for fractured igneous rock. We attribute this weak diffusivity contrast to elevated permeability in the bedrock associated with weathering (chemical and mechanical), and fracturing.

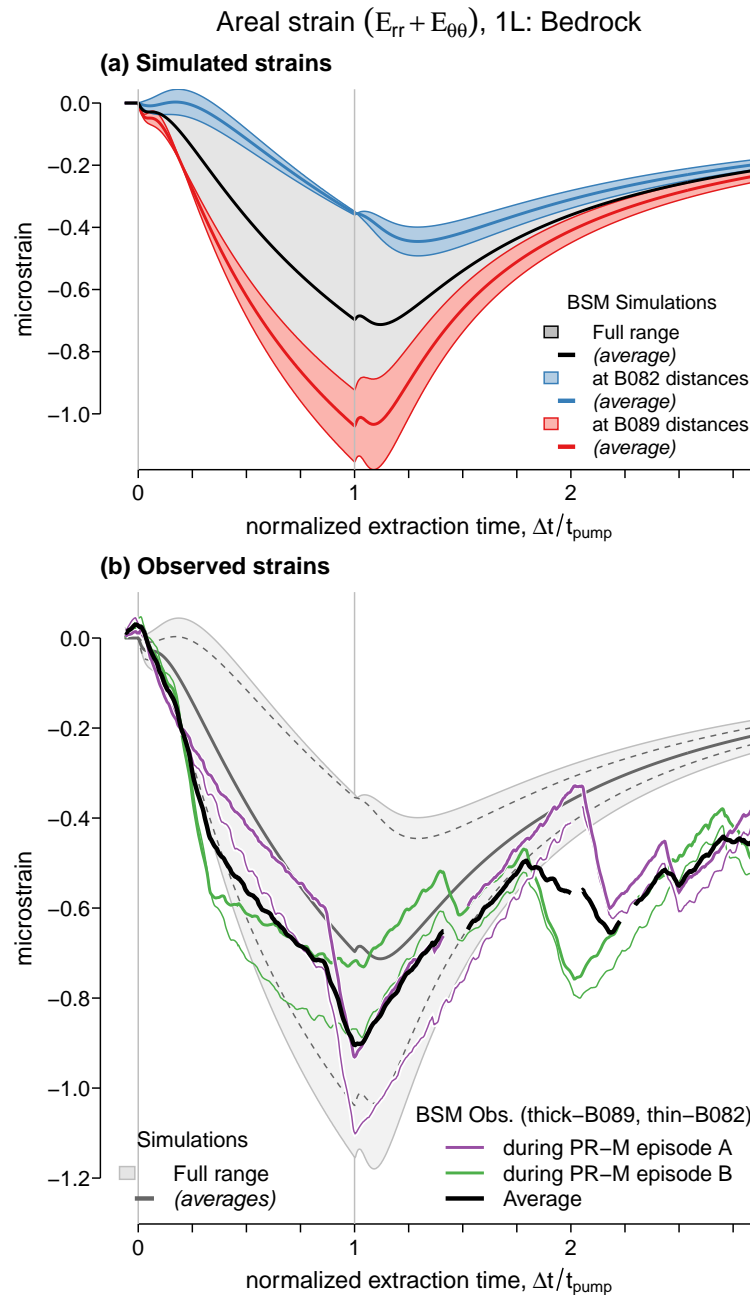


Figure 5.7: Best-fitting poroelastic halfspace simulations of areal strain during isolated pumpdown episodes at PR-M. The top frame shows the range of simulations for the observation distances and depths; the bottom frame compares average simulation values with the observations. Tensor strain observations have been rotated into their respect directions towards PR-M, and time is normalized by 16, and 13 days – the durations of episodes A and B respectively; the origin times ($\Delta t/t_{\text{pump}} = 0$) are 2012-01-26 and 2012-04-05, respectively.

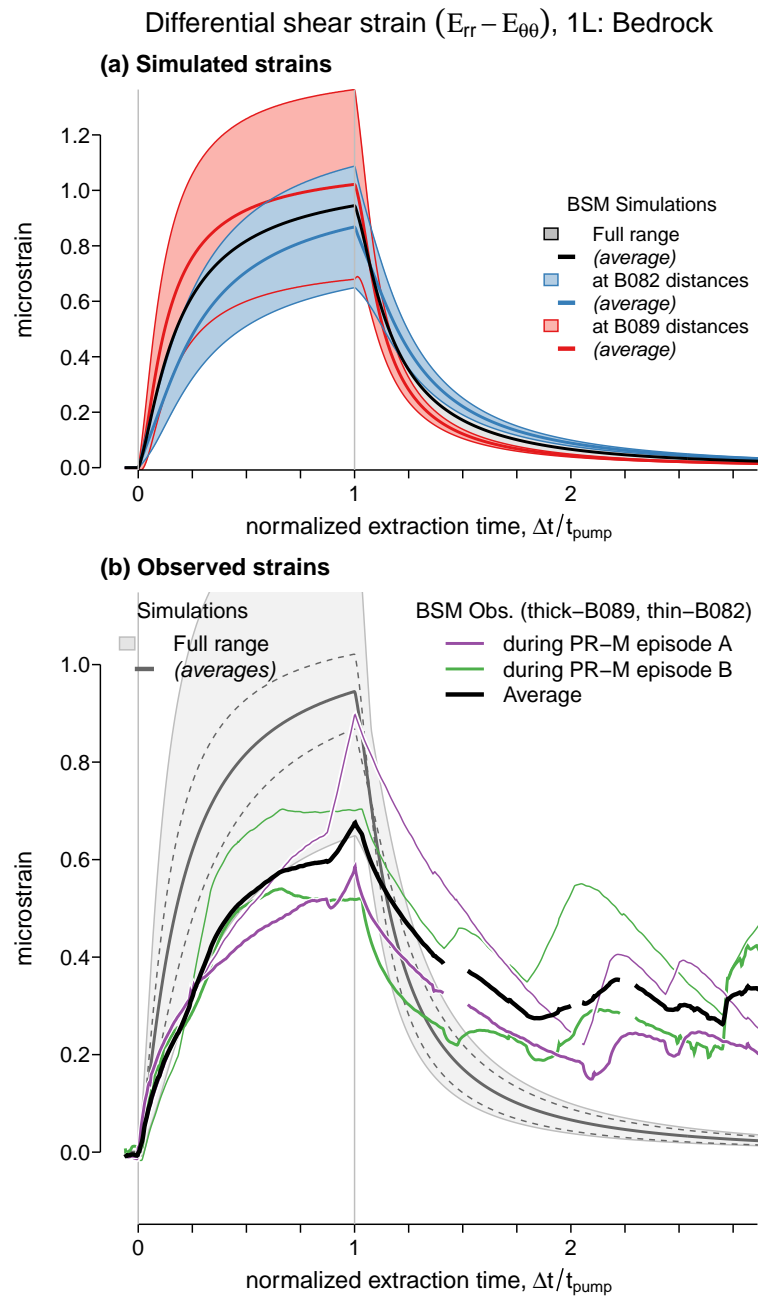


Figure 5.8: Best-fitting poroelastic halfspace simulations of differential extension ($E_{11} - E_{22}$) during isolated pumpdowns at PR-M. See Figure 5.7 for a description.

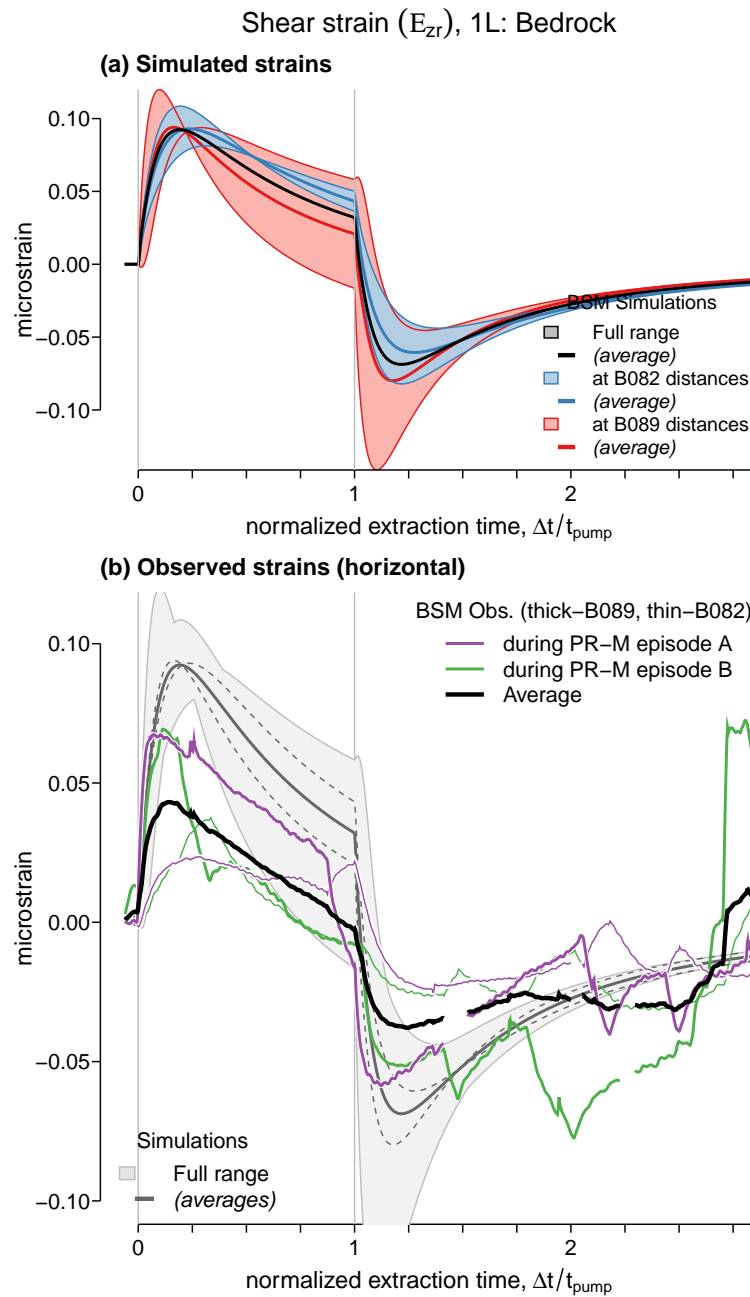


Figure 5.9: Best-fitting poroelastic halfspace simulations of shear strains (E_{12}) during isolated pumpdowns at PR-M. See Figure 5.7 for a description.

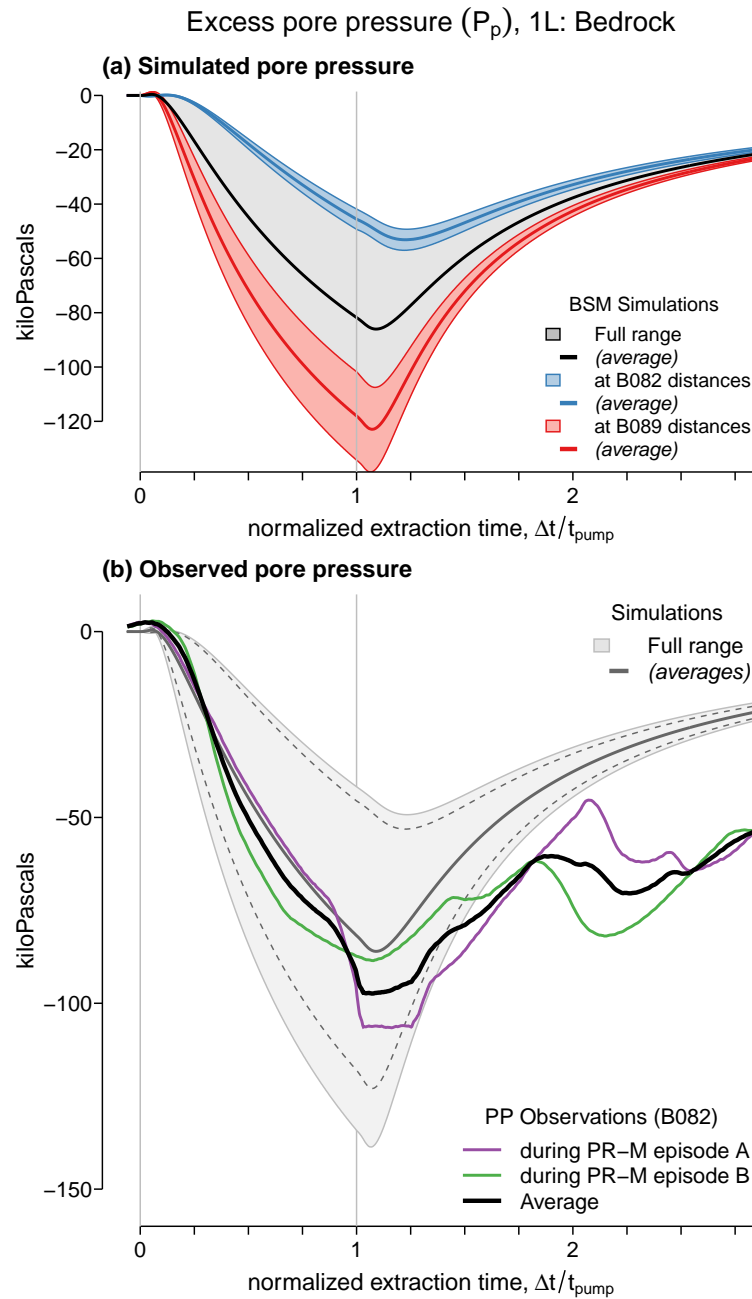


Figure 5.10: Best-fitting poroelastic halfspace simulations of excess pore pressure during isolated pumpdowns at PR-M. See Figure 5.7 for a description.

Elevated permeability in the bedrock may also be associated with the large slip displacements on the San Jacinto fault – a highly active, geometrically complex strike-slip fault system accommodating a substantial portion of plate-boundary strain accumulation (*Lindsey and Fialko, 2013*). Structural changes created by faulting (i.e., micro- and macro-fractures) can substantially alter the effective hydraulic properties of the rock (*Wibberley, 2002*), and the effective permeability of rock – which scales with diffusivity – appears to depend strongly on the inverse of effective stress of the material ($p_c - p$) following a power law (*Morrow et al., 1984; Evans et al., 1997*). At the average depths of the strainmeter installations (133 m and 241 m), the overburden stress from the rock is 3.3 and 5.9 MPa (assuming an average density of $2520 \pm 50 \text{ kg m}^{-3}$, estimated from Vp logs at B082), and represents an approximate upper bound on confining stress. For these relatively low stresses, the permeability of bulk granite is expected to be highest (*Brace et al., 1968*), and *in situ* estimates of permeability tend to vary most strongly (*Brace, 1980*).

5.5.2 Low Shear Modulus

Our second major result is the requirement that the shear modulus of the rock be extremely low in relation to values expected for crystalline rock. *Brocher (2005)* compiled a number of laboratory estimates of seismic velocities of various crustal rock from California. We converted these values to shear modulus and bulk modulus using standard relationships derived from the elastic wave equation:

$$\mu' = \rho V_S^2 \quad (5.19)$$

$$\kappa' = \rho (V_P^2 - 4V_S/3) \quad (5.20)$$

and plotted them over the range of our best estimates for the sediment and bedrock models in Figure 5.12. Based on our bedrock model, a shear modulus from 39.7 to 101 MPa gives good agreement with observations, with the best agreement from 62 to 66 MPa; whereas, as Figure 5.12 shows, estimates for deep crustal rock are two to three orders of magnitude larger (of order 10 to 100 GPa). We note that despite this large discrepancy, a number of data points with a comparable Poisson's ratio and

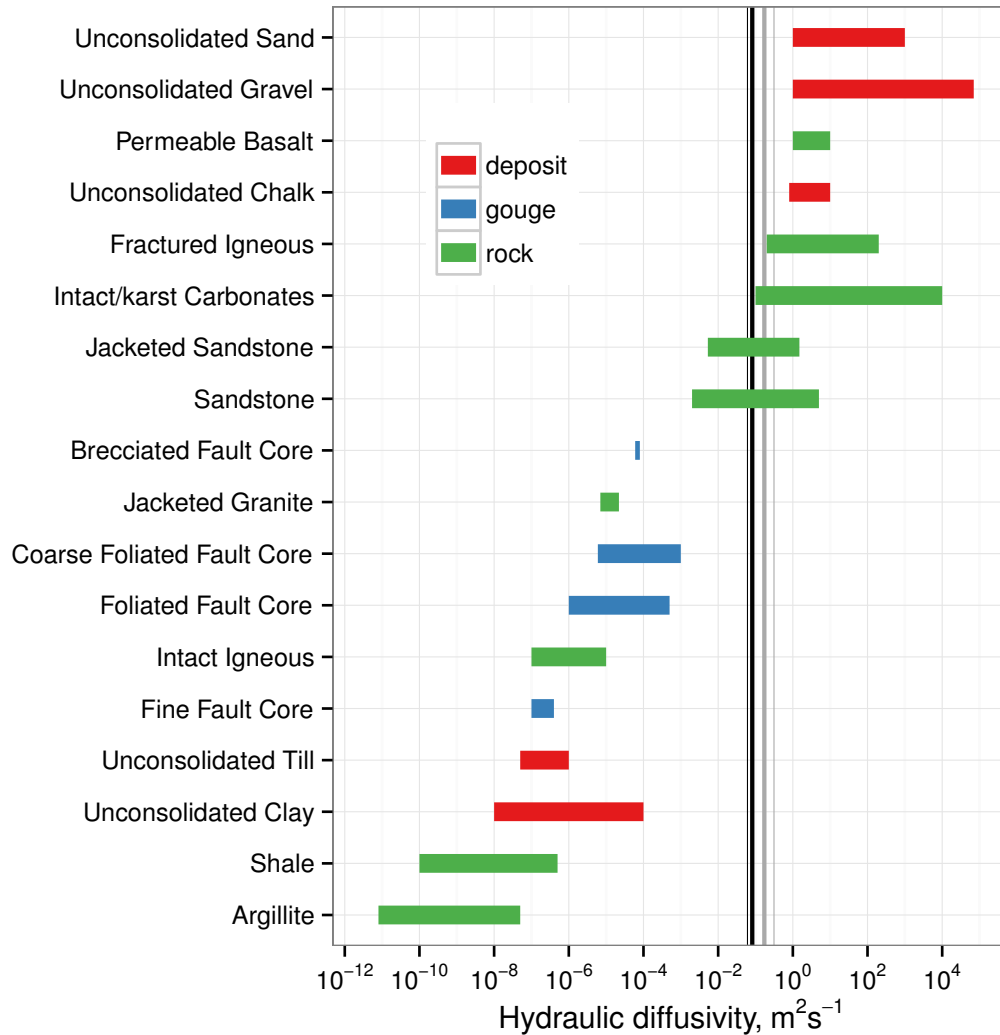


Figure 5.11: Values of hydraulic diffusivity for common geologic materials, compiled from *Brace* (1980); *Roeloffs* (1996); *Wang* (2000); *Wibberley* (2002); and *Doan et al.* (2006). Vertical lines show the range of values which produce the greatest agreement between poroelastic models and observations at Pathfinder Ranch: dark for the bedrock model, and light for the sediment model. Thick vertical lines are the preferred value, and a thin line is either the lower or upper range for bedrock or sediment, respectively.

shear modulus can be found: these are generally weathered rock at shallow depths. It's not clear how deep a reduced modulus of this magnitude would be observed to, but these results indicate that weathering and fracturing of the bedrock has reduced its rigidity at shallow depths substantially. We have also found that for the equivalent source-time function and hydraulic diffusivity, pore pressure amplitudes are modulated strongly by changes in shear modulus: a low-rigidity material will produce a low amplitude pressure signal relative to a high-rigidity material.

5.5.3 Effects of Basin Geometry?

Although we have found good agreement with observations using a simplified poroelastic model, we are unable to quantify effects from geometric features of the sedimentary basin, and fault interactions. A pair of geologic transects illustrating the generalized lithology of the valley to the North of the Pathfinder Ranch in *Durbin* (1975); *GSi/water* (2007); indicate the depths to intact bedrock is around 100 m. Above that is roughly a 60 m thick layer of weathered material and above that a 30 to 40 m layer of sedimentary material at the deepest point; the thicknesses of these layers tapers sharply to the bedrock contact at the edges of the valley. We summarize this interpretation in Figure 5.13.

Clearly, the simplifying assumption that the aquifer system has infinite areal extent is something for further review, especially at the edge of the valley (where the strainmeters are). This effect may be strengthening drawdown near the boundary (in this case between the sediment and bedrock), and we might expect that the hydraulic constants we obtained are biased (*Freeze and Cherry*, 1979, Ch. 8). In order to test for basin effects in our numerical analyses, we would need to consider the effects of varying layer thicknesses from the shoaling of the alluvium contact towards the edges of the valley; but, this would require a more sophisticated modeling method (finite elements), and quite a few additional observational wells.

There are two faults which could potentially affect the PR observations. The Thomas Mountain fault, to the West, is likely too far away for any associated effects to manifest in PR observations. The other fault – the Hot Springs (HS)

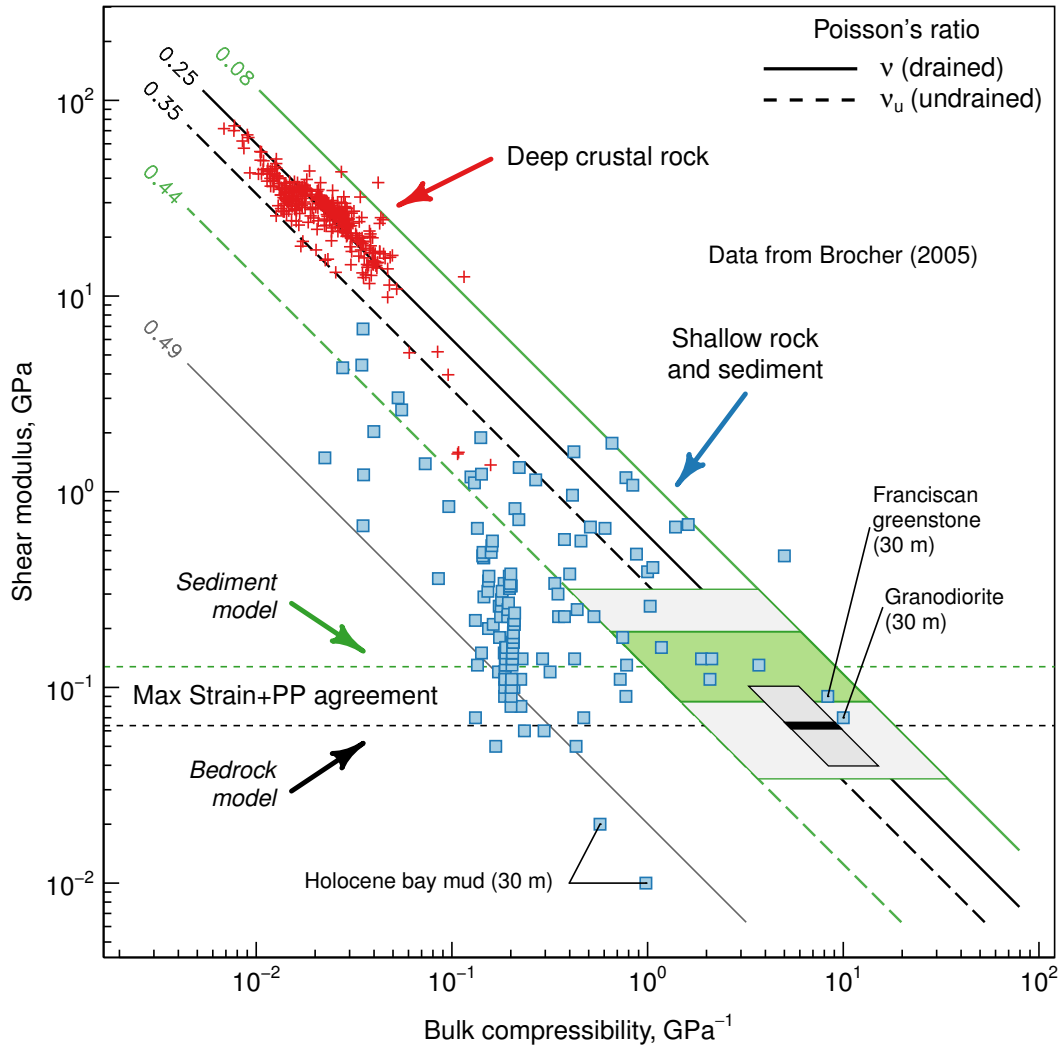


Figure 5.12: Shear modulus of crustal rock in California (from *Brocher* (2005)) as a function of bulk compressibility, with contours of Poisson's ratio (diagonal lines), and the range of values which produce the highest agreement between poroelastic models and observations at Pathfinder Ranch (filled regions). The light-green filled region is associated with maximum values in the the sediment model, and the black region is associated with the bedrock model (e.g., Figure 5.6).

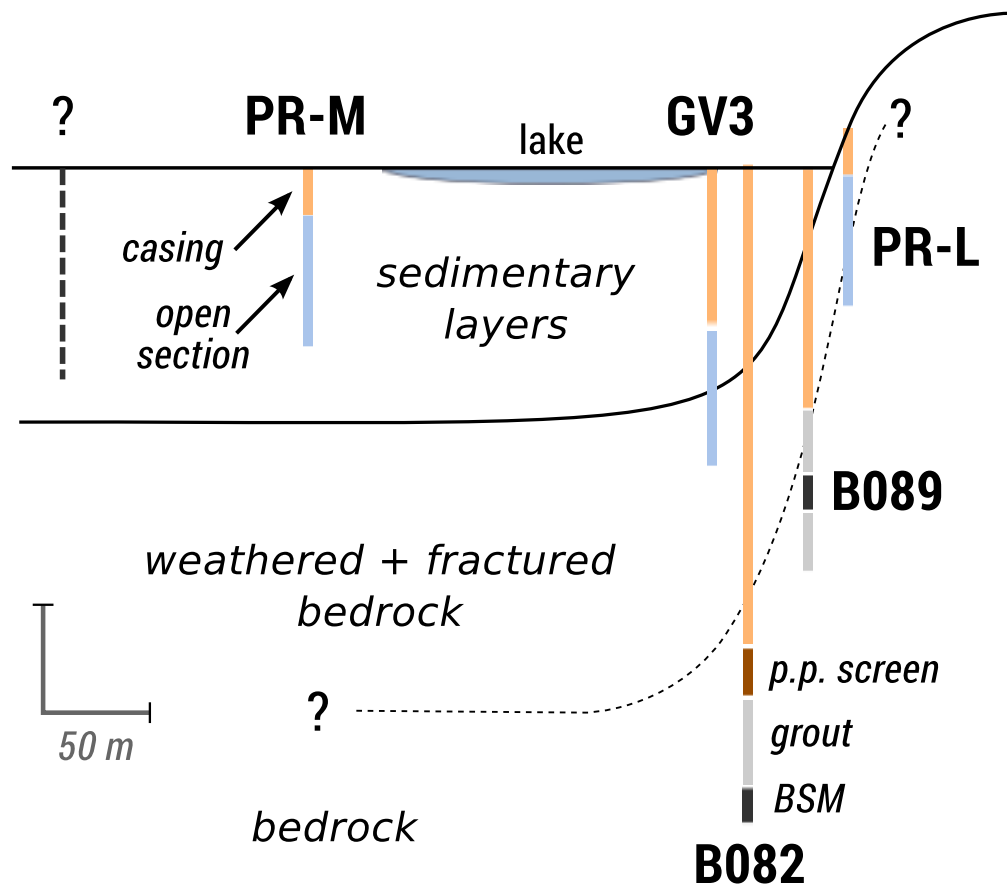


Figure 5.13: A generalized interpretation of the lithology along a cross-section perpendicular to the strike of the toeslope at the Pathfinder Ranch. Installation details (e.g., casing depths) of the water wells and strainmeters are shown roughly to scale (no vertical exaggeration).

fault – is located at the Northern end of the Garner Valley (Figure 5.1). The HS fault has accrued ≈ 5 km of cumulative offset since the initiation of the San Jacinto fault system (*Sharp, 1967; Hill, 1981*), and *Onderdonk (2008)* has mapped an inactive section extending along the Eastern edge of the valley. If the fault is expressed at shallow depths, in contact with the alluvium, it could be acting as an impermeable boundary, which would tend to amplify drawdown near it, and possibly bias our parameter estimates. Again, more observation points and a more sophisticated modeling approach would be required to test for these effects.

5.5.4 Hydraulic Properties from GV3

The municipal well ‘GV-3’ (Figure 5.2) is known to be inactive; but, has been used once since the strainmeters have been recording, for a controlled drawdown test (*GSi/water, 2007*). Specifically, on 2007-04-02 LHMWD commissioned a rate-controlled drawdown test where, in two hour increments, the pump operators increased the volume extraction rate from zero, to 1.3×10^{-3} , to 3.2×10^{-3} , to $4.4 \times 10^{-3} \text{ m}^3 \text{ s}^{-1}$, and finally back again to zero. This test occurred rather fortuitously when both strainmeters were active: they show changes in areal strain-rate correlated to extraction-rate. Although the size of the strain signals is not large compared to those commonly produced by pumping at PR-M, and the pore pressure sensor was inactive at the time, these data provide further evidence that the strainmeters directly measure deformation associated with fluid extraction, among other signals.

While the test was used to estimate aquifer yield characteristics, we performed a basic hydrologic analysis of this step-drawdown test to estimate the effective permeability of the aquifer. Following (*Bear, 1979, Ch. 11*), we firstly first estimate specific capacity (the effective flow-rate per unit of hydraulic head) of the aquifer to 9.7×10^{-8} , 1.1×10^{-7} and $1.5 \times 10^{-7} \text{ m}^2 \text{ s}^{-1}$ for the the three increments in flow-rate. The steady-state drawdown near the well, s , as a function of flow rate q can then be expressed as

$$s(q) = 0.672q + 0.012q^2 \quad (5.21)$$

(*Jacob, 1947*), with standard errors of the linear and quadratic coefficients of 0.033 and 0.001 respectively. The size of the coefficient of the linear term indicates this is a lossy aquifer. A crude conversion from specific capacity to transmissivity, based on a relationship for alluvial aquifers (*Razack and Huntley, 1991*), gives a range of 9×10^{-7} to $8 \times 10^{-5} \text{ m}^2 \text{ s}^{-1}$. If the saturation thickness of the aquifer is 60 m to 100 m, this gives a range of permeability of 9×10^{-16} to 10^{-13} m^2 (or 0.9 to 100 md) – roughly the range from laboratory measurements of sandstone, and *in situ* measurements of fractured crystalline rock (*Brace, 1984; Wang, 2000*). Although these estimates are for shallow material ($< 500 \text{ m}$), the values may persist over greater scales (*Townend and Zoback, 2000*), which suggests pore-fluid pressures much larger than hydrostatic levels are not supported by shallow rock in this region.

5.6 Conclusion

We have collected multi-year records of the pumping activity at two water wells near two PBO borehole strainmeters in southern California using low-cost data loggers. These records demonstrate a clear connection between extraction volumes and strain and pore pressure signals. A simplified poroelastic model explains the strain and pore pressure signals with excellent agreement. The ‘best’ model has a range of hydraulic diffusivity much higher than expected for bulk material, and a range of shear modulus much lower than expected. Instead, the diffusivity and rigidity are comparable to values expected for fractured crystalline rock, which suggests that hydraulically conductive fractures pervade the shallow crust. Our findings indicate that as a result of changes in applied stress, shallow crustal rock near the San Jacinto fault favors vigorous fluid flow over elevated pore pressures. This condition may help explain, for example, the lack of any observable shallow fault creep on the fault (*Lindsey et al., 2013*).

Other stations in the PBO network show similar behavior too: strainmeters on Vancouver Island, British Columbia, show large signals suspected to be from pumping at a nearby farm (H. Dragert, pers. commun., Oct. 2012). This is un-

fortunate given that strainmeters in this area were installed, in part, to record the smaller signals associated with episodic slip events on the Cascadia subduction interface (*Dragert and Wang, 2011; Hawthorne and Rubin, 2013*). Recent developments in low-cost strain sensing systems (*Hisz et al., 2013; Zumberge et al., 2013*) suggest that systematic testing of BSM data for suspected hydrologic influence using strain recordings alone is now a tractable problem; tests presented here establish that with supplementary measurements it is possible to place bounds on some geophysically relevant parameters of fluid-saturated rock in areas of tectonic significance.

5.7 Appendix A: Nomenclature

Table 5.3: List of poroelasticity nomenclature

Symbol	Represents
β^{-1}	bulk compressibility
p_c	confining pressure
χ	Darcy conductivity
\mathbf{v}	Darcy flux (discharge rate vector)
\mathbf{u}	displacement vector
α	effective stress coefficient
∇	gradient operator
D	hydraulic diffusivity
\mathbf{I}	identity tensor
δ	incremental change
λ, μ	Lamé constants
k	permeability
ν	Poisson's ratio (drained)
ν_u	Poisson's ratio (undrained)
p	pore pressure (excess)
B	Skempton's ratio ($\equiv \delta p / \delta p_c$)
\mathbf{x}	spatial position vector
\mathbf{E}	strain tensor
\mathbf{T}	stress tensor
t	time
q	volume injection rate

5.8 Appendix B: Analytical Solutions to Fluid Extraction/Injection Problems

Table 5.4: Closed-form solutions for steady-state displacements, pore pressures, and stresses due to fluid extraction (or injection).

Type	Source/Sink	Reference(s)
whole space	point	<i>Cleary</i> (1977) (†)
		<i>Rudnicki</i> (1986) (‡)
half space	point	<i>Booker and Carter</i> (1986) (†)
		<i>Wang and Kümpel</i> (2003) (‡)
symmetric disk	layer	<i>Geertsma</i> (1973)
buried, horizontal	layer	<i>Segall</i> (1985)
axisymmetric disk	layer	<i>Segall</i> (1992)
sinusoidal	surface flux	<i>Roeloffs</i> (1988)

† Original derivation

‡ Alternatively derived, or corrected

5.9 Acknowledgements

We thank Don Elliott for field assistance, Rongjiang Wang for making his poroelasticity modeling code available to us, and the administrative staff of the Pathfinder Ranch for being receptive and accommodating. Stewart Jewell was especially helpful, and his enthusiasm is greatly appreciated. The well-pumping data has been added to the Zenodo Open Access data repository (*Barbour*, 2013).

Chapter 6

Strain Sensitivities of Well-Aquifer Systems in Southern California: Effects of the San Jacinto Fault

Well-aquifer systems respond to dynamic strains over a wide frequency band, and can be sensitive to atmospheric pressure fluctuations, earth tides, and seismic waves. The pore pressure in damaged rock in the vicinity of active strike-slip faults is likely to have a reduced response to strain: the rock will be highly drained, with enhanced permeability and mechanical compliance. However, the expected spatial patterns of such a reduction in response are poorly understood. Here we use seismic waves to analyze the pore pressure response using shallow borehole measurements from Plate Boundary Observatory (PBO) stations, focusing on southern California. Stations near the San Jacinto fault (< 5 km) show a marked decrease in response compared to stations much farther away (in the fault-normal direction), and this reduction is strongly dependent on crustal shear strain rates, following an inverse power law. We propose that the observed spatial pattern in near-surface response is directly related to the earthquake cycle: recurring periods of high interseismic strain accumulation punctuated by large moment release have strongly enhanced the hydraulic transport characteristics of the surrounding rock, while also reducing structural rigidity.

6.1 Introduction

The response of well-aquifer systems to harmonic or quasistatic stresses depends primarily on the dimensions of the well, the mechanical properties of the rock matrix, and the effective hydraulic parameters (*Cooper et al.*, 1965; *Hsieh et al.*, 1987). Displacements derived from inertial seismometers can be used in conjunction with well measurements to estimate hydrological site conditions from seismic waves, as *Brodsky et al.* (2003) have done, but direct measurements of dynamic strains are more informative (*Ohno et al.*, 1997), and eliminate the need to assume a phase velocity. The only systematic study of the response to seismic waves (*Woodcock and Roeloffs*, 1996) suggests a scaling relationship between water heights and peak Rayleigh wave displacements in fractured crystalline rock; but, this is for only a single site.

It has long been known that faults are surrounded by a zone of more-fractured rock (*Sibson*, 1982; *Stierman*, 1984; *Sibson*, 1986) with the result that, at least at shallow depths, the fault zone is a region of lower elastic modulus, something shown by fault-zone trapped waves (*Li et al.*, 1997, 1999) and slip induced by coseismic stress changes (*Fialko et al.*, 2002; *Cochran et al.*, 2009). The fault zone is a region of elevated permeability (*Chester and Logan*, 1986), which opens up the possibility that fluid flow plays a significant role in fault-zone processes. For example, on the San Jacinto fault (SJF) in southern California, *Morton et al.* (2012) have found evidence of abnormally high porosity and significant dilatational strain in the fault core and the surrounding damage zone; they speculate that these regions can allow hydrothermal circulation that dissipates heat generated during earthquakes.

Surface waves from large teleseismic earthquakes generate dynamic dilatational strains, and these waves provide a robust method to estimate hydraulic and mechanical properties of the surrounding rock using borehole instrumentation. We have analyzed concurrent records of colocated strain and pore pressure from Plate Boundary Observatory (PBO) boreholes to examine the response to surface waves from large earthquakes from late 2006 (the start of the data) through 2012: a total of 48 events, with magnitudes from 4.5 to 9.0.

Focusing on stations near the SJF in the Anza area, we observe a strong correlation between seismic strain and pore pressure at each station, and the size of the effect (scaling) appears to be strongly dependent on the fault-normal distance to the fault. Spectral analyses of the largest surface wave signals, reveals a strong reduction in elastic modulus near the fault, a result which is corroborated by tidal analyses. The response coefficients also scales with crustal shear-strain rates, following an inverse power law.

6.2 Permeability and Fluid Flow in the Crust

A quantity central to any discussion of fluid flow in the crust is the permeability of rock (see *Rojstaczer et al.*, 2008, for a review). Simplistically, the permeability k is one of two key parameters controlling the proportionality between fluid flux q and pressure gradient ∇P in a Darcy-flow regime:

$$q \propto -k\nabla P/\mu' \quad (6.1)$$

the other being the kinematic viscosity of the fluid (μ'). (The fluid velocity would thus be the flux divided by the effective porosity.) In the theory of poroelasticity, the conservation of mass depends on both the fluid mass changes and deformation, which implies that strain in the crust is also a function of permeability. While it is relatively easy to measure *in situ* permeability at a single well, it is difficult to predict the permeability of rock elsewhere because estimates vary greatly among wells. This variation exists mainly because the magnitude of fluid pressure disturbances at some distance away from the well will be strongly affected by heterogeneities (e.g., fractures) that create fast pore pressure diffusion pathways (*Brace et al.*, 1968; *Brace*, 1980). Such heterogeneities are hypothesized to be the source of transient changes in permeability, too. For example, observations of enhanced stream-flow discharge after moderate to large earthquakes are best explained by temporary permeability enhancement, occurring on time scales less than earthquake recurrence intervals (e.g., *Rojstaczer and Wolf*, 1992; *Rojstaczer et al.*, 1995).

Seismic waves can induce permeability changes in the far field of earthquakes as well. *Elkhoury et al.* (2006) found that the amplitude and phase of the tidal signal in water wells changes temporarily in response to large seismic waves, again on relatively short time scales. Changes in tidal response are interpreted as changes in the transmissivity (a proxy for permeability) of the aquifer (*Hsieh et al.*, 1987), where the size of the change appears to be directly proportional to the magnitude of the seismic stress. A number of studies have since investigated the proposed efficacy of permeability enhancement via transient stressing (*Wang et al.*, 2009; *Elkhoury et al.*, 2011; *Manga et al.*, 2012). The primary mechanisms for permeability enhancement by seismic activity (other than fracture development) have been categorized as mobilization of either colloids (particles with diameters on the order of 10^{-9} m to 10^{-6} m) or gas bubbles, but determining the precise mechanism(s) remains elusive, and a topic of considerable interest (*Manga et al.*, 2012).

6.3 Methods

Due in part to the long observational history of water wells, there is a considerable literature on the response of water wells to seismic waves and tides (e.g., *Cooper et al.* (1965); *Kamp and Gale* (1983); *Hsieh et al.* (1987); *Rojstaczer* (1988a,b); *Rojstaczer and Agnew* (1989); *Liu et al.* (1989); *Shapiro* (1989); *Brodsky et al.* (2003); *Kano and Yanagidani* (2006); *Kitagawa et al.* (2011); *Kano and Ito* (2011)). Most of this literature models the surrounding material as a porous medium rather than a set of fractures (but see *Bower* (1983)) and, for seismic waves, deals with the frequency-dependent response produced by the movement of mass in and out of a large diameter well (“wellbore storage”), an effect irrelevant to the PBO pore pressure data.

Most analyses of pore pressure signals focus on a single station and often a narrow range of frequencies (the tides), and so cannot offer much insight into larger-scale variations. Here we analyze all stations in the PBO network which have a pore pressure measurement system (PP) colocated with a borehole strainmeter (BSM) –

see Table 6.1. We use maximum likelihood to estimate strain sensitivities for each station, and estimate local hydraulic and mechanical properties from empirical transfer functions derived from cross spectral density analyses.

6.3.1 Instruments

The PBO BSM is a Gladwin-style strainmeter, which has been perviously described in detail (e.g., *Gladwin*, 1984; *Agnew*, 1986; *Hart et al.*, 1996; *Barbour and Agnew*, 2011; *Hodgkinson et al.*, 2013). Here we describe the pore pressure measurement system, which is rather simple: a section of the borehole – typically very close to the strainmeter – is packed with high-permeability sand, exposing the screened portion of a rigid, small-diameter tube to fluid saturated rock; above and below the sand-packed section is filled with grout. An absolute pressure transducer (Paroscientific 8WD060-I) is affixed rigidly to the borehole-casing inside the fluid-filled tube, near the surface, but below the phreatic level (to allow for any potential seasonal variation due to recharge and discharge). At some stations where the well is artesian (naturally flowing) the tube is sealed with an inflatable ‘packer’ or capped at the surface (D. Mencin, pers. commun., Sept. 2011). Others are left exposed to atmospheric pressure.

In this paper we focus on the ‘Anza’ subset of stations (Table 6.1), because these fall on both sides of the San Jacinto fault (SJF) system, roughly forming a fault-normal transect over a range of distances. It is important to note that no other subset of PBO borehole instruments has such an advantageous configuration. The SJF is of great interest because it is a maturing (*Marliyani et al.*, 2013) strike-slip fault with high slip rates (in excess of 10 mm yr^{-1} (*Rockwell et al.*, 2006; *Lindsey and Fialko*, 2013)), a seismic-slip gap (*Thatcher et al.*, 1975), and is a proposed location for aseismic slip (*Wdowinski*, 2009) apparently unaccompanied by continuous low-frequency earthquakes (*Gomberg et al.*, 2008; *Wang et al.*, 2013). Previous studies have proposed a roughly 5 km zone of mechanically and chemically altered zone of material around the fault: *Stierman* (1984) modeled regional Bouguer gravity anomalies with a wide zone of reduced density material, and seismic tomography of the crust in this region (*Allam and Ben-Zion*, 2012) images a

Table 6.1: Plate Boundary Observatory boreholes with pore pressure instrumentation.

Region	Site	Date of installation	Lon.	Lat.	Elev. (m)	Depths	
						PP (m)	BSM (m)
Cascadia	B012	2005:264	-125.5420	48.9246	13	149	169
	B010	2005:269	-123.4513	48.6502	5	174	198
	B011	2005:256	-123.4482	48.6495	22	204	224
	B004 [†]	2005:166	-124.4270	48.2019	30	141	166
	B003	2005:172	-124.1409	48.0624	285	152	169
	B005	2005:200	-123.5033	48.0595	303	144	161
	B001	2005:180	-123.1314	48.0431	237	137	152
Mendocino	B022 [†]	2006:034	-123.9310	45.9546	10	134	220
	B028 [‡]	2007:078	-122.9638	44.4937	140	219	240
S. J. B.	B066	2007:158	-121.5922	36.8575	67	210	235
	B058	2007:137	-121.5808	36.7995	114	142	166
	B067	2007:163	-121.5655	36.7650	126	140	158
Parkfield	B073	2006:291	-120.4717	35.9467	535	226	241
	B076 [‡]	2006:286	-120.4248	35.9398	445	183	197
	B078	2006:285	-120.3452	35.8377	387	165	181
	B079	2006:286	-120.2057	35.7157	437	164	180
Anza	B081	2006:166	-116.7142	33.7112	1467	212	243
	B084	2006:169	-116.4564	33.6116	1271	135	158
	B082 [×]	2006:161	-116.5960	33.5982	1375	192	242
	B086 [‡]	2006:168	-116.5310	33.5575	1392	216	244
	B946 [‡]	2010:204	-116.5925	33.5373	1429	134	147
	B087 [‡]	2006:168	-116.6027	33.4955	1139	94	161
	B088 [†]	2007:027	-116.6205	33.3749	1404	137	160

PP systems are contained with an inflatable packer inside the sensing tube, unless marked with [†] (tube capped at surface), or [‡] (tube uncapped – exposed to atmosphere).

[×] Inflatable packer failed on 2010:190 (9-July).

comparably-wide low P - and S -velocity zone, but with elevated V_P/V_S (which can also indicate enhanced fluid saturation (*O’Connell and Budiansky, 1974*)).

Figure 6.1 is a map of the Anza stations plotted in a fault-centric coordinate system, plotted with locations of broadband seismometers, relocated seismicity, and mapped fault traces. Colored areas in the map are principal stress ratios (*Engelder, 1993; Fialko et al., 2005*):

$$\frac{S_V - S_h}{S_H - S_h} = \sin^2(\theta - \theta_{SH}), \quad S_H > S_V > S_h \quad (6.2)$$

where we have assumed the intermediate principal stress is in the vertical direction, and taken maximum horizontal stress orientations (θ_{SH}) in the region from a bi-cubic spline interpolation of World Stress Map data (*Heidbach et al., 2010*); a uniform fault-strike (θ) is assumed to be $W42^\circ N$. Stations near the fault are located in regions where the maximum horizontal stress is arguably at least twice as large as the vertical stress (warm colors in Figure 6.1), and faulting is predominately right-lateral strike-slip (*Yang et al., 2012*).

6.3.2 Surface Wave Catalog and Data Processing

In order to ensure the earthquakes would produce reasonably strong surface waves at the Anza stations, we selected events (Table 6.2) with an approximately logarithmic relationship between magnitude and epicentral distance (Figure 6.2).

Table 6.2: Earthquakes used in this study.

Date and Time (Y:D:H:M:S, UTC)	M_W	Latitude	Longitude	Depth (km)
2012:103:07:15:48	6.9	28.7899	-113.1418	10.3
2012:103:07:06:01	6.2	28.8409	-113.0715	10.1
2012:102:10:43:09	8.2	0.7730	92.4520	16.4
2012:102:08:38:37	8.6	2.3110	93.0630	22.9
2012:080:18:02:48	7.4	16.6620	-98.1880	20.0

Table 6.2 – *continued*

Date and Time (Y:D:H:M:S, UTC)	M _W	Latitude	Longitude	Depth (km)
2011:345:01:47:26	6.5	18.0380	-99.7960	64.9
2011:294:17:57:16	7.4	-28.9980	-176.1830	32.9
2011:252:19:41:34	6.4	49.4930	-126.9670	23.0
2011:245:10:55:54	6.8	52.1850	-171.6840	35.5
2011:187:19:03:16	7.6	-29.3120	-176.2040	20.0
2011:175:03:09:40	7.3	52.0080	-171.8590	62.6
2011:070:05:46:24	9.0	38.2970	142.3720	30.0
2011:068:02:45:20	7.3	38.4400	142.8400	32.0
2011:012:08:51:04	4.5	36.7705	-121.4987	8.4
2010:298:14:42:22	7.7	-3.4840	100.1130	20.6
2010:294:17:53:14	6.7	24.8430	-109.1710	10.0
2010:163:19:26:50	7.5	7.8480	91.9190	35.0
2010:096:22:15:02	7.8	2.3600	97.1320	31.0
2010:058:06:34:14	8.8	-35.9090	-72.7330	35.0
2009:321:15:30:46	6.6	52.1510	-131.3780	11.6
2009:280:22:18:26	7.8	-12.5540	166.3200	35.0
2009:272:17:48:10	8.1	-15.5090	-172.0340	18.0
2009:222:19:55:39	7.5	14.0130	92.9230	33.1
2009:196:09:22:29	7.8	-45.7500	166.5770	12.0
2009:148:08:24:45	7.3	16.7330	-86.2200	10.0
2009:078:18:17:40	7.6	-23.0500	-174.6680	34.0
2009:015:17:49:39	7.4	46.8620	155.1560	36.0
2009:003:22:33:40	7.4	-0.7070	133.3610	23.0
2009:003:19:43:50	7.7	-0.4080	132.8860	17.0
2008:290:19:41:26	6.6	14.4430	-92.4230	24.0
2008:133:06:28:01	7.9	30.9860	103.3640	19.0
2008:051:08:08:32	7.4	2.7780	95.9780	35.0

Table 6.2 – *continued*

Date and Time (Y:D:H:M:S, UTC)	M_W	Latitude	Longitude	Depth (km)
2008:005:11:01:05	6.6	51.2760	-130.7500	10.0
2007:353:09:30:30	7.2	51.4950	-179.4730	56.3
2007:318:15:40:50	7.7	-22.2040	-69.8690	40.0
2007:273:05:23:34	7.4	-49.4180	163.9540	10.0
2007:255:11:10:26	8.5	-4.5200	101.3740	34.0
2007:227:23:40:57	8.0	-13.3540	-76.5090	39.0
2007:164:19:29:41	6.7	13.6230	-90.7970	23.0
2007:021:11:27:45	7.5	1.2220	126.3950	22.0
2007:013:04:23:20	8.1	46.2720	154.4550	10.0
2006:319:11:14:16	8.3	46.6070	153.2300	30.3
2006:288:17:07:48	6.7	19.8200	-156.0270	29.0
2006:198:08:19:28	7.7	-9.2220	107.3200	34.0
2006:123:15:26:39	8.0	-20.1300	-174.1640	55.0
2006:110:23:25:02	7.6	61.0750	167.0850	22.0
2006:004:08:32:31	6.6	28.0770	-112.0960	14.0
2006:002:06:10:49	7.4	-60.8070	-21.4740	10.0

The data are processed as follows. For each event we assemble all available high-frequency strain and pore pressure measurements, align them in time and window them around the expected S -wave arrival time by a factor proportional to the magnitude and distance. We bandpass filter these records to have significant energy only in the surface wave frequency band (0.001 Hz to 0.1 Hz) which eliminates any potential bias from real or spurious coseismic offsets, and tidal curvature. The series are then transformed into the so-called ‘analytic’ function using the Hilbert transform, and we take the modulus of this to calculate the signal envelope. To illustrate, if we have a pressure timeseries $p(t)$, the envelope pressure is expressed as the amplitude of $p(t) + i\mathcal{H}\{p(t)\}$, where $\mathcal{H}\{\cdot\}$ denotes the Hilbert

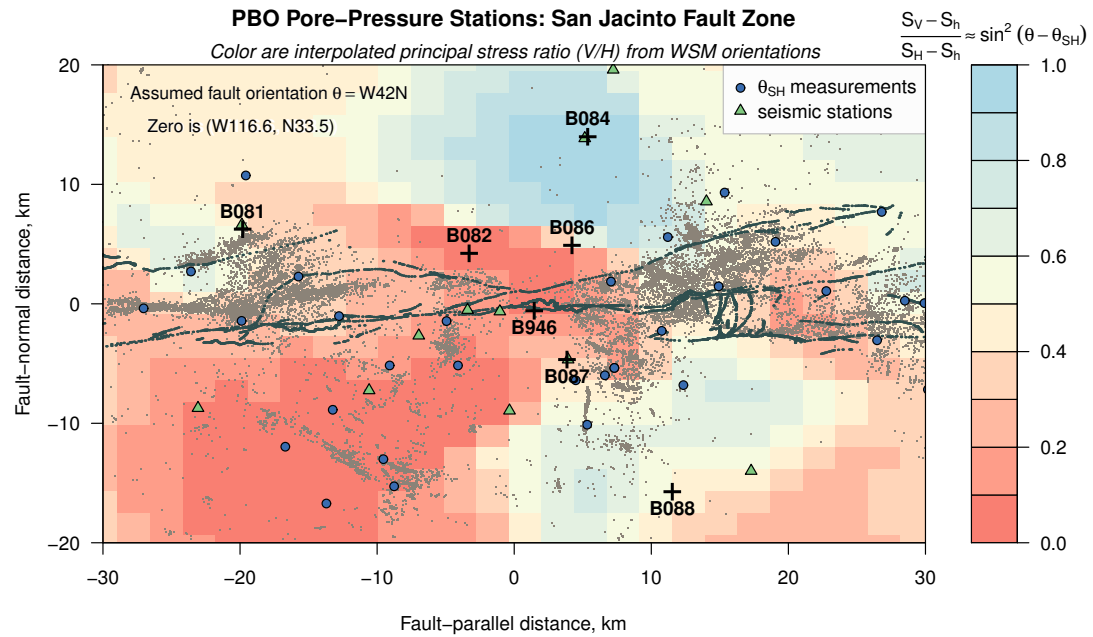


Figure 6.1: Map of stations in Anza with collocated pore pressure sensor and strainmeter, in fault-normal (vertical) and fault-parallel (horizontal) coordinates. Colors are the principal stress ratio, derived from maximum horizontal stress orientations and an assumed fault trace. Broadband seismometers, relocated seismicity, and mapped fault traces are also shown.

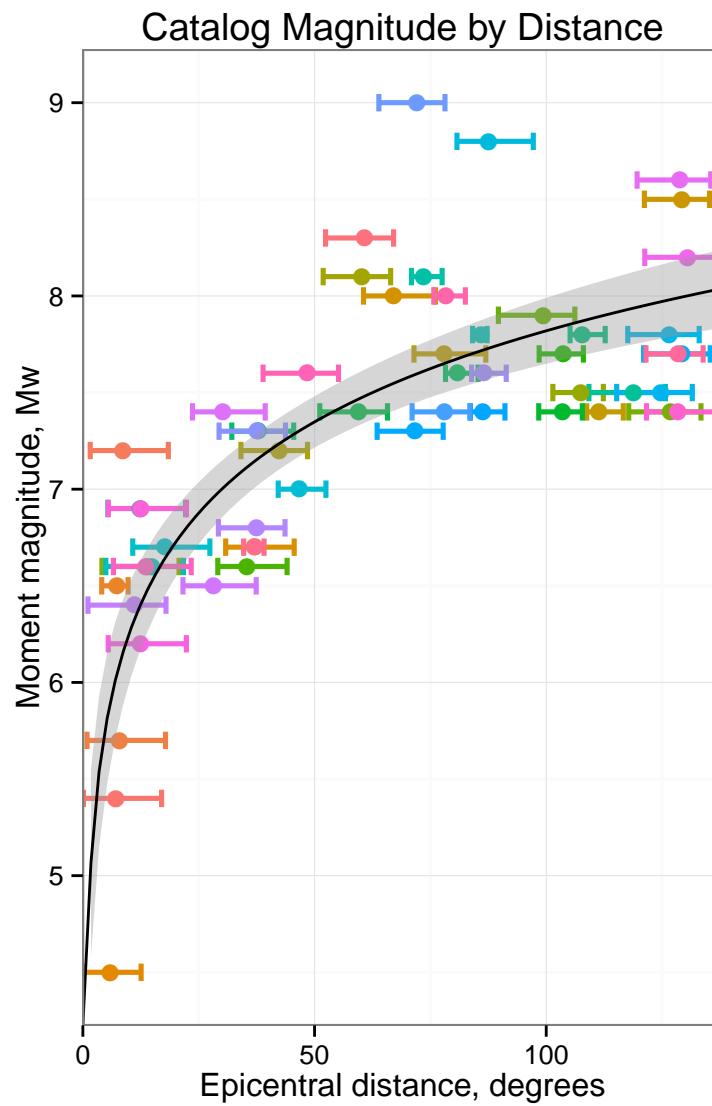


Figure 6.2: Earthquake catalog magnitude versus epicentral distance; these follow a logarithmic magnitude-distance relationship.

transform.

Figure 6.3 shows example timeseries for large surface waves from the 2011 M_W 9 Tohoku-Oki earthquake (*Ozawa et al.*, 2011; *Simons et al.*, 2011). In the top figure we show tensor strains at station B084 (far from the SJF), transformed into a radial-transverse coordinate system and corrected for orientation errors. Note the relatively small amplitude variation in the transverse extension: this indicates the waves are well-polarized (zero amplitudes are predicted for a pure plane wave). Highly polarized waves are not always observed in teleseismic strain records, which can be affected by multipathing (*Agnew and Wyatt*, 2014). In the bottom figure we show excess pore pressure for three stations (B084, B087, and B081) sorted by their approximate distance to the surface trace of the San Jacinto fault. It is immediately evident that the pore pressure variations are quite different, even though the strains are not (the strain series in the top figure are largely representative of the dynamic strains seen on other stations in the region), and there is increasingly strong frequency dependence near the fault. This is a consistent feature throughout the catalog, and we investigate this feature further in later sections.

One interpretation of this reduction in response is that the product of Skempton's coefficient and the bulk modulus ($B\kappa$) is small near the fault, which suggests the material there is relatively weak and permeable. When the response is approximately undrained – meaning that deformation occurs at a greater rate than pore fluid diffusion, the pressure is expected to be related to volume strain E_{kk} by (*Roeloffs*, 1996)

$$p = -B\kappa E_{kk} = -B\mu \frac{2}{3} \frac{1 + \nu_u}{1 - 2\nu_u} E_{kk} \quad (6.3)$$

where μ is the shear modulus (not to be confused with the viscosity term in Equation (6.1)). Assuming plane stress conditions, the vertical strain is

$$E_{zz} = -\frac{\nu}{1 - \nu}(E_{11} + E_{22}) \quad (6.4)$$

and Equation (6.3) can be expressed in terms of areal strain:

$$p = -B\mu \frac{2}{3} \frac{1 + \nu_u}{1 - 2\nu_u} \left(1 - \frac{\nu_u}{1 - \nu_u}\right) (E_{11} + E_{22}) \quad (6.5)$$

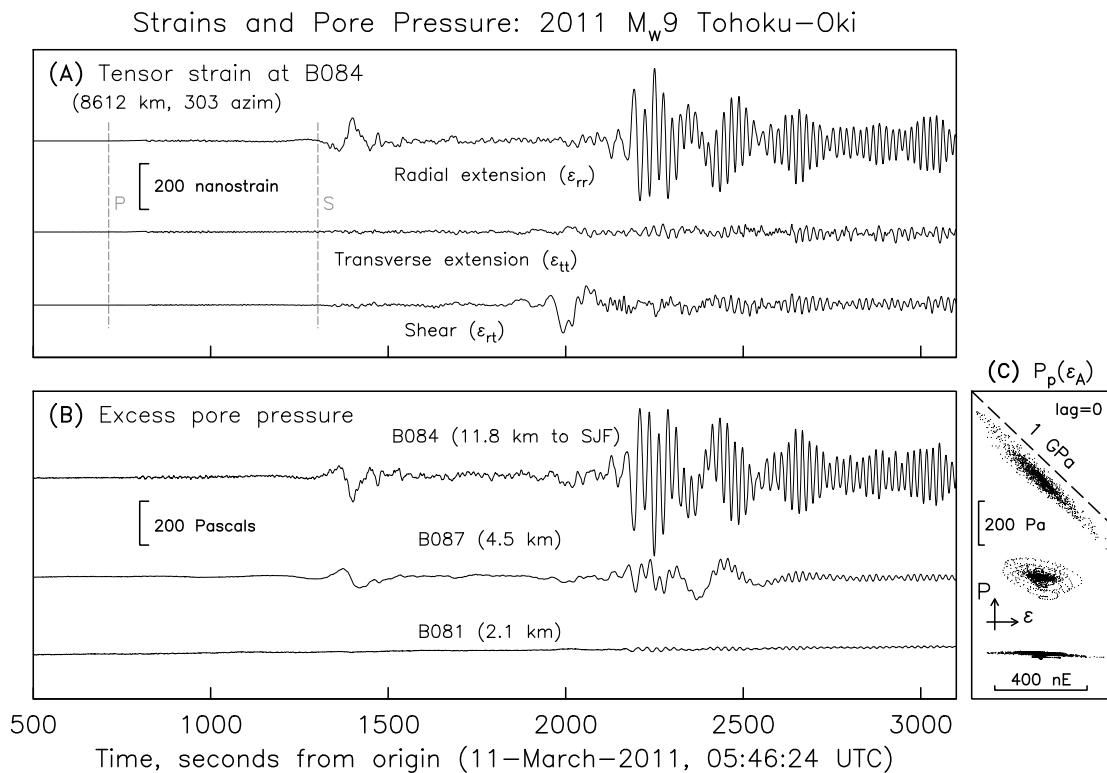


Figure 6.3: Strains and pore pressures in Anze from the 2011 M_w 9 Tohoku-Oki earthquake: (A) tensor strain records from B084, in a radial-transverse coordinate system, which are representative of strains at other stations in Anza; (B) varying pore pressure response at three stations, ranked their distance to the nearest fault; and (C) zero-lag correlation between areal strain (horizontal axis) and pore pressure (vertical axis), with a $1 \text{ GPa } \epsilon^{-1}$ reference (dashed line).

In Figure 6.3c the zero-lag correlation between the areal strain ($E_{rr} + E_{tt}$) and pressures are plotted, with a reference line corresponding to an undrained response of 1 GPa. Assuming, for this reference response, values of $\nu_u = 0.25$ and $B = 0.1$, estimates of shear and bulk moduli are of the order 9 GPa, and 15 GPa, respectively: rock at B084 is relatively rigid, and incompressible, which we expect for crystalline rock.

The observed reduction in response among nearby stations is an observation not apparently isolated to the Anza subset. Figure 6.4 shows the empirical distribution of peak values of pore pressure for all events at every station. It is clear that some stations are more sensitive to seismic waves than others, within geographical groups.

6.3.3 Regression Analysis

In order to (statistically) test for scaling relationships between pressure and strain, we assume the peak envelope pore pressure p is related to peak envelope strain e by the following functional model

$$p = ce^d \tag{6.6}$$

which implies

$$\log p = \log c + d \log e \tag{6.7}$$

The envelope-based estimates of pressure are assumed to be χ^2 distributed with two degrees of freedom, and the conditional pdf Φ of the pressure estimate is

$$\Phi(p|e) = \exp(e/p)/p, \quad p \geq 0 \tag{6.8}$$

The logarithm of the likelihood function for an observed pressure \hat{p} conditional on the scaling coefficients is the product of pdfs using the observed pressure in place

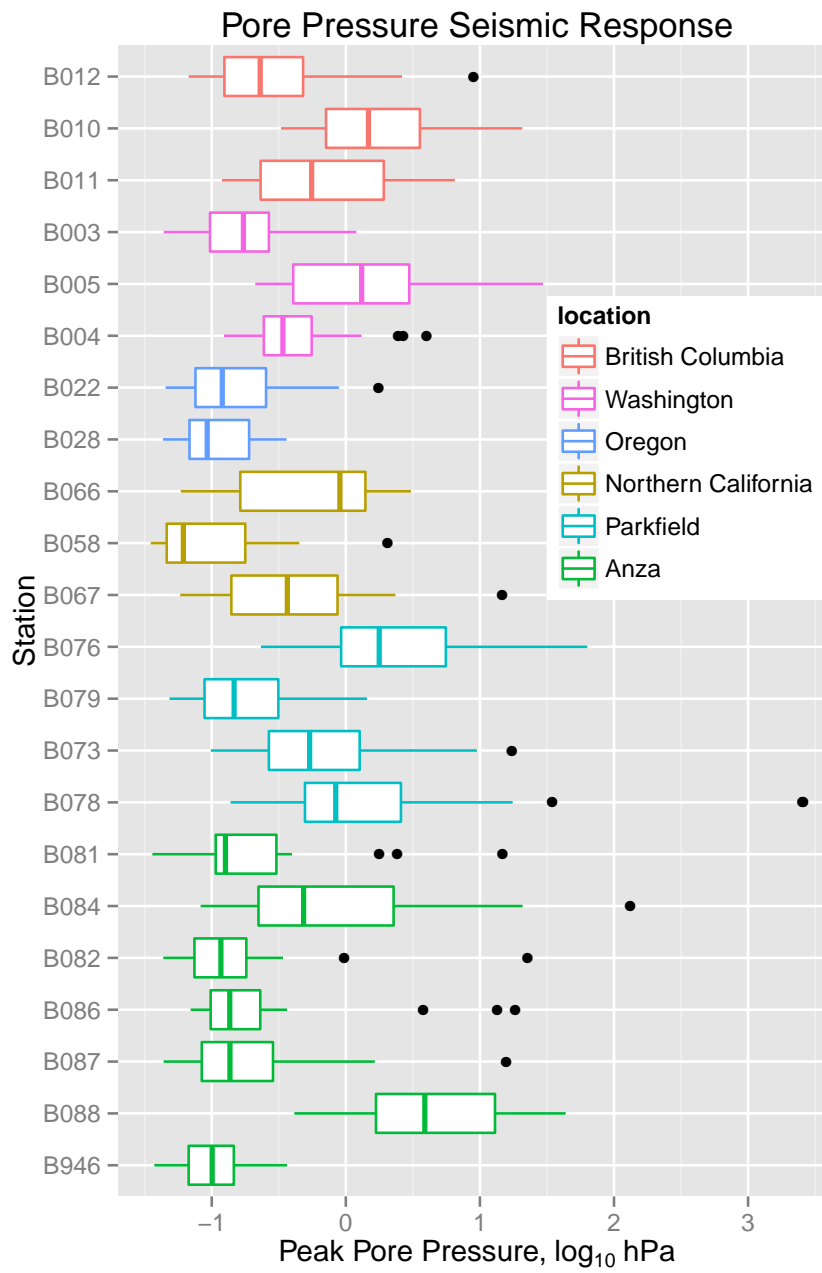


Figure 6.4: Ranges of peak pore pressure amplitudes across the PBO network for the earthquake catalog used here.

of e , or

$$L(\hat{p}|\alpha, \beta) = \ln \left[\prod_n \Phi(\hat{p}_n) \right] \quad (6.9)$$

$$= \sum_n \ln [\Phi(\hat{p}_n)] \quad (6.10)$$

$$= \sum_n \{ \hat{p}_n/p - \ln p \} \quad (6.11)$$

where p is the true pressure. We maximize L to find the most-probable estimates of $\log c$ and d , with standard errors from the second-partial derivatives of the expression.

6.3.4 Spectral Analysis: Empirical Transfer Functions

Even though surface waves are not stationary signals in a strict sense, they are approximately harmonic over short periods of time (quasi-stationary), and cross spectral density (csd) estimation can be used to calculate an empirical transfer function $R(f)$ which maps the amplitude spectra ($S(f)$) of strain to pore pressure ($\epsilon \mapsto p$).

The statistical model of this mapping is

$$S_p(f) = R(f)S_\epsilon(f) + \mathcal{N} \quad (6.12)$$

where \mathcal{N} is normally distributed random noise. For a given csd based on the covariance between strain and pressure signals, S_{ep} , the coherence spectrum is

$$\gamma^2(f) = \frac{|S_{ep}(f)|^2}{S_\epsilon(f)S_p(f)}, \quad 0 \leq f \leq f_s/2, \quad 0 \leq \gamma \leq 1 \quad (6.13)$$

where S_ϵ is the power spectral density (psd) of the strain signal S_p is the psd of the pressure signal. The absolute gain of R (also known as the ‘admittance’) is

$$G(f) = \gamma(f) \left(\frac{S_p(f)}{S_\epsilon(f)} \right)^{1/2} \quad (6.14)$$

And, the phase spectrum is the argument of the csd:

$$\Theta(f) \equiv \arg S_{ep}(f), \quad -\pi \leq \Theta \leq \pi \quad (6.15)$$

$$= \tan^{-1} \frac{\Re\{S_{ep}(f)\}}{\Im\{S_{ep}(f)\}} \quad (6.16)$$

We use the adaptive sine multitaper method developed by *Prieto et al.* (2009b) for spectral density estimation, which minimizes mean square error (the sum of squared bias, and variance) at each frequency (c.f., *Barbour and Parker*, 2014). To minimize the bias in the spectral estimation procedure, we first bandpass filter the input series to have maximum energy density in the desired frequency band 0.001 Hz to 1 Hz. The series are then aligned in time using cross correlation, and the effect of removing the delay is added back to the phase spectrum. Uncertainties of the real and imaginary parts of the transfer function are uncorrelated and have equivalent variance; hence, standard errors of the estimates are well approximated using the coherence, and the number of tapers K applied at each frequency:

$$\sqrt{(1 - \gamma^2)/K} \quad (6.17)$$

Priestley (1981) shows that a combination of K and the coherency (γ) is distributed as a central F -distribution:

$$\frac{2K\gamma}{1 - \gamma} \sim F(2, 4K) \quad (6.18)$$

From this statistic it follows that the probability that the absolute coherency is greater than some threshold λ (conditional on K) is

$$p(|\gamma| \geq \lambda, K) = (1 - \lambda^2)^{K-1}, \quad 0 \leq \lambda \leq 1 \quad (6.19)$$

We use estimates with coherence probabilities of $p \geq 0.95$.

6.4 Results

6.4.1 Regression Analyses

Using the functional model in Equation (6.7) and log-likelihood function in Equation (6.9), we regressed the entire catalog of peak pressures, in units of 10^2 Pa, against peak strains, in units of 10^{-6} ϵ with a linear mixed-effects algorithm, where observations are grouped by station. In other words, the full sample set is described by a linear combination of regressions for each station. In Figure 6.5 we present these results, plotted by station. It is immediately clear that each

stations has a unique set of regression coefficients, and the full set would not be well-described by a standard linear regression. It is also striking that the effect sizes vary substantially, for we expect the wavelength of the surface waves to be much greater than the inter-station spacing (on the order of 5 to 10 km).

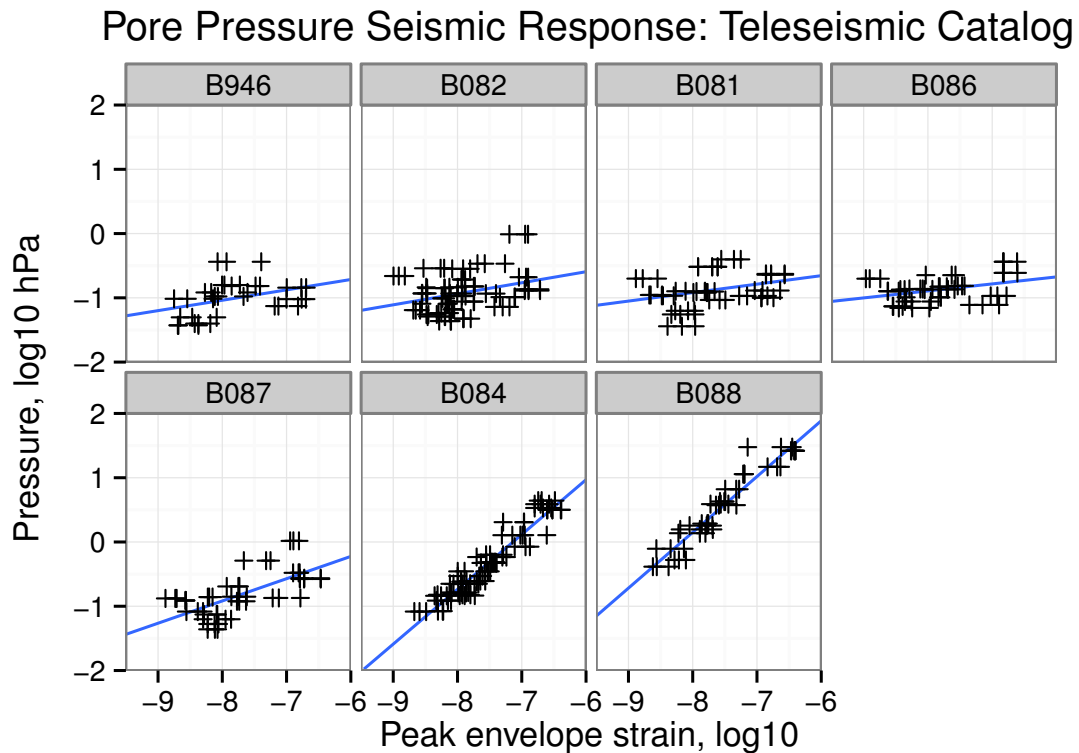


Figure 6.5: Relationships between pore pressure and strain in southern California.

6.4.2 Spectral Analyses

Small amplitude events do not yield stable transfer functions; this is because an implicit assumption in transfer function estimation is that the input signal is noise free (Equation (6.12)). In practice this means the pore pressure must have a high signal-to-noise ratio, and yet we are analyzing pressure signals not much greater than ambient noise levels, in many cases (see, for example, the signals for B081 in Figure 6.3). However, of the largest earthquakes in Table 6.2, we obtain

the best results for stations with low-amplitude responses from the Tohoku-Oki earthquake. Figure 6.6 shows the result of using an iterative method to estimate the transfer function between areal strain and pore pressure for stations B081, B087, B084, and B088. Values with statistically insignificant ($p = 0.95$) coherence are shown as muted colors. The admittance and phase spectra are relatively flat over a wide band of frequencies: this indicates the undrained assumption is reasonable. B087 is a notable exception, however: the admittance is not flat, and the phase is shifted roughly 60° away (greater lag in pressure) from the expected 180° . These differences for B087 are likely due to environmental and inertial effects: the tube is not sealed, and fluid pressures are exposed to atmospheric pressure. Shear strain coupling with optimally oriented fractures (*Bower, 1983*) may also be influencing the transfer function at B087.

Based on the transfer functions in Figure 6.6, we estimate the shear and bulk moduli of the rock as a function of Skempton's ratio B , following Equation (6.5) and assuming $\nu_u = 0.25$. These are given in Table 6.3. It is apparent that the elastic properties of the surface rock are reduced substantially in the vicinity of the fault, which is consistent with the modulus parameters from the regression results ($\log c$).

6.5 Discussion

Investigation of the response of well-aquifer systems in southern California for a catalog of earthquakes has illuminated an apparent reduction in rigidity and pore pressure sensitivity in shallow crustal rock within a ± 5 km zone around the San Jacinto fault. Although these results are based on direct measurements of strain pore-fluid pressure, it is important to understand how the values we obtain from our regression and spectral analyses relate to properties of the rock. In a manner similar to seismic waves, the response of well-aquifer systems to earth tides yields useful material properties, and we look to these signals for supporting evidence.

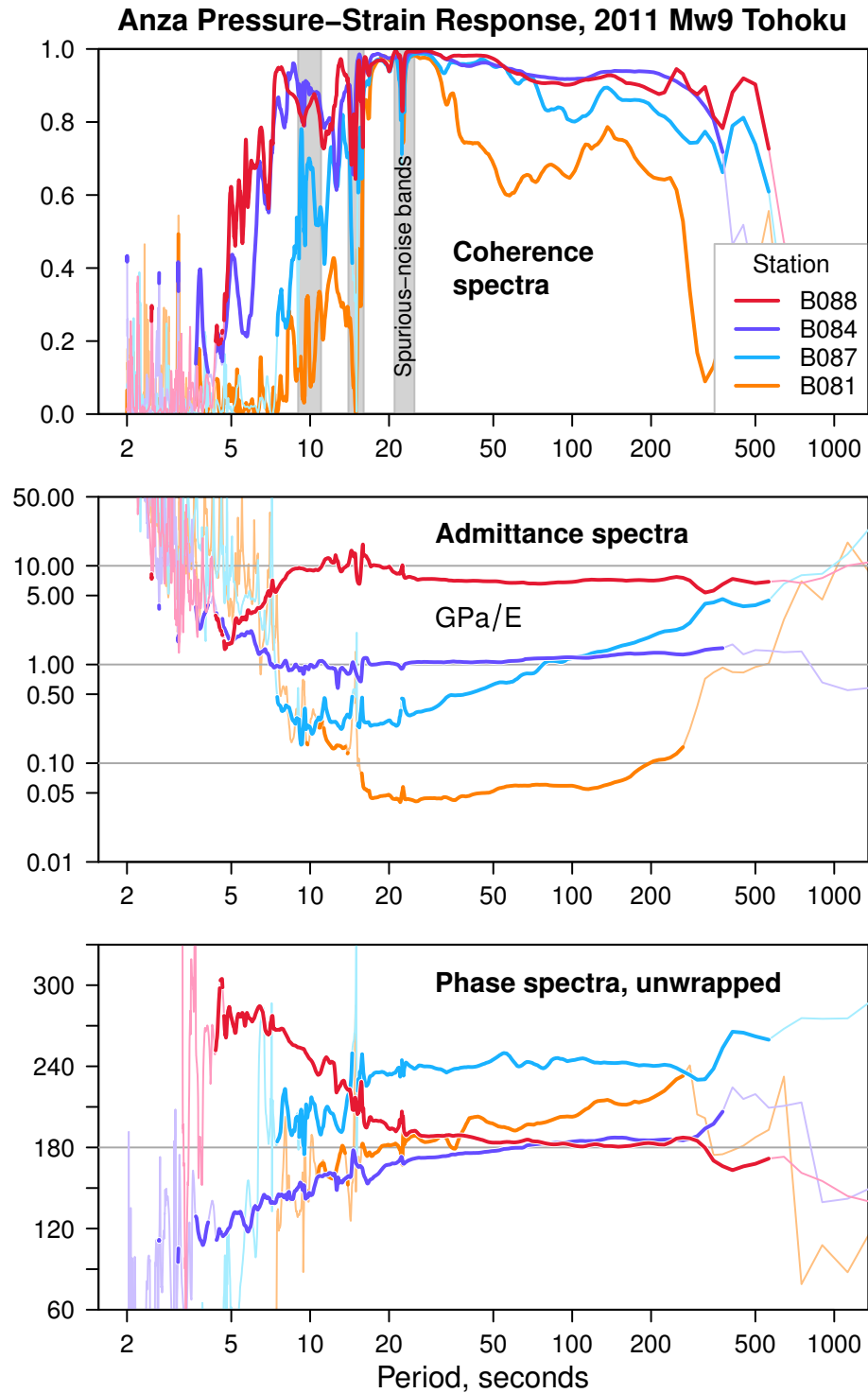


Figure 6.6: Cross-spectral density analysis for the Tohoku-Oki earthquake.

Table 6.3: Elastic moduli from pore pressure response to Tohoku-Oki as a function of Skempton’s ratio B

Station	Band	Gain [†]	Elastic Moduli [‡]		
			κ_u	μ	
	[s]	[GPa ϵ^{-1}]		[GPa]	[GPa]
B081	17–26	0.044 (0.003)	$B = 0.1$	0.664	0.398
			0.3	0.221	0.133
			0.5	0.133	0.080
			0.7	0.095	0.057
			0.9	0.074	0.044
B087	16–73	0.373 (0.025)	$B = 0.1$	5.59	3.35
			0.3	1.86	1.12
			0.5	1.12	0.67
			0.7	0.80	0.48
			0.9	0.62	0.37
B084	8–265	1.019 (0.006)	$B = 0.1$	15.3	9.2
			0.3	5.1	3.1
			0.5	3.1	1.8
			0.7	2.2	1.3
			0.9	1.7	1.0
B088	7–500	7.750 (0.010)	$B = 0.1$	116	70
			0.3	39	23
			0.5	23	14
			0.7	17	10
			0.9	13	8

[†] Estimate and standard error (below, in parenthesis) in stable frequency band (‘Band’)

[‡] Calculated for $\nu_u = 0.25$

6.5.1 Tidal Response

The areal strain sensitivity of an aquifer to solid earth tides is equivalent to Equation (6.5) (*Rojstaczer and Agnew, 1989*), and can be related to the volume of water released from (or taken into) an aquifer for a unit reduction in head – the specific storage (*Bredehoeft, 1967; Hsieh et al., 1988*) S_s :

$$S_s \equiv \rho g(\beta + \phi\beta_f) \quad (6.20)$$

$$= -\frac{\Delta}{h} \quad (6.21)$$

$$= \rho g \frac{\Delta}{p} \quad (6.22)$$

where Δ is the volumetric strain, β is the bulk compressibility (subscript f for fluid), and ϕ is the porosity. Assuming Equation (6.4) applies, we can rearrange terms and express the pressure response to areal strain in terms of the compressibilities:

$$\frac{p}{E_{11} + E_{22}} = \frac{\rho g}{S_s} \frac{1 - \nu_u}{1 - 2\nu_u} \quad (6.23)$$

$$= \frac{1 - \nu_u}{(1 - 2\nu_u)(\beta + \phi\beta_f)} \quad (6.24)$$

which reduces further assuming $\nu_u = 0.25$:

$$\frac{p}{E_{11} + E_{22}} = \frac{3}{2(\beta + \phi\beta_f)} \quad (6.25)$$

We analyzed pore pressure data at tidal frequencies for stations B082 and B084 from 2007:109 to 2011:299, estimating the amplitude and phase of the primary tidal constituents (M2 and O1). We also calculated the predicted areal strain from a solid earth model, with corrections for ocean loading (*Agnew, 1997*). Appendix 6.7 shows the tidal amplitudes and phases in the pore pressure relative to the solid-earth tidal potential as a function of time. Figure 6.7 shows the strain and pressure tidal amplitudes, as well as estimates of the left side of Equation (6.25). We find values of $4.5 \pm 1.3 \text{ GPa } \epsilon^{-1}$ and $12.5 \pm 0.3 \text{ GPa } \epsilon^{-1}$ for B082 and B084, respectively. Based on our interpretation of P -wave velocities logged during the instrument installations, the median rock porosities (*Brocher, 2005*) at B082

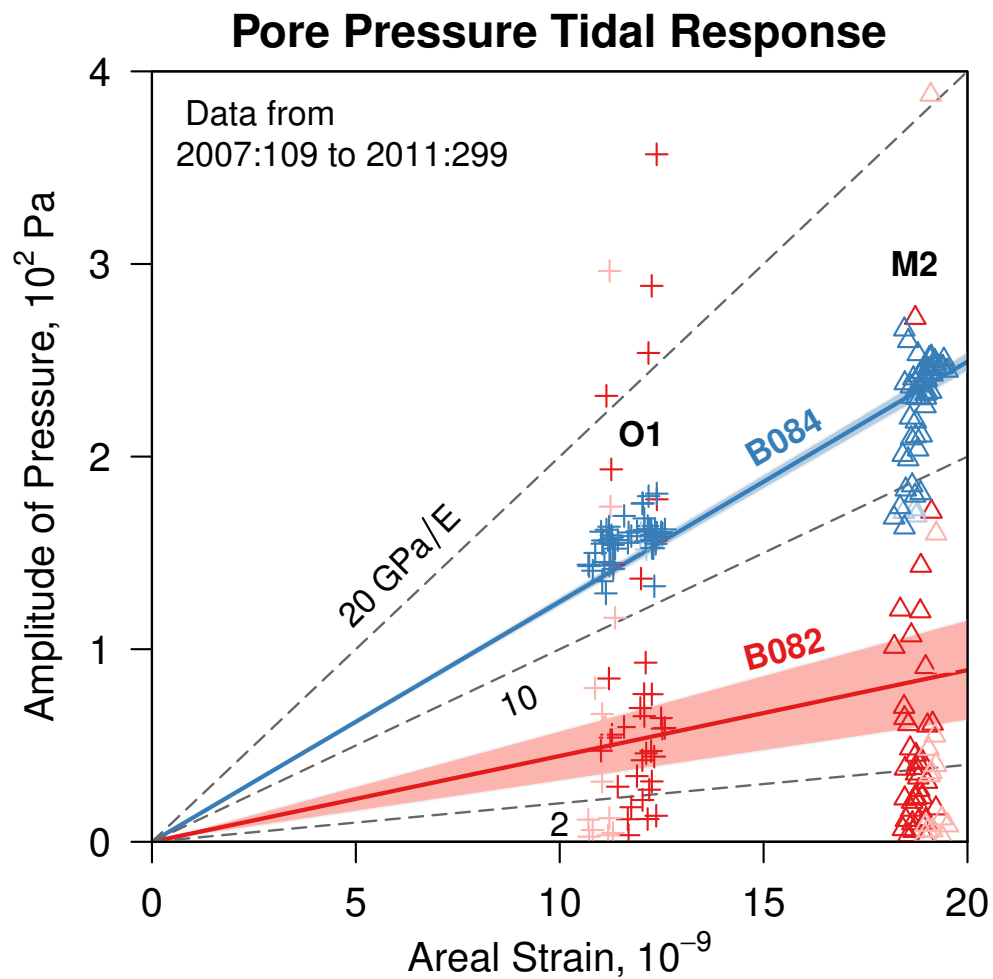


Figure 6.7: Pore pressure tidal response at B082 and B084 in Anza. Filled region are confidence intervals for a linear regression tied to zero. Selected contours of constant modulus ($\text{GPa } \epsilon^{-1}$) are shown as dashed lines. Data points with muted colors are determined to be inaccurate or spurious.

and B084 are 0.16 and 0.09, respectively (see Figure 6.8). Using these porosities in Equation (6.25), with an assumed fluid compressibility of $4.4 \times 10^{-10} \text{ Pa}^{-1}$ gives bulk modulus estimates of 3.8 GPa and 12.4 GPa, which are comparable to the seismic-based estimates. Converting these estimates back to specific storage

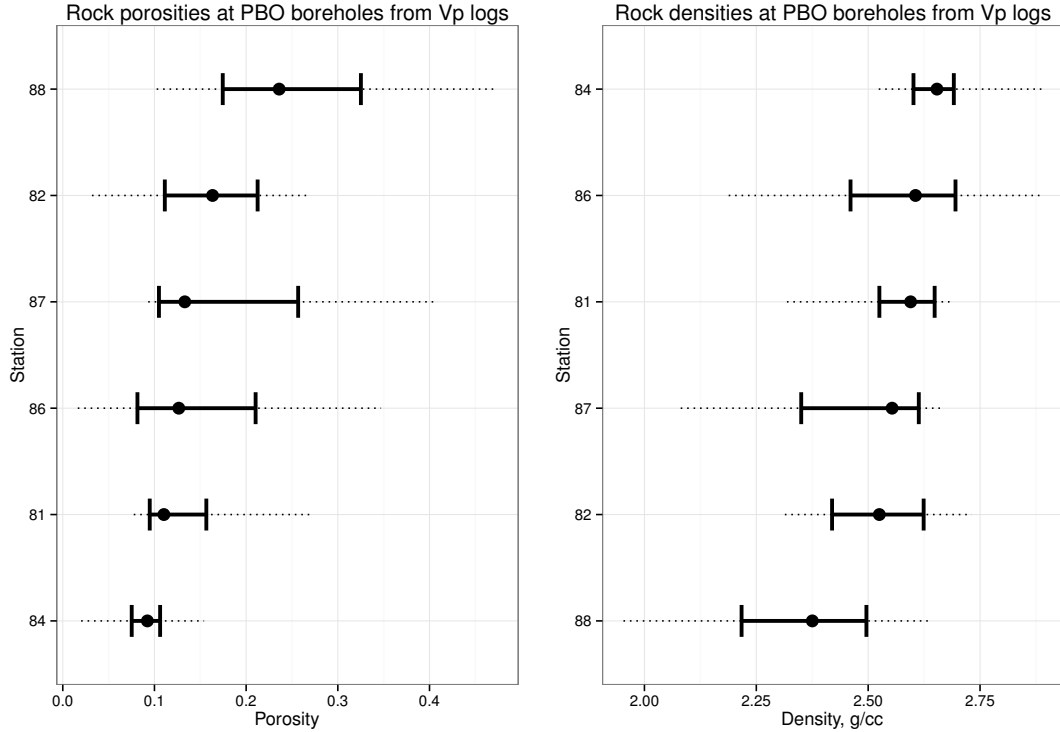


Figure 6.8: Rock porosities (left) and densities (right) at Anza PBO stations, estimated from V_P logging data using the relations given in *Brocher* (2005). The median value (dot) is shown along with the interquartile range (thick line), and the full range (dotted line). The order in each figure is based on the median.

yields values of $1.2 \times 10^{-6} \text{ m}^{-1}$ and $3.3 \times 10^{-6} \text{ m}^{-1}$, respectively. Considering how S_s relates to hydraulic diffusivity D (*Roeloffs*, 1996),

$$D = \frac{C}{S_s} = \frac{T}{S} \quad (6.26)$$

where C is the hydraulic conductivity, T is transmissivity, and S is storativity; the difference in values could equate to a factor of nearly two enhancement in the pore-fluid diffusion parameter, all things remaining equal.

It remains of interest whether the transmissivity – an aquifer’s capacity to transmit fluids horizontally – can be reasonably estimated. *Hsieh et al.* (1987)

gives a method to convert tidal phase shifts into transmissivity; using M2 phase shifts and known well-dimensions, we estimate transmissivities to be 2.6×10^{-7} to $1.3 \times 10^{-6} \text{ m}^2 \text{ s}^{-1}$ for B082, and 5.2×10^{-6} to $1.3 \times 10^{-5} \text{ m}^2 \text{ s}^{-1}$ for B084. It follows that horizontal fluid flux is favored at B082 more so than at B084.

6.5.2 Hydraulic Properties from Radial-flow Models

Standard models for well-response to harmonic waves are based on homogeneous, isotropic flow-model. In such a model the waves induce strain in a confined aquifer (one having aquitards above and below it), and fluid flows radially (horizontally) into, and out of a well penetrating the aquifer. The flow-induced drawdown, s , is governed by the following partial differential equation, expressed in radial coordinates (r):

$$\frac{\partial^2 s}{\partial r^2} + \frac{1}{r} \frac{\partial s}{\partial r} - \frac{S}{T} \frac{\partial s}{\partial t} = 0 \quad (6.27)$$

Solving the partial differential equation with periodic discharge boundary conditions gives the amplitude and phase response we are interested in. The solution for seismic waves and an open well was first presented by *Cooper et al.* (1965), and subsequently modified by *Rojstaczer* (1988a) and *Liu et al.* (1989). Later, *Kitagawa et al.* (2011) adapted the solution by *Hsieh et al.* (1987) to a sealed well. Appendix 6.8 compiles these solutions under a unified notation.

These models are generally applicable to quasistatic aquifer-scale processes (e.g., traveling Rayleigh waves, or changes in the Earth's tidal potential). In practice, however, we are unable to adequately (and repeatedly) fit radial flow models to the empirical transfer functions for the Tohoku-Oki earthquake using standard non-linear inversion techniques. The most likely reason for this is the existence of numerous dipping fractures which intersect the borehole axis (Figure 6.9) which tend to alter the frequency structure of the transfer function significantly (c.f., *Bower*, 1983; *Hsieh et al.*, 1987); and, because the models are highly-nonlinear, we rarely find stable convergence. If hydraulically conductive fractures are responsible for the poor fits to radial flow models, the assumption of horizontal fluid flow is clearly violated and the transmissivity estimates would be invalid: models would thus need to incorporate fracture permeability anisotropic permeability; but, such

a complication would require numerical analysis, which is beyond the scope of this work.

6.5.3 Fault-normal Variation in Response

One of the most striking feature of our results is the apparent dependency on fault-normal distance: within 5 km of the fault stations show a distinct reduction in response in relation to stations outside that zone. Figure 6.10 shows the spatial patterns of the best-fitting coefficients from Equation 6.7, as seen in Figure 6.5: the intercept, $\log c$ (relative to a pressure of 10^8 Pa), and the unitless strain exponent, d . (See Appendix 6.9 for the spatial pattern of calibration coefficients.) Based on the observed pattern, it is reasonable to suspect that the reduction is strongly linked to the San Jacinto fault system, which is highly active tectonically.

The dominant crustal deformation mechanism in this region is a result of the San Jacinto fault accommodating a large proportion of the relative plate motion between the North American and Pacific plates in southern California (e.g., *Sharp, 1967; Fialko, 2006; Lindsey and Fialko, 2013*). Recent work by *Lindsey et al. (2013)* provides SJF-parallel (1-axis) surface velocities derived through a combined analysis of ERS-InSAR and GPS data, which we denote $2\dot{u}_1$. Taking the spatial derivative of this velocity in the fault-normal direction (2-axis) gives a reasonable estimation of the engineering shear strain rate, defined as twice the tensor shear strain rate: $\dot{\gamma} \equiv 2\dot{E}_{12}$. In order to extract the regional trend apparent in the velocity data, we use locally weighted regression (*Cleveland and Devlin, 1988*), with a windowing fraction of 0.2; standard errors of the smoothed profile are readily calculated. Figure 6.11 shows the results, with a prediction of strain rate based on a homogeneous dislocation model assuming typical locking depths and far-field velocities for the three major faults in the region: the Elsinore, San Jacinto, and San Andreas.

Comparing the response coefficients with the estimates of crustal shear strain reveals a strong power-law relationship where increasing strain-rate predicts decreasing pore pressure response. Figure 6.12 compares the response coefficients

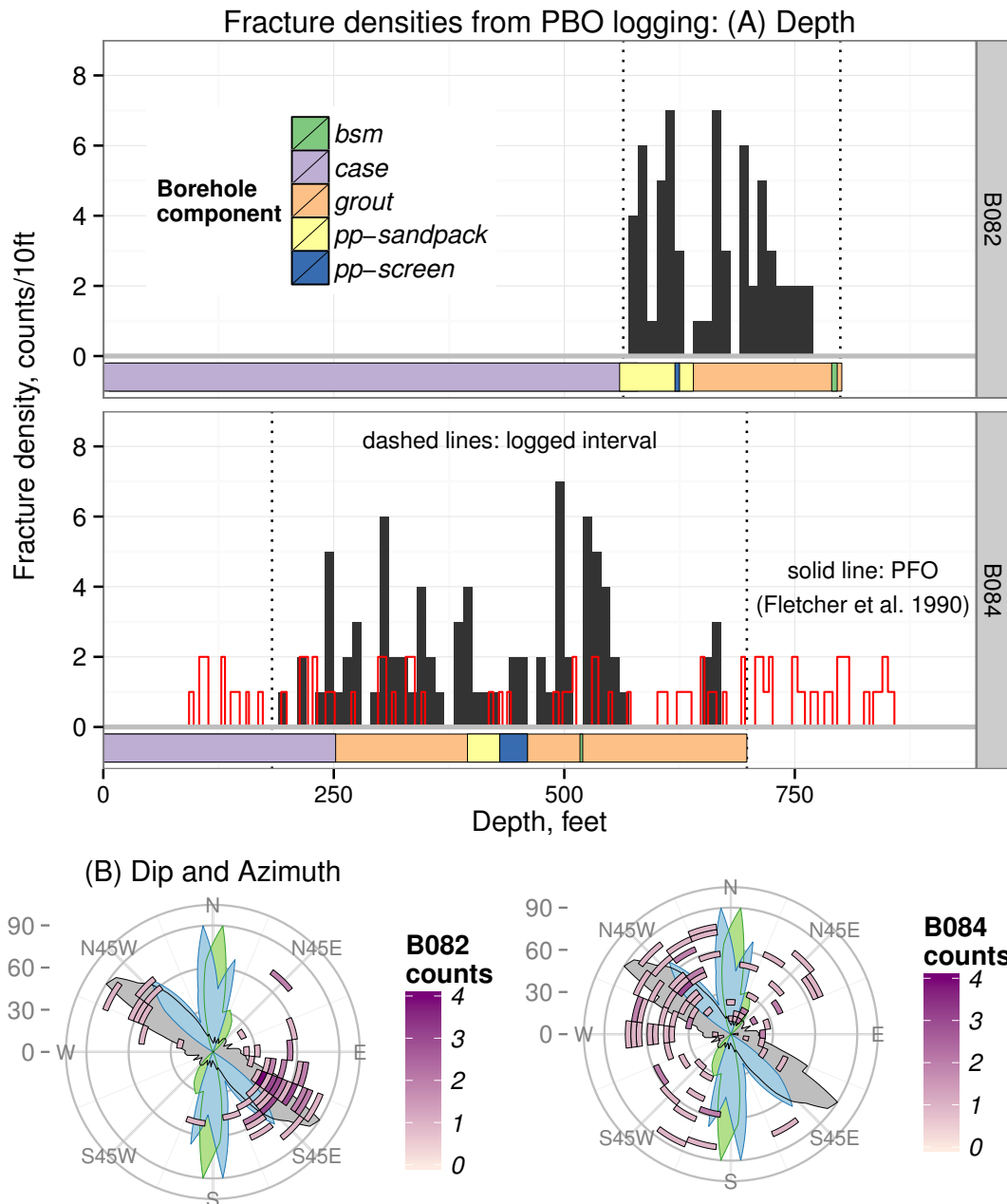


Figure 6.9: Borehole-intersecting fractures identified from acoustic-televviewer images for B082 and B084. In (A) fracture counts per 10 feet of depth within the logged interval, alongside approximate locations the of borehole instruments; For B084 the interpretations of *Fletcher et al.* (1990) are shown. In (B) fracture counts by dip and strike, with polar histograms of SJF fault-strike (grey), θ_{SH} from the World Stress Map (green), and shear-wave fast-axes (blue) from *Yang et al.* (2011).

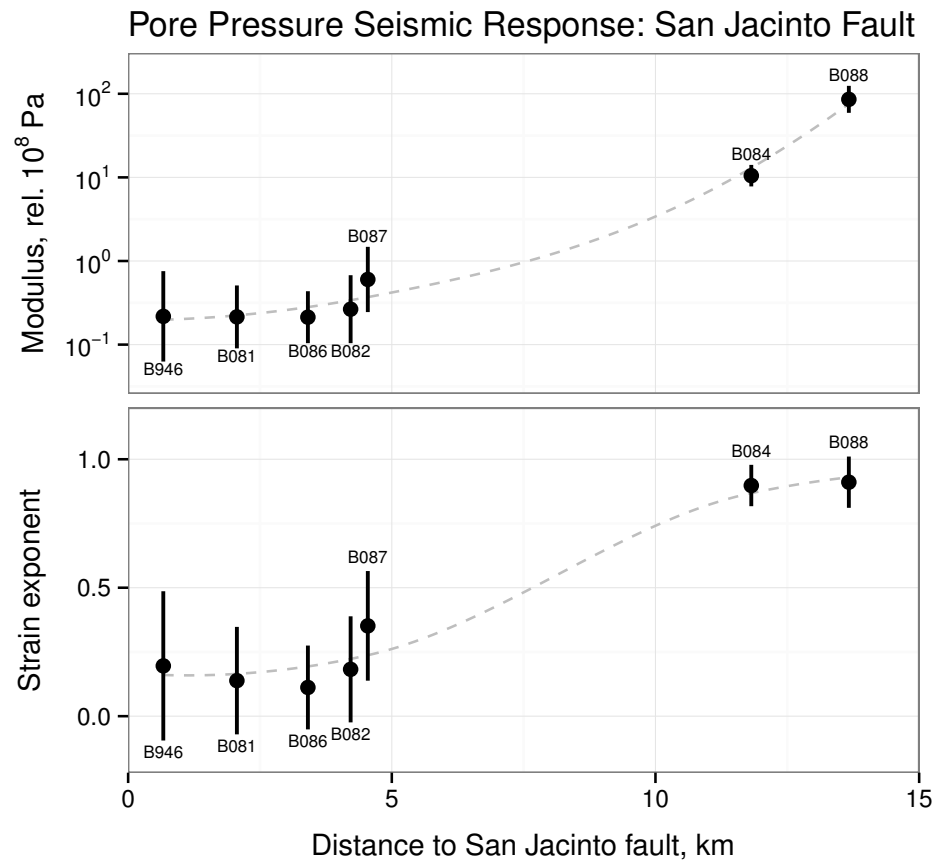


Figure 6.10: Fault-normal variation in pore pressure response coefficients based on the regression model in Equation 6.7. Top: intercept coefficients ($\log c$) relative to 10^8 Pa. Bottom: scaling coefficients (d). Smoothed profiles are shown as dashed lines, for visual guidance.

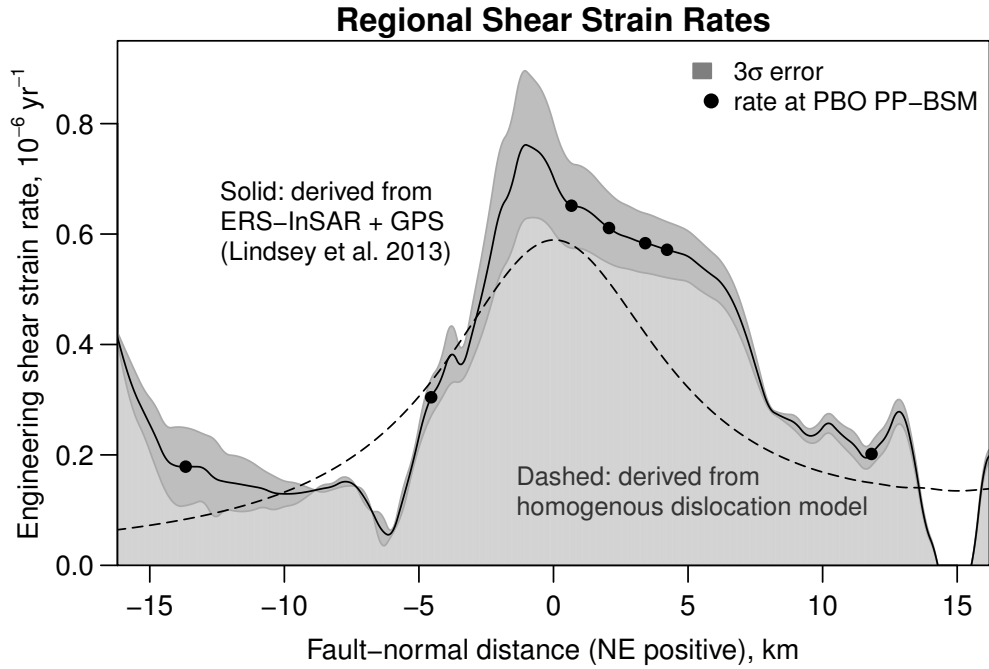


Figure 6.11: San Jacinto fault-normal variation in engineering shear strain rates, derived from regional fault-parallel surface velocities from *Lindsey et al. (2013)*.

with a new quantity, namely the ‘interseismic strain slowness’:

$$\xi = \frac{1}{\dot{E}_{12}} \quad (6.28)$$

Equation (6.28) can be thought of as the amount of time needed to accumulate a single unit of pure shear strain; typical values for the San Jacinto fault range from 1 to 7 Myr ϵ^{-1} . Infinitesimally small pore pressure responses are expected as ξ approaches zero (high strain rates): excess pore pressure will be difficult to maintain in fractured rock, on timescales greater than the characteristic fluid-diffusion time, $C(\lambda/2)^2/S_s$, where λ is the characteristic aperture of the fluid-pathway.

Figure 6.12a shows the effective poroelastic modulus (intercept coefficients) plotted against ξ . We tested a number of functional power-law models and find that one based on the Pareto distribution provides a robust fit to the data (shown with confidence intervals in the figure). Below a threshold slowness ξ_u , the coefficient is

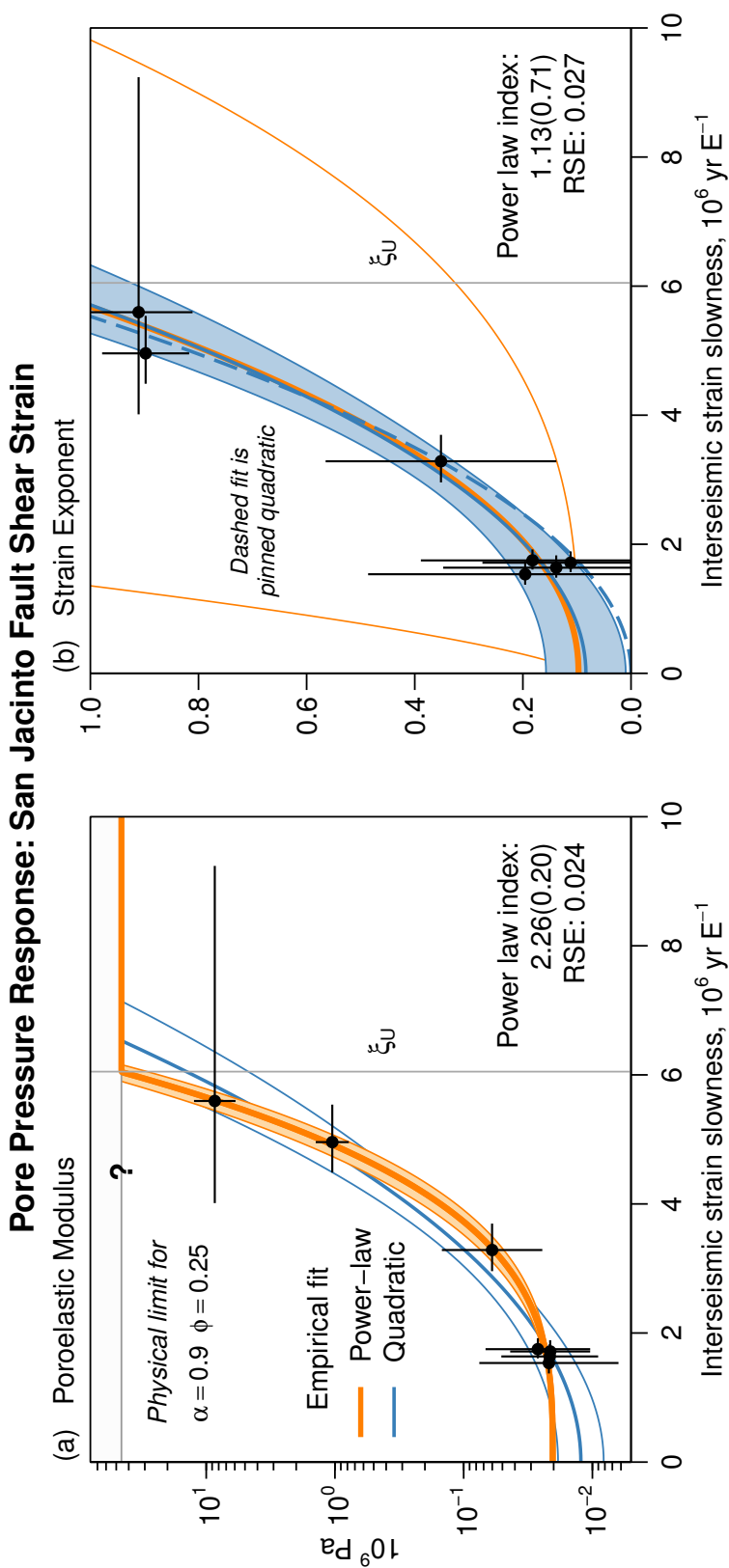


Figure 6.12: Power-law dependency of pore pressure response to crustal shear-strain slowness (ξ). In (A): the effective poroelastic modulus (intercept coefficients) fit by an empirical power-law, and a second-order polynomial; the power law gives the strongest fit. The upper limit is related to intrinsic rock properties, and the value shown corresponds to a reasonable upper bound expected for deep crustal rock in California (see text). In (B): the strain exponent (scaling coefficients) fit with a power-law and quadratic functions; the general quadratic function gives the strongest fit.

well-described by three empirical parameters:

$$\log c(\xi) = \begin{cases} \delta c_1 + m^{-1} \hat{\xi}^{-m} \xi^{m+1}, & \xi < \xi_u \\ \log B \kappa_u, & \xi \geq \xi_u \end{cases} \quad (6.29)$$

where δc_1 is the shift parameter, m is the scale parameter (or power-law index), and $\hat{\xi}$ is the shape parameter. The difference $\hat{\xi} - \xi_u$ may reflect uncertainties in the slowness estimates, which are proportionally larger for increasingly-small shear strain rates. Above ξ_u the model follows the undrained response, $B \kappa_u$, where the Skempton's ratio B is defined as (*Rojstaczer and Agnew, 1989*)

$$B = \frac{\beta - \beta_u}{(\beta - \beta_u) + \phi(\beta_f - \beta_u)}, \quad (6.30)$$

and the κ_u is undrained bulk modulus. The β_f, β_u , and β terms are compressibilities of the pore-fluid (0.44 GPa^{-1} for water), the solid matrix ($\equiv \kappa_u^{-1}$), and the fluid-saturated matrix. The bulk modulus will vary spatially, but seismic velocities of Californian crustal rock give an upper bound of $\approx 100 \text{ GPa}$ (*Brocher, 2005*). Since B is difficult to predict *in situ*, we assume a value of 0.9 for effective stress coefficient

$$\alpha = 1 - \beta_u/\beta \quad (6.31)$$

and a porosity $\phi = 0.25$, which gives a rather conservative lower bound on $B \kappa_u$ of 46 GPa (corresponding to $\xi_u = 6.1 \text{ Myr } \epsilon^{-1}$); the true limit is likely higher because the effective stress tends to be higher, and porosity can be much lower.

Figure 6.12b shows the strain exponents (slope coefficients) plotted against ξ . With these data the power-law model fits arguably well, but has a large standard error associated with the power-law index. Although the pinned second-order polynomial model makes more intuitive sense (zero strain at zero slowness), the non-pinned model fits the coefficients with greater statistical rigor, and has smaller standard errors in the parameters. Using this model the coefficients are well-described by two empirical parameters:

$$d(\xi) = \begin{cases} \delta c_2 + n \xi^2, & \xi < \xi_u \\ 1, & \xi \geq \xi_u \end{cases} \quad (6.32)$$

where δc_2 is a shift parameter, similar to Equation (6.29). It is interesting to note how similar the non-pinned polynomial model is to the power-law model (compare this with Figure 6.12a).

Combining Equation (6.7), the regression model, with Equation (6.29) and Equation (6.32), the empirical models, gives a general expression relating the expected pore pressure response to dynamic strain e and interseismic strain slowness (the inverse of crustal shear strain in a fault-parallel coordinate system):

$$\log_{10} p = \begin{cases} \delta c_1 + m^{-1} \hat{\xi}^{-m} \xi^{m+1} + (\delta c_2 + n \xi^2) \log_{10} e, & \xi < \xi_u \\ B \kappa_u + \log_{10} e, & \xi \geq \xi_u \end{cases} \quad (6.33)$$

where p is in units of 10^2 Pa, ξ parameters are in units of $10^6 \text{ yr } \epsilon^{-1}$, and e is in units of $10^{-6} \epsilon$. Parameters can be obtained from Table 6.4, where estimates and goodness-of-fit values are from weighted non-linear least squares (for power-law fits) and weighted linear least squares (for quadratic fits). Plugging the best-fitting estimates and standard errors into Equation (6.33) gives

$$\log_{10} p = -0.69 + 0.0095 \xi^{3.26} + (0.08 + 0.028 \xi^2) \log_{10} e \quad (6.34)$$

for $\xi < \xi_u$, with errors propagating as

$$\log_{10} p = 0.03 + 6.77 \xi^{0.20} + (0.03 + 0.002 \xi^2) \log_{10} e \quad (6.35)$$

Table 6.4: Parameter estimates of pore pressure response as a function of interseismic strain slowness, for Equation (6.33).

Model		Estimates [†]			
		Quadratic n	Shift $\delta c_{1,2}$	Shape $\hat{\xi}$	Scale m
<i>Poroelastic Modulus</i>					
Power-law [‡] (★)	Estimate		-0.69	5.47	2.26
	Std. Error		0.03	0.22	0.20
	$RSE = 0.024$	t -value	-27	25	11
		$p(> t)$	< 0.01	< 0.01	< 0.01
Quadratic	Estimate	0.08	-0.91		
	Std. Error	0.01	0.07		
	$RSE = 0.080$	t -value	14	-13	
	$R^2 = 0.97$	$p(> t)$	< 0.01	< 0.01	
<i>Strain Exponent</i>					
Power-law [‡]	Estimate		0.097	25.7	1.13
	Std. Error		0.074	37.9	0.71
	$RSE = 0.027$	t -value	1.3	0.7	1.6
		$p(> t)$	0.26	0.54	0.18
Pinned Quadratic	Estimate	0.0327			
	Std. Error	0.0028			
	$RSE = 0.037$	t -value	12		
	$R^2 = 0.96$	$p(> t)$	< 0.01		
Quadratic (★)	Estimate	0.0281	0.08		
	Std. Error	0.0024	0.03		
	$RSE = 0.024$	t -value	12	3	
	$R^2 = 0.96$	$p(> t)$	< 0.01	0.03	

Modulus estimates are based on pressure units of [10^8 Pa], and strain slownesses are in units of [$1 \text{ Myr } \epsilon^{-1}$]

[†] Based on the coefficients of Equation (6.7)

[‡] Based on weighted non-linear least squares and Equation (6.29)

(★) Preferred functional form

The power-law dependence with strain rate may be controlled by the density of hydraulically-conductive fractures in the crust. There is substantial evidence that, in general, fracture networks are scale invariant (*Hirata et al.*, 1987; *Bonnet et al.*, 2001), and the effective spatial distribution around major strike slip systems appears to be a superposition of fracture networks from individual fault strands (*Savage and Brodsky*, 2011). The effect we observe is likely a combination of enhancements to hydraulic conductivity and reductions in specific storage (see Equation (6.20)). It follows that hydraulic diffusivity (see Equation (6.26)) and thus permeability ($\propto C$) are also enhanced.

The observed spatial variation in pore pressure response is explained very well by a composite empirical model (Equation (6.34)); but, this model is only loosely tied to physics of fluid-flow in fractured rock. In fact, very little is known about the spatial distribution of pore pressure response around major strike slip fault systems (*Wibberley et al.*, 2008; *Faulkner et al.*, 2010; *Bense et al.*, 2013). We may gain some insight into appropriate values of the arbitrary upper limit of response, imposed by the model, by considering observations from deep boreholes in intraplate rock: fluid flow occurs primarily within fractures in a critically stressed state (*Barton et al.*, 1995; *Townend and Zoback*, 2000), even though strain rates are extremely low (high strain slowness). An asymptotically large pore pressure response (as an unbounded power law would predict) can be expected to induce failure on preexisting faults, and even hydraulic fracturing; but, this is not commonly observed outside of regions of sustained fluid-injection (e.g., *Ellsworth*, 2013; *van der Elst et al.*, 2013). In accordance with Mohr-Coulomb failure theory, the response is likely limited to the upper bound of yield strength for deep crustal rock, on the order of 50 GPa to 100 GPa.

Despite these restrictions the power-law model remains testable. It is of great interest whether other strike-slip faults demonstrate the same behavior. For example, an interesting comparison would be with the southern-most segment of the San Andreas fault (sSAF): seismicity rates on the SJF are significantly higher than on the sSAF (*Lin et al.*, 2007); cumulative displacements on the sSAF are nearly an order of magnitude greater (*Dickinson*, 1996), which predicts less

structural complexity (*Brodsky et al.*, 2011) than the SJF; and shallow creep is nearly ubiquitous along the sSAF (*King et al.*, 1977; *Lindsey and Fialko*, 2013; *Wei et al.*, 2013) in contrast to the apparent lack of creep along the SJF (*Lindsey et al.*, 2013). All of this suggests that there may be some additional dependence of the pore pressure response on the level of fault maturity (cumulative displacement) which, if true, would have important implications for general understanding of the earthquake cycle on major strike-slip faults.

6.6 Conclusions

We have analyzed concurrent teleseismic records of colocated pore pressure and strain at PBO borehole stations on either side of the San Jacinto fault in southern California, finding that in all cases peak dynamic pore pressure scales with peak dynamic strain. We observe a strong dependence between the size of the response at each station and the crustal strain-rate there, which is dominated by effects associated with interseismic strain accumulation on the fault. The relationship between strain-rate and pore pressure response appears to follow an inverse power law where high strain rates predict substantially reduced response coefficients. The earthquake cycle of strain accumulation and release has apparently created a ± 5 km zone around the fault where shallow rock has enhanced permeability and compliance associated with scale invariant damage features. It remains of great interest whether the power-law relationship holds for other maturing strike-slip fault systems with high interseismic strain accumulation.

6.7 Appendix A: Time Varying Tidal Responses

In this Appendix we present timeseries of the tidal response at pore pressure stations in Anza (Figures (6.13)-(6.17)) In all figures the top frame gives amplitudes of the principal tidal constituents (O1, blue squares; M2, red circles), relative to the predicted strains in a homogeneous earth; a reference value of $10^6 \text{ m } \epsilon^{-1}$ (where $10^{-9} \epsilon$ produces a 1 mm change in water height) is shown with a dashed line. The

bottom frames show the phase of the pore pressure tide relative to the strain tide; negative values indicate a lag in pressure. Estimates are based on a 30-day non-overlapping window.

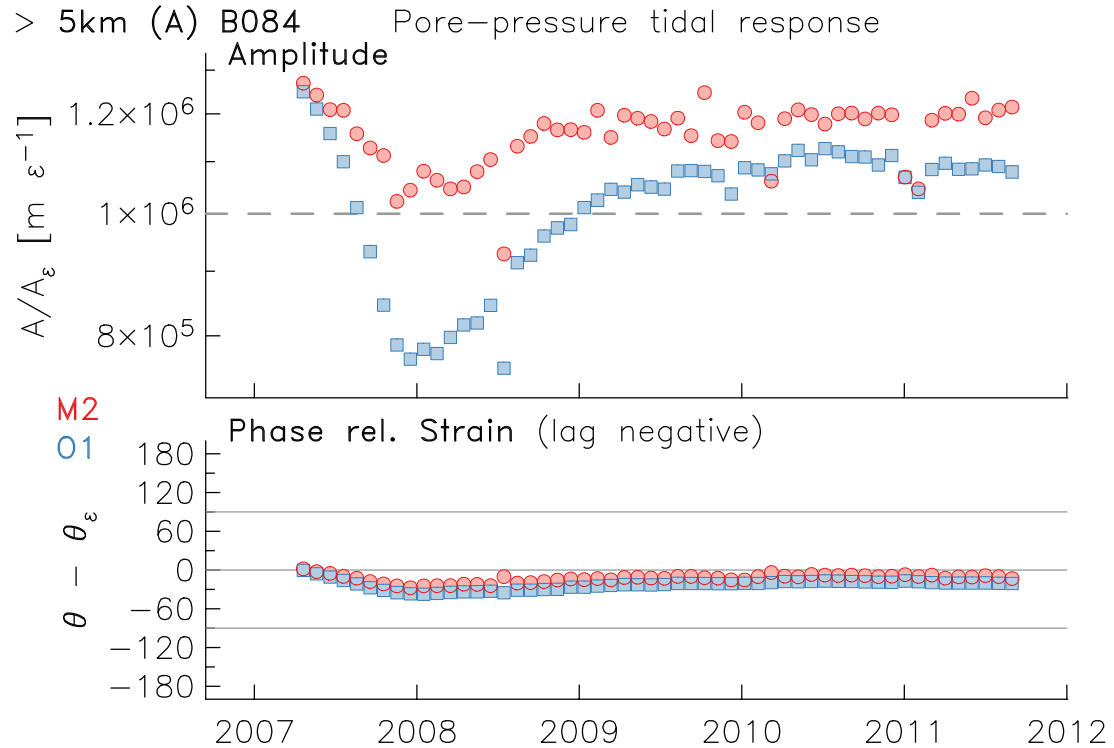


Figure 6.13: Comparison of the time-varying pore pressure tidal response at B084, in Anza, located greater than 5 km from the SJF. Top: amplitudes at the dominant tidal-frequencies (O1,M2), relative to the predicted strains in a homogeneous earth; a reference value of $10^6 \text{ m } \epsilon^{-1}$ (where $10^{-9} \epsilon$ produces a 1 mm change in water height) is shown with a dashed line. Bottom: phases of the pore pressure tides relative to the strain tides; negative values indicate a pressure lag. Estimates are based on a 30-day non-overlapping window.

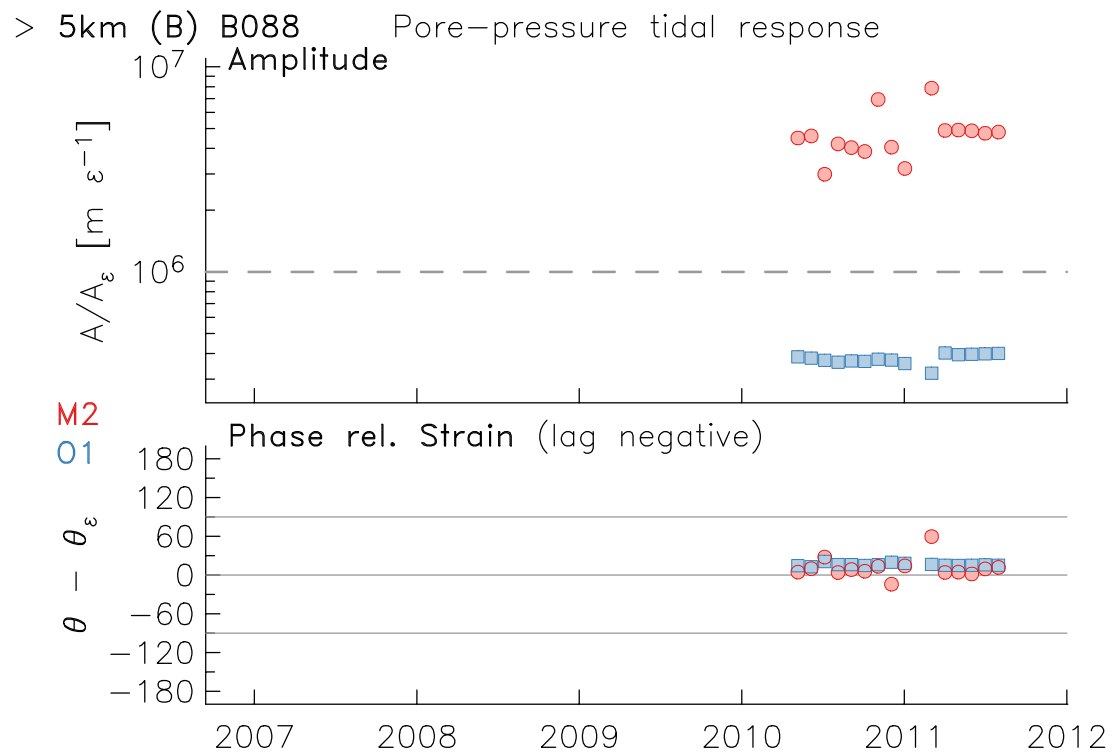


Figure 6.14: Comparison of the time-varying pore pressure tidal response at B088, comparable to Figure 6.13.

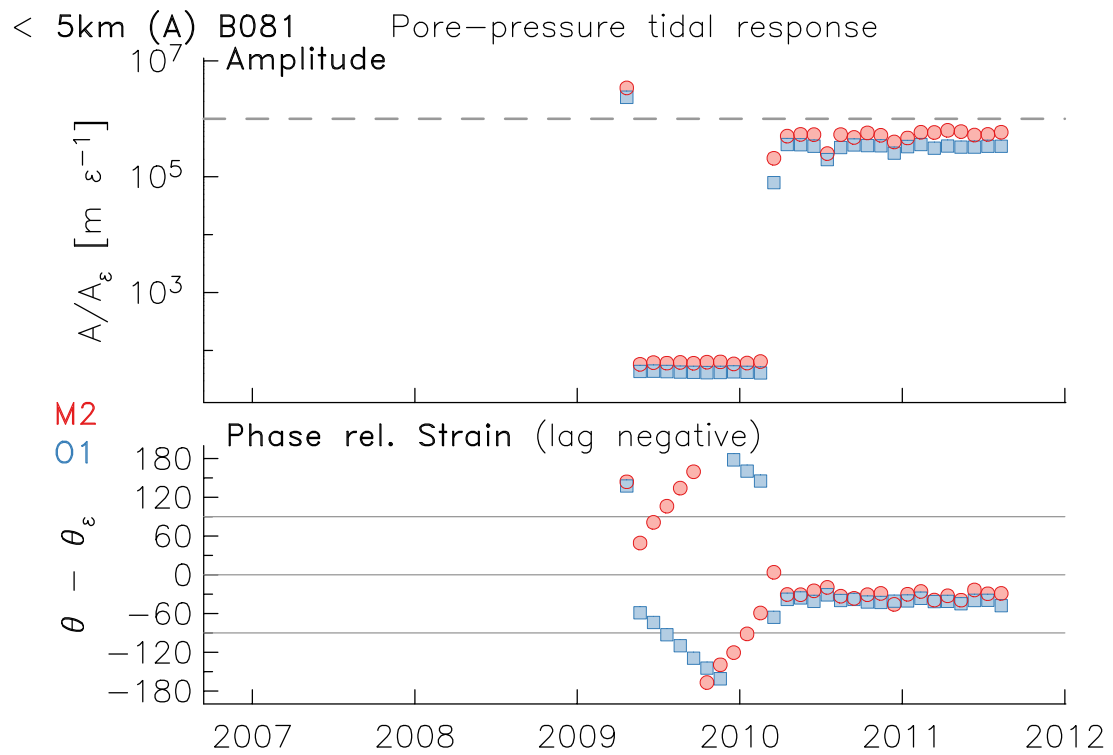


Figure 6.15: Comparison of the time-varying tidal response at B081, comparable to Figure 6.13. The rapid change in response is associated with an instrumental problem.

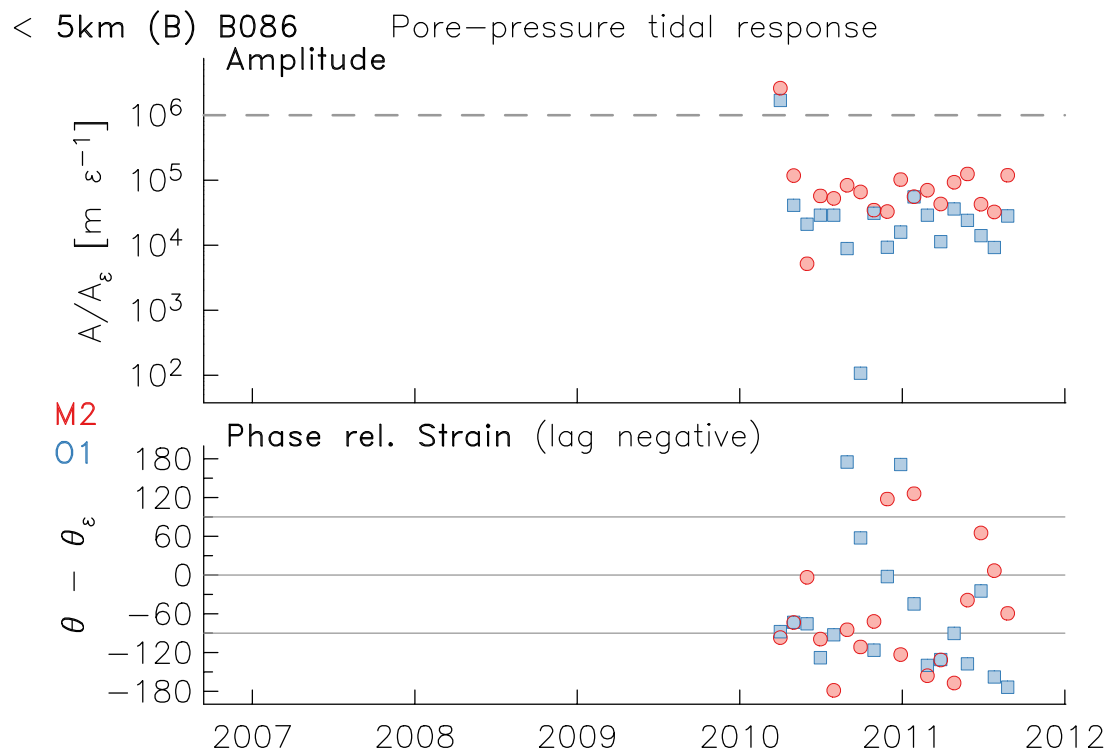


Figure 6.16: Comparison of the time-varying tidal response at B086, comparable to Figure 6.13.

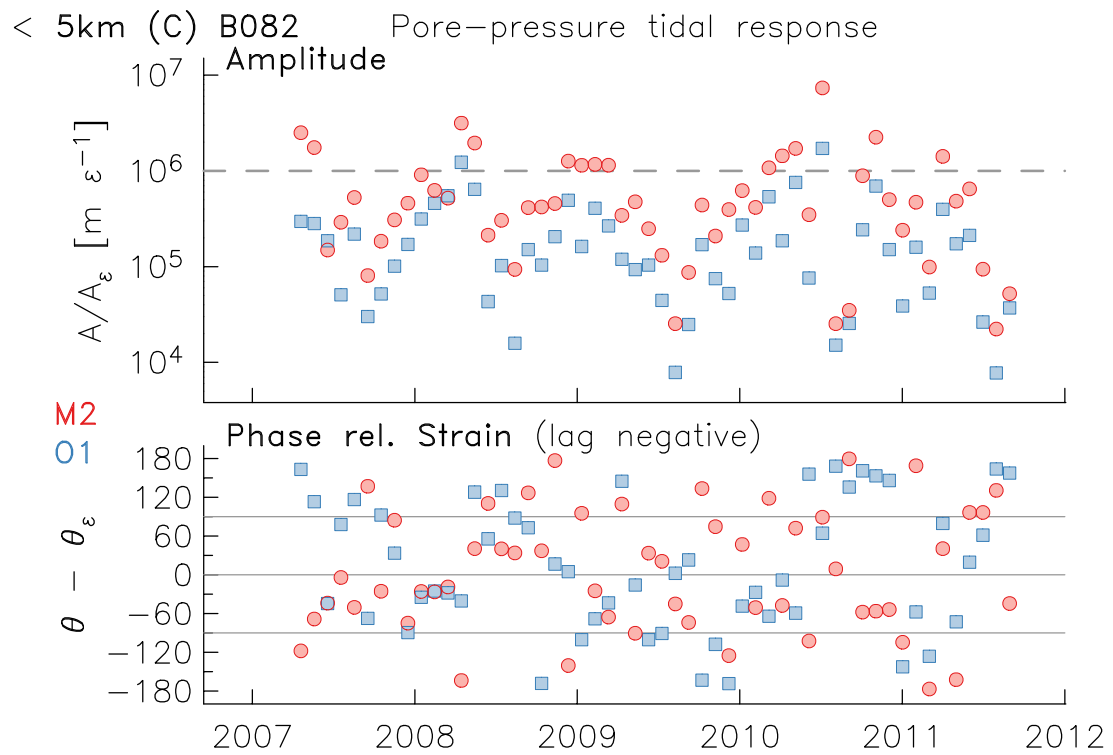


Figure 6.17: Comparison of the time-varying tidal response at B082, comparable to Figure 6.13. The highly variable nature of the estimates is linked to short episodes of water-well pumping, which happens frequently at this location.

6.8 Appendix B: Radial Flow Models of Harmonic Well Response

In this Appendix we give expressions for the response of water wells to harmonic forcing (e.g., long-period seismic waves, and tides). The complex response Z is given, which means the amplitude response is simply the modulus of Z ($\equiv \sqrt{A_x^2 + B_x^2}$ where the subscript x indicates the model) and the phase response is the argument of Z ($\equiv \tan^{-1} B_x/A_x$). For clarity and consistency, the response coefficients are expressed using a unified notation.

6.8.1 Water Heights from Pressure Head

Cooper et al. (1965) was first to derive the expression water-heights associated with ground displacements from seismic waves ($Z = H/z$), namely those producing harmonic pressure head perturbations:

$$A_c = 1 - \text{Kei}_\alpha R - \omega^2 H_e/g \quad (6.36)$$

$$B_c = \text{Ker}_\alpha R \quad (6.37)$$

where

$$R = r_c^2 \omega / 2T \quad (6.38)$$

$$\text{Kei}_\alpha = \text{Kei}_0(\alpha_w) \quad (6.39)$$

$$\text{Ker}_\alpha = \text{Ker}_0(\alpha_w) \quad (6.40)$$

$$\alpha_w = r_c \sqrt{\omega S/T} \quad (6.41)$$

$$H_e = H_w + 3d/8 \quad (6.42)$$

Hsieh et al. (1987) derived a similar model, but made additional assumptions which tailored the expressions to signals at tidal frequencies (again, $Z = H/z$):

$$A_h = 1 - RU_1 \quad (6.43)$$

$$B_h = -RU_2 \quad (6.44)$$

where

$$U_1 = \Psi \text{Ker}_\alpha + \Phi \text{Kei}_\alpha \quad (6.45)$$

$$U_2 = \Phi \text{Ker}_\alpha + \Psi \text{Kei}_\alpha \quad (6.46)$$

$$\Phi = -(\text{Ker}_{1,\alpha} + \text{Kei}_{1,\alpha}) / \sqrt{2}\alpha_w (\text{Ker}_{1,\alpha}^2 + \text{Kei}_{1,\alpha}^2) \quad (6.47)$$

$$\Psi = -(\text{Ker}_{1,\alpha} - \text{Kei}_{1,\alpha}) / \sqrt{2}\alpha_w (\text{Ker}_{1,\alpha}^2 + \text{Kei}_{1,\alpha}^2) \quad (6.48)$$

$$\text{Kei}_{1,\alpha} = \text{Kei}_1(\alpha_w) \quad (6.49)$$

$$\text{Ker}_{1,\alpha} = \text{Ker}_1(\alpha_w) \quad (6.50)$$

Liu et al. (1989) improved the accuracy of the Cooper-solution for seismic waves by accounting for variation in aquifer thicknesses, and thus the effective transmissivity (again, $Z = H/z$):

$$A_l = 1 - \left[H_w + \zeta^{-1} \frac{1 - \exp(-\zeta d)}{1 + \exp(-\zeta d)} \right] \omega^2 / g \quad (6.51)$$

$$B_l = \mathcal{U} \omega r_c^2 \zeta \frac{\exp(-\zeta d)}{1 - \exp(-2\zeta d)} \quad (6.52)$$

where

$$\mathcal{U} = \mathcal{K}_\alpha d / T \quad (6.53)$$

$$\mathcal{K}_\alpha = \text{Ker}_\alpha + i \text{Kei}_\alpha \quad (6.54)$$

$$\zeta = \sqrt{2i\omega / r_c^2 \mathcal{U} g} \quad (6.55)$$

6.8.2 Pore Pressure from Strain

Kitagawa et al. (2011) adapted the *Hsieh et al.* (1987) model to describe the response of a sealed well to harmonic volumetric strains ($Z = p/\epsilon_{kk}$):

$$A_k = \frac{N [(U_1 - \kappa_u BC / A_w)(\kappa_f C - U_1) - U_3^2]}{(C\kappa_f - U_1)^2 + U_3^2} \quad (6.56)$$

$$B_k = NU_3 C (\kappa_u B / A_w - \kappa_f) \quad (6.57)$$

where

$$N = \kappa_f a_w / a_\epsilon \quad (6.58)$$

$$C = 2\pi T / \rho g \omega V_w \quad (6.59)$$

$$U_3 = \Phi \text{Ker}_\alpha - \Psi \text{Kei}_\alpha \quad (6.60)$$

$$V_w = \pi [r_c^2 (l_c - l_s) + r_s^2 l_s] \quad (6.61)$$

$$l_s \approx d \quad (6.62)$$

and B is Skempton's coefficient ($\equiv [\delta p / \delta \sigma_{kk}]_u$). The model derived by *Rojstaczer* (1988a) was derived for harmonic areal strains, and is valid for open wells ($Z = p / \epsilon_a$):

$$A_r = \rho g \left(\exp(-\sqrt{\Omega}) \cos(\sqrt{\Omega}) - 1 \right) \quad (6.63)$$

$$B_r = -\rho g \exp(\sqrt{\Omega}) \sin(\sqrt{\Omega}) \quad (6.64)$$

where

$$\Omega = z^2 \omega / 2D' \quad (6.65)$$

$$D' = \frac{k}{\mu} \left\{ \rho g \beta \gamma \left[1 - \gamma \frac{2(1-2\nu)}{3(1-\nu)} \right] + \phi (\kappa_f^{-1} - \kappa_u^{-1}) \right\}^{-1} \approx T/S \quad (6.66)$$

$$\gamma = 1 - (\kappa_u \beta)^{-1} \quad (6.67)$$

$$\beta = \frac{1 - \kappa_u B}{\kappa_u (1 - B)} [(1 + \phi) \kappa_u^{-1} + \phi \kappa_f^{-1}] \quad (6.68)$$

The expression Ω is a dimensionless frequency based on the hydraulic diffusivity D' , and the squared depth to the water table, z^2 .

Figure 6.18 compares the amplitude and phase response of the models outlined above, assuming standard values for water, well dimensions based on station B084, and poroelastic parameters $D' = 0.2 \text{ m}^2 \text{ s}^{-1}$, $\kappa_u = 15 \text{ GPa}$, $B = 0.25$. In practice we have found that robust parameter estimates are difficult to obtain through gradient-based non-linear inverse methods: the response is highly non-linear in parameter space, and convergence is rarely obtained. The Simulated Annealing or Simplex method may be better suited for parameter estimation, or even brute-force grid-search.

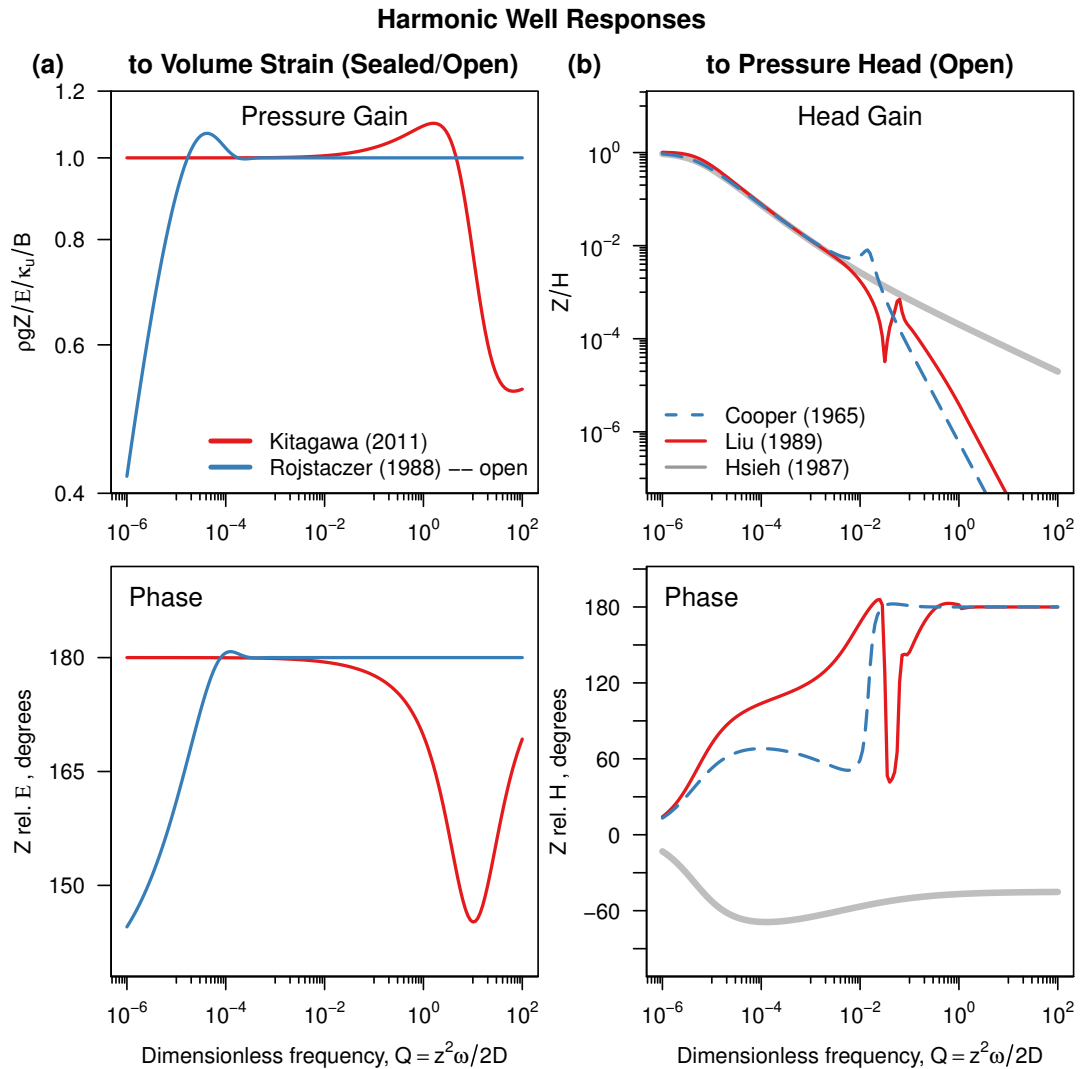


Figure 6.18: Amplitude and phase response of water wells to (a) harmonic volumetric strains, and (b) harmonic pressure head fluctuations, as a function of dimensionless frequency. The amplitude response in (a) is normalized to $B\kappa_w$. See text for parameter assumptions.

6.9 Appendix C: Fault-normal Variation in BSM Calibrations

It is plausible to expect that calibration coefficients relating tensor strains in the rock to strains in the instrument might reflect the proposed depression in elastic properties near the fault. Figure 6.19 shows the average absolute value of all published calibration coefficients (with bootstrap confidence intervals) as a function of fault distance. Although there is a visual suggestion of a fault-related difference in means, there is no clear statistical evidence in support of this: any difference is more-likely associated with effects from smaller scale geologic heterogeneities. A notable oddity is the closest station (B946), which has a generally negative tidal response; it has a low response to barometric pressure (not shown).

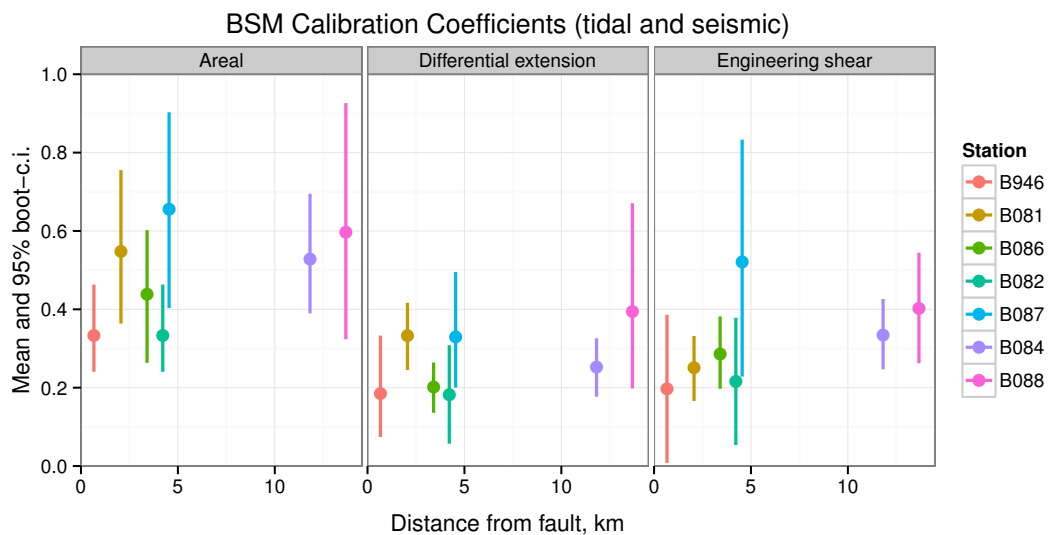


Figure 6.19: Fault-normal variation in calibration coefficients for strainmeters near the San Jacinto fault.

6.10 Acknowledgements

Thanks are also due to Evelyn Roeloffs, who originally proposed the collocation of a high-quality pressure-measurement system with the BSMs. The content of

this paper benefited from critical discussions with Steve Hickman, and Nick Beeler (who originally suggested using “interseismic slowness”). Dave Mencin, Mike Gottlieb, and Wade Johnson provided invaluable insight into finer workings of the instruments. Bob Parker’s adaptive cross spectral density estimation program, *cross*, was been used extensively. This work was supported by NSF Grant EAR10-53208.

Appendix A

psd: Adaptive Sine Multitaper Power Spectral Density Estimation for R

We present an R package for computing univariate power spectral density estimates with little or no tuning effort. We employ sine multitapers, allowing the number to vary with frequency in order to reduce mean square error, the sum of squared bias and variance, at each point. The approximate criterion of *Riedel and Sidorenko* (1995) is modified to prevent runaway averaging that otherwise occurs when the curvature of the spectrum goes to zero. An iterative procedure refines the number of tapers employed at each frequency. The resultant power spectra possess significantly lower variances than those of traditional, non-adaptive estimators. The sine tapers also provide useful spectral leakage suppression. Resolution and uncertainty can be estimated from the number of degrees of freedom (twice the number of tapers).

This technique is particularly suited to long time series, because it demands only one numerical Fourier transform, and requires no costly additional computation of taper functions, like the Slepian functions. It also avoids the degradation of the low-frequency performance associated with record segmentation in Welch's method. Above all, the adaptive process relieves the user of the need to set a tuning parameter, such as time-bandwidth product or segment length, that fixes

frequency resolution for the entire frequency interval; instead it provides frequency-dependent spectral resolution tailored to the shape of the spectrum itself.

We demonstrate the method by applying it to continuous borehole strainmeter data from a station in the Plate Boundary Observatory, namely station B084 at the Piñon Flat Observatory in southern California. The example illustrates how `psd` elegantly handles spectra with large dynamic range and mixed-bandwidth features – features typically found in geophysical datasets.

A.1 Introduction

Power spectra play an important role in every branch of geophysics where time series are encountered. By decomposing complex signals into their frequency components, one can usually separate out phenomena according to their physical causes, or distinguish geophysically significant signals from instrumental noise. The process by which power spectra or, more precisely, power spectral densities are estimated from a discretely sampled series has, of course, evolved over many decades. Papers discussing spectral analysis in some form number in the thousands, and we make no attempt to review them here. However, we can point to a few landmark studies which have addressed the issues of both bias (from spectral leakage and curvature) and variance in a profound way: *Welch* (1967), *Thomson* (1982), and *Riedel and Sidorenko* (1995). As we will see all of these appeal to the idea of multitapers.

Geophysical time series often exhibit very large dynamic ranges, great record lengths, and a mixture of wide and narrow-band processes. An effective computer program must be able to handle these issues efficiently and, in our view, should not require the user to experiment repeatedly with parameter settings in order to obtain a satisfactory spectrum. The sine-multitaper approach of *Riedel and Sidorenko* (1995) meets our requirements best: it is adaptive, so that the resolution and variance are set by the spectral shape, not the user; it is fast, requiring only one numerical Fourier transform for the whole analysis; bias and variance are kept in balance at every frequency.

The plan of the paper is as follows: we give a brief outline of the theory, summarizing the results of *Riedel and Sidorenko* (1995) and describing our modest contribution. Then we describe the implementation as a program, and conclude with an illustration from a fairly typical geophysical record.

A.2 Power Spectral Density Estimation

The standard method of decomposition of a record by frequency is to estimate the power spectral density (PSD) of the series. For a stationary stochastic signal $x(t)$ (the ideal statistical entity on which the theory is predicated), the PSD $S_x(f)$ gives the variance per unit bandwidth; essentially $S_x(f)df$ is the energy level of the signal after it has been passed through a perfect narrow band-pass filter centered on f with width df . Our task is to make an estimate from a uniformly sampled, finite-length sample of $x(t)$, the only kind realistically available. The ‘raw periodogram’ is obtained from the digital Fourier transform of the finite record, and is in fact the basis for all the so-called ‘direct’ estimation procedures:

$$\hat{S}_x(k\Delta f) = \frac{1}{T} \left| \sum_{j=0}^{N-1} x_j \exp \frac{2\pi i j k}{N} \right|^2, \quad k = 0, 1, 2, \dots, N/2 \quad (\text{A.1})$$

where T is the record length of the N samples x_j and $\Delta f = 1/T$. It is well known (see, for example, *Percival and Walden* (1993)) that these estimates of $S_x(k\Delta f)$ are very unsatisfactory: they suffer from very large variances yielding uncertainties as large as the estimates themselves, and from a kind of bias, spectral leakage, where energy at one frequency spills into neighboring frequencies.

An established technique to reduce spectral leakage is to ‘taper’ the record, which means multiplying $x(t)$ by a carefully chosen function $\phi(t)$, the taper, before taking the numerical Fourier transform. The result is a spectrum that is the convolution of the periodogram with $|\Phi(f)|^2$, where $\Phi(f)$ is the Fourier transform of ϕ . The literature is replete with recipes for good tapers, but it is now generally recognized that the prolate spheroidal functions introduced by *Slepian and Pollak* (1961) provide optimal suppression of leakage; see also *Thomson* (1982). These tapers, while not eliminating the bias completely, do a remarkably good job.

But tapering the series does nothing to reduce the variance of the periodogram estimate; for that we need some sort of averaging scheme. A popular approach is Welch's method (*Welch*, 1967), which briefly goes as follows: the record is broken into M equal-length, tapered segments; a periodogram is then calculated for each segment, and the final spectrum is the mean of the M periodograms. Although this method does address the issues of bias and variance together, it is unsatisfactory for several reasons. First, because the effective record is shortened by a factor of M , there is a severe loss of low frequency resolution, particularly when a lot of averaging is needed. Second, there is no good theory for choosing M , the number of segments; this parameter sets an inherent tradeoff between resolution and variance reduction for the whole spectrum. Third, the variance reduction and resolution are fixed for all frequencies.

Another approach for reducing variance is to smooth the tapered periodogram. The success of any smoothing procedure depends strongly on the choice of smoothing kernel. For example, using a relatively wide kernel will improve higher-frequency features, but will tend to degrade and actually distort lower-frequency spectra. Furthermore, neighboring spectral estimates after tapering are not statistically independent, reducing the efficiency of variance reduction produced by smoothing. We note the non-parametric spectrum-estimation tool in R, `stats::spec.pgram`, can apply a single taper to the series, form a periodogram, and then (optionally) apply a smoothing kernel (*Cowpertwait and Metcalfe*, 2009).

A more satisfactory technique to reduce both spectral bias and variance is the multitaper method. *Percival and Walden* (1993) provide an accessible account of the topic, which was initiated by the seminal work of *Thomson* (1982). Thomson showed that, for a series of length T , tapering with an orthogonal set of functions ϕ_k satisfying

$$\int_0^T \prod_{k=1}^M \phi_k(t) dt = 0 \quad (\text{A.2})$$

results in a set of statistically independent periodograms which may be averaged. This is the basis of multitaper spectral analysis.

Welch's method is an example. If non-overlapping sections are chosen and the taper for each segment is the function $\phi_0(t)$, we combine this with normal-

ized boxcar functions Π_k centered at t_k ; then the set of multitapers is $\phi_k(t) = \phi_0(t) \cdot \Pi_k(t)$, $k = 1, 2, 3 \dots M$. The functions $\phi_k(t)$ are orthogonal and they satisfy equation (A.2). Although this form of Welch's method qualifies as a multitaper analysis, its results are none-the-less plagued with the limitations previously mentioned. Far better performance can be achieved with different choices of ϕ_k .

The poor low-frequency behavior of Welch's method is completely eliminated in the following scheme. *Thomson* (1982) proposes the discrete prolate spheroidal (or Slepian) sequences as the family of orthogonal tapers; these functions are constructed to exhibit maximal leakage rejection. Unlike the Welch tapers, which vanish on a large fraction of the time interval, each function oscillates throughout the whole record. Once the frequency resolution parameter, the time-bandwidth product, has been set, the number of tapers needed to achieve the best variance can be calculated. The problem of leakage having been effectively dealt with, another form of bias becomes more serious: tapered periodograms are affected by curvature bias, a local effect that tends to flatten peaks in the spectrum. Peaks in Slepian-tapered spectra take on a characteristic 'boxy' shape. Though not widely known, there is a cure for the problem; see *Prieto et al.* (2007). None-the-less, the Slepian-tapered spectra suffer from two drawbacks. First, the user still must decide on a single parameter (the time-bandwidth product) that sets the resolution and variance reduction everywhere in the spectrum. Second, for very long records, the calculations of the multiple Fourier transforms and of the tapers themselves becomes expensive, particularly when heavy variance reduction (averaging periodograms) is required. Both these questions are addressed by the next family of tapers.

Riedel and Sidorenko (1995) consider the question of curvature bias described in the previous paragraph. By solving the appropriate optimization they find tapers that minimize a measure of the curvature bias, and furthermore, demonstrate that the family is well approximated by a set of simple sine functions:

$$\phi_k(t) = \sqrt{\frac{2}{T}} \sin \frac{k\pi t}{T}, \quad 0 \leq t \leq T, \quad k = 1, 2, 3, \dots \quad (\text{A.3})$$

Next they tackle the question of how many tapers should be used by examining the mean square error (MSE) at each frequency. The MSE is the sum of the squared

bias, β^2 , and the variance, \mathcal{V} , the two quantities that degrade spectral estimates. They find an approximation for MSE

$$L = \beta^2 + \mathcal{V}\{\hat{S}(f)\} = \frac{S''(f)^2 K^4}{576T^4} + \frac{S(f)^2}{K} \quad (\text{A.4})$$

where K is the number of tapered periodograms averaged, and $S''(f)$ is the second derivative of the PSD with frequency. A simple differentiation yields the following expression for the value associated with the smallest possible MSE:

$$K_{\text{opt}}(f) = \left(\frac{12T^2 S(f)}{|S''(f)|} \right)^{2/5} = 2.70192 \left(\frac{T^2 S(f)}{|S''(f)|} \right)^{2/5} \quad (\text{A.5})$$

Application of this formula completely avoids the difficulty of having to choose some overall balance between resolution and variance applicable to the whole spectrum: equation (A.5) does this automatically at each frequency. It means spectra with a mixture of narrow-band and wide-band features present no difficulty. This is called ‘adaptive’ estimation because the estimator adapts the balance of resolution and variance to the local shape of the spectrum.

Remarkably, the sine multitapers also dispose of another drawback mentioned earlier, computational expense for very long records. As Riedel and Sidorenko casually remark, there is no need to perform more than one (double length) numerical Fourier transform for the whole record. Multiplying the signal by a sine function like those in equation (A.3) merely causes frequency shifts in the transform; all the information needed to find the transform of any tapered record is available after one FFT.

The sine multitapers are designed to minimize curvature bias; what about spectral leakage? The tapers in equation (A.3) offer a moderate amount of leakage protection (see the next Section), but far less than the Slepian functions. Here again the advantage tilts to sine multitapers for long records: at any fixed frequency the error from spectral leakages tends to zero as the record length increases, since periodograms are asymptotically unbiased.

Finally, we must mention a paradox inherent in equation (A.5): to find K_{opt} one apparently needs to know the spectrum and its second derivative. There is no analytic solution to the problem of simultaneously finding K_{opt} and S and so

one must resort to an iterative procedure. Starting from a pilot estimate of the spectrum, which provides preliminary values for the number of tapers, one makes another estimate; this yields values for K_{opt} , which are employed to estimate a new spectrum, and so on. This naive approach fails because equation (A.5) is an approximation with a fatal flaw: when the second derivative $S''(f)$ vanishes, the expression demands infinitely many tapers. Very small values of $|S''|$, if not exact zeros, arise in almost every real spectrum, and so this is a serious matter. The consequent runaway averaging must be suppressed: we have adopted an *ad hoc* procedure, which will be described in Section A.4.

A.3 Further Properties of Sine Multitapers

The effect in the frequency domain of tapering the record with the function $\phi(t)$ is to convolve the corresponding periodogram with a function closely approximated by the squared Fourier transform $|\Phi(f)|^2$; see *Percival and Walden (1993)*. The convolution broadens spectral peaks, but also reduces the energy that would otherwise spill out of the peak into neighboring frequencies, thus curtailing the bias called spectral leakage. For the sine tapers in equation (A.3) this gives:

$$|\Phi_k(f)|^2 = \frac{2Tk^2}{(k + 2Tf)^2} \text{sinc}(Tf - k/2)^2 \quad (\text{A.6})$$

These functions, which we will call spectral kernels, are illustrated in Figure A.1. We see that the width of the central portion is roughly $k\Delta f$ and, from equation (A.6), outside that region $|\Phi_k(f)|^2$ dies away as f^{-4} .

The convolved periodograms must be averaged to obtain the multitaper estimate. In principle each periodogram is providing an estimate of the same function S , but those associated with higher k are relying more heavily on spectral values further from the central frequency. For this reason Riedel and Sidorenko suggest a parabolic weighting scheme that gives less weight to the outer members:

$$\hat{S}_x(f) = \sum_{k=1}^K N_k^{-1} [K^2 - (k-1)^2] \hat{S}_k(f) = \sum_{k=1}^K \mu_k \hat{S}_k(f) \quad (\text{A.7})$$

where $\hat{S}_k(f)$ is the periodogram tapered with ϕ_k and $N_k = K(4K-1)(K+1)/6$. The weighting is shown in Figure A.2.

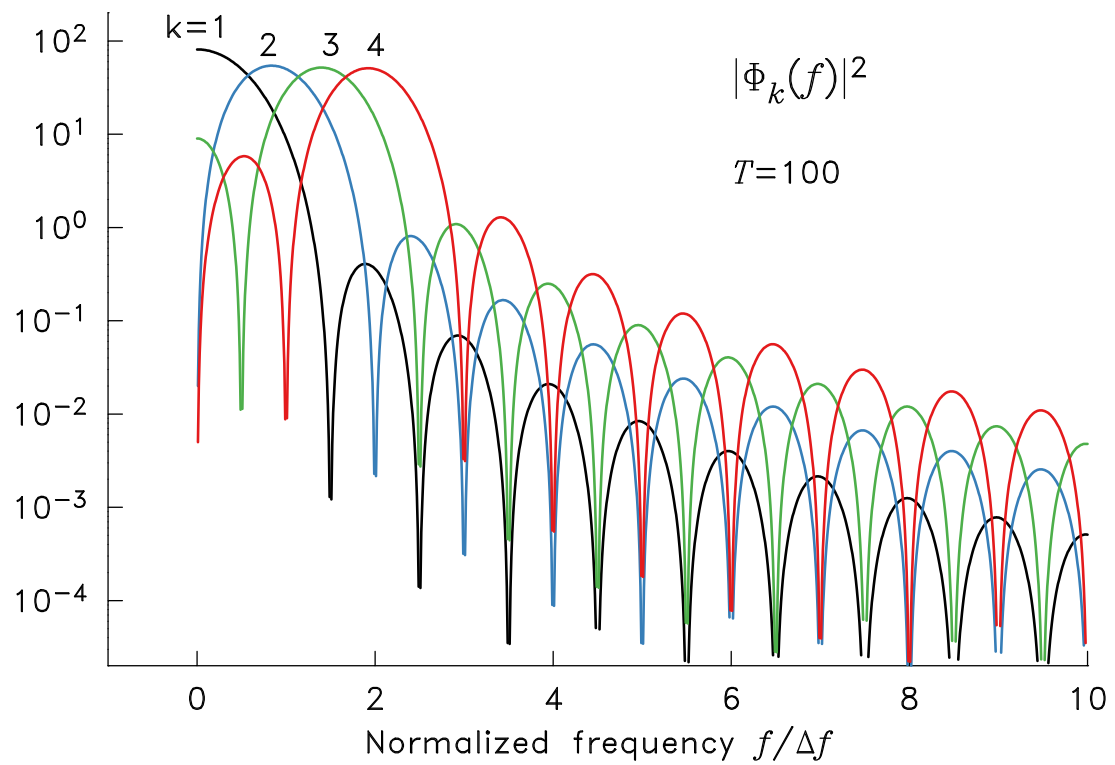


Figure A.1: Spectral kernels given in equation (A.6). These functions are symmetrical about $f = 0$; only the right side is shown.

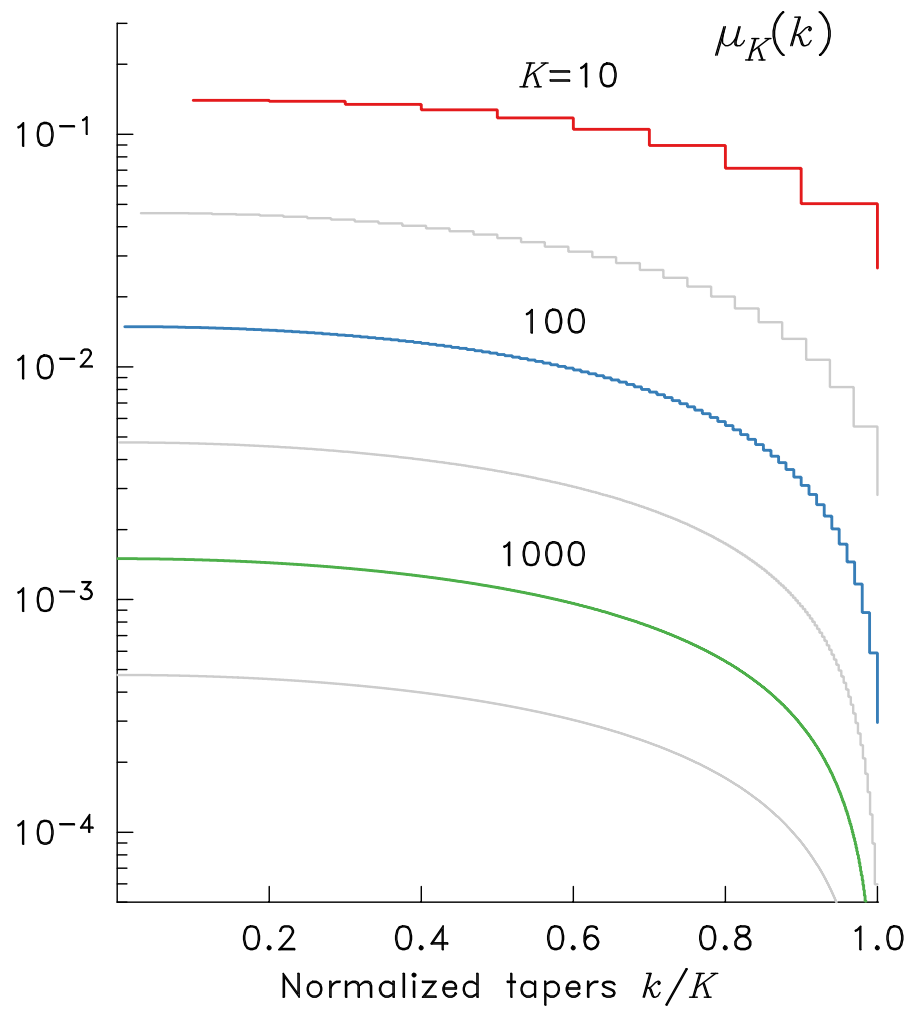


Figure A.2: Spectral weighting factors given by equation (A.7) for selected taper sequences. These curves are quantized depending on the length of the taper sequence.

With parabolic weighting the optimal number of tapers is slightly different:

$$K_{\text{opt}} = 480^{1/5} \left(\frac{T^2 S(f)}{|S''(f)|} \right)^{2/5} = 3.43754 \left(\frac{T^2 S(f)}{|S''(f)|} \right)^{2/5} \quad (\text{A.8})$$

The effective spectral kernel for the complete sum is obtained by the weighted average

$$U_K(f) = \sum_{k=1}^K \mu_k |\Phi_k(f)|^2 \quad (\text{A.9})$$

and this function is illustrated in Figure A.3.

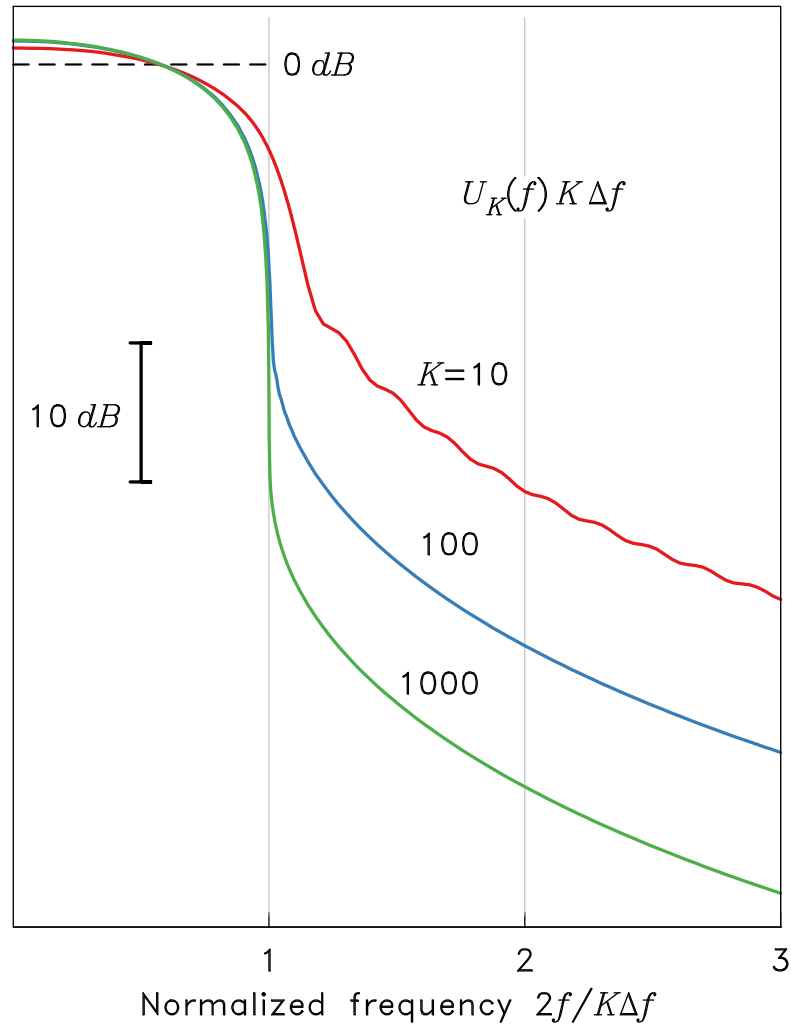


Figure A.3: Effective spectral kernels given by equation (A.9). Only the right side is shown of these symmetric functions.

As expected the width of $U_K(f)$ is $K\Delta f$, which can be identified as the

spectral resolution of the estimate. Somewhat surprisingly, the fraction of energy outside the central band, the part contributing to leakage, decreases as the number of tapers grows.

Given the statistical independence of the K periodogram estimates, and the parabolic weighting, it is a short calculation to show that the variance of the final estimate is approximately

$$\mathcal{V}\{\hat{S}(f)\} = \frac{6S(f)^2}{5K} \quad (\text{A.10})$$

If the time series has a Gaussian distribution, \hat{S} will be distributed as χ^2 with $2K$ degrees of freedom. One can compute confidence limits knowing this, but for most purposes the asymptotic approximation of a Gaussian distribution for \hat{S} is perfectly adequate.

An important distinction between adaptive and non-adaptive PSD estimates is the far smaller variance of the former in many cases. As we will see in the final Section, it is not uncommon for K to be many hundreds in regions of the spectrum where $S(f)$ is flat. Such strong averaging is essentially impossible for Welch's method, because it could lead to ridiculously short segments. This difficulty obviously does not apply to Slepian-tapered estimates, but because the same amount of averaging would be applied to the whole spectrum, any narrow-band features would be completely ironed out. If an adaptive scheme is contemplated for these tapers to overcome the defect, the computational cost (hundreds of Fourier transforms per frequency) suggests it would be impractical for any but the shortest series.

A.4 Algorithm Summary

The function `pspectrum` applies the sine-multitaper adaptive method to produce a PSD of the input series. A rough sketch of the iterative algorithm is as follows. An initial multitaper PSD is calculated with a fixed number of tapers for all frequencies. Spectral derivatives are then estimated and applied in equation (A.5) to generate taper numbers for the next iterate. A new PSD is computed on this basis. The process of refinement of the spectral derivatives and the number

of tapers is repeated as many times as desired by the user, although three or four iterations seems to result in a stable result.

We now flesh out some of the details. First, estimating second derivatives of a noisy signal like $\hat{S}_x(f)$ requires some care. Because we require the ratio $S(f)/S''(f)$ in equation (A.8), it is more stable to work with the logarithm $Y(f) = \ln S(f)$ and estimate from the identity

$$\frac{S(f)}{S''(f)} = Y''(f) + Y'(f)^2 \quad (\text{A.11})$$

rather than finding $S(f)$ and $S''(f)$ separately. Our approach is to fit a degree-two polynomial to the function $Y(f)$ over a small interval about each frequency. With least-squares fitting, the estimates of $Y''(f)$ and $Y'(f)$ becomes weighted averages of the values of $Y(f)$ in the interval. But what is the proper interval? Here we allow the spectral resolution to set the scale, taking K (as determined in the previous iteration) points on either side of the central frequency.

We come now to the difficulty mentioned at the end of Section A.3. If we imagine a frequency interval in which the second derivative S'' passes smoothly through zero, we see from equation (A.8) that the number of tapers increases rapidly without bound. It is found empirically that large values of $|dK_{\text{opt}}/df|$ cause gross distortions in the shape of the estimated spectrum because then the size of the averaging interval fluctuates wildly. The simplification on which the bias in equation (A.4) is based – that the spectrum is well approximated by just three terms of the Taylor series over the averaging interval – must have broken down when one averaging interval entirely covers another. To eliminate this possibility we place constraints on the derivative by requiring

$$|K(f_{j+1}) - K(f_j)| \leq 1 \quad (\text{A.12})$$

which is achieved by running over the K_{opt} series forwards and backwards, enforcing the condition at each frequency index. We find that this simple, *ad hoc* recipe stabilizes the iterative process and leads to quite satisfactory spectra, even though it adds some computational expense. For almost all data-based spectra, however, it has the consequence that the actual number of tapers applied satisfies equation

(A.8) only around peaks; elsewhere, much less averaging is done, although, as mentioned earlier, the value of K can still rise to many hundreds (Figure A.4).

A.5 Application to Borehole Strainmeter Noise

In this section we show an example using `psd` with borehole strainmeter data from the Plate Boundary Observatory (PBO) network. Specifically, we have taken a four-hour sample of high-frequency data (1 Hz sampling) from station B084, located near the San Jacinto fault in southern California. These data are centered in time about the origin of the the great M_w 9 Tohoku-oki earthquake on 2013/03/11, which occurred offshore of the northeast coast of Japan. We split the record into two approximately equal length segments: one for strain signals prior to any seismic wave arrivals, that we term “pre-seismic” (Figure A.5a); and the other for strains from teleseismic surface waves created by the earthquake (Figure A.5b). The raw records from the four-axis, GTSM-style instrument (see *Gladwin* (1984) for details), are in digitizer counts. We have converted these to extensions e_{ij} in a North-East coordinate system using the tidal calibrations of *Hodgkinson et al.* (2013), and then in combination to form three commonly used measures: areal strain ($e_{NN} + e_{EE}$), engineering shear strain ($2e_{NE}$), and differential extension ($e_{NN} - e_{EE}$). Even though there are more appropriate estimation methods for non-stationary signals, such as the evolutionary spectrum (*Priestley*, 1981), we isolated three sections in the seismic record which might be considered weakly stationary for comparison; these are labeled ‘A’—‘C’ in Figure A.5b.

We use `pspectrum` to produce adaptive multitaper PSDs for each component in each section of the seismic record, and for the full pre-seismic record. We remove a second order polynomial from the records to minimize their biasing effects, and perform a four-stage estimation. No other settings are changed from their defaults. Figure A.4 shows how the PSD estimates, the number of tapers, and the uncertainties change with sequential iterations for the pre-seismic data: confidence intervals are smaller, as expected, and after only two iterations the variance is reduced drastically, revealing a spectrum rich with mixed bandwidth

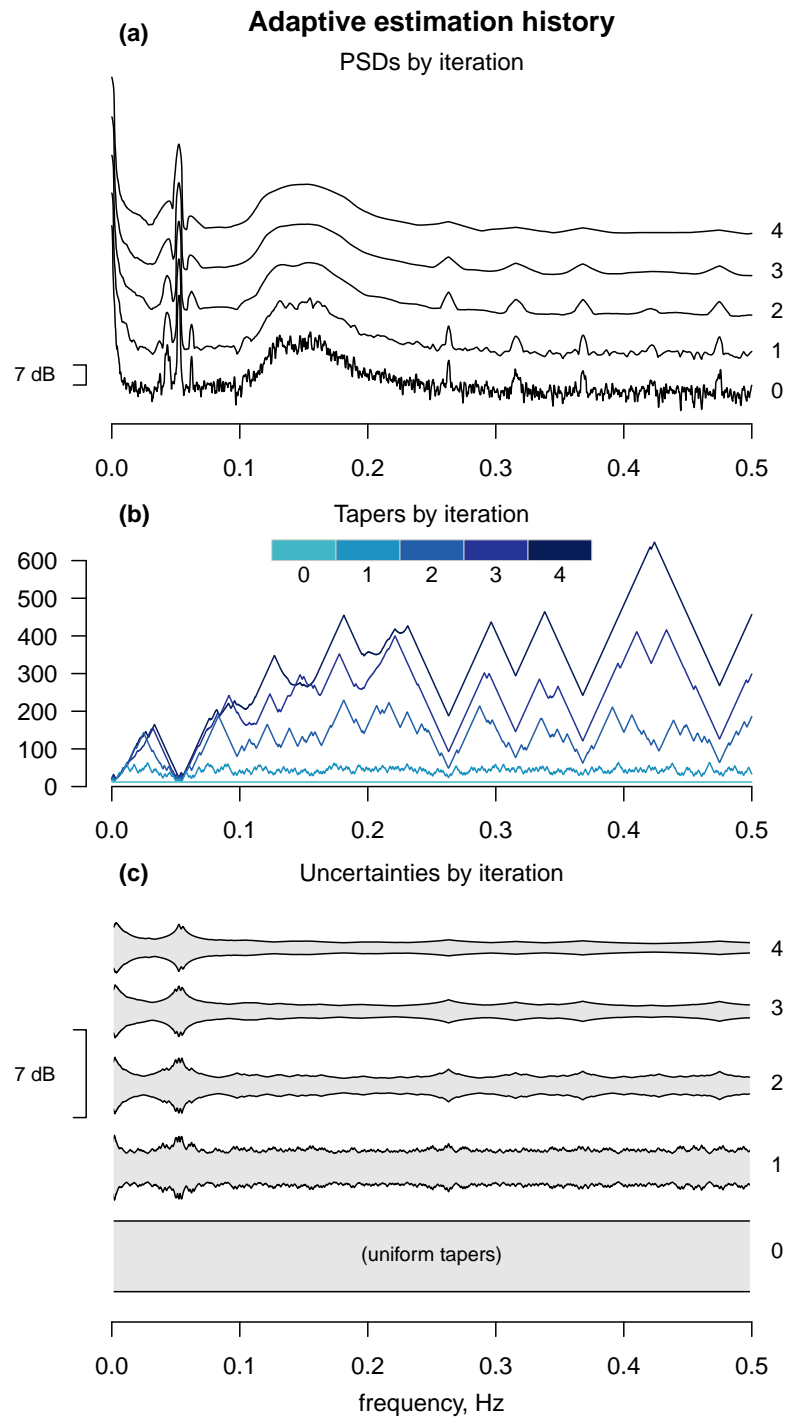


Figure A.4: Adaptive estimation history for pre-seismic areal strains at B084. The quantities shown – for each iteration stage, with zero representing the pilot spectrum – include (a) power spectral density curves, (b) the number of tapers applied, and (c) relative 95% confidence intervals.

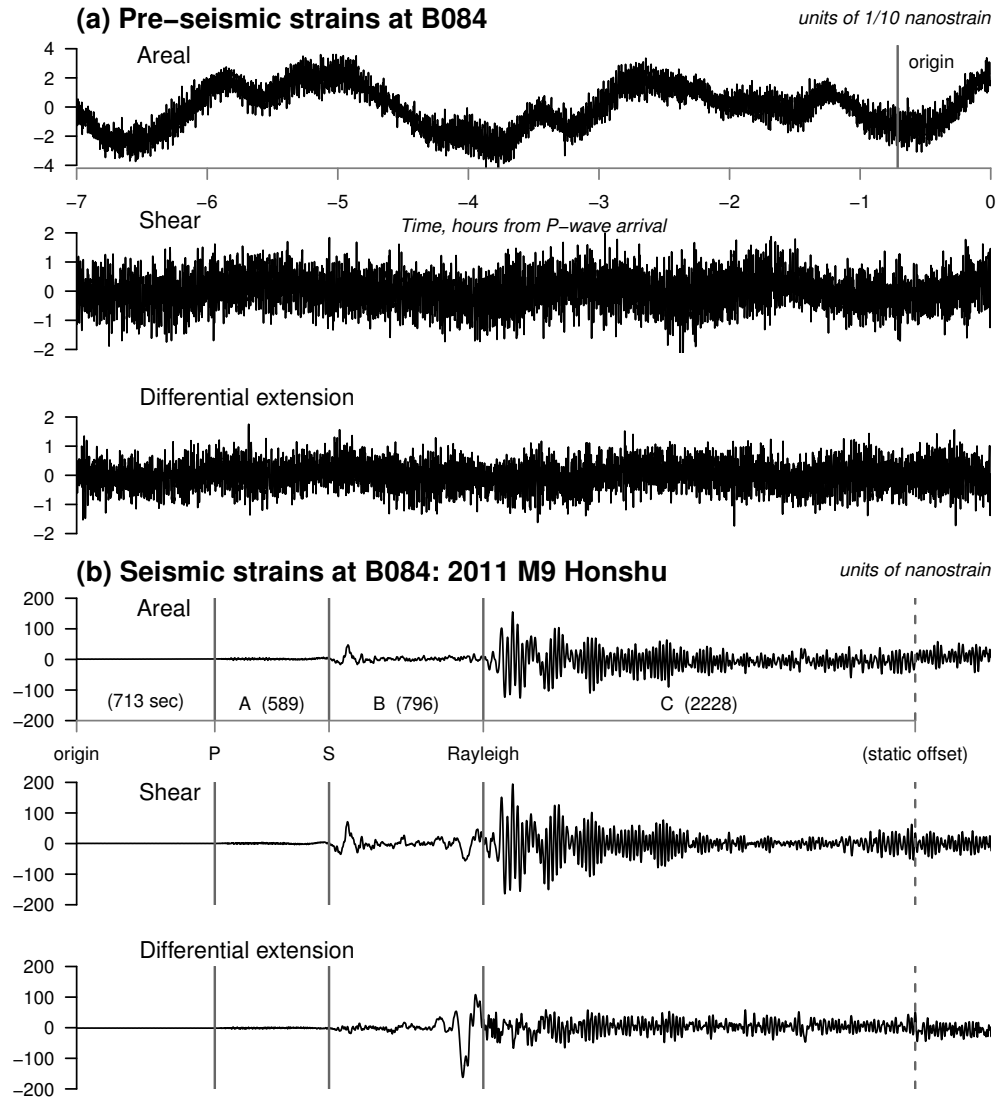


Figure A.5: Strainmeter data at PBO station B084 (a) before, and (b) after the 2011 M_w 9 Tohoku-oki earthquake (8640 km away at 307 deg). The sections shown in (b), labeled ‘A’—‘C’, correspond to those in Figure A.6; section (C) ends arbitrarily at a spurious, static offset. Note the scale changes within (a), and between (a) and (b). One nanostrain is 10^{-9} , extension positive.

features. And these features would be better resolved had we used a much longer record.

Barbour and Agnew (2011) first documented the statistical variation in noise levels found in data from some PBO strainmeters (including B084) in the ‘seismic’ frequency band ($10^{-3} - 10$ Hz). They studied the variation in PSD estimates for a year of segmented data, and provide empirical cumulative distribution functions (ecdf) as a function of frequency. The ecdf contours all show a mix of wide and narrow band features, and a “red” colored spectra commonly found in timeseries having noise with power-law variation (*Agnew*, 1992). In Figure A.6 we show the spectral estimates for both the pre-seismic and the sectioned seismic records on top of the median and 10th percentiles of the noise model.

The primary wide-band feature seen in the pre-seismic spectra is due to signals from so called ‘dual-frequency’ microseisms. Signals in this band arise from interactions between ocean waves and coastal bathymetry, which generate nearly stationary vibrations in the earth’s crust. Microseisms are common to every properly functioning seismometer on earth, but have varying amplitudes and dispersion characteristics that depend on local earth structure and distant storm activity.

The narrow-band features seen in the strain spectra are less interesting from a geophysical perspective, unfortunately, because they are associated with artificial signals created by cycling of the power system (see Instrumental Noise in *Barbour and Agnew*, 2011). Studies involving surface waves and strain data should thus be scrutinized carefully for contamination by these non-physical signals. Low-power peaks are apparent at much higher frequencies, thanks to the remarkably low noise levels found outside the microseism band during this period of time. The regularly spaced nature of these peaks suggest some sort of cyclic mechanical device is in operation nearby – a water pump, or an electric generator, perhaps.

See A.8 for an example using these data and `pspectrum`, and A.9 for references to alternative PSD estimation tools available for R.

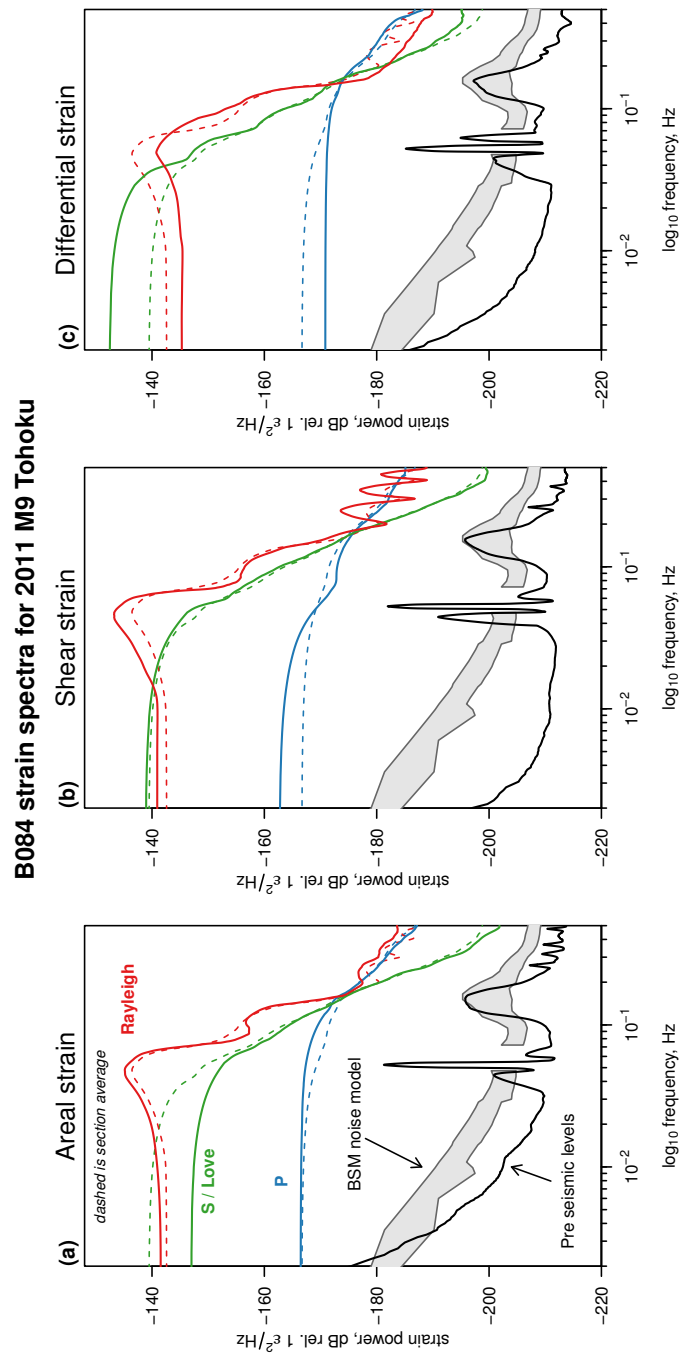


Figure A.6: Strain spectra at PBO station B084 before, and after the 2011 M_w 9 Tohoku-oki earthquake. Curves labeled P, S/Love, and Rayleigh correspond to data sections labeled ‘A’—‘C’ in Figure A.5(b), respectively; dashed lines show average levels over all components in the data section. Pre-seismic levels are compared to the 10 – 50th percentile levels from *Barbour and Agnew* (2011).

A.6 Conclusion

We have presented the software package `psd`, an adaptive power spectral density estimation tool using the sine multitapers, and written for the R programming language. The results are PSD estimates with lower variance and bias relative to commonly used methods (e.g. Welch's). It is also more efficient than non-adaptive multitaper methods (e.g. Slepian tapers) because it requires only one Fourier transform calculation, and needs very little tuning to achieve acceptable results. We used high-frequency borehole strainmeter data to demonstrate how the adaptive multitaper spectrum estimation can resolve a combination of wide- and narrow-bandwidth features in data having a very high dynamic range. In contrast, non-adaptive methods must be adjusted depending on the type of feature to be resolved, and can never produce a single spectrum that combines both types of features.

A.7 Data and Resources

The R programming language is free, and open source under the GNU General Public License (GPL). The source code can be found at <http://www.r-project.org>, and precompiled installation files exist for a number of common operating systems. The source code and a full reference manual for `psd` is also available under the GPL license, and is hosted by the Comprehensive R Archive Network (CRAN) at <http://cran.r-project.org/package=psd>. We used R version 3.0.2 and `psd` version 0.4-0 for the examples in this paper. The Tohoku dataset comes from the PBO high-frequency earthquake catalog maintained by K. Hodgkinson. We registered the URL for these data to <http://goo.gl/Gx7Ww>, and they are included in `psd` (see Appendix A). Websites were last accessed in September, 2013.

A.8 Appendix A: Example Usage

In this appendix we provide a basic script of R commands demonstrating how to use `psd` to produce an adaptive PSD estimate for the Tohoku data, specifically the pre-seismic strains (shown in Figure A.5a).

Within the R environment the package can be installed from the CRAN archive with the command

```
install.packages("psd", dependencies=TRUE)
```

which installs all the necessary packages needed to run `psd`, its examples, tests, and vignettes. (Version updates should be applied using the `update.packages` function.) Once the necessary packages are installed, the library of functions in `psd` is loaded with the command

```
library(psd)
```

The Tohoku dataset is included with the package, but not loaded by default. We can load this dataset with the command `data`, and inspect its contents (stored as an object of the class ‘data.frame’) with the command `str`:

```
data(Tohoku)
str(Tohoku)
```

For this example we want to analyze the pre-seismic portion, so we extract it with the command `subset`:

```
Dat <- subset(Tohoku, epoch=="preseismic")
```

This data may be visualized in various ways. For example, the commands

```
Areal <- ts(Dat$areal)
plot(ts.union(Areal, ts(Dat$gamma1), ts(Dat$gamma2)))
```

will produce a single figure showing each timeseries in a separate frame, with time in seconds from the beginning of the record.

It's considered good practice to remove a linear model (offset and trend) prior to PSD estimation to prevent potential bias. Various methods exists to do this, but in `psd` the function `prewhiten` has this capability:

```
Dat <- prewhiten(Areal, plot=FALSE)
```

and can also be used to remove an auto-regressive model from the data. Next we run `pspectrum` using default settings for the sampling interval (1 Hz) and the number of iterations (three), which creates a PSD estimate:

```
mtpsd <- pspectrum(Dat$prew_lm, plot=TRUE)
```

Setting the logical argument `plot=TRUE` will create a figure (in a new window) which compares the final result from `pspectrum` to a raw periodogram estimate of the same data from `spec.pgram` in the built-in `stats` package library; however, the default is `plot=FALSE`.

The resulting object, `mtpsd`, will have the class ‘spec’ which implies that any available methods may be used. For example, the command

```
plot(mtpsd, log="dB")
```

accesses the `plot.spec` method from the `stats` library, and plots the adaptive power spectral density estimates in units of decibels. Additional properties of the spectrum (e.g., uncertainty) may be calculated with the following command:

```
sprop <- spectral_properties(mtpsd)
```

calculates various properties of the PSD, stored in object `sprop`, and the commands

```
Ntap <- sprop$taper/max(sprop$taper)
plot(Ntap, type="h", ylim=c(0,2), col="dark grey")
lines(sprop$stderr.chi.lower)
lines(sprop$stderr.chi.upper)
```

overplot 95% confidence intervals of the spectrum on the number of normalized tapers.

Finally, the documentation for `psd`, or any of its functions may be accessed with the `?` command. For example, `?psd` opens documentation for the package, and `?pspectrum` opens documentation for that function.

A.9 Appendix B: Comparisons with Other Methods in R

In Table A.1 we summarize known power spectral density estimation algorithms which are readily available in R (either built in, or through extensions). We have excluded any functions (from extensions) which only estimate raw periodograms. Spectrum normalizations are shown as either ‘single’ or ‘double’ for either single- or double-sided spectra, and ‘various’ if there are other normalizations. The symbol ‘*’ indicates the function has an option for either single or double, but defaults to the normalization shown.

Comparisons between our method and others shown in Table A.1 can be found in the vignette named “psd_overview”, which can be accessed within the R environment with the command `vignette`. For example, the command

```
vignette("psd_overview", package="psd")
```

will open the vignette as a pdf document. See `?vignette` for more details.

Table A.1: Power spectral density estimators in R

FUNCTION	PACKAGE	SINE M.T. [†]	ADAPTIVE [‡]	NORM.*	REFERENCE
bspec	bspec	NO	NO	single*	<i>Roever (2013)</i>
mtapspec	RSEIS	YES	NO	various	<i>Lees (2013)</i>
pspectrum	psd	YES	YES	single	(this paper)
spectrum	stats	NO	NO	double	<i>R Core Team (2013)</i>
spec.mtm	multitaper	YES	YES	double	<i>Rahim and Burr (2012)</i>
SDF	sapa	YES	NO	single*	<i>Constantine and Percival (2012)</i>

[†] Sine multitapers can be applied.

[‡] Spectrum estimation is adaptive.

* Spectrum normalization can be either single-sided, double-sided, or a variety.

* The default normalization, but with an option to be either single, or double.

A.10 Acknowledgments

We wish to thank Duncan Agnew for comments and discussions which helped shape the focus of this paper. The development of this software was supported by NSF Grant EAR10-53208.

Appendix A is a reprint of Barbour and Parker (2014), adapted for the dissertation. The dissertation author was the primary investigator and author of this paper.

Appendix B

Figures from Published Electronic Supplements

B.1 Laser and Wire Strainmeter Noise Variation

There are two figures in this section which show strain noise statistical variation for other types of strainmeters used as comparisons to the PBO results, namely LSMs in California (Figure B.1), and buried wire-strainmeters located at the Black Forest Observatory (BFO) in Germany (Figure B.2).

B.2 Seismic Noise, and Seismometer and LSM Detection Curves

B.2.1 Seismometer Noise Levels and Variation

There are four figures in this section. The first (Figure B.3) shows noise levels for borehole strainmeters used for Figure 3.2; Figure B.4 shows variation in these noise levels. The third (Figure B.5) is similar to Figure B.3, except it shows noise levels for surface broadband seismometers Figure 3.1; Figure B.6 shows noise variation in these noise levels.

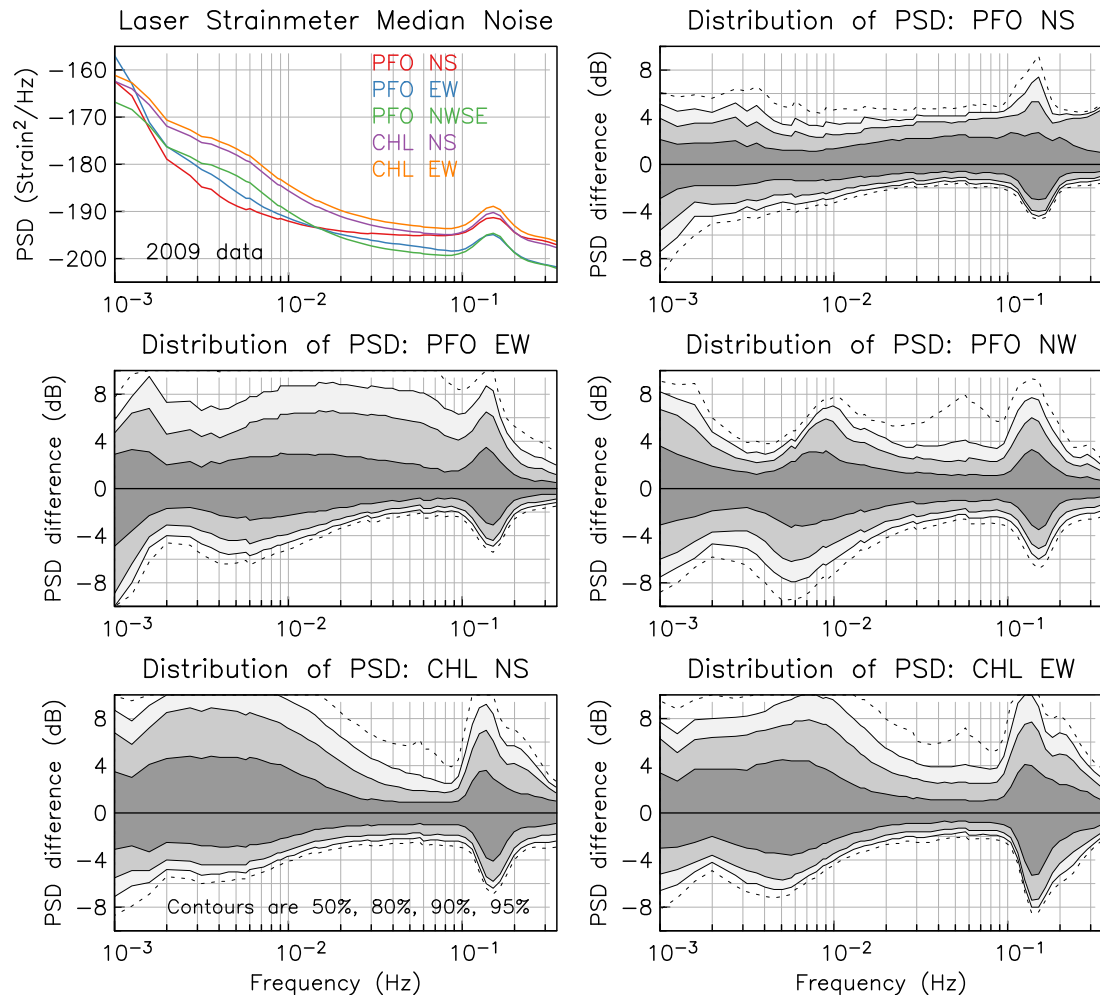


Figure B.1: Noise variation of a few long-baseline laser strainmeters throughout California. We show CHL at Cholame, in central CA; and PFO at the Piñon Flat Observatory, in the Anza region. The contoured plots show power variation relative to median levels. Specifically, shaded contours are 50%, 80%, and 90% variation, and dashed lines are 95% variation.

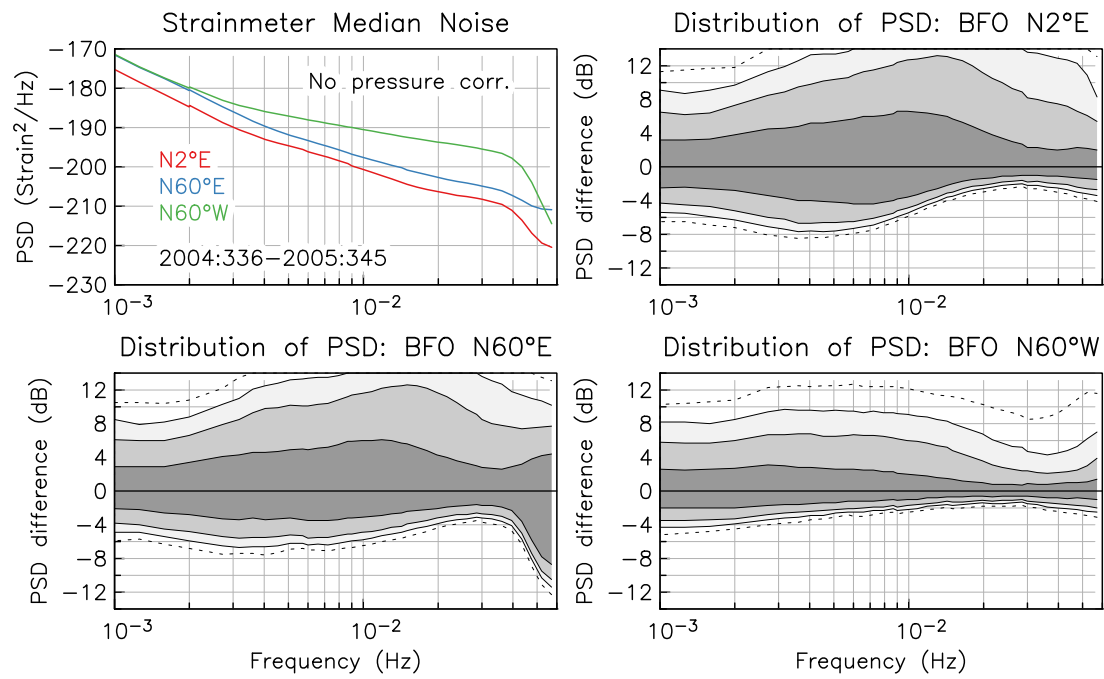


Figure B.2: Noise variation of the buried wire-strainmeters at the Black Forest Observatory (BFO) in Germany. Contour levels are similar to Figure B.1.

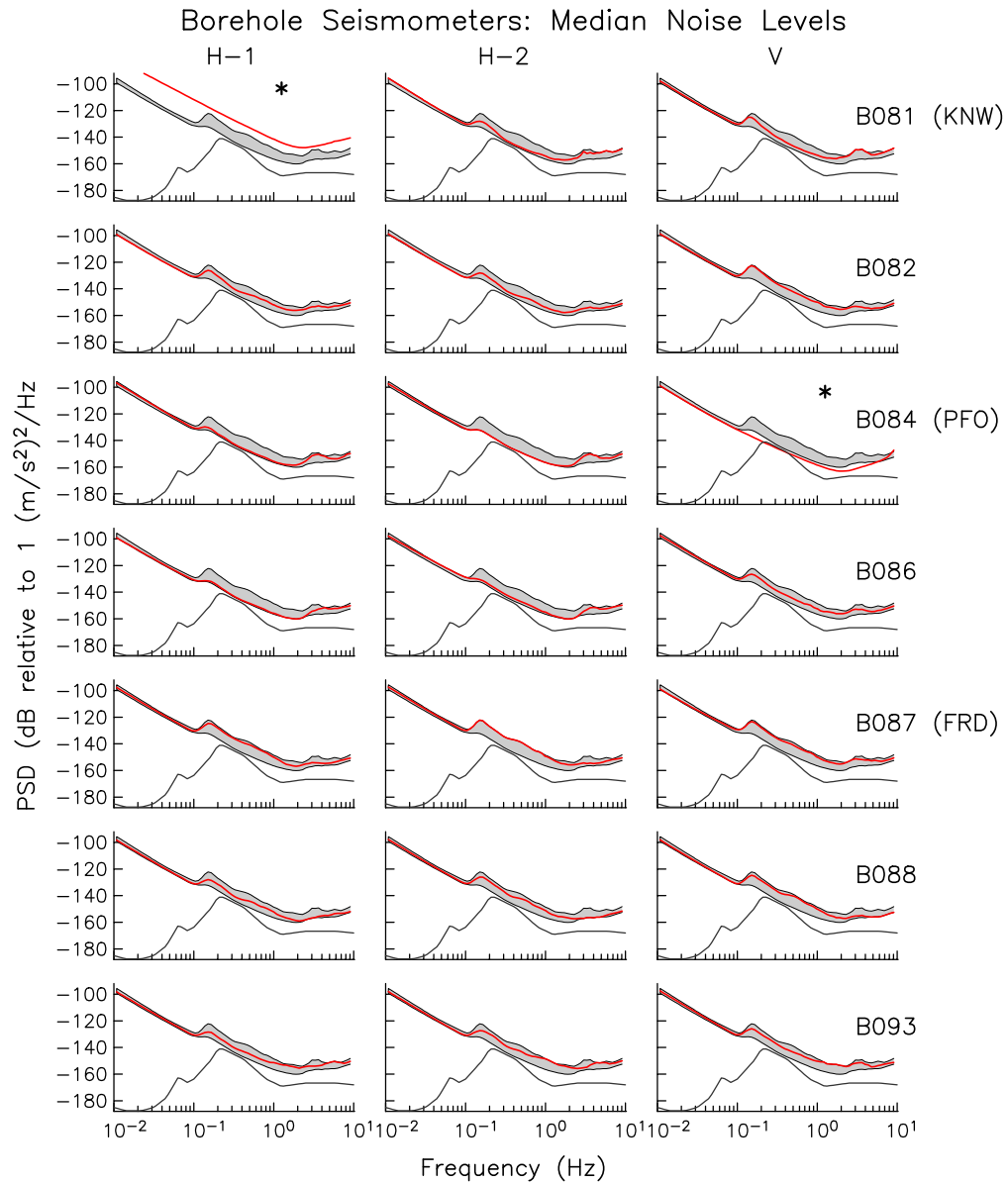


Figure B.3: Median seismic noise levels above 10 mHz, for borehole seismometers. Filled regions show variation across all instruments, whereas thick red lines show levels for individual channels.

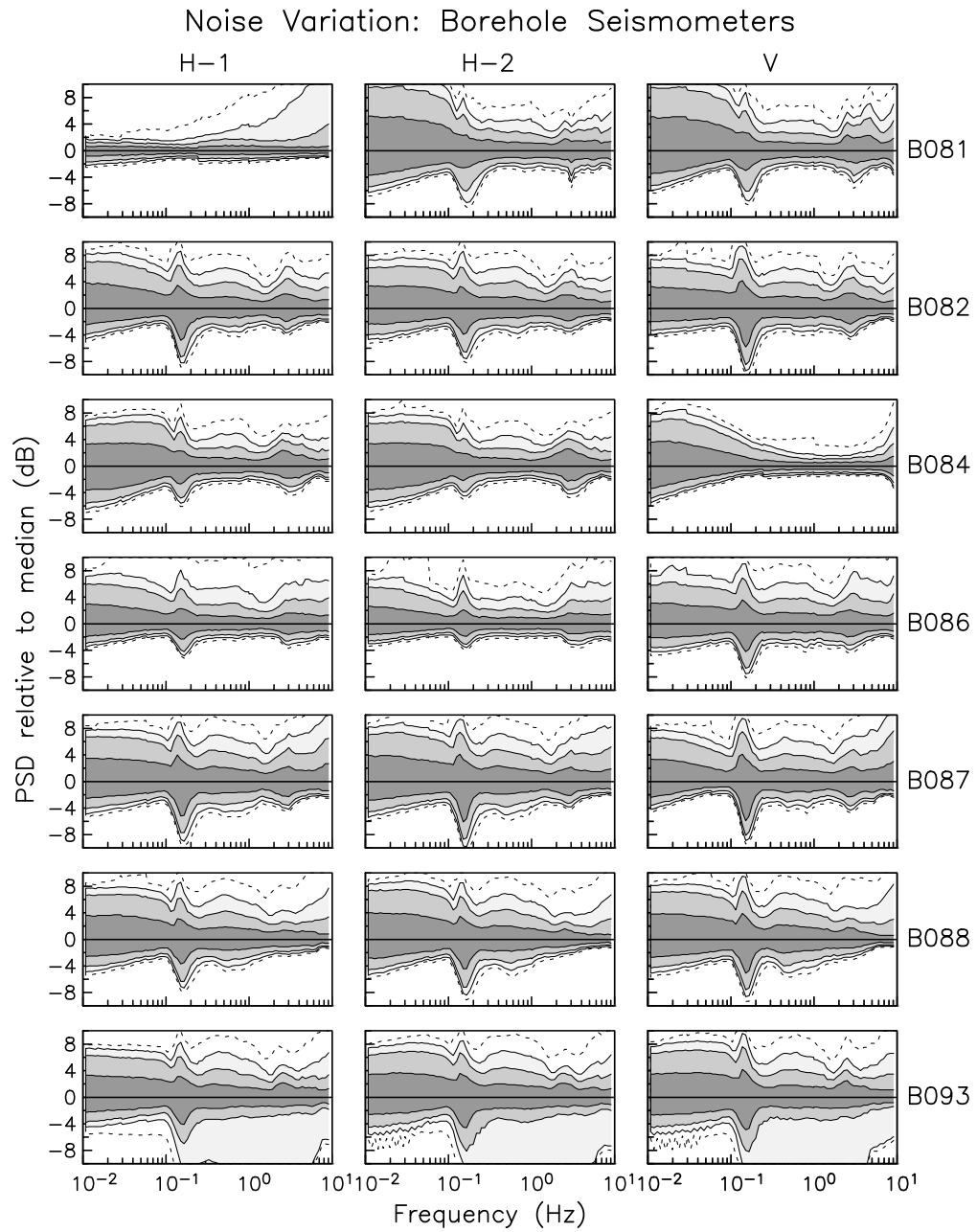


Figure B.4: Variation of borehole seismic noise (pdfs) relative to median values. The contoured plots show power variation relative to median levels. Specifically, shaded contours are 50%, 80%, and 90% variation, and dashed lines are 95% variation.

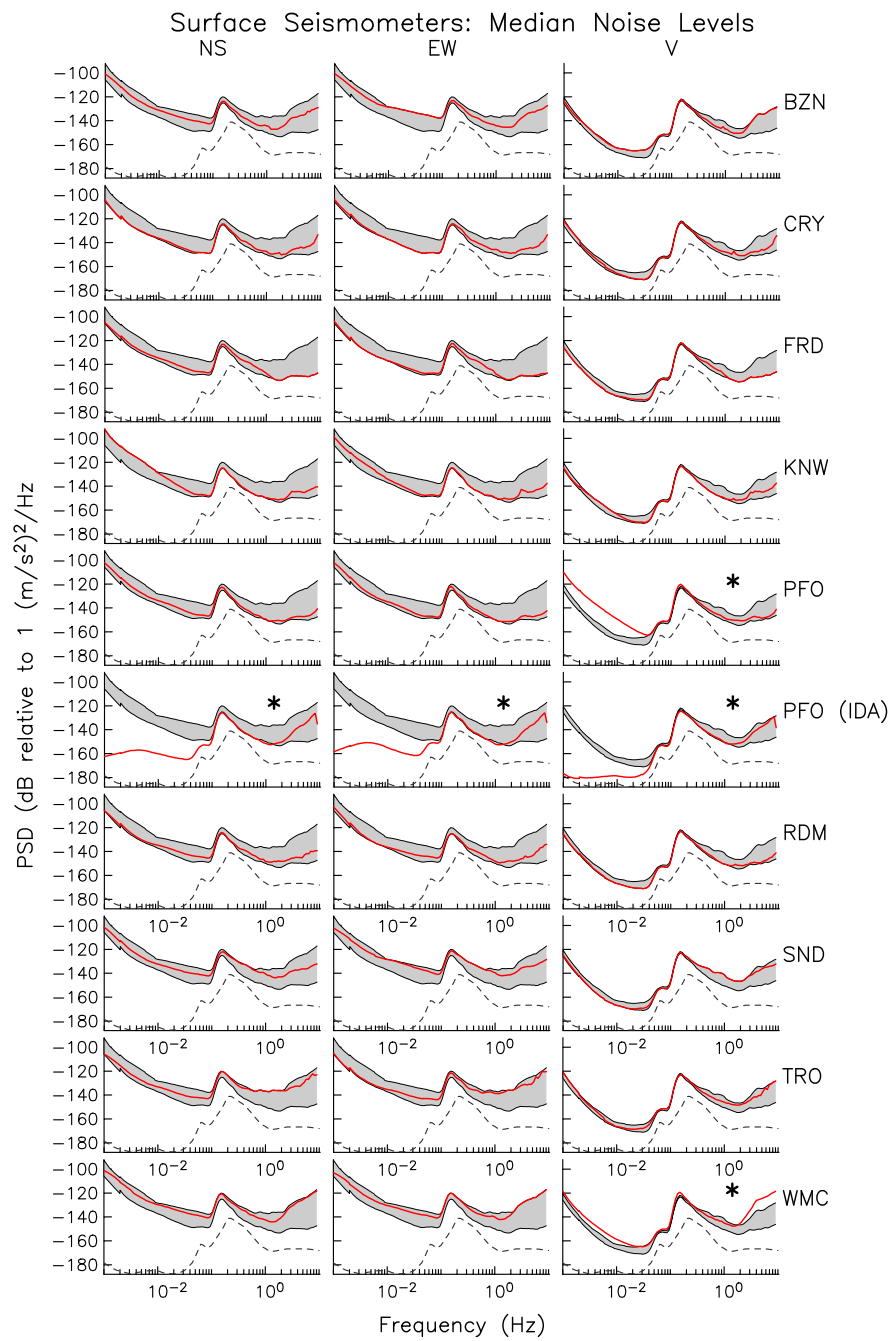


Figure B.5: Median seismic noise levels above 1 mHz, for surface broadband seismometers; this is similar to Figure B.3.

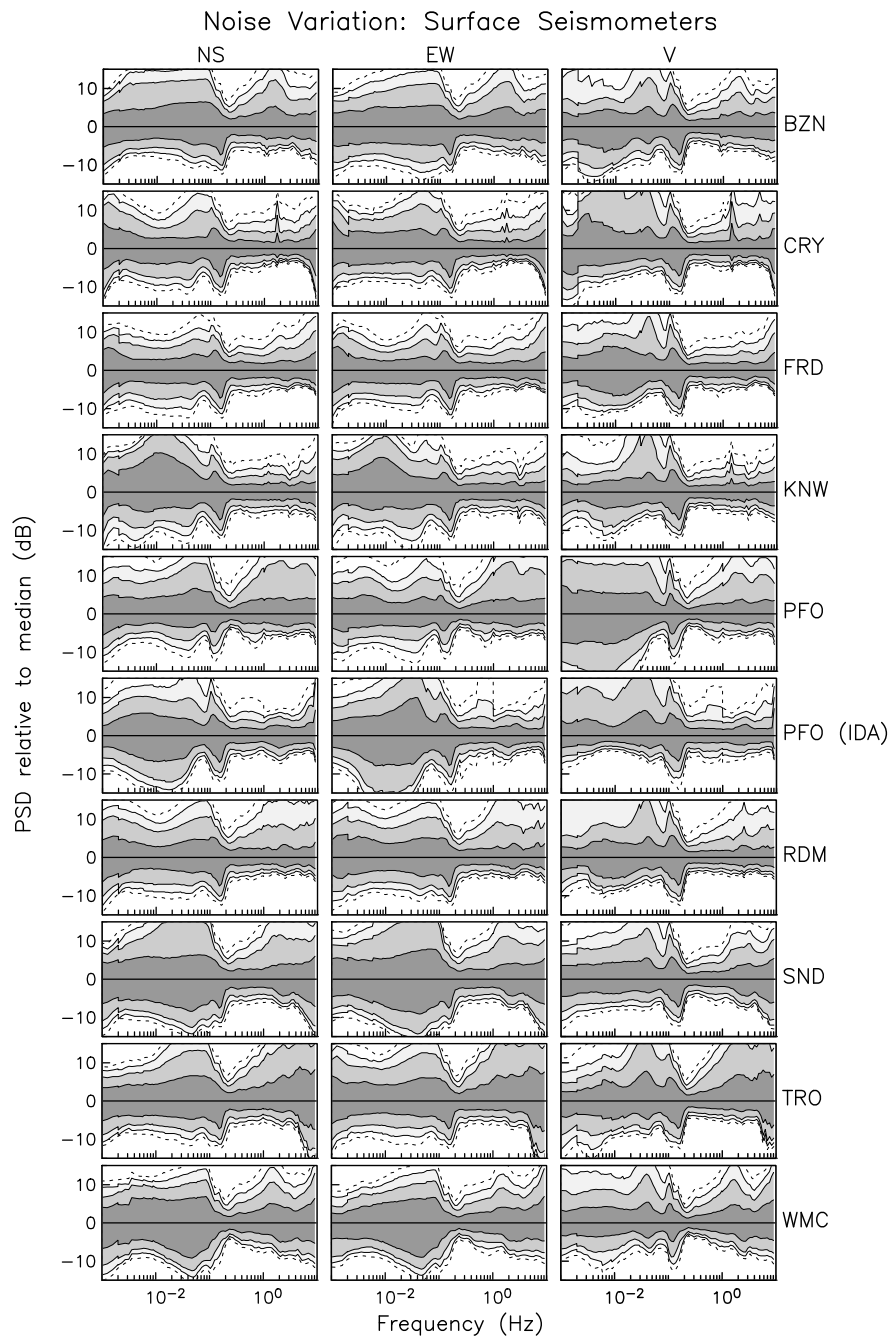


Figure B.6: Variation of surface broadband seismic noise (pdfs) relative to median values; the contouring scheme is the same as in Figure B.4.

B.2.2 Detection Curves for Seismometer Pairs

There are three figures in this section. The first (Figure B.7) is similar to Figure 3.3 except that the comparisons are based on relative signal-to-noise ratios for seismometer pairs, namely the surface broadband seismometers in the Anza network and the other seismometer types. The second and third (Figure B.8, and Figure B.9) are similar to Figure 3.2 and Figure 3.3, except that comparisons are based on the noise model for the longbase laser strainmeters (LSM). In Figure B.8 the detection curve does not extend above 0.5 Hz – the Nyquist frequency of LSM data.

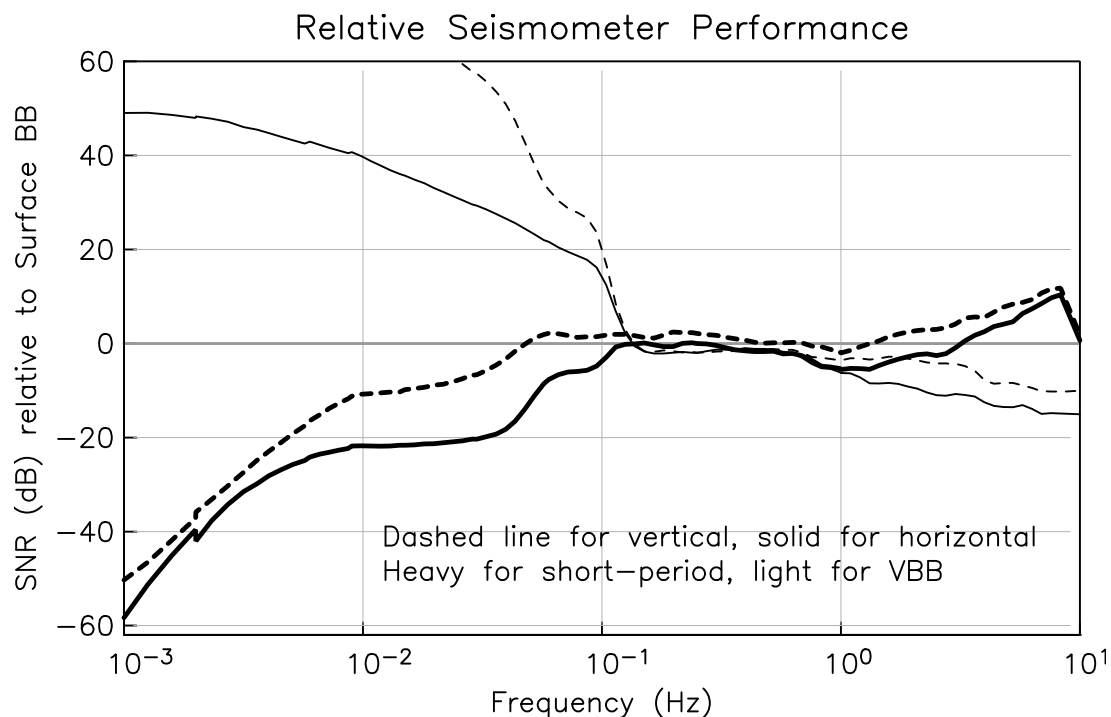


Figure B.7: Seismometer performance as a function of frequency, in decibels (dB), for the different seismometer types analyzed here, similar to Figure 3.3. The comparisons shown are for short-period borehole geophones of the PBO network (thick lines), and surface very-broadband (VBB) instruments of the IDA-IRIS network (thin lines); each comparison is relative to median noise levels for the vertical components of surface broadband (BB) instruments in the Anza network. Dashed lines show comparisons using vertical components, and solid lines show comparisons using horizontal components.

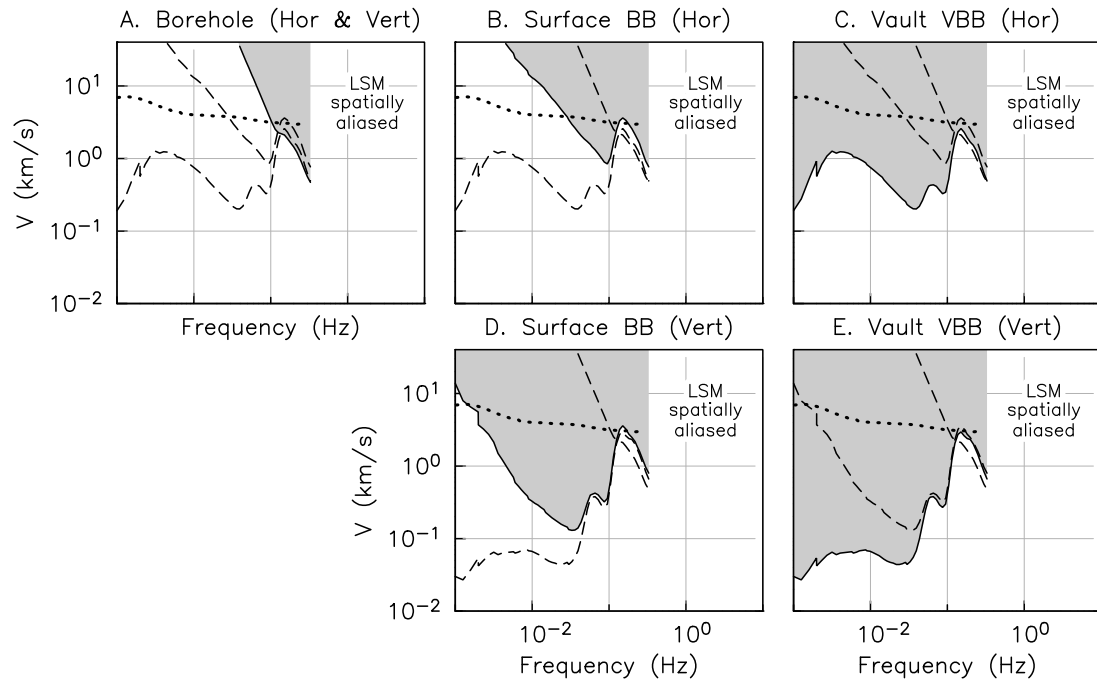


Figure B.8: Unity signal-detection curves ($D(f) = 1$) using longbase laser strainmeter (LSM) noise levels similar to Figure 3.2. The gray region highlights where a seismometer will have a greater sensitivity to seismic waves, and the black dotted-line shows the composite dispersion spectrum observed in the earth. The upper frequency limit of the curves is at the Nyquist frequency of the LSM data (0.5 Hz); above this the data are affected by spatial aliasing.

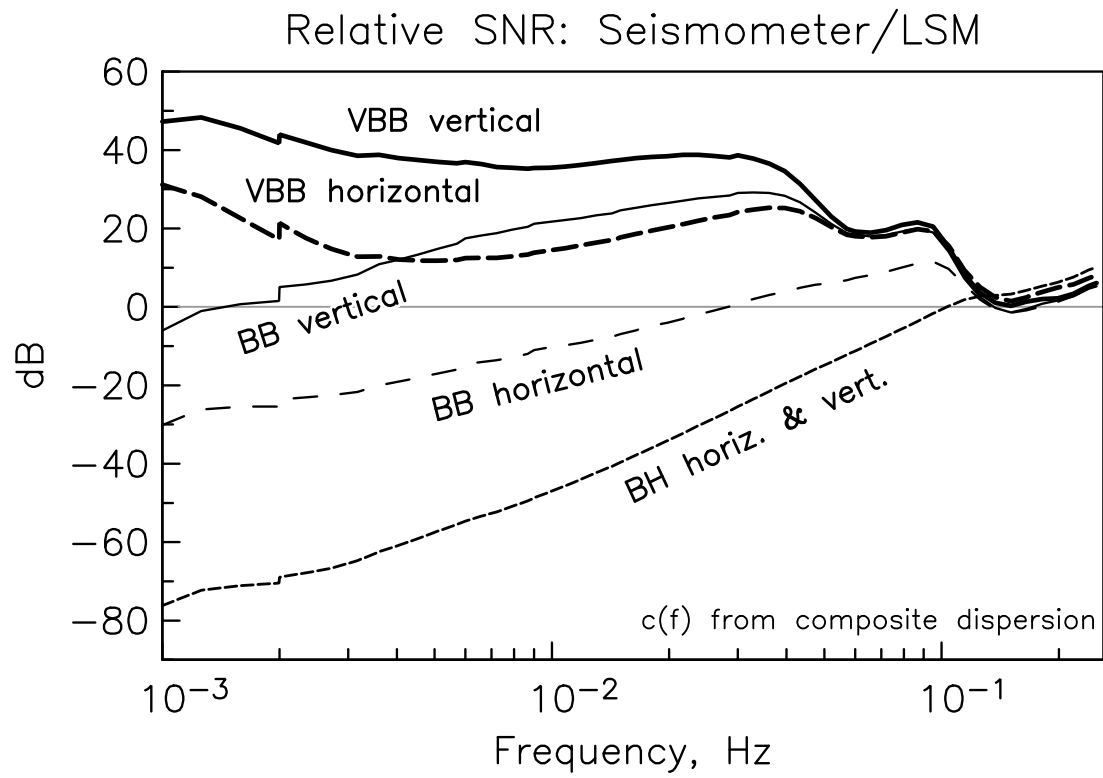


Figure B.9: Relative signal-to-noise ratio (SNR) for seismometers relative to longbase laser strainmeters, for the lowest expected phase velocity for seismic signals, similar to Figure 3.3.

B.3 Acknowledgements

Figures in this appendix are figures from the electronic supplements of Barbour and Agnew (2011, 2012), adapted for the dissertation. The dissertation author was the primary investigator and author of these papers.

Bibliography

- Agnew, D. C., Strainmeters and tiltmeters, *Rev. Geophys.*, *24*, 579–624, doi:10.1029/RG024i003p00579, 1986.
- Agnew, D. C., The time-domain behavior of power-law noises, *Geophys. Res. Lett.*, *19*(4), 333–336, doi:10.1029/91GL02832, 1992.
- Agnew, D. C., NLOADF: A program for computing ocean-tide loading, *Journal of Geophysical Research: Solid Earth*, *102*(B3), 5109–5110, doi:10.1029/96JB03458, 1997.
- Agnew, D. C., Before PBO: an overview of continuous strain and tilt measurements in the United States, *J. Geod. Soc. Japan*, *53*, 157–182, doi:10.11366/sokuchi1954.53.157, 2007a.
- Agnew, D. C., Earth Tides, in *Treatise on Geophysics*, edited by G. Schubert, chap. 3, pp. 163 – 195, Elsevier, doi:10.1016/B978-044452748-6.00056-0, 2007b.
- Agnew, D. C., and J. Berger, Vertical seismic noise at very low frequencies, *J. Geophys. Res.*, *83*, 5420–5424, doi:10.1029/JB083iB11p05420, 1978.
- Agnew, D. C., and K. Hodgkinson, Designing compact causal digital filters for low-frequency strainmeter data, *Bull. Seismol. Soc. Amer.*, *97*(1B), 91–99, doi:10.1785/0120060088, 2007.
- Agnew, D. C., and F. K. Wyatt, Long-base laser strainmeters: a review, *Sio technical report*, Scripps Institution of Oceanography, available at http://escholarship.org/uc/sio_techreport, 2003.
- Agnew, D. C., and F. K. Wyatt, Dynamic Strains from Regional and Teleseismic Earthquakes, *submitted*, 2014.
- Aki, K., and P. G. Richards, *Quantitative Seismology*, University Science Books, Sausalito, 2002.
- Allam, A. A., and Y. Ben-Zion, Seismic velocity structures in the southern California plate-boundary environment from double-difference tomography, *Geophysical Journal International*, *190*(2), 1181–1196, doi:10.1111/j.1365-246X.2012.05544.x, 2012.

- Auger, I. E., and C. E. Lawrence, Algorithms for the optimal identification of segment neighborhoods, *Bulletin of Mathematical Biology*, 51(1), 39–54, doi:10.1007/BF02458835, 1989.
- Barbour, A. J., Systematic reduction of pore pressure response near the San Jacinto fault, *Abstract S21B-2456 presented at 2012 Fall Meeting*, AGU, San Francisco, Calif., 3-7 Dec., 2012.
- Barbour, A. J., Pathfinder Ranch pumping data, doi:10.5281/zenodo.7582, Available at <https://zenodo.org/record/7582>, 2013.
- Barbour, A. J., and D. C. Agnew, Noise Levels on Plate Boundary Observatory Borehole Strainmeters in Southern California, *Bull. Seismol. Soc. Amer.*, 101(5), 2453–2466, doi:10.1785/0120110062, 2011.
- Barbour, A. J., and D. C. Agnew, Detection of Seismic Signals Using Seismometers and Strainmeters, *Bull. Seismol. Soc. Amer.*, 102(6), 2484–2490, doi:10.1785/0120110298, 2012.
- Barbour, A. J., and R. L. Parker, psd: Adaptive, sine multitaper power spectral density estimation for R, *Computers & Geosciences*, 63(0), 1 – 8, doi:10.1016/j.cageo.2013.09.015, 2014.
- Barton, C. A., M. D. Zoback, and D. Moos, Fluid flow along potentially active faults in crystalline rock, *Geology*, 23(8), 683–686, doi:10.1130/0091-7613(1995)023<0683:FFAPAF>2.3.CO;2, 1995.
- Bear, J., *Hydraulics of Groundwater*, 569 pp., Dover Publications, New York, 1979.
- Beaumont, C., and J. Berger, An analysis of tidal strain observations from the United States of America: I. The laterally homogeneous tide, *Bulletin of the Seismological Society of America*, 65(6), 1613–1629, 1975.
- Bellman, R. E., and S. E. Dreyfus, *Applied dynamic programming*, vol. 7962, Princeton University Press, Princeton, New Jersey, 1966.
- Benioff, H., and B. Gutenberg, The response of strain and pendulum seismographs to surface waves, *Bull. Seismol. Soc. Am.*, 42, 229–237, 1952.
- Bense, V. F., T. Gleeson, S. E. Loveless, O. Bour, and J. Scibek, Fault zone hydrogeology, *Earth-Science Reviews*, 127, 171–192, doi:10.1016/j.earscirev.2013.09.008, 2013.
- Berger, J., and C. Beaumont, An analysis of tidal strain observations from the United States of America II. The inhomogeneous tide, *Bulletin of the Seismological Society of America*, 66(6), 1821–1846, 1976.

- Berger, J., and J. Levine, The Spectrum of Earth Strain From 10^{-8} to 10^2 Hz, *J. Geophys. Res.*, *79*(8), 1210, doi:10.1029/JB079i008p01210, 1974.
- Berger, J., P. Davis, and G. Ekström, Ambient Earth noise: A survey of the Global Seismographic Network, *J. Geophys. Res.*, *109*, B11,307, doi:10.1029/2004JB003408, 2004.
- Biot, M. A., General theory of three-dimensional consolidation, *Journal of Applied Physics*, *12*(2), 155–164, doi:10.1063/1.1712886, 1941.
- Blum, J., H. Igel, and M. Zumberge, Observations of Rayleigh-Wave phase velocity and coseismic deformation using an optical fiber, interferometric vertical strainmeter at the SAFOD borehole, California, *Bull. Seismol. Soc. Am.*, *100*, 1879–1891, doi:10.1785/0120090333, 2010.
- Bonnefoy-Claudet, S., F. Cotton, and P.-Y. Bard, The nature of noise wavefield and its application for site effects studies. A literature review., *Earth Sci. Rev.*, *79*, 205–227, doi:10.1016/j.earscirev.2006.07.004, 2006.
- Bonnet, E., O. Bour, N. Odling, P. Davy, I. Main, P. Cowie, and B. Berkowitz, Scaling of fracture systems in geological media, *Reviews of Geophysics*, *39*(3), 347–383, doi:10.1029/1999RG000074, 2001.
- Booker, J. R., and J. P. Carter, Analysis of a point sink embedded in a porous elastic half space, *International Journal for Numerical and Analytical Methods in Geomechanics*, *10*(2), 137–150, doi:10.1002/nag.1610100204, 1986.
- Borcherdt, R. D., M. J. S. Johnston, and G. Glassmoyer, On the use of volumetric strain meters to infer additional characteristics of short-period seismic radiation, *Bull. Seismol. Soc. Amer.*, *79*(4), 1006–1023, 1989.
- Bower, D. R., Bedrock fracture parameters from the interpretation of well tides, *J. Geophys. Res.*, *88*, 5025–5035, doi:10.1029/JB088iB06p05025, 1983.
- Brace, W., Permeability of crystalline and argillaceous rocks, *International Journal of Rock Mechanics and Mining Sciences & Geomechanics Abstracts*, *17*(5), 241 – 251, doi:10.1016/0148-9062(80)90807-4, 1980.
- Brace, W. F., Permeability of crystalline rocks: New in situ measurements, *Journal of Geophysical Research: Solid Earth*, *89*(B6), 4327–4330, doi:10.1029/JB089iB06p04327, 1984.
- Brace, W. F., J. B. Walsh, and W. T. Frangos, Permeability of Granite under High Pressure, *J. Geophys. Res.*, *73*(6), 2225–2236, doi:10.1029/JB073i006p02225, 1968.

- Bredehoeft, J. D., Response of well-aquifer systems to earth tides, *Journal of Geophysical Research*, 72(12), 3075–3087, doi:10.1029/JZ072i012p03075, 1967.
- Brocher, T. M., Empirical relations between elastic wavespeeds and density in the earth's crust, *Bull. Seismol. Soc. Am.*, 95, 2081–2092, doi:10.1785/0120050077, 2005.
- Brodsky, E. E., and L. J. Lajoie, Anthropogenic Seismicity Rates and Operational Parameters at the Salton Sea Geothermal Field, *Science*, 341(6145), 543–546, doi:10.1126/science.1239213, 2013.
- Brodsky, E. E., E. Roeloffs, D. Woodcock, I. Gall, and M. Manga, A mechanism for sustained groundwater pressure changes induced by distant earthquakes, *J. Geophys. Res.*, 108(B4), doi:10.1029/2002JB002321, 2003.
- Brodsky, E. E., J. J. Gilchrist, A. Sagy, and C. Collettini, Faults smooth gradually as a function of slip, *Earth and Planetary Science Letters*, 302(1-2), 185 – 193, doi:10.1016/j.epsl.2010.12.010, 2011.
- Brune, J. N., and J. Oliver, The seismic noise of the earth's surface, *Bull. Seismol. Soc. Am.*, 49(4), 349–353, 1959.
- Castro, R. R., C. Valdes-Gonzalez, P. Shearer, V. Wong, L. Astiz, F. Vernon, A. Perez-Vertti, and A. Mendoza, The 3 August 2009 Mw 6.9 Canal de Ballenas Region, Gulf of California, Earthquake and Its Aftershocks, *Bull. Seismol. Soc. Amer.*, 101(3), 929–939, doi:10.1785/0120100154, 2011.
- Chester, F. M., and J. M. Logan, Implications for mechanical properties of brittle faults from observations of the Punchbowl fault zone, California, *Pure and Applied Geophysics*, 124(1-2), 79–106, doi:10.1007/BF00875720, 1986.
- Cleary, M. P., Fundamental solutions for a fluid-saturated porous solid, *International Journal of Solids and Structures*, 13(9), 785 – 806, doi:10.1016/0020-7683(77)90065-8, 1977.
- Cleveland, W., *Visualizing Data*, Hobart, Summit, New Jersey, 1993.
- Cleveland, W. S., and S. T. Devlin, Locally weighted regression: an approach to regression analysis by local fitting, *J. Amer. Stat. Ass.*, 83(403), 596–610, doi:10.1080/01621459.1988.10478639, 1988.
- Cochran, E., Y. Li, P. Shearer, S. Barbot, Y. Fialko, and J. Vidale, Seismic and geodetic evidence for extensive, long-lived fault damage zones, *Geology*, 37, 315–318, doi:10.1130/G25306A.1, 2009.
- Constantine, W., and D. Percival, *sapa: Spectral Analysis for Physical Applications*, R package version 1.1-0, 2012.

- Cooper, H. H., J. D. Bredehoeft, I. S. Papadopoulos, and R. R. Bennett, The response of well-aquifer systems to seismic waves, *J. Geophys. Res.*, *70*(16), 3915–3926, doi:10.1029/JZ070i016p03915, 1965.
- Cowpertwait, P. S. P., and A. V. Metcalfe, *Introductory Time Series with R*, 1st ed., Springer Publishing Company, Incorporated, doi:10.1007/978-0-387-88698-5, 2009.
- Day-Lewis, A., Characterization and Modeling of In Situ Stress Heterogeneity, Ph.D. thesis, Stanford University, 2007.
- Dickinson, W. R., Kinematics of Transrotational Tectonism in the California Transverse Ranges and Its Contribution to Cumulative Slip Along the San Andreas Transform Fault System, *Geological Society of America Special Papers*, *305*, 1–46, doi:10.1130/0-8137-2305-1.1, 1996.
- Doan, M. L., E. E. Brodsky, Y. Kano, and K. F. Ma, In situ measurement of the hydraulic diffusivity of the active Chelungpu Fault, Taiwan, *Geophys. Res. Lett.*, *33*(16), L16,317, doi:10.1029/2006GL026889, 2006.
- Dragert, H., and K. Wang, Temporal evolution of an episodic tremor and slip event along the northern Cascadia margin, *J. Geophys. Res.*, *116*(B12), B12,406, doi:10.1029/2011JB008609, 2011.
- Durbin, T. J., Ground-water hydrology of Garner Valley, San Jacinto Mountains, California; a mathematical analysis of recharge and discharge, *Open-File Report 75-305*, U.S. Geological Survey, 1975.
- Eckley, I. A., P. Fearnhead, and R. Killick, *Analysis of changepoint models*, chap. 10, Bayesian Time Series Models, Cambridge University Press, 2011.
- Elkhoury, J., A. Niemeijer, E. Brodsky, and C. Marone, Laboratory observations of permeability enhancement by fluid pressure oscillation of in situ fractured rock, *J. Geophys. Res.*, *116*, B02,311, doi:10.1029/2010JB007759, 2011.
- Elkhoury, J. E., E. E. Brodsky, and D. C. Agnew, Seismic waves increase permeability, *Nature*, *441*(7097), 1135–8, doi:10.1038/nature04798, 2006.
- Ellsworth, W. L., Injection-Induced Earthquakes, *Science*, *341*(6142), doi:10.1126/science.1225942, 2013.
- Engelder, T., *Stress regimes in the lithosphere*, 457 pp., Princeton University Press, Princeton, New Jersey, 1993.
- Evans, J. P., C. B. Forster, and J. V. Goddard, Permeability of fault-related rocks, and implications for hydraulic structure of fault zones, *Journal of Structural Geology*, *19*(11), 1393 – 1404, doi:10.1016/S0191-8141(97)00057-6, 1997.

- Evans, K., and F. Wyatt, Water table effects on the measurement of earth strain, *Tectonophysics*, 108(3–4), 323 – 337, doi:10.1016/0040-1951(84)90242-7, 1984.
- Fabian, M., and H.-J. Kumpel, Poroelasticity: observations of anomalous near surface tilt induced by ground water pumping, *Journal of Hydrology*, 281(3), 187 – 205, doi:10.1016/S0022-1694(03)00234-8, 2003.
- Faulkner, D. R., C. A. Jackson, R. J. Lunn, R. W. Schlische, Z. K. Shipton, C. A. Wibberley, and M. O. Withjack, A review of recent developments concerning the structure, mechanics and fluid flow properties of fault zones, *Journal of Structural Geology*, 32(11), 1557 – 1575, doi:10.1016/j.jsg.2010.06.009, 2010.
- Fialko, Y., Interseismic strain accumulation and the earthquake potential on the southern San Andreas fault system, *Nature*, 441(7096), 968–971, doi:10.1038/nature04797, 2006.
- Fialko, Y., D. Sandwell, D. Agnew, M. Simons, P. Shearer, and B. Minster, Deformation on nearby faults induced by the 1999 Hector Mine earthquake, *Science*, 297, 1858–1862, doi:10.1126/science.1074671, 2002.
- Fialko, Y., L. Rivera, and H. Kanamori, Estimate of differential stress in the upper crust from variations in topography and strike along the San Andreas fault, *Geophysical Journal International*, 160(2), 527–532, doi:10.1111/j.1365-246X.2004.02511.x, 2005.
- Fialko, Y., J. A. Gonzalez-Ortega, J. Gonzallez, S. Barbot, S. Leprince, D. T. Sandwell, and D. C. Agnew, Static Rupture Model of the 2010 M7.2 El Mayor-Cucapah Earthquake from ALOS, ENVISAT, SPOT and GPS Data, *Abstract T53B-2125 presented at 2010 Fall Meeting*, AGU, San Francisco, Calif., 13-17 Dec., 2010.
- Fix, J. E., Strain-inertial seismograph complexes, *Rep. TR-73-16*, Teledyne-Geotech, Garland, Texas, nTIS AD-A005 708/3GI, 1973.
- Fix, J. E., and J. R. Sherwin, A high-sensitivity strain-inertial seismograph installation, *Bull. Seismol. Soc. Am.*, 60, 1803–1822, 1970.
- Fix, J. E., and J. R. Sherwin, Development of LP wave discrimination capability using LP strain instruments, *Rep. TR-72-3*, Teledyne-Geotech, Garland, Texas, nTIS AD-748-232 Available at <http://www.dtic.mil/srch/doc?collection=t3&id=AD0748232>, 1972.
- Fletcher, J. B., T. Fumal, H.-P. Liu, and L. C. Carroll, Near-surface velocities and attenuation at two boreholes near Anza, California, from logging data, *Bull. Seismol. Soc. Amer.*, 80(4), 807–831, 1990.

- Fox, D. G., Judging Air Quality Model Performance, *Bull. Amer. Meteor. Soc.*, 62(5), 599–609, doi:10.1175/1520-0477(1981)062<0599:JAQMP>2.0.CO;2, 1981.
- Freeze, R. A., and J. A. Cherry, *Groundwater*, 604 pp., Prentice-Hall, Englewood Cliffs, New Jersey, 1979.
- Gazeaux, J., S. Williams, M. King, M. Bos, R. Dach, M. Deo, A. W. Moore, L. Ostini, E. Petrie, M. Roggero, F. N. Teferle, G. Olivares, and F. H. Webb, Detecting offsets in GPS time series: First results from the detection of offsets in GPS experiment, *Journal of Geophysical Research: Solid Earth*, 118(5), 2397–2407, doi:10.1002/jgrb.50152, 2013.
- Geertsma, J., Land subsidence above compacting oil and gas reservoirs, *J. Pet. Tech.*, 25(6), 734–744, doi:10.2118/3730-PA, 1973.
- Given, H. K., Variations in broadband seismic noise at IRIS/IDA stations in the USSR with implications for event detection, *Bull. Seismol. Soc. Amer.*, 80(6B), 2072–2088, 1990.
- Gladwin, M. T., High precision multi-component borehole deformation monitoring, *Rev. Sci. Instrum.*, 55(12), 2011, doi:10.1063/1.1137704, 1984.
- Gladwin, M. T., and R. Hart, Design Parameters for Borehole Strain Instrumentation, *Pure Appl. Geophys.*, 123, doi:10.1007/BF00877049, 1985.
- Gomberg, J., and D. C. Agnew, The accuracy of seismic estimates of dynamic strains: an evaluation using strainmeter and seismometer data from Piñon Flat Observatory, California, *Bull. Seismol. Soc. Am.*, 86, 212–220, 1996.
- Gomberg, J., J. L. Rubinstein, Z. Peng, K. C. Creager, J. E. Vidale, and P. Bodin, Widespread Triggering of Nonvolcanic Tremor in California, *Science*, 319(319), 173, doi:10.1126/science.1149164, 2008.
- Grant, E. B., Gladwin Tensor Strainmeter Calibration Using Seismic Data: Instrument Calibration Methods and Wave Gradiometry Applications, Ph.D. thesis, University of Memphis, 2010.
- GSi/water, Ground Water Resource Evaluation, Pine Meadow, Riverside County, California, *Tech. rep.*, Lake Hemet Municipal Water District, 2004.
- GSi/water, Hydrogeologic Investigation for “Safe Yield”, Pine Meadow, Riverside County, California, *Tech. rep.*, Lake Hemet Municipal Water District, 2007.
- Hart, R. H. G., M. T. Gladwin, R. L. Gwyther, D. C. Agnew, and F. K. Wyatt, Tidal calibration of borehole strain meters: Removing the effects of small-scale inhomogeneity, *J. Geophys. Res.*, 101(B11), 25,553–25,571, doi:10.1029/96JB02273, 1996.

- Hauksson, E., J. Stock, K. Hutton, W. Yang, J. Vidal-Villegas, and H. Kanamori, The 2010 Mw 7.2 El Mayor-Cucapah Earthquake Sequence, Baja California, Mexico and Southernmost California, USA: Active Seismotectonics along the Mexican Pacific Margin, *Pure and Applied Geophysics*, 168, 1255–1277, doi:10.1007/s00024-010-0209-7, 2011.
- Hauksson, E., W. Yang, and P. M. Shearer, Waveform Relocated Earthquake Catalog for Southern California (1981 to June 2011), *Bulletin of the Seismological Society of America*, 102(5), 2239–2244, doi:10.1785/0120120010, 2012.
- Hawthorne, J. C., and A. M. Rubin, Short-time scale correlation between slow slip and tremor in Cascadia, *Journal of Geophysical Research: Solid Earth*, 118(3), 1316–1329, doi:10.1002/jgrb.50103, 2013.
- Healy, J. H., W. W. Rubey, D. T. Griggs, and C. B. Raleigh, The Denver Earthquakes, *Science*, 161(3848), 1301–1310, doi:10.1126/science.161.3848.1301, 1968.
- Heidbach, O., M. Tingay, A. Barth, J. Reinecker, D. Kurfeř, and B. Müller, Global crustal stress pattern based on the World Stress Map database release 2008, *Tectonophysics*, 482, 3–15, doi:10.1016/j.tecto.2009.07.023, 2010.
- Helstrom, C. W., *Statistical Theory of Signal Detection*, Pergamon, New York, 1968.
- Hetényi, M., *Handbook of Experimental Stress Analysis*, Wiley, New York, New York, 1950.
- Hill, R. I., Geology of Garner Valley and vicinity, *Geology of the San Jacinto Mountains, Field Trip Guide*, 9A, 90–99, 1981.
- Hirata, T., T. Satoh, and K. Ito, Fractal structure of spatial distribution of microfracturing in rock, *Geophysical Journal International*, 90(2), 369–374, doi:10.1111/j.1365-246X.1987.tb00732.x, 1987.
- Hisz, D. B., L. C. Murdoch, and L. N. Germanovich, A portable borehole extensometer and tiltmeter for characterizing aquifers, *Water Resources Research*, 49, 7900–7910, doi:10.1002/wrcr.20500, 2013.
- Hodgkinson, K., A. Borsa, D. Mencin, C. Walls, O. Fox, and E. VanBoskirk, The July 7th 2010 M5.4 Borrego Springs Earthquake as Recorded by PBO Geodetic and Seismic Instruments, *Abstract 83:2-437 presented at 2012 Fall Meeting, SSA*, San Diego, Calif., 17-19 Apr., 2012.
- Hodgkinson, K., J. Langbein, B. Henderson, D. Mencin, and A. Borsa, Tidal calibration of Plate Boundary Observatory borehole strainmeters, *Journal of*

- Geophysical Research: Solid Earth*, 118(1), 447–458, doi:10.1029/2012JB009651, 2013.
- Hsieh, P. A., J. D. Bredehoeft, and J. M. Farr, Determination of Aquifer Transmissivity From Earth Tide Analysis, *Water Resour. Res.*, 23(10), 1824–1832, doi:10.1029/WR023i010p01824, 1987.
- Hsieh, P. A., J. D. Bredehoeft, and S. A. Rojstaczer, Response of well aquifer systems to Earth tides: Problem revisited, *Water Resources Research*, 24(3), 468–472, doi:10.1029/WR024i003p00468, 1988.
- Jacob, C. E., Drawdown test to determine effective radius of artesian well, *Transactions of the American Society of Civil Engineers*, 112(1), 1047–1064, 1947.
- Johnston, M. J. S., A. T. Linde, M. T. Gladwin, and R. D. Borchardt, Fault failure with moderate earthquakes, *Tectonophysics*, 144, 189–206, doi:10.1016/0040-1951(87)90017-5, 1987.
- Jónsson, S., P. Segall, R. Pedersen, and G. Bjornsson, Post-earthquake ground movements correlated to pore-pressure transients, *Nature*, 424(6945), 179–183, doi:10.1038/nature01776, 2003.
- Kaiser, J. F., and W. A. Reed, Data smoothing using low-pass digital filters, *Rev. Sci. Instrum.*, 48(11), 1447–1457, doi:10.1063/1.1134918, 1977.
- Kamp, G. V. D., and J. E. Gale, Theory of earth tide and barometric effects in porous formations with compressible grains, *Water Resour. Res.*, 19, 538–544, doi:10.1029/WR019i002p00538, 1983.
- Kano, Y., and H. Ito, Modeling of permeability structure using pore pressure and borehole strain monitoring, *EOS Trans. Am. Geophys. Union*, 92, Fall Meet. Suppl. Abstract T33F–2490, 2011.
- Kano, Y., and T. Yanagidani, Broadband hydroseismograms observed by closed borehole wells in the Kamioka mine, central Japan: Response of pore pressure to seismic waves from 0.05 to 2 Hz, *J. Geophys. Res.*, 111, B03,410, doi:10.1029/2005JB003656, 2006.
- Kennett, B. L. N., and E. R. Engdahl, Traveltimes for global earthquake location and phase identification, *Geophysical Journal International*, 105(2), 429–465, doi:10.1111/j.1365-246X.1991.tb06724.x, 1991.
- Keranen, K. M., H. M. Savage, G. A. Abers, and E. S. Cochran, Potentially induced earthquakes in Oklahoma, USA: Links between wastewater injection and the 2011 Mw 5.7 earthquake sequence, *Geology*, 41(6), 699–702, doi:10.1130/G34045.1, 2013.

- Killick, R., and I. A. Eckley, changepoint: An R package for changepoint analysis, *Journal of Statistical Software*, *In press*, 2014.
- Killick, R., P. Fearnhead, and I. A. Eckley, Optimal Detection of Changepoints With a Linear Computational Cost, *Journal of the American Statistical Association*, *107*(500), 1590–1598, doi:10.1080/01621459.2012.737745, 2012.
- King, C.-Y., R. D. Nason, and R. O. Burford, Coseismic steps recorded on creep meters along the San Andreas Fault, *Journal of Geophysical Research*, *82*(11), 1655–1662, doi:10.1029/JB082i011p01655, 1977.
- King, G. C. P., and R. Bilham, A geophysical wire strainmeter, *Bull. Seismol. Soc. Am.*, *66*, 2039–2047, 1976.
- Kitagawa, Y., S. Itaba, N. Matsumoto, and N. Koizumi, Frequency characteristics of the response of water pressure in a closed well to volumetric strain in the high-frequency domain, *J. Geophys. Res.*, *116*(B8), doi:10.1029/2010JB007794, 2011.
- Kugler, S., T. Bohlen, T. Forbriger, S. Bussat, and G. Klein, Scholte-wave tomography for shallow-water marine sediments, *Geophys. J. Internat.*, *168*, 551–570, doi:10.1111/j.1365-246X.2006.03233.x, 2007.
- Kümpel, H. J., Poroelasticity: parameters reviewed, *Geophysical Journal International*, *105*(3), 783–799, doi:10.1111/j.1365-246X.1991.tb00813.x, 1991.
- Langbein, J., Computer algorithm for analyzing and processing borehole strainmeter data, *Computers & Geosciences*, *36*(5), 611 – 619, doi:10.1016/j.cageo.2009.08.011, 2010a.
- Langbein, J., Effect of error in theoretical Earth tide on calibration of borehole strainmeters, *Geophys. Res. Lett.*, *37*(L21303), doi:10.1029/2010GL044454, 2010b.
- Langston, C. A., and C. Liang, Gradiometry for polarized seismic waves, *Journal of Geophysical Research*, *113*(B8), doi:10.1029/2007JB005486, 2008.
- Lee, J., and G. Fenves, Plastic-Damage Model for Cyclic Loading of Concrete Structures, *Journal of Engineering Mechanics*, *124*(8), 892–900, doi:10.1061/(ASCE)0733-9399(1998)124:8(892), 1998.
- Lees, J. M., *RSEIS: Seismic Time Series Analysis Tools*, R package version 3.2-5, 2013.
- Li, Y. G., K. Aki, and F. L. Vernon, San Jacinto fault zone guided waves: a discrimination for recently active fault strands near Anza, California, *J. Geophys. Res.*, *102*, 11,689–11,701, 20,437, 1997.

- Li, Y. G., K. Aki, J. E. Vidale, and F. Xu, Shallow structure of the Landers fault zone from explosion-generated trapped waves, *J. Geophys. Res.*, *104*, 20,257–20,275, 1999.
- Lin, G., P. M. Shearer, and E. Hauksson, Applying a three-dimensional velocity model, waveform cross correlation, and cluster analysis to locate southern California seismicity from 1981 to 2005, *J. Geophys. Res.*, *112*, doi:10.1029/2007JB004986, 2007.
- Linde, A. T., and M. J. S. Johnston, Source parameters of the October 1, 1987 Whittier Narrows earthquake from crustal deformation data, *J. Geophys. Res.*, *94*, 9633–9643, doi:10.1029/JB094iB07p09633, 1989.
- Linde, A. T., and S. Sacks, Sacks-Evertson borehole strainmeters: New designs, volcanic activity and slow earthquakes, *Eos Trans. AGU, Fall Meet. Suppl.*, *89*, G21B–0693, 2008.
- Lindsey, E. O., and Y. Fialko, Geodetic slip rates in the southern San Andreas Fault system: Effects of elastic heterogeneity and fault geometry, *Journal of Geophysical Research: Solid Earth*, *118*(2), 689–697, doi:10.1029/2012JB009358, 2013.
- Lindsey, E. O., V. J. Sahakian, Y. Fialko, Y. Bock, S. Barbot, and T. K. Rockwell, Interseismic Strain Localization in the San Jacinto Fault Zone, *Pure and Applied Geophysics*, pp. 1–18, doi:10.1007/s00024-013-0753-z, 2013.
- Liu, L.-B., E. Roeloffs, and X.-Y. Zheng, Seismically Induced Water Level Fluctuations in the Wali Well, Beijing, China, *J. Geophys. Res.*, *94*(B7), 9453–9462, doi:10.1029/JB094iB07p09453, 1989.
- Longuevergne, L., N. Florsch, F. Boudin, L. Oudin, and C. Camerlynck, Tilt and strain deformation induced by hydrologically active natural fractures: Application to the tiltmeters installed in Sainte-Croix-aux-Mines observatory (France), *Geophysical Journal International*, *178*(2), 667–677, doi:10.1111/j.1365-246X.2009.04197.x, 2009.
- Manga, M., I. Beresnev, E. Brodsky, J. Elkhoury, D. Elsworth, S. Ingebritsen, D. Mays, and C. Wang, Changes in permeability caused by transient stresses: Field observations, experiments, and mechanisms, *Rev. Geophys.*, *50*, RG2004, doi:10.1029/2011RG000382, 2012.
- Marliyani, G. I., T. K. Rockwell, N. W. Onderdonk, and S. F. McGill, Straightening of the Northern San Jacinto Fault, California, as Seen in the Fault-Structure Evolution of the San Jacinto Valley Stepover, *Bulletin of the Seismological Society of America*, *103*(3), 2047–2061, doi:10.1785/0120120232, 2013.

- McGarr, A., I. S. Sacks, A. T. Linde, S. M. Spottiswoode, and R. W. E. Green, Coseismic and other short-term strain changes recorded with Sacks-Evertson strainmeters in a deep mine, South Africa, *Geophysical Journal of the Royal Astronomical Society*, 70(3), 717–740, doi:10.1111/j.1365-246X.1982.tb05980.x, 1982.
- McNamara, D. E., and R. I. Boaz, Seismic noise analysis system using power spectral density probability density functions: A stand-alone software package, *U.S. Geol. Surv. Open-File Rep.*, 2005-1438, 30, 2005.
- McNamara, D. E., and R. P. Buland, Ambient Noise Levels in the Continental United States, *Bull. Seismol. Soc. Amer.*, 94(4), 1517–1527, doi:10.1785/012003001, 2004.
- Mikumo, T., and K. Aki, Determination of local phase velocity by intercomparison of seismograms from strain and pendulum instruments, *J. Geophys. Res.*, 69, 721–731, doi:10.1029/JZ069i004p00721, 1964.
- Molnar, P., R. S. Anderson, and S. P. Anderson, Tectonics, fracturing of rock, and erosion, *J. Geophys. Res.*, 112(F03014), doi:10.1029/2005JF000433, 2007.
- Morrow, C. A., L. Q. Shi, and J. D. Byerlee, Permeability of fault gouge under confining pressure and shear stress, *J. Geophys. Res.*, 89(B5), 3193–3200, doi:10.1029/JB089iB05p03193, 1984.
- Morton, N., G. Girty, and T. Rockwell, Fault zone architecture of the San Jacinto fault zone in Horse Canyon, southern California: A model for focused post-seismic fluid flow and heat transfer in the shallow crust, *Earth Planet. Sci. Lett.*, 329-330, 71–83, doi:10.1016/j.epsl.2012.02.013, 2012.
- O’Connell, R. J., and B. Budiansky, Seismic Velocities in Dry and Saturated Cracked Solids, *J. Geophys. Res.*, 79(35), 5412–5426, doi:10.1029/JB079i035p05412, 1974.
- Ohno, M., H. Wakita, and K. Kanjo, A water well sensitive to seismic waves, *Geophys. Res. Lett.*, 24(6), 691–694, doi:10.1029/97GL00471, 1997.
- Okada, Y., Surface deformation due to shear and tensile faults in a half-space, *Bull. Seismol. Soc. Amer.*, 75, 1135–1154, 1985.
- Onderdonk, N., The role of the Hot Springs fault in the development of the San Jacinto fault zone and uplift of the San Jacinto Mountains, in *Oasis in the Desert: Geology, Hydrogeology, and History of Groundwater in the Coachella Valley, California*, San Diego Association of Geologists Field Guidebook, 2008.
- Owens, T. J., H. P. Crotwell, C. Groves, and P. Oliver-Paul, SOD: Standing Order for Data, *Seismol. Res. Lett.*, 75, 515–520, doi:10.1785/gssrl.75.4.515-a, 2004.

- Ozawa, S., T. Nishimura, H. Suito, T. Kobayashi, M. Tobita, and T. Imakiire, Coseismic and postseismic slip of the 2011 magnitude-9 Tohoku-Oki earthquake, *Nature*, 475(7356), 373–376, doi:10.1038/nature10227, 2011.
- Park, J., A. Amoroso, L. Crescentini, and E. Boschi, Long-period toroidal earth free oscillations from the great Sumatra-Andaman earthquake observed by paired laser extensometers in Gran Sasso, Italy, *Geophys. J. Internat.*, 173, 887–905, doi:10.1111/j.1365-246X.2008.03769.x, 2008.
- Peltzer, G., P. Rosen, F. Rogez, and K. Hudnut, Poroelastic rebound along the Landers 1992 earthquake surface rupture, *Journal of Geophysical Research: Solid Earth*, 103(B12), 30,131–30,145, doi:10.1029/98JB02302, 1998.
- Percival, D., and A. Walden, *Spectral analysis for physical applications*, Cambridge University Press, ISBN 978-0521435413, 1993.
- Peterson, J., Observations and Modeling of Seismic Background Noise, *U.S. Geol. Surv. Open-File Rep.*, 93-322, 1993.
- Press, F., Displacements, Strains, and Tilts at Teleseismic Distances, *J. Geophys. Res.*, 70(10), 2395–2412, doi:10.1029/JZ070i010p02395, 1965.
- Priestley, M. B., *Spectral Analysis and Time Series*, 890 pp., Academic, Orlando, Fla., 1981.
- Prieto, G. A., R. L. Parker, D. J. Thomson, F. L. Vernon, and R. L. Graham, Reducing the bias of multitaper spectrum estimates, *Geophysical Journal International*, 171(3), 1269–1281, doi:10.1111/j.1365-246X.2007.03592.x, 2007.
- Prieto, G. A., J. F. Lawrence, and G. C. Beroza, Anelastic Earth structure from the coherency of the ambient seismic field, *J. Geophys. Res.*, 114, B07,303, doi:10.1029/2008JB006067, 2009a.
- Prieto, G. A., R. L. Parker, and F. L. Vernon, A Fortran 90 library for multitaper spectrum analysis, *Computers & Geosciences*, 35(8), 1701 – 1710, doi:10.1016/j.cageo.2008.06.007, 2009b.
- R Core Team, *R: A Language and Environment for Statistical Computing*, R Foundation for Statistical Computing, Vienna, Austria, ISBN 3-900051-07-0, 2013.
- Radzevicius, S. J., and G. L. Pavlis, High-frequency reflections in granite: Delineation of the weathering front in granodiorite at Piñon Flat, California, *Geophysics*, 64, 1828–1835, doi:10.1190/1.1444688, 1999.
- Rahim, K., and W. Burr, *multitaper: Multitaper spectral analysis tools*, R package version 1.0, 2012.

- Razack, M., and D. Huntley, Assessing transmissivity from specific capacity in a large and heterogeneous alluvial aquifer, *Groundwater*, 29(6), 856–861, doi:10.1111/j.1745-6584.1991.tb00572.x, 1991.
- Reinhardt, H. W., Fracture Mechanics of an Elastic Softening Material like Concrete, *HERON*, 29, 2, 1984.
- Reuveni, Y., S. Kedar, S. E. Owen, A. W. Moore, and F. H. Webb, Improving sub-daily strain estimates using GPS measurements, *Geophys. Res. Lett.*, 39(11), L11,311, doi:10.1029/2012GL051927, 2012.
- Rice, J. R., and M. P. Cleary, Some Basic Stress Diffusion Solutions for Fluid-Saturated Elastic Porous Media with Compressible Constituents, *Rev. Geophys.*, 14(2), doi:10.1029/RG014i002p00227, 1976.
- Richter, B., H. Wenzel, W. Zürn, and F. Kopping, From Chandler wobble to free oscillations: comparison of cryogenic gravimeters and other instruments in a wide period range, *Phys. Earth Planet. Inter.*, 91, 131–148, doi:10.1016/0031-9201(95)03041-T, 1995.
- Riedel, K. S., and A. Sidorenko, Minimum bias multiple taper spectral estimation, *IEEE Trans. Signal Proc.*, 43(1), 188–195, doi:10.1109/78.365298, 1995.
- Riedel, K. S., and A. Sidorenko, Adaptive smoothing of the log-spectrum with multiple tapering, *IEEE Trans. Signal Proc.*, 44(7), 1794–1800, doi:10.1109/78.510625, 1996.
- Rockwell, T. K., G. G. Seitz, T. E. Dawson, and J. Young, The long record of San Jacinto fault paleoearthquakes at Hog Lake: implications for regional patterns of strain release in the southern San Andreas fault system, *Seismol. Res. Lett.*, 77, 270, 2006.
- Rodgers, P. W., S. R. Taylor, and K. K. Nakanishi, System and site noise in the Regional Seismic Test Network from 0.1 to 20 Hz, *Bull. Seismol. Soc. Amer.*, 77(2), 663–678, 1987.
- Roeloffs, E., Poroelastic Techniques in the Study of Earthquake-Related Hydrologic Phenomena, in *Advances in Geophysics*, vol. 37, edited by R. Dmowska and B. Saltzman, pp. 135 – 195, Elsevier, doi:10.1016/S0065-2687(08)60270-8, 1996.
- Roeloffs, E., Tidal calibration of Plate Boundary Observatory borehole strainmeters: Roles of vertical and shear coupling, *J. Geophys. Res.*, 115(B06405), doi:10.1029/2009JB006407, 2010.

- Roeloffs, E. A., Fault Stability Changes Induced Beneath a Reservoir With Cyclic Variations in Water Level, *J. Geophys. Res.*, *93*(B3), 2107–2124, doi:10.1029/JB093iB03p02107, 1988.
- Roeloffs, E. A., S. S. Burford, F. S. Riley, and A. W. Records, Hydrologic Effects on Water Level Changes Associated With Episodic Fault Creep Near Parkfield, California, *J. Geophys. Res.*, *94*(B9), 12,387–12,402, doi:10.1029/JB094iB09p12387, 1989.
- Roeber, C., *bspec: Bayesian spectral inference*, R package version 1.4, 2013.
- Rojstaczer, S., Intermediate Period Response of Water Levels in Wells to Crustal Strain: Sensitivity and Noise Level, *J. Geophys. Res.*, *93*(B11), 13,619–13,634, doi:10.1029/JB093iB11p13619, 1988a.
- Rojstaczer, S., Determination of fluid flow properties from the response of water levels in wells to atmospheric loading, *Water Resour. Res.*, *24*(11), 1927–1938, doi:10.1029/WR024i011p01927, 1988b.
- Rojstaczer, S., and D. C. Agnew, The Influence of Formation Material Properties on the Response of Water Levels in Wells to Earth Tides and Atmospheric Loading, *J. Geophys. Res.*, *94*(B9), 12,403–12,411, doi:10.1029/JB094iB09p12403, 1989.
- Rojstaczer, S., and S. Wolf, Permeability changes associated with large earthquakes: An example from Loma Prieta, California, *Geology*, *20*(3), 211–214, doi:10.1130/0091-7613(1992)020<0211:PCAWLE>2.3.CO;2, 1992.
- Rojstaczer, S., S. Wolf, and R. Michel, Permeability enhancement in the shallow crust as a cause of earthquake-induced hydrological changes, *Nature*, *373*(6511), 237–239, doi:10.1038/373237a0, 1995.
- Rojstaczer, S. A., S. E. Ingebritsen, and D. O. Hayba, Permeability of continental crust influenced by internal and external forcing, *Geofluids*, *8*(2), 128–139, doi:10.1111/j.1468-8123.2008.00211.x, 2008.
- Romney, C., Combinations of strain and pendulum seismographs for increasing the detectability of P, *Bull. Seismol. Soc. Am.*, *54*, 2165–2174, 1964.
- Rudnicki, J. W., Fluid mass sources and point forces in linear elastic diffusive solids, *Mechanics of Materials*, *5*(4), 383–393, doi:10.1016/0167-6636(86)90042-6, 1986.
- Sacks, I. S., S. Suyehiro, D. W. Evertson, and Y. Yamagishi, Sacks-Evertson strainmeter, its installation in Japan and some preliminary results concerning strain steps, *Pap. Meteor. Geophys.*, *22*, 195–207, 1971.

- Sacks, I. S., J. A. Snoke, R. Evans, G. King, and J. Beavan, Single-site phase velocity measurements, *Geophys. J. Roy. Astron. Soc.*, *46*, 253–258, doi:10.1111/j.1365-246X.1976.tb04157.x, 1976.
- Sakata, S., S. Shimada, and S. Noguchi, Development of new-type three-component borehole strainmeters, in *Proc. Third Joint Panel Meeting of the U.N.J.R. Panel on Earthquake Prediction Technology*, 1982.
- Savage, H. M., and E. E. Brodsky, Collateral damage: Evolution with displacement of fracture distribution and secondary fault strands in fault damage zones, *Journal of Geophysical Research: Solid Earth*, *116*(B03405), doi:10.1029/2010JB007665, 2011.
- Savage, J. C., Steketee's paradox, *Bulletin of the Seismological Society of America*, *59*(1), 381–384, 1969.
- Schwarz, G., Estimating the Dimension of a Model, *The Annals of Statistics*, *6*(2), 461–464, doi:10.1214/aos/1176344136, 1978.
- Segall, P., Stress and subsidence resulting from subsurface fluid withdrawal in the epicentral region of the 1983 Coalinga Earthquake, *J. Geophys. Res.*, *90*(B8), 6801–6816, doi:10.1029/JB090iB08p06801, 1985.
- Segall, P., Earthquakes triggered by fluid extraction, *Geology*, *17*(10), 942–946, doi:10.1130/0091-7613(1989)017<0942:ETBFE>2.3.CO;2, 1989.
- Segall, P., Induced stresses due to fluid extraction from axisymmetric reservoirs, *Pure and Applied Geophysics*, *139*, 535–560, doi:10.1007/BF00879950, 1992.
- Segall, P., *Earthquake and Volcano Deformation*, 432 pp., Princeton University Press, Princeton, New Jersey, 2010.
- Segall, P., S. Jónsson, and K. Ágústsson, When is the strain in the meter the same as the strain in the rock?, *Geophys. Res. Lett.*, *30*(19), doi:10.1029/2003GL017995, 2003.
- Shapiro, A. M., Interpretation of oscillatory water levels in observation wells during aquifer tests in fractured rock, *Water Resour. Res.*, *25*, 2129–2137, doi:10.1029/WR025i010p02129, 1989.
- Sharp, R. V., San Jacinto Fault Zone in the Peninsular Ranges of Southern California, *Geological Society of America Bulletin*, *78*(6), 705–730, doi:10.1130/0016-7606(1967)78[705:SJFZIT]2.0.CO;2, 1967.
- Sheen, D.-H., J. S. Shin, T.-S. Kang, and C.-E. Baag, Low frequency cultural noise, *Geophys. Res. Lett.*, *36*(L17314), doi:10.1029/2009GL039625, 2009.

- Sibson, R. H., Fault zone models, heat flow, and the depth distribution of earthquakes in the continental crust of the United States, *Bull. Seismol. Soc. Am.*, *72*, 151–163, 1982.
- Sibson, R. H., Earthquakes and rock deformation in crustal fault zones, *Ann. Rev. Earth Planet. Sci.*, *14*, 149–175, 1986.
- Silver, P. G., Y. Bock, D. C. Agnew, T. Henyey, A. T. Linde, T. V. McEvilly, J. B. Minster, B. A. Romanowicz, I. S. Sachs, and R. B. Smith, A plate boundary observatory, *IRIS Newsletter*, *16*(2), 7–9, 1998.
- Simons, M., S. E. Minson, A. Sladen, F. Ortega, J. Jiang, S. E. Owen, L. Meng, J.-P. Ampuero, S. Wei, R. Chu, D. V. Helmberger, H. Kanamori, E. Hetland, A. W. Moore, and F. H. Webb, The 2011 Magnitude 9.0 Tohoku-Oki Earthquake: Mosaicking the Megathrust from Seconds to Centuries, *Science*, *332*(6036), 1421–1425, doi:10.1126/science.1206731, 2011.
- Slepian, D., and H. Pollak, Prolate spheroidal wave functions, Fourier analysis and uncertainty. I, *Bell System Tech. J.*, *40*, 43–63, doi:10.1002/j.1538-7305.1961.tb03976.x, 1961.
- Stacey, F. D., and J. M. W. Rynn, Spurious local effects associated with teleseismic tilts and strains, in *Earthquake Displacement Fields and the Rotation of the Earth*, edited by L. Mansinha, D. E. Smylie, and A. E. Beck, pp. 230–234, Springer-Verlag, New York, doi:10.1007/978-94-010-3308-4_22, 1970.
- Stacey, F. D., J. M. W. Rynn, E. C. Little, and C. Croskell, Displacement and tilt transducers of 140 dB range, *J. Phys. E: Sci. Instrum.*, *2*(11), 945–949, doi:10.1088/0022-3735/2/11/310, 1969.
- Stierman, D. J., Geophysical and geological evidence for fracturing, water circulation, and chemical alteration in granitic rocks adjacent to major strike-slip faults, *J. Geophys. Res.*, *89*, 5849–5857, doi:10.1029/JB089iB07p05849, 1984.
- Stutzmann, E., M. Schimmel, G. Patau, and A. Maggi, Global climate imprint on seismic noise, *Geochem. Geophys. Geosyst.*, *10*(11), doi:10.1029/2009GC002619, 2009.
- Thatcher, W., J. A. Hileman, and T. C. Hanks, Seismic Slip Distribution along the San Jacinto Fault Zone, Southern California, and Its Implications, *Geol. Soc. Am. Bull.*, *86*, 1140–1146, doi:10.1130/0016-7606(1975)86<1140:SSDATS>2.0.CO;2, 1975.
- Thomson, D. J., Spectrum Estimation and Harmonic Analysis, in *Proc. IEEE*, vol. 70, pp. 1055–1096, Bell Labs, doi:10.1109/PROC.1982.12433, 1982.

- Townend, J., and M. D. Zoback, How faulting keeps the crust strong, *Geology*, *28*(5), 399–402, doi:10.1130/0091-7613(2000)28<399:HFKTCS>2.0.CO;2, 2000.
- van der Elst, N. J., H. M. Savage, K. M. Keranen, and G. A. Abers, Enhanced remote earthquake triggering at fluid-injection sites in the midwestern United States, *Science*, *341*(6142), 164–167, doi:10.1126/science.1238948, 2013.
- Vasco, D., K. Karasaki, and C. Doughty, Using surface deformation to image reservoir dynamics, *Geophysics*, *65*(1), 132–147, doi:10.1190/1.1444704, 2000.
- Vernon, F., Analysis of data recorded on the Anza seismic network, Ph.D. thesis, University of California, San Diego, La Jolla, 1989.
- Wang, C.-Y., Liquefaction beyond the near field, *Seismological Research Letters*, *78*(5), 512–517, doi:10.1785/gssrl.78.5.512, 2007.
- Wang, C.-Y., Y. Chia, P. Wang, and D. Dreger, Role of S waves and Love waves in coseismic permeability enhancement, *Geophys. Res. Lett.*, *36*, L09,404, doi:10.1029/2009GL037330, 2009.
- Wang, H. F., *Theory of Linear Poroelasticity with Applications to Geomechanics and Hydrogeology*, Princeton Series in Geophysics, Princeton University Press, 41 William St., Princeton, New Jersey, 08540, 2000.
- Wang, K., H. Dragert, H. Kao, and E. Roeloffs, Characterizing an “uncharacteristic” ETS event in northern Cascadia, *Geophys. Res. Lett.*, *35*, L15,303, doi:10.1029/2008GL034415, 2008.
- Wang, R., A simple orthonormalization method for stable and efficient computation of Green’s functions, *Bulletin of the Seismological Society of America*, *89*(3), 733–741, 1999.
- Wang, R., and H.-J. Kumpel, Poroelasticity: Efficient modeling of strongly coupled, slow deformation processes in a multilayered half-space, *Geophysics*, *68*(2), 705–717, doi:10.1190/1.1567241, 2003.
- Wang, T.-H., E. S. Cochran, D. Agnew, and D. D. Oglesby, Infrequent Triggering of Tremor along the San Jacinto Fault near Anza, California, *Bulletin of the Seismological Society of America*, *103*(4), 2482–2497, doi:10.1785/0120120284, 2013.
- Wdowinski, S., Deep creep as a cause for the excess seismicity along the San Jacinto fault, *Nature Geoscience*, *2*(12), 882–885, doi:10.1038/ngeo684, 2009.
- Webb, S., Seismic noise on land and on the seafloor, in *IASPEI International Handbook of Earthquake and Engineering Seismology*, edited by W. H. K. Lee, pp. 305–318, Academic Press, San Diego, 2002.

- Wei, M., Y. Kaneko, Y. Liu, and J. J. McGuire, Episodic fault creep events in California controlled by shallow frictional heterogeneity, *Nature Geoscience*, *6*(7), 566–570, doi:10.1038/ngeo1835, 2013.
- Wei, S., E. Fielding, S. Leprince, A. Sladen, J.-P. Avouac, D. Helmberger, E. Hauksson, R. Chu, M. Simons, K. Hudnut, T. Herring, and R. Briggs, Superficial simplicity of the 2010 El Mayor-Cucapah earthquake of Baja California in Mexico, *Nature Geoscience*, *4*(9), 615–618, doi:10.1038/ngeo1213, 2011.
- Welch, P., The use of fast Fourier transform for the estimation of power spectra: a method based on time averaging over short, modified periodograms, *Audio and Electroacoustics, IEEE Transactions on*, *15*(2), 70–73, doi:10.1109/TAU.1967.1161901, 1967.
- Wibberley, C. A., G. Yielding, and G. Di Toro, Recent advances in the understanding of fault zone internal structure: A review, *Geological Society, London, Special Publications*, *299*(1), 5–33, doi:10.1144/SP299.2, 2008.
- Wibberley, C. A. J., Hydraulic diffusivity of fault gouge zones and implications for thermal pressurization during seismic slip, *Earth Planets and Space*, *54*(11), 1153–1172, 2002.
- Wideman, C. J., and M. W. Major, Strain steps associated with earthquakes, *Bull. Seismol. Soc. Am.*, *57*(6), 1429–1444, 1967.
- Widmer, R., W. Zürn, and G. Masters, Observation of low-order toroidal modes from the 1989 Macquarie Rise event, *Geophys. J. Internat.*, *111*, 226–236, doi:10.1111/j.1365-246X.1992.tb00572.x, 1992.
- Williams, S. D. P., Offsets in Global Positioning System time series, *J. Geophys. Res.*, *108*(B6), 2310, doi:10.1029/2002JB002156, 2003.
- Willmott, C. J., Some Comments on the Evaluation of Model Performance, *Bull. Amer. Meteor. Soc.*, *63*, 1309–1313, doi:10.1175/1520-0477(1982)063<1309:SCOTEO>2.0.CO;2, 1982.
- Willmott, C. J., S. G. Ackleson, R. E. Davis, J. J. Feddema, K. M. Klink, D. R. Legates, J. O'Donnell, and C. M. Rowe, Statistics for the evaluation and comparison of models, *Journal of Geophysical Research: Oceans*, *90*(C5), 8995–9005, doi:10.1029/JC090iC05p08995, 1985.
- Wilson, D., J. Leon, R. Aster, J. Ni, J. Schlue, S. Grand, S. Semken, S. Baldrige, and W. Gao, Broadband Seismic Background Noise at Temporary Seismic Stations Observed on a Regional Scale in the Southwestern United States, *Bull. Seismol. Soc. Amer.*, *92*(8), 3335–3342, doi:10.1785/0120010234, 2002.

- Woessner, J., S. Jónsson, H. Sudhaus, and C. Baumann, Reliability of Coulomb stress changes inferred from correlated uncertainties of finite-fault source models, *J. Geophys. Res.*, *117*(B7), B07,303, doi:10.1029/2011JB009121, 2012.
- Woodcock, D., and E. Roeloffs, Seismically-induced water level oscillations in a fractured-rock aquifer well near Grants Pass, Oregon, *Oreg. Geol.*, *58*(2), 27–33, 1996.
- Wyatt, F. K., Measurements of Coseismic Deformation in Southern California: 1972–1982, *J. Geophys. Res.*, *93*(B7), 7923–7942, doi:10.1029/JB093iB07p07923, 1988.
- Yang, W., E. Hauksson, and P. M. Shearer, Computing a Large Refined Catalog of Focal Mechanisms for Southern California (1981–2010): Temporal Stability of the Style of Faulting, *Bulletin of the Seismological Society of America*, *102*(3), 1179–1194, doi:10.1785/0120110311, 2012.
- Yang, Y., and D. M. Forsyth, Rayleigh wave phase velocities, small-scale convection, and azimuthal anisotropy beneath southern California, *J. Geophys. Res.*, *111*, B07,306, doi:10.1029/2005JB004180, 2006.
- Yang, Z., A. Sheehan, and P. Shearer, Stress-induced upper crustal anisotropy in southern California, *J. Geophys. Res.*, *116*(B2), B02,302, doi:10.1029/2010JB007655, 2011.
- Zoback, M. D., and S. M. Gorelick, Earthquake triggering and large-scale geologic storage of carbon dioxide, *Proceedings of the National Academy of Sciences*, *109*(26), 10,164–10,168, doi:10.1073/pnas.1202473109, 2012.
- Zumberge, M. A., S. DeWolf, F. K. Wyatt, D. C. Agnew, D. Elliott, and W. Hatfield, Results from a borehole optical fiber interferometer for recording earth strain, in *Fifth European Workshop on Optical Fibre Sensors*, vol. 8794, edited by L. R. Jaroszewicz, Proc. of SPIE, doi:10.1117/12.2025896, 2013.